


12-2018

Growth and Characterization of Silicon-Germanium-Tin Semiconductors for Future Nanophotonics Devices

Bader Saad Alharthi

University of Arkansas, Fayetteville

Follow this and additional works at: <https://scholarworks.uark.edu/etd>

 Part of the [Electromagnetics and Photonics Commons](#), and the [Semiconductor and Optical Materials Commons](#)

Recommended Citation

Alharthi, Bader Saad, "Growth and Characterization of Silicon-Germanium-Tin Semiconductors for Future Nanophotonics Devices" (2018). *Theses and Dissertations*. 3012.
<https://scholarworks.uark.edu/etd/3012>

This Dissertation is brought to you for free and open access by ScholarWorks@UARK. It has been accepted for inclusion in Theses and Dissertations by an authorized administrator of ScholarWorks@UARK. For more information, please contact scholar@uark.edu, ccmiddle@uark.edu.

Growth and Characterization of Silicon-Germanium-Tin Semiconductors for Future
Nanophotonics Devices

A dissertation submitted in partial fulfillment
of the requirements for the degree of
Doctor of Philosophy in Engineering with a concentration in Electrical Engineering

by

Bader Saad Alharthi
King Saud University
Bachelor of Science in Physics, 2003
King Fahd University of Petroleum and Minerals
Master of Science in Physics, 2009
University of Arkansas
Master of Science in Electrical Engineering, 2018

December 2018
University of Arkansas

This dissertation is approved for recommendation to the Graduate Council.

Hameed A. Naseem, Ph.D.
Dissertation Director

Shui-Qing (Fisher) Yu, Ph.D.
Dissertation Co-Director

Simon Ang, Ph.D.
Committee Member

Zhong Chen, Ph.D.
Committee Member

Hugh Churchill, Ph.D.
Committee Member

Abstract

The bright future of silicon (Si) photonics has attracted research interest worldwide. The ultimate goal of this growing field is to develop a group IV based Si foundries that integrate Si-photonics with the current complementary metal–oxide–semiconductor (CMOS) on a single chip for mid-infrared optoelectronics and high speed devices. Even though group IV was used in light detection, such as photoconductors, it is still cannot compete with III-V semiconductors for light generation. This is because most of the group IV elements, such as Si and germanium (Ge), are indirect bandgap materials. Nevertheless, Ge and Si attracted industry attention because they are cheap to be used with low cost and high volume manufacturing. Thus, enhancing their light efficiency is highly desired. A key solution to improve the light efficiency of Ge is by growing tensile strained Ge-on-Si and $\text{Si}_x\text{Ge}_{1-x-y}\text{Sn}_y$ (Sn: tin) alloys. In this dissertation, Si-Ge-Sn material system was grown using chemical vapor deposition technique and further characterized by advanced optical and material techniques.

Ge-on-Si was grown at low growth temperatures by using plasma enhancement in order to achieve growth conditions compatible with CMOS technology with high quality Ge layers. First, a single step Ge layer was grown at low temperatures ($T \leq 450^\circ\text{C}$). The material and optical characterization of the single step reveal low material and optical qualities. Second, a two-step Ge-on-Si was grown ($T \leq 525^\circ\text{C}$) to improve the quality. The results show low threading dislocation density on the order of 10^7 cm^{-2} with roughness values on the order of several nm. Optical characterization reveal optical quality close to a Ge buffer grown by a traditional high temperature method.

In addition, bulk and quantum well $\text{Si}_x\text{Ge}_{1-x-y}\text{Sn}_y$ alloys were grown. The results indicate that lattice matched bulk SiGeSn/Ge can be grown with high optical and material qualities using

low cost commercial precursors. In addition, band structure and optical analysis results from a single $\text{Ge}_{0.865}\text{Sn}_{0.135}$ quantum well with $\text{Si}_{0.04}\text{Ge}_{0.895}\text{Sn}_{0.065}$ double barriers on a relaxed $\text{Ge}_{0.918}\text{Sn}_{0.08}$ buffer indicate a type-I band alignment with direct bandgap emission. Moreover, SiGeSn barriers improved the optical confinement as compared to GeSn barriers.

©2018 by Bader Saad Alharthi
All Rights Reserved

Acknowledgment

In the beginning, I would like to express my highest gratitude and appreciation to my dissertation advisors Dr. Hameed Naseem and Dr. Shui-Qing (Fisher) Yu for their continuous support and motivation during the research work of this dissertation. Their inspiration helped me to gain the deep knowledge that will help me to lead industrial and research projects at the cutting-edge technology in the field of photonics and microelectronics. My sincere thanks are also expressed to my research and course work committee members Dr. Simon Ang, Dr. Zhong Chen, and Dr. Hugh Churchill for giving me some of their valuable time to attend my oral presentations and exams. Their guidance and inspiration to improve my research work is also appreciated.

It was a pleasure for me to work with my UHV-CVD growth fellows Perry Grant, Wei Dou, and Joshua Grant. Together, we worked to keep the UHV-CVD system maintained and capable to produce high quality samples. Special appreciation goes to Dr. Wei Du and Dr. Baohua Li for helping me in editing my writing and discussions for publications. Thanks to the rest of my research group Aboozar Mosleh, Seyed Amir Ghetmiri, Sattar Al-Kabi, Yiyin Zhou, and Huong Tran, and Thach Pham for helping me to learn the research tools. I am also grateful to Joe Margetis and Dr. John Tolle from ASM for growing high quality SiGeSn bulk and GeSn quantum wells samples that were used in this work. I would like to extend my thanks and appreciation to Dr. Mourad Benamara and Dr. Andrian Kuchuk from the Institute for Nanoscience and Engineering for teaching me sample preparation and how to operate independently transmission and scanning electron microscopies and x-ray diffraction.

A lot of thanks and appreciation for the Ministry of Defense of the Kingdom of Saudi Arabia for the unlimited support during my study. I am grateful to Major General Nasser Alsubaie for giving me this opportunity. There are many other who helped me; I apologize for not naming

them one by one, but I would like to thank them one by one. In addition, I would like to thank the financial support from:

1. National Aeronautics and Space Administration Established Program to Stimulate Competitive Research (NASA EPSCoR) under contract numbers NNX15AN18A and NNX15AK32A:RID 17004;
2. Air Force Office of Scientific Research (AFOSR) under the contract number FA9550-14-1-0205;
3. Phase II of the air force Small Business Innovation Research (SBIR) "Epitaxial Technologies for SiGeSn High Performance Optoelectronics Devices" under the contract number FA9550-16-C-0016.

for partially supporting me by covering supplies, samples costs, and research equipment operation fees.

Finally, thanks from the bottom of my heart to my small family. Thanks for being with me far away from home all of these years; I will never forget your patience. Thanks for my parents and my brother Ali for their continuous Doaa and support.

Dedication

To my wife and my sons Fahd and Battal. To my family and all who gave me the true support.

Table of Contents

Chapter 1: Introduction	1
1.1 Motivation	1
1.2 Background:	5
1.2.1 Germanium-on-Silicon	5
1.2.2 (Si)GeSn Material System	10
1.3 Dissertation Organization	14
Chapter 2: Growth Techniques	16
2.1 Chemical Vapor Deposition (CVD)	16
2.2 Ultra-high Vacuum-Plasma Enhanced Chemical Vapor Deposition (UHV-PECVD)	18
2.2.1 Heater and Substrate Assembly	21
2.2.2 Vacuum	21
2.2.3 Wafer Cleaning	22
2.2.4 Plasma Enhancement	23
2.3 Reduced Pressure Chemical Vapor Deposition (RP-CVD)	27
Chapter 3: Characterization Methods	28
3.1 Material Characterization	28
3.1.1 Raman Spectroscopy	28
3.1.2 X-Ray Diffraction	30
3.1.3 Transmission Electron Microscopy	33
3.2 Optical Characterization	34
3.2.1 Ellipsometry	34
3.2.2 Photoluminescence	36
Chapter 4: One-step Germanium-on-Silicon Using RF in UHV-PECVD.....	39
4.1 Introduction	39
4.2 Experimental Procedure	40
4.3 Results and Discussion	41
4.3.1 Growth Findings	41
4.3.2 Material and Optical Characterization	45

4.3.3 Comparison of material and optical properties of Plasma Enhancement and Non-Plasma Enhancement:	52
4.4 Tin Incorporation in One-step Ge Layer Using Plasma Enhancement	55
4.5 Conclusion	61
Chapter 5: High Quality Ge Buffer Layer Grown by Plasma Enhancement in UHV-CVD System for Photonic Devices	63
5.1 Introduction	63
5.2 Experimental	63
5.3 Results and Discussions	66
5.3.1 One-step Ge Layer	66
5.3.2 Two-step Ge Buffer Layer using Non-plasma Enhancement	69
5.3.3 Two-step Ge Buffer Layer using Plasma Enhancement	71
5.3.4 Material, Surface, and Optical Properties Comparison between Non-plasma Enhancement and Plasma Enhancement Ge Buffers	77
5.3.5 Active GeSn Layer Comparison on Non-plasma Enhancement and Plasma Enhancement Ge Buffers	83
5.4 Conclusion	85
Chapter 6: Structural and Optical Properties of SiGeSn Alloys for Si Photonics Devices..	87
6.1 Introduction	87
6.2 Experimental	88
6.3 SiGeSn Alloys with Similar Compositions but with Different Thicknesses	92
6.3.1 Material Properties	92
6.3.2 Optical Properties	95
6.3.3 SiGeSn Based Photoconductors	98
6.4 SiGeSn Alloys with Similar Sn Compositions and Thickness but with Different Si Compositions	99
6.4.1 Material Properties	99
6.4.2 Optical Properties	102
6.5 Lattice Matched SiGeSn/Ge Structures	104
6.5.1 Material Properties	104

6.5.2 Optical Properties	108
6.5.3 Annealing Study	114
6.6 Conclusion	117
Chapter 7: SiGeSn Double Barrier in GeSn Quantum Well for Laser Diode Applications	
.....	119
7.1 Introduction	119
7.2 Experimental	120
7.3 Results and Discussions	121
7.4 Conclusion	128
Chapter 8: Summary and Future Work.....	129
8.1 Summary	129
8.2 Future Work	131
8.2.1 Plasma Enhancement UHV-CVD	131
8.2.2 Hot-Filament	132
References	133
Appendix A: Published, Submitted, and Planned Publications	143
A.1: List of Peer Reviewed Published Papers	143
A2: List of Conference Proceedings	144

List of Figures

Figure 1.1: Schematic of the design logic of on-chip optical interconnects [4].	1
Figure 1.2: Applications that can utilize Si-photonics technology. Imaging, atmospheric transmission, night vision, data transmission, and space photovoltaic.	2
Figure 1.3: Semiconductors bandgap energy diagram as a function of lattice constant. Arrows are pointing to Si-Ge-Sn.	3
Figure 1.4: Band diagram of Ge at the $\langle 111 \rangle$ direction of the Brillouin zone that shows the direct (Γ) and indirect (L) bandgaps at the three general cases: (a) Bulk Ge; (b) Intrinsic tensile strained Ge; (c) n^+ doped tensile strained Ge.	5
Figure 1.5: Absorption coefficient as a function of energy of Si and Ge compared to other group III-V compounds [25].	6
Figure 1.6: Schematic illustration of the Ge-on-Si structure. (a) Two Ge and Si layers before epitaxy; (b) Pseudomorphic strained Ge-on-Si; (c) Strain relaxed Ge-on-Si. The relaxation is formed by generating misfit dislocation (T) at the Ge/Si interface.	7
Figure 1.7: The possible growth modes of Ge-on-Si. (a) Layer-by-layer growth; (b) island growth; (c) Mixed growth mode.	8
Figure 1.8: The band diagrams of Ge, GeSn, and SiGeSn in the $\langle 111 \rangle$ direction of the Brillouin zone. The diagram shows the effect of tensile strain on the $E\Gamma$ and EL in the conduction band and HH and LH in the valance band.	12
Figure 1.9: (a) Band diagram of a direct bandgap with type I band offset alignment of a $Ge_{0.84}Sn_{0.16}$ quantum well with $Si_{0.09}Ge_{0.8}Sn_{0.11}$ double barriers DHS [85]. (b) Schematic of the GeSn/SiGeSn DHS on relaxed GeSn buffer [87].	13
Figure 2.1: Schematic representation of the CVD reaction process near and on the surface of substrate.	16

Figure 2.2: Variation of deposition rate with temperature in CVD growth chamber. The temperature range typically depends on growth chamber conditions and precursors.	17
Figure 2.3: (a) Schematic layout of UAF's UHV-CVD system. (b) Photo of the system.....	19
Figure 2.4: Deposition stage of the process chamber with heating and substrate components [91].	20
Figure 2.5: (a) Structure of the RF delivery components. (b) Side view of custom designed plasma electrode with active plasma in center, for UHV-CVD growth process of GeH ₄	23
Figure 2.6: (a) RF coaxial cable that is used for RF power transmission outside the chamber. (b) Braided Stainless Steel coaxial cable for UHV environment.	24
Figure 2.7: Schematic of PE setup inside UHV-CVD process chamber as: (a) The RF design inside the process chamber. (b) Shows the buildup of electric potential in both bulk plasma and sheath and the reaction mechanism when the upper electrode is powered.	25
Figure 2.8: ASM's Epsilon [®] 2000 Plus RPCVD system.....	26
Figure 3.1: (a) Schematic of laser-matter surface interaction. (b) The interaction process of Raleigh and Raman.	29
Figure 3.2: Schematic of the Raman setup with 532 nm and 632 nm lasers.	30
Figure 3.3: Geometry of the two diffraction methods from lattice planes: (a) For symmetrical scan with 2θ varies ($\omega_i = \omega_d$) and (b) for asymmetrical scan with both 2θ and ω vary.	31
Figure 3.4: Illustration of effect of lateral correlation and peak spread on peak-broadening in (004) and (224) directions.	32
Figure 3.5: Photo of Philips X'pert PRO XRD system in the Institute for Nanoscience Engineering at the University of Arkansas. From left to right: (1) detector; (2) diffraction optics; (3) sample stage; (4) detector slits; and (5) x-ray source.....	32

Figure 3.6: A comparison between optical and electronic microscopes.....	33
Figure 3.7: TEM sample preparation sequence. (a) Piece of the sample; (b) gluing; (c) mechanical thinning (polishing); (d) ion milling; (e) top illustration of the final TEM sample shows the hole surrounded by an optically transparent area.	34
Figure 3.8: Schematic of basic concept of ellipsometry. The interaction and reflection polarized light from surface of a thin film sample.....	35
Figure 3.9: Experimental ellipsometry data and model fitting of a $\text{Si}_{0.19}\text{Ge}_{0.783}\text{Sn}_{0.027}$ sample. (a) Ψ spectra and (b) Δ spectra.	36
Figure 3.10: Illustration of the conduction and valance band in the E-K diagram in semiconductors that shows the photoluminescence process. (a) Radiative recombination and (b) Shockley-Read-Hall recombination.....	37
Figure 3.11: Figure 3-11: Optical alignment of the PL measurements setup of the 532 nm and 1064 nm lasers. The major instrumentation tools are also shown.	38
Figure 4.1: Normalized and stacked Raman results. (a) At the temperature range 250-300°C. (b) At the temperature range 350-450°C.....	41
Figure 4.2: Raman shift and peak FWHM variation at temperatures that exhibit Ge-Ge LO modes at the temperature range 350-450°C.....	42
Figure 4.3: Film thickness versus growth time at three different temperatures: (a) 350°C, (b) 400°C, and (c) 450°C. Solid lines show linear fittings.....	43
Figure 4.4: Growth rate as a function of pressure at the three selected temperatures 350, 400, and 450°C. Solid lines indicate linear fittings.....	44
Figure 4.5: Illustration of the 2Theta-Omega XRD scans measured from the (004) plane of the samples. (a) At 400°C and (b) at 450°C. The reference Ge sample is used for comparison.	45

Figure 4.6: XRD-RSM contour plots from the (224) direction. (a) Sample A3 and (b) sample B3.	46
Figure 4.7: Stacked PL spectra of samples A3 and B3 compared to bulk Ge reference. Sold red lines show PL fittings.....	48
Figure 4.8: Room temperature PL spectra of the two sets of samples. (a) At 400°C (A1, A2, and A3) and (b) at 450°C (B1, B2, and B3).....	49
Figure 4.9: Absorption coefficient curves as the temperature and pressure change. (a) At 400°C and (b) at 450°C. Dashed lines represent the absorption coefficient curves of a bulk Ge reference.	50
Figure 4.10: TEM imaging of the sample A3. (a) Dark filed cross-sectional TEM image. (b) Bright field cross-sectional TEM image. Both images shows threading dislocations that were generated at the Ge/Si interface, and propagated through the entire film.	51
Figure 4.11: SEM imaging of the sample A3. (a) EDX surface map of the etched Ge layer. (b) Surface view shows the Ge film after etching. (c) An SEM image of the Ge film surface after it was exposed to etch pit solution; the black dots represent pit density near the.....	52
Figure 4.12: A comparison between the thickness of plasma enhanced (PE) and the non-plasma enhanced (NPE) growths at 400°C.....	53
Figure 4.13: (a) XRD (004) rocking curve for material comparison between plasma enhancement (PE) and non-plasma enhancement (NPE) growths at 400°C. (b) Shows PL spectra comparison for optical quality improvement for the same samples.....	54
Figure 4.14: Raman comparison between the plasma enhancement (PE) sample and the non-plasma enhancement (NPE) sample.....	54

Figure 4.15: (a) A photograph from inside the chamber during the plasma generation of a GeSn growth. (b) A photograph of a GeSn sample that was grown with plasma enhancement. The wafer features three distinct spots (I, II, and III).	56
Figure 4.16: Thickness of two Ge samples compared to two GeSn samples that were grown using plasma enhancement (PE).....	57
Figure 4.17: The 2θ - ω XRD curves of samples B and D from the (004) direction.....	57
Figure 4.18: XRD-RSM contour plots of samples C and D from the (224) direction.	58
Figure 4.19: TEM images of sample D. (a) and (b) Dark and bright field TEM image of sample B (spot III), respectively. (c) A zoom-in image of the interface between GeSn and Si. Stacking faults (S.F.) are clearly seen at the interface. (d) A zoom-in TEM image of the GeSn surface.	59
Figure 4.20: Comparison of PL shift as Sn incorporated. (a) Sample A and C at 350°C. (b) Sample B and D at 400°C.....	60
Figure 5.1: Calibration results for selected growth before and after maintenance. (a) Shows the drift in growth thickness at 350°C under F.R. of 10:25 (GeH ₄ :Ar). (b) A log scale illustration of the variation of thickness before and after maintenance at 350°C and 400°C under F.R. of 5:200.	64
Figure 5.2: (a) Variation of thickness with the applied RF power for one-step Ge growth at 400°C. (b) Raman shift comparison between non-plasma (0 W) and plasma (30 W) enhancement for samples were grown at 400°C. The dashed line corresponds to the Ge-Ge mode of a relaxed Ge layer.....	67
Figure 5.3: Variation of thickness and mean free path as a function of chamber pressure of growths at an applied RF power of 4 W and at a growth temperature of 400°C.	68

Figure 5.4: Room temperature PL spectra of sample A as-grown and after thermal annealing A*. The dashed line depicts RT PL of bulk Ge.	69
Figure 5.5: SEM micrographs of the as-grown buffer A and the annealed buffer A* that show etch pit on the surface.	70
Figure 5.6: AFM images and RMS values of sample A and A*. Images were taken on a surface area of $10 \times 10 \mu\text{m}^2$ scans for each sample.	71
Figure 5.7: Two-step Ge buffer cross section that shows growth parameters of each step.	71
Figure 5.8: The variation of the growth thickness with temperature at an RF power of 5 W.	72
Figure 5.9: Temperature-dependent XRD around the Bragg angle of (004) of growths at 5 W. Inset shows the calculated strain and FWHM of each Ge curve.	73
Figure 5.10: Room temperature PL spectra as the temperature changes from 450 to 525°C at 5 W. The direct bandgap position of a bulk Ge is marked by dashed lines.	74
Figure 5.11: Power-dependent XRD around the Bragg angle of (004) of growths at 525°C. Inset shows the calculated strain and FWHM of each Ge curve.	76
Figure 5.12: Room temperature PL spectra as the RF power changes at 525°C. The direct bandgap position of a bulk Ge is marked by dashed lines.	77
Figure 5.13: XRD (004) rocking curve of buffer C. The inset shows the calculated strain and the FWHM of each buffer.	78
Figure 5.14: Topographical three-dimensional AFM surface images and RMS values for buffer A, B, and C.	79
Figure 5.15: SEM micrographs of selected surface areas of buffer B and C after exposure to EPD solution. The measured EPD of buffer B and C are $2.7 \times 10^7 \text{ cm}^{-2}$ and $7.4 \times 10^7 \text{ cm}^{-2}$, respectively.	80

Figure 5.16: Room temperature PL spectra of buffer A, B, and C measured using 1064 nm laser with 340 mW power.....	81
Figure 5.17: Absorption coefficients of buffer A, B, and C. The dashed line is a Ge reference for comparison. Inset: absorption fitting and direct bandgap determination.....	82
Figure 5.18: Asymmetrical RSM scans from the (224) plane of sample D and E.....	84
Figure 5.19: Cross sectional TEM. Dark field TEM images of (a) sample D and (b) sample E. (c) High resolution TEM images of the first step Ge/Si interface of sample E. Insets: HR-TEM images of two selected defects near the interface in c1 highlighted by red frame and c2 pointed by an arrow. (d) HR-TEM of the second step GeSn/Ge interface of sample E. A TD propagating the GeSn is pointed with an arrow. Insets: HR-TEM image of an interfacial defect.	84
Figure 5.20: Room temperature PL for sample D and E measure using 532 nm green laser with 500 mW excitation power.....	86
Figure 6.1: Schematic of the proposed space solar photovoltaic with $\text{Si}_x\text{Ge}_{1-x-y}\text{Sn}_y$ junction.....	87
Figure 6.2: Dark field cross sectional TEM image of the Ge/Si interface. The black points with periodic spacing ranging from 4 to 9 nm located near the interface are 90° Lomer misfit dislocations to accommodate the large lattice mismatch between Si and Ge.....	89
Figure 6.3: A cross sectional view of the samples structure and growth procedure.....	89
Figure 6.4: (a) normalized channeling and random RBS spectra of a $\text{Si}_{0.073}\text{Ge}_{0.872}\text{Sn}_{0.055}$ sample; (b) SIMS profile of a $\text{Si}_{0.117}\text{Ge}_{0.859}\text{Sn}_{0.025}$ sample.	90
Figure 6.5: 2θ - ω scan from (004) plane for three samples A, B, and C that feature the same Si and Sn compositions but different film thicknesses.	92
Figure 6.6: RSMs from (224) plane for samples A, B, and C with similar compositions but different thicknesses.....	94

Figure 6.7: (a) Absorption coefficient of sample C. Inset: the refractive index of the same sample.	
(b) Absorption curves as a function of energy of each sample.....	95
Figure 6.8: Room temperature PL spectra as a function of energy and wavelength for samples A, B, and C.	97
Figure 6.9: Figure 6.9: Room temperature spectral response of a SiGeSn based photoconductors that were fabricated using sample A and C with a cut-off wavelength near 1.8 μm . Inset: optical image from the top of the device [116].....	98
Figure 6.10: 2θ - ω scan from (004) plane for three samples A, D, and E that feature the same Sn compositions and film thicknesses but with different Si compositions.....	99
Figure 6.11: RSMs from (224) plane for samples A, D, and E with similar Sn compositions and thicknesses but different Si compositions.....	101
Figure 6.12: Raman spectra of samples A, D, and E. The inset shows a zoomed-in plot of the Ge-Sn modes region.....	101
Figure 6.13: (a) Absorption coefficient of sample D. Inset: the refractive index of the same sample.	
(b) Absorption curves as a function of energy of samples A, D, and E.....	102
Figure 6.14: Photoluminescence spectra as a function of energy and wavelength of samples A, D, and E measured at room temperature.....	103
Figure 6.15: 2θ - ω scans from (004) plane for the four SiGeSn samples F, G, H, and J that feature relatively high Si incorporation.	105
Figure 6.16: RSM contour plots for the four SiGeSn samples F, G, H, and J that feature relatively high Si incorporation.....	106
Figure 6.17: Dark field (DF) and high resolution (HR) TEM images of sample H. (a) Shows the DF TEM of a cross sectional view of all layers. Dislocations that are initiated from misfit	

dislocations in the Ge/Si interface propagate through the Ge buffer to the SiGeSn film. (b) The HRTEM image of $\text{Si}_{0.13}\text{Ge}_{0.804}\text{Sn}_{0.066}/\text{Ge}$ interface verifies high quality growth.	107
Figure 6.18: Dark field (DF) and high resolution (HR) TEM images of lattice matched samples F and J. (a) DF TEM cross sectional image of sample F. (b) HRTEM image of sample showing only the top SiGeSn film. (c) Shows the cross section of the $\text{Si}_{0.19}\text{Ge}_{0.783}\text{Sn}_{0.027}$ film grown on a Ge buffer and (d) shows HR TEM of the SiGeSn film.	108
Figure 6.19: (a) Absorption coefficient of sample D. Inset: the refractive index of the same sample. (b) Absorption curves as a function of energy of samples F, G, H, and J.	109
Figure 6.20: Photoluminescence spectra as a function of energy and wavelength of samples F, G, H, and J measured at room temperature.	110
Figure 6.21: Temperature-dependent photoluminescence spectra as a function of energy and wavelength of (a) sample F and (b) sample J.	112
Figure 6.22: Temperature-dependent analysis of the PL spectra of sample J as a function of (a) Line-widths and (b) PL peak positions. The solid lines in (b) denote Varshni fittings.	113
Figure 6.23: Power-dependent measurements of sample J at three temperatures (a) 300K, (b) 77K, and (c) 10K.	114
Figure 6.24: (a) $2\theta-\omega$ scans and (b) RSM contour plots of sample G as-grown and after annealing.	114
Figure 6.25: Cross sectional TEM of sample G. As-grown in (a) and (b). After rapid thermal annealing in (c) and (d).	116
Figure 6.26: Sample G as-grown and after annealing. (a) Stacked Raman spectra. The inset shows the Ge-Sn modes. (b) PL spectra.	117

Figure 7.1: (a) Cross section of a 4QWs GeSn with SiGeSn barriers and thick GeSn buffer. (b) Calculated TE mode with an average optical confinement $\Gamma = 4.1\%$. (c) Laser-output versus pumping-laser-input of the same 4QWs sample. The inset shows the lasing and PL spectra at 10 K [120].	119
Figure 7.2: (a) SIMS profile of the sample in this study. The TEM image is overlapped with SIMS profile to illustrate the material quality of each layer. (b) Cross sections of the sample (not to scale) that summaries the layers thicknesses and compositions. Numbers help in the identification of each layer in SIMS and TEM.	121
Figure 7.3: (a) Rocking curve scan of the SiGeSn/GeSn/SiGeSn QW along the (004) direction. The black and red curves show the measured and simulated data, respectively. (b) RSM plot of the sample along the asymmetrical (224) plane.	122
Figure 7.4: The calculated band diagram results showing the carrier confinement and the possible band-to-band optical transitions between (a) Γ -HH; (b) Γ -LH; (c) L-HH; and (d) L-LH. Units are in meV.	123
Figure 7.5: Temperature-dependent PL spectra of the SiGeSn/GeSn/SiGeSn QW sample. The dashed line is for eye guidance of the QW peak shift.	126
Figure 7.6: The cross section of a typical GeSn/GeSn/GeSn QW that has shown a type-I direct bandgap behavior.	127
Figure 7.7: PL results of the SiGeSn/GeSn/SiGeSn sample (a) PL peak positions, (b) FWHM, and (c) integrated PL. A type-I direct bandgap GeSn/GeSn/GeSn QW is shown for comparison. ..	128
Figure 8.1: Schematic diagram of the hot-filament design in the UHV-CVD system.	132

List of Tables

Table 2.1: Vacuum levels and pumps.....	22
Table 3.1: Pumping lasers parameters [95].....	38
Table 4.1: Summary of sample information and XRD results.....	45
Table 4.2: Summary of growth conditions of GeSn samples A and B.....	55
Table 4.3: Summary of typical Ge growth methods by other research groups compared with this work.....	62
Table 5.1: Ge buffer IDs and growth conditions, RMS, and EPD of buffers A, B, and C.....	78
Table 5.2: RSM results of two GeSn films.....	83
Table 6.1: Summary of SiGeSn samples composition and thickness.....	91
Table 6.2: Summary of material information of SiGeSn films in samples A, B, and C.....	93
Table 6.3: C11 and C12 of Si, Ge, and Sn [113].....	94
Table 6.4: Summary of optical characterization results of samples A, B, and C.....	96
Table 6.5: Summary of material information of SiGeSn films in samples A, D, and E.....	100
Table 6.6: Summary of optical characterization results of samples A, D, and E.....	103
Table 6.7: Summary of material information of SiGeSn films in samples F, G, H, and J.....	106
Table 6.8: Summary of optical characterization results of samples F, G, H, and J.....	109
Table 6.9: Varshni's equation fitting parameters of sample J.....	113
Table 7.1: List of parameters that were used in the band structure calculations.....	125

Chapter 1: Introduction

1.1 Motivation

In the past five years, microelectronic technology reached its upper limits for data transmission since the number of transistors on a chip double the packing density of electronic devices every 18 months to benchmark Moore's law. Adding more transistors on a chip would deteriorate the performance of integrated circuits because of the low capability of metallic interconnects for high speed data transmission. To overcome this technological hurdle, nanophotonics has been proposed as a key solution that minimize the usage of metallic interconnects with optical interconnects on chip. On other word, photons or light in optical interconnects will allow data in miniaturized devices to be transmitted faster and with low loss and cost compared to electrons in metallic interconnects [1]-[3]. Therefore, integrating photonic chip, which has optical interconnects for ultrafast data transmission, monolithically with a complementary metal oxide semiconductors (CMOS) chip, which is used for data processing, will revolutionize optoelectronic technology.

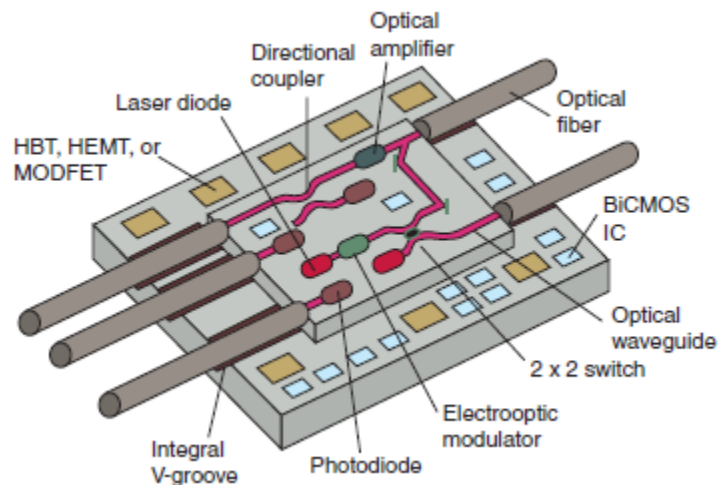


Figure 1.1: Schematic of the design logic of on-chip optical interconnects [4].

In addition, group III-V photonic materials on InP substrate are the best light emitters in the market nowadays. However, III-V materials are very expensive to produce in high volume manufacturing and not fully compatible with the CMOS technology. Therefore, they are not

avored by industry. Thus, Si-photonics technology (or group IV photonics) is a unique option. First, it allows the low cost production with higher performance as it monolithically integrated with the current integrated circuit technology to form an optoelectronic system on a single chip [5]. Second, it can be bandgap engineered to cover a wide range of the infrared (IR) broadband range that permits a wide range of device applications. Investing in Si-photonics industry is also promising. Most of the components of Si-photonics technology, such as waveguides, modulators, and photodetectors have reached a good level of maturity. Nevertheless, the light source, such as room temperature laser, is still under development [6], [7]. The market value of Si-photonics is expected to exceed US\$1.5 billion in 2025 [8]. In 2015, the American Institute for Manufacturing Integrated Photonics (AIM Photonics) was established with a US\$0.6 billion budget for the following five years. AMI Photonics mission is to establish a foundry for commercializing academic laboratory photonics related breakthroughs [9].

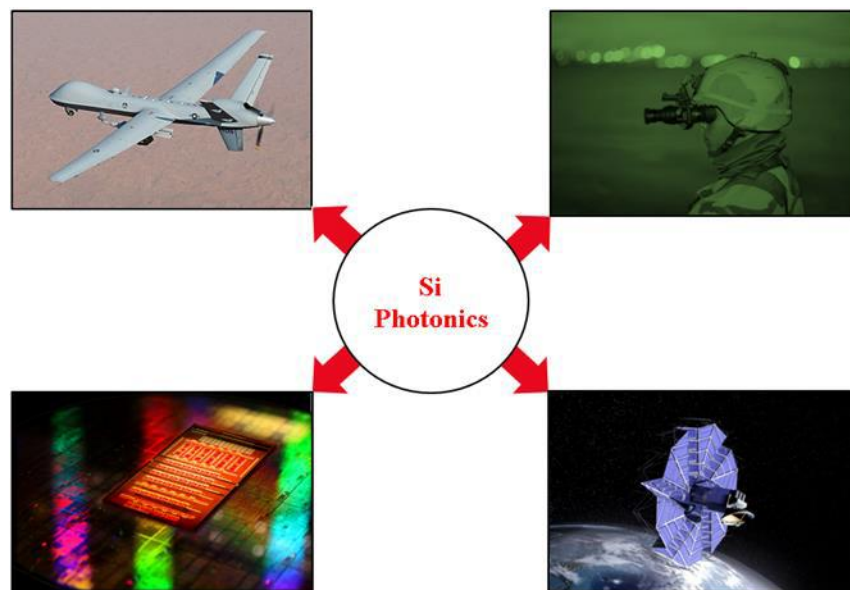


Figure 1.2: Applications that can utilize Si-photonics technology. Imaging, atmospheric transmission, night vision, data transmission, and space photovoltaic.

It was predicted that Si-Ge-Sn material system from group IV is a promising candidate for photonic devices. In 1991, R. A. Soref and C. H. Perry published an article that estimated

theoretically the compositional dependent direct and indirect bandgaps of $\text{Si}_{1-x-y}\text{Ge}_x\text{Sn}_y$ material system using energies of the binaries $\text{Si}_{1-y}\text{Ge}_y$, $\text{Ge}_{1-x}\text{Sn}_x$, and $\text{Si}_{1-y}\text{Sn}_y$ [10]. Later in 1993, R. A. Soref and L. Friedman proposed the first direct bandgap system designed with Ge and GeSn heterostructure [11]. The long wavelength broadband coverage of SiGeSn alloys can cover up to 12 μm , which can be utilized in large number of device applications in the IR range [12]. In addition, every sub-band region of this wavelength range can be dedicated to a desired application. For example, the long wave IR range from 3.0 to 12.0 μm can be applied in atmospheric transmission and in missile tracking systems. In spite of the above attractions of Si-photonics, making them available for commercial applications needs a lot of research work to make group IV photonics that competes the current technology. On core issue is that group IV semiconductors, such as Si, Ge, and SiGe alloys, were excluded from being an efficient light emitters due to their indirect bandgap nature [13].

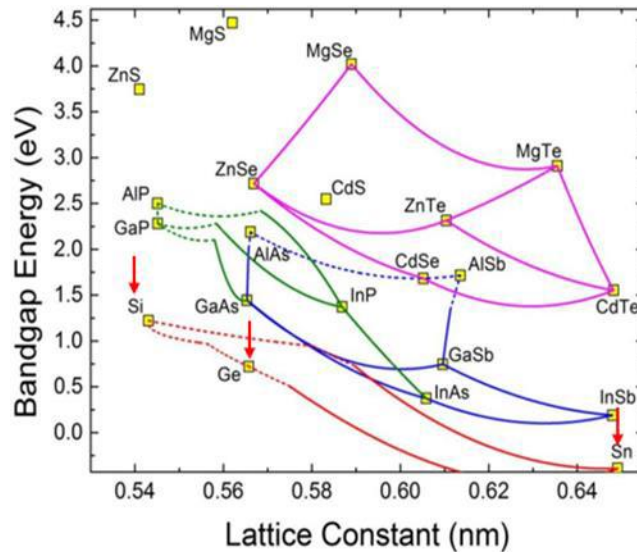


Figure 1.3: Semiconductors bandgap energy diagram as a function of lattice constant. Arrows are pointing to Si-Ge-Sn.

The binary $\text{Ge}_{1-x}\text{Sn}_x$ alloys have been fully investigated and demonstrated in device applications. For example, a focal plane array made of GeSn pixels that operate within the short-

wave IR range from 1.55 to 3.0 μm are an exceptional candidate for photodetection and night vision [14]. In addition, $\text{Ge}_{1-x}\text{Sn}_x$ with Sn incorporation of 12.6% and 9.0% can provide lasing at temperatures $\leq 90\text{K}$ and 110K , respectively, with relatively low threshold voltage [15], [16]. However, SiGeSn material system is still understudy from growth to characterization to device applications.

It is worth noting here that $\text{Si}_{1-x-y}\text{Ge}_x\text{Sn}_y$ alloys are not a simple supplement to $\text{Ge}_{1-x}\text{Sn}_x$; in fact, the technological impact of $\text{Si}_{1-x-y}\text{Ge}_x\text{Sn}_y$ is much higher. This comes from its bandgap engineering uniqueness from which the bandgap and lattice constant can be tuned independently by varying Si, Ge, and Sn compositions. The bandgap energy as a function of lattice constant of semiconductor materials is shown in Fig. 1.3. As the figure illustrates, bandgap engineering allows SiGeSn alloys to cover a broad energy band. This gives $\text{Si}_{1-x-y}\text{Ge}_x\text{Sn}_y$ alloys the potential to cover wavelength from the near to mid IR range up to the long wave IR range, 12 μm . This wavelength range is favored in light detection and infrared detectors, and can be achieved by band-to-band transitions, which is dominated by Auger recombination process in ultrahigh quality materials and under high injection level. However, the growth of high-quality SiGeSn alloys that satisfy the device-level criteria is a formidable challenge. This is mainly due to the low thermodynamic solubility of α -Sn in both Si and Ge [17]; and the large lattice mismatch between Ge, Sn, and Si [18], [19]. Moreover, in order for SiGeSn photonic devices to be adopted by industry, their growth temperatures have to be low ($< 400^\circ\text{C}$) using low cost precursors. This is not only going to reduce the production costs but also will pave the way for CMOS compatibility.

Therefore, low temperature growth using chemical vapor deposition (CVD) technique is highly desired to grow Si-Ge-Sn material system. The approach to solve this issue can be addressed as follow:

- (1) CVD growth of $\text{Si}_{1-x-y}\text{Ge}_x\text{Sn}_y$ using low cost and commercially available Si and Ge precursors, such as silane (SiH_4) and germane (GeH_4), should be investigated. That should cover SiGeSn alloys material and optical properties.
- (2) Since the decomposition of SiH_4 and GeH_4 needs high temperatures ($>400^\circ\text{C}$) compared to disilane (Si_2H_6) and digermane (Ge_2H_6), plasma enhancement in CVD systems could be a solution to lower the growth temperature of Si and Ge. This includes SiGe and high quality Ge buffer at low growth level range ($< 500^\circ\text{C}$).
- (3) Finally, from the findings in the first approach, a type-I band alignment quantum structure with high quality SiGeSn barriers and a direct bandgap GeSn as an active layer worth investigation. These quantum structures are mainly used as light emitters, such as lasers and light emitting diodes.

1.2 Background:

1.2.1 Germanium-on-Silicon

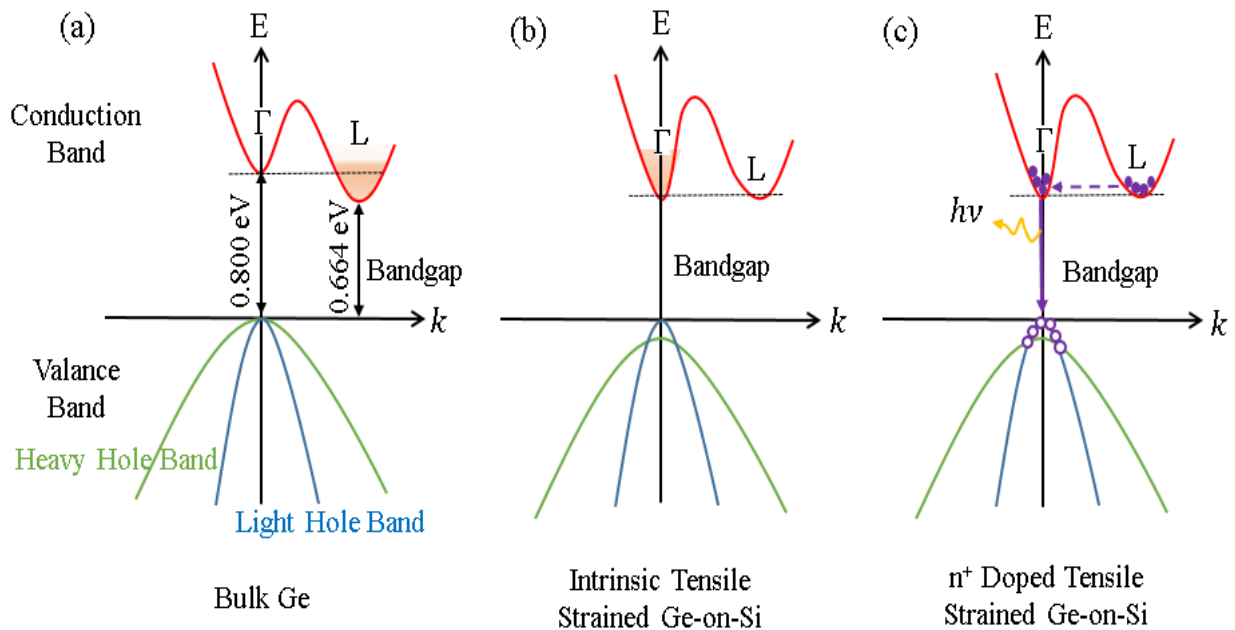


Figure 1.4: Band diagram of Ge at the $\langle 111 \rangle$ direction of the Brillouin zone that shows the direct (Γ) and indirect (L) bandgaps at the three general cases: (a) Bulk Ge; (b) Intrinsic tensile strained Ge; (c) n^+ doped tensile strained Ge.

Silicon (Si) is the second largest element of the 12 abundant elements of Earth’s crust [20]. This natural abundance of Si along with its ultrahigh purity make it economically valuable for integrated circuits. While the production of integrated circuits technology increases massively, pure Si production cost is continually decreasing [21]. On the other hand, Ge is a good candidate for optical devices because it has a 136 meV energy difference between the bottom of the indirect bandgap (L) valley to the bottom of the direct (Γ) valley in the conduction band as shown in the bulk Ge bandgap diagram in Fig. 1.4(a). This allows Ge to emit light as electrons can overcome this small energy barrier either by tensile strain or doping, which gives Ge an advantage of being a pseudo-direct bandgap material compared to other group IV semiconductors [22].

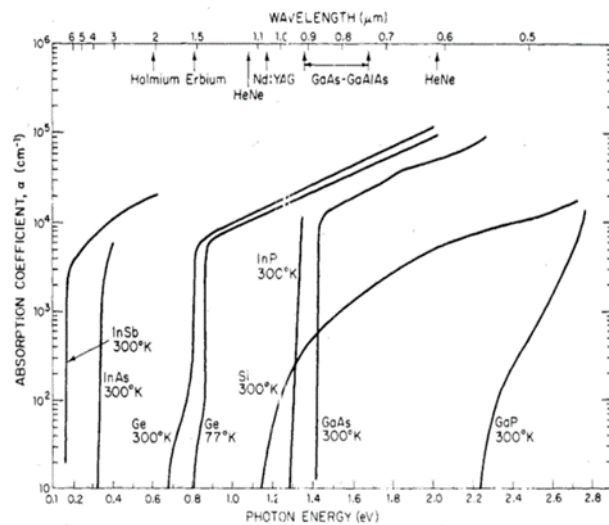


Figure 1.5: Absorption coefficient as a function of energy of Si and Ge compared to other group III-V compounds [25].

Since both Si and Ge belong to group IV elements, they exhibit similar crystal structure with different electrical and optical properties. Alloying Ge in Si as well as growing Ge on Si has enabled Si technology to benefit from the unique properties of Ge using CMOS [23]. One important benefit of using Ge in electronic devices is the high electronic mobility when used as a p-type metal–oxide–semiconductor field-effect transistors [24]. Germanium also possesses a better

optical absorption compared to other group IV materials. Figure 1.5 shows Ge and Si absorption coefficients compared to absorption of some direct bandgap compounds from group III-V materials. It is obvious that the absorption of group III-V compounds increases sharply near and beyond the bandgap energy. In contrast, the absorption of Si is weak near and beyond the bandgap while for Ge the absorption behavior shows better absorption behavior. This is a good indication about the optical characteristics of Ge that makes it as a good candidate for photodetectors operating in the wavelength range from 1.3 to 1.55 μm [26].

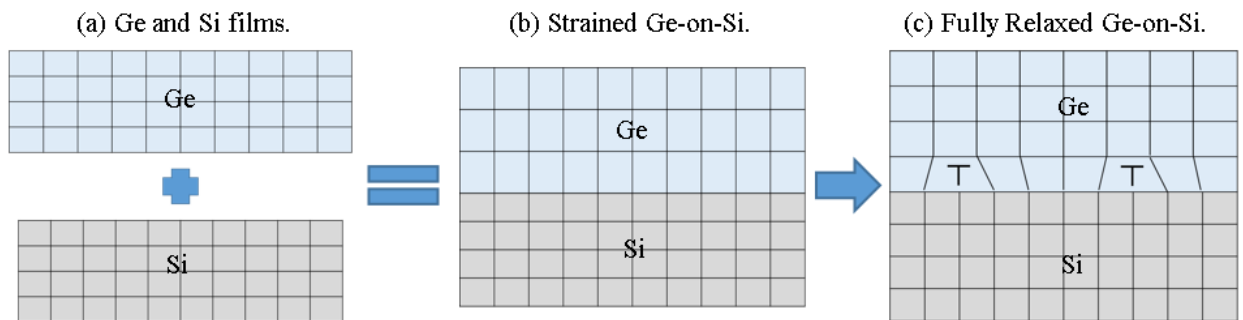


Figure 1.6: Schematic illustration of the Ge-on-Si structure. (a) Two Ge and Si layers before epitaxy; (b) Pseudomorphic strained Ge-on-Si; (c) Strain relaxed Ge-on-Si. The relaxation is formed by generating misfit dislocation (T) at the Ge/Si interface.

A remarkable advantage of Ge and Si heteroepitaxy is that they can be grown monolithically since they both belong to the same group and share similar material properties. However, Ge-on-Si growth is difficult due to two fundamental problems that are associated with the large lattice mismatch (4.2%) between the Ge epilayer ($a_{\text{Ge}} = 5.657 \text{ \AA}$) and the Si substrate ($a_{\text{Si}} = 5.431 \text{ \AA}$) [27]. Figure 1.6 illustrates the epitaxial structure of Ge-on-Si. As Ge layer deposited directly on Si, it grows pseudomorphically, tetragonal or compressively strained structure, until a certain thickness, termed the critical thickness (h_c), as shown in Fig. 1.6(b). Above h_c , the structure becomes fully relaxed, where the relaxation is relieved by forming 60° misfit dislocation cores at the Ge/Si interface as shown in Fig. 1.6(c). This network of misfit dislocations at the Ge/Si interface can cause one type of defects called threading dislocations (TDs) [28]. In addition,

thermal expansion mismatch between Ge ($5.9 \times 10^{-6} \text{ K}^{-1}$) and Si ($2.7 \times 10^{-6} \text{ K}^{-1}$) increases the tensile strain and makes the TDs propagate parallel to the interface. Such a case occurs for thick Ge layers when cooling the chamber from high temperatures [29].

Another hurdle that is associated with Ge-on-Si growth is the surface roughness. The growth mechanisms depends on the attraction energy between the vapor atoms and the substrate. At low temperature growth, atoms of the vapor are weakly attracted to each other and strongly attracted to the substrate leading to the formation of layer-by-layer growth that is known by Frank–van der Merwe mode as shown in Fig. 1.7(a). In contrast, at high growth temperatures, vapor atoms attract each other stronger than the substrate to form a 3D island growth known by Volmer-Weber mode as shown in Fig. 1.7(b). The 3D growth on the surface cause the surface roughness. Finally, a mixture between both modes gives Stranski-Krastanov mode as in Fig. 1.7(c) [30]. Such a growth mode also causes surface roughness [31]-[34]. These two major issues, namely high TDD and surface roughness, could reduce the device performance in practical applications. Therefore, a systematic growth approach is needed to reduce their effects.

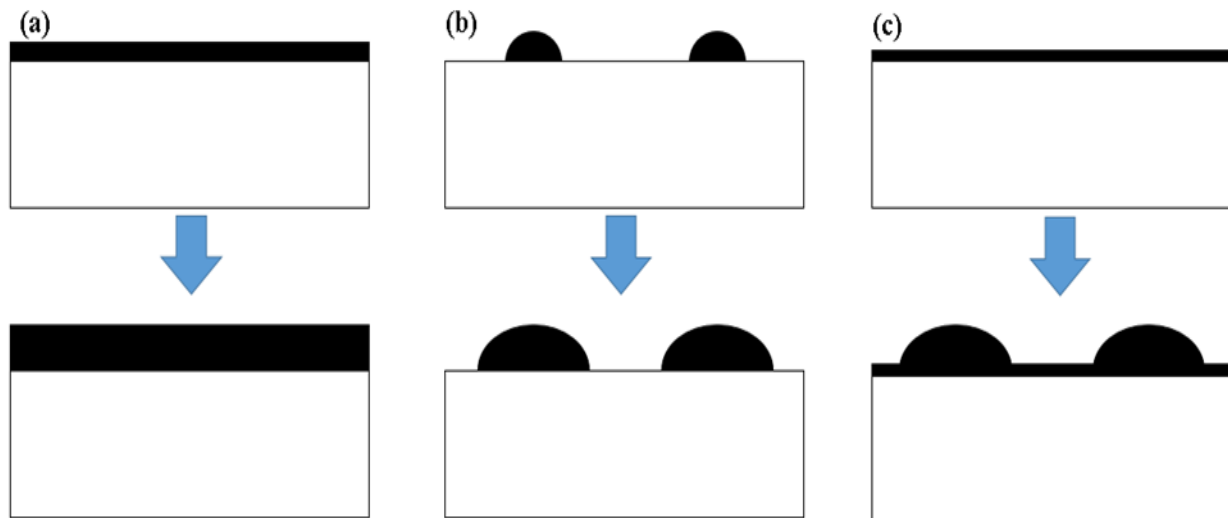


Figure 1.7: The possible growth modes of Ge-on-Si. (a) Layer-by-layer growth; (b) island growth; (c) Mixed growth mode.

Research attempts have been developed to address these problems. The growth of Ge on an ultrathin silicon-on-insulator [35] and on graded SiGe virtual substrate [36], and hydrogen annealing for surface roughness reduction [37] are examples to improve the material quality of Ge. However, a two-step method followed by post high temperature cycling or annealing step is the conventional growth approach. The first step in the two-step method is a thin layer that is grown at low temperature (LT), typically in the range from 340-450°C. The role of this step is to promote the layer-by-layer growth mode and relax the elastic energy, which limits and confines dislocations [38]. The second step is the growth at high temperature (600-850°C), which lowers the dislocations further and enhances the deposition rate for a thicker Ge buffer [38], [39]. Finally, the buffer is annealed, either by single step or multi cycle annealing, under high temperatures (700-900°C) to lower the TDDs by up to two orders of magnitude [40], [41]. Even though this growth approach produces high quality Ge buffer, the high temperature processing increases the thermal budget and could limit its compatibility with CMOS technology [42].

A more sound solution to lower the growth temperature with maintaining high deposition rate and appropriate material and optical qualities is by assisting the dissociation process with energetic plasma ions. In 1992 Varhue *et al.* proposed a low temperature Ge-on-Si growth method using plasma enhancement-CVD (PE-CVD [43]). A mixture of helium and GeH₄ was used at a substrate temperature in the range from 300 to 350°C. However, the material quality was low due to surface roughness caused by ion bombardment and hydrogen bubbles. Later, the PECVD method was developed toward two-step LT/HT growth [44], [45] and high-density plasma-CVD (HDP-CVD) [46]. Even though some research groups have developed new Ge growth methods resulting in low TDD, these involve higher order Ge hydrides (Ge_nH_{2n+2}, n being an integer), multilayers, and high temperatures. Therefore, there is a need for a systematic study to grow Ge-

on-Si at low temperatures using low cost precursor such as GeH₄ while also omitting the post-deposition annealing step. This will reduce the growth costs as well as make it CMOS compatible.

1.2.2 (Si)GeSn Material System

As discussed in the previous section of this chapter, bandgap indirectness of Ge as well as SiGe can be diminished by incorporating the group IV element tin (Sn) from the same group. From the material properties of Sn, the energy dispersion diagram of Sn indicates that Sn has an overlapped conduction and valance band, which suggests nearly zero bandgap at the direct Γ valley [47]. Another common property of Sn is that it forms a metallic white Sn or β -Sn with a body centered tetragonal crystal structure at room temperature with -0.41 eV bandgap. When β -Sn is cooled below 13.2°C, it experience a phase transition from to a semiconducting gray Sn or α -Sn with diamond structure [48]. The growth of α -Sn was reported for the first time by R.F.C Farrow et al. in 1981 [49]. They used molecular beam epitaxy (MBE) to grow heteroepitaxial α -Sn thin films nearly lattice matched with InSb and CdTe substrates. It was found early in 1982 that incorporating Sn in Ge crystals would be an alternative for Hg-Cd-Te material system [50]. Because of the negative bandgap of Sn, Ge could transform to a direct bandgap material. However, GeSn epitaxy is limited by a few factors that makes GeSn growth possess at higher level of difficulty compared to Ge-on-Si. First, the low sold suability of Ge in α -Sn (< 1%). Second, the instability of α -Sn above 13.2°C [50], [51]. Third, the large lattice mismatch between GeSn and the Si substrate, which becomes lower in the ternary alloy SiGeSn.

The cubic lattice constant of Ge_{1-x}Sn_x alloys can be the calculated using Vegard's law given by [52]:

$$a_{GeSn} = a_{Ge}(1 - x) + xa_{Sn} + bx(1 - x) \quad \text{Equation 1.1}$$

where a_{Ge} and a_{Sn} are 5.657 and 6.489 Å, respectively [53]. The constant b is known by the bowing parameter, which is taken as 0.066 Å [54]. The bowing is defined as the deviation of the experimental results from the linear Vegard's law because of the induced deformation in the crystal structure as an effect of the strain. The lattice constant of $\text{Ge}_{1-x}\text{Sn}_x$ causes a large lattice mismatch value between 4.48 to 19% when $\text{Ge}_{1-x}\text{Sn}_x$ is grown on Si substrate and 0.41 to 15% when $\text{Ge}_{1-x}\text{Sn}_x$ is grown on Ge buffer, which escalates the strain and defects in the film compared to Ge-on-Si. Finally, Sn surface segregation at high growth temperatures that causes low Sn concentration near the interface and the formation of Sn droplets on the surface [55]-[57].

The growth methods of (Si)GeSn have been investigated widely. The (Si)GeSn material growth by molecular beam epitaxy [58]-[62], by magnetron sputtering [63], and by chemical vapor deposition (CVD) have been reported [64]-[69]. However, most of the CVD reported works were done using high-cost higher order hydrides, e.g. $\text{Ge}_x\text{H}_{2x+2}$ and $\text{Si}_x\text{H}_{2x+2}$. These high order hydrides are expensive, which is not favorable in industry. In addition, deuterium-stabilized stannane (SnD_4) and tin tetrachloride (SnCl_4) are the most common Sn precursors. However, the reaction of Si and Ge precursor byproducts with SnCl_4 causes the formation of hydrogen chloride (HCl) byproduct. The HCl is an etching agent that etches Ge faster than Si [70].

The role of Sn incorporation on the band diagram of Ge is shown in Fig. 1.8. Incorporating Sn in the Ge lattice at low temperatures ($<400^\circ\text{C}$) and heavily n-type doping will introduce a strain as discussed before. The strain causes deformation of the periodic potential. The deformation of the potential causes a decrease of the energy difference between the Γ and L valleys in the conduction band, and a split of the light hole (LH) and the heavy hole (HH) bands in the valance band. With the effect of the tensile strain, the energies of Γ and L bandgaps shrink. However, it shrinks faster in the case of Γ valley, which makes the GeSn alloy a direct bandgap material having

electrons transition and recombination through the direct bandgap [71]-[77]. The amount of Sn that is needed for a direct bandgap crossover was estimated theoretically with Sn dilution ratio of $x > 8\%$ [78], [79].

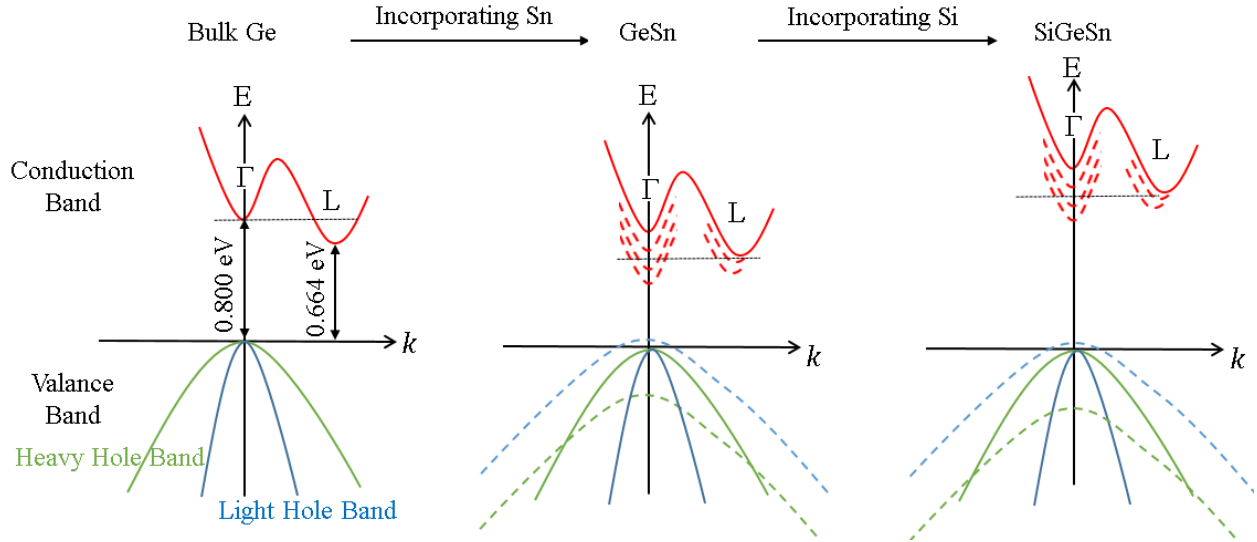


Figure 1.8: The band diagrams of Ge, GeSn, and SiGeSn in the $\langle 111 \rangle$ direction of the Brillouin zone. The diagram shows the effect of tensile strain on the $E\Gamma$ and EL in the conduction band and HH and LH in the valance band.

Incorporating Si in GeSn will increase the valance and conduction bands separation as shown in Fig. 1.8. It was found that alloying Si with GeSn would enhances the thermal stability of GeSn alloys, which allows them to be used in high temperature applications approaching 700°C without Sn segregation [80]. These two feature of SiGeSn namely the high energy bandgap and the high thermal stability make SiGeSn alloys as candidate material for multi-junction space solar cells. In this regard, a SiGeSn that is lattice matched with Ge can absorb efficiently the 1.0 eV band of the solar spectrum while a GaAs can be grown on top of it using metal organic-CVD reactors at high temperatures [81]. However, incorporating Si in GeSn will increase the growth difficulties. Moreover, the growth temperature of SiGeSn is higher compared to GeSn since the binding energy of silane precursor requires higher temperatures to dissociate as compared to

germane [17]. Also, it is difficult to stabilize Sn in SiGe alloys because of the large difference in the lattice size of Sn (5.65 Å) compared to SiGe [12].

Multi quantum wells double heterostructure (DHS) helps in shortening the emission wavelength, lowering the current threshold, and increasing the optical confinement of charge carriers, which enhance the light extraction process [82]. The GeSn/Ge multi quantum well structures were used to improve light efficiency of light emitting diodes (LEDs) [83], [84]. However, using Ge as a barrier layer could not achieve type-I band alignment [84].

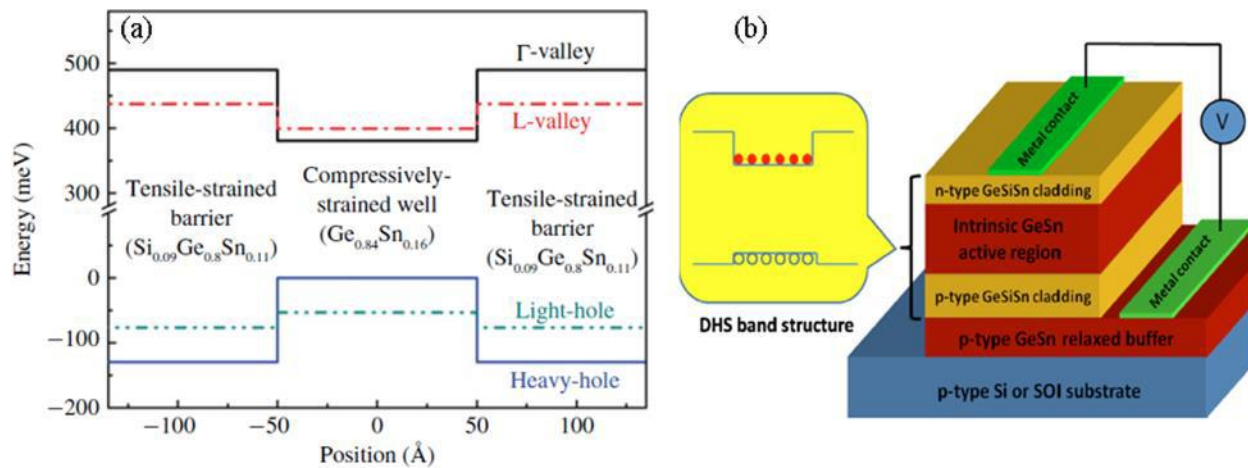


Figure 1.9: (a) Band diagram of a direct bandgap with type I band offset alignment of a $\text{Ge}_{0.84}\text{Sn}_{0.16}$ quantum well with $\text{Si}_{0.09}\text{Ge}_{0.8}\text{Sn}_{0.11}$ double barriers DHS [85]. (b) Schematic of the GeSn/SiGeSn DHS on relaxed GeSn buffer [87].

In GeSn/SiGeSn quantum structures, in addition to the capability to tune the bandgap and lattice constant, the high bandgap energy of SiGeSn alloys provides an extraordinary optical confinement of charge carriers inside the active GeSn well when used as barrier. This feature makes SiGeSn a better barrier layer compared to GeSn alloys. On the other hand, quantum well with GeSn as a gain medium exhibits more carrier concentration because of the density of states improves. Figure 1.9(a) shows the energy profile of a proposed compressively strained $\text{Ge}_{0.84}\text{Sn}_{0.16}$ that is buried between tensile strained $\text{Si}_{0.09}\text{Ge}_{0.8}\text{Sn}_{0.11}$ barriers. The diagram indicates a direct bandgap alignment as the Γ valley is set below the L valley. Meanwhile the conduction and valance

band minimum (Γ) and maximum (heavy hole), respectively, are located in the GeSn well region, which indicate type I structure [85]. A laser diode was simulated using DHS with $\text{Ge}_{0.94}\text{Sn}_{0.06}$ as the well region and confined with $\text{Ge}_{0.75}\text{Si}_{0.15}\text{Sn}_{0.1}$ double barriers that could be built above a relaxed GeSn as shown in Fig. 1.9(b) [86], [87].

1.3 Dissertation Organization

This dissertation is organized as follow:

Chapters 2 discusses the growth techniques that were used in this dissertation. The chapters with introductory information about the UHV-CVD system that was used to grow bulk Ge and GeSn. The plasma setup in the UHV-CVD system is also discussed in details. Chapters 3 discusses the material and optical characterization methods that were used more frequently in the research work of this dissertation. Each measurement system is discussed briefly with the basic concepts and illustration drawings.

Chapters 4 and 5 were dedicated to Ge growth and characterization discussions. Chapter 4 discusses growth results of a one-step Ge-on-Si films using plasma enhancement in UHV-CVD system at the low temperature range from 250 to 450°C to make this growth process compatible with the CMOS technology process. The material properties were investigated using Raman, x-ray diffraction, and transmission and scanning electron microscopies. The optical properties were investigated using photoluminescence and spectroscopic ellipsometry. In addition, the effect of incorporating Sn in the one-step Ge layer were studied using plasma enhancement for the first time worldwide. Chapter 5, discusses the two-step Ge buffer layers growth by plasma enhancement at low temperatures with high optical and material quality. A comparison between plasma enhancement and non-plasma enhancement was made to further investigate how far this method

can be used as a growth technique in monolithic integration of group IV semiconductors with the current available Si complementary metal-oxide-semiconductor (CMOS) technology.

Chapters 6 and 7 are discussing SiGeSn alloys that were grown using commercial reduced pressure chemical vapor deposition and low cost commercial precursors. In chapter 6, the optical and materials properties of a bulk SiGeSn/Ge heterostructures with different compositions and thickness were explained. Photoconductor fabricated using SiGeSn alloys and thermal stability in multi-junction space solar cells were studied as device applications. Chapter 7 explains the results of a GeSn quantum well with SiGeSn double barriers. Finally, an overall summery of the dissertation and future work is discussed in chapter 8.

Chapter 2: Growth Techniques

2.1 Chemical Vapor Deposition (CVD)

Chemical vapor deposition (CVD) is defined as the use of chemical reactions of volatile gases to synthesize materials in the form of thin films. These reactions mainly take place in the vapor phase close to a heated substrate that helps in the decomposition process to form a solid film at the surface of the substrate. The gases, on the other hand, are in the form of precursors, which play a vital role in CVD growth mechanism.

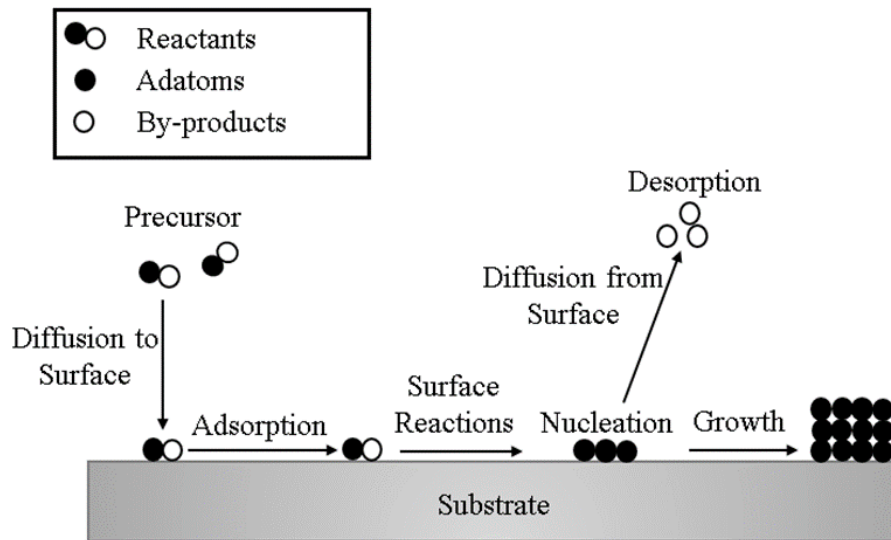


Figure 2.1: Schematic representation of the CVD reaction process near and on the surface of substrate.

The CVD reaction process is shown in Fig. 2.1. Near and on the surface of the substrate the reaction mechanism can be described as follow [88], [89]:

- (1) The diffusion of precursor through a stagnant (buffer) layer to the surface. Here, the precursor molecules arrive and diffuse to the surface of the substrate;
- (2) The adsorption. In this step the interfacial phase of molecules starts to change from the gas phase to solid phase;
- (3) Surface chemical reactions. At this step the precursor starts to decompose on the surface followed by surface migration. The film starts to nucleate homogenously, and by increasing

the growth time, more adatoms are accumulated to create either single crystal structure, polycrystalline, or amorphous;

- (4) Desorption of by-products of the chemical reactions that occur on the surface during the previous step. This is the last step of chemical reactions process on the surface, where the desorption increases as the occupied surface sites increases;
- (5) Finally, diffusion of by-products away from the growth chamber through the exhausting line of the CVD system.

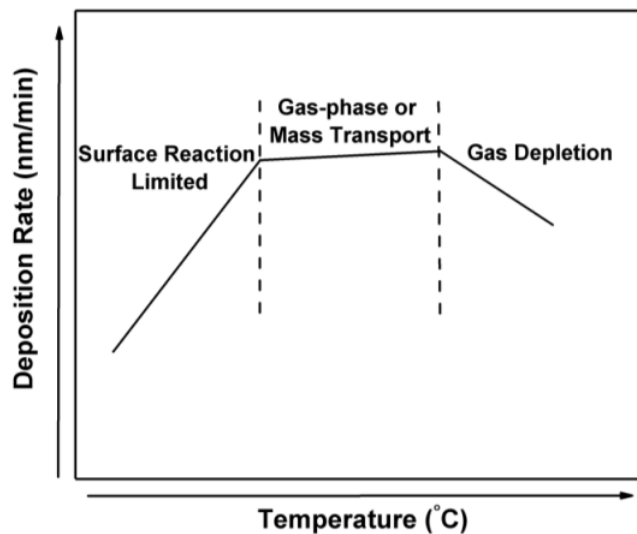


Figure 2.2: Variation of deposition rate with temperature in CVD growth chamber. The temperature range typically depends on growth chamber conditions and precursors.

The decomposition rate, or the growth rate, is an important term that should be investigated in the growth process to understand the growth trend. The deposition rate is defined as the number of monolayers that are deposited in a specific time at a certain growth temperature. The decomposition rate depends mainly on the temperature, and the hydride bonding, where the higher-order hydride, such as the Ge precursor digermane (Ge_2H_6), decomposes faster at low temperature than the hydride, such as germane (GeH_4). However, the decomposition rate as a function of temperature is limited by several factors. These factors divide the deposition rate vs. temperature diagram, as shown in Fig. 2.2, into the following domains [90]:

- (1) Surface reaction limited. In this growth domain, the deposition rate depends on the reaction rate at the surface of the substrate, which is directly related to the chamber pressure.
- (2) Diffusion control or mass transport. When the temperature exceeds a certain level in the intermediate range, the growth rate becomes insensitive to temperature, and depends on the diffusion region, a boundary layer above the surface that becomes thicker. In this case, reaching the substrate surface is difficult. However, this phenomenon is compensated by higher dissociation rate of reactants, which increases the deposition rate saturated at a maximum point.
- (3) Gas depletion or transport limited regime. In this growth region at high temperature the growth rate decreases with increasing the temperature due to higher dissipation of precursor. This phenomenon makes the growth zone to be depleted from reactants since most of them are decomposing and depositing near the heater or at the chamber wall before reaching the wafer surface.

The CVD growth technique can compete with other common growth methods, such as Molecular Beam Epitaxy (MBE). In addition, CVD is the most adopted growth technique in industry. CVD provides semiconductor epitaxy with high growth rate and low cost that is favored by industry especially for group IV epitaxy (Si, Ge, SiGe, SiC...etc.). For material quality, CVDs delivers high quality material when operated at ultra-high vacuum (UHV) conditions similar to MBE systems.

2.2 Ultra-high Vacuum-Plasma Enhanced Chemical Vapor Deposition (UHV-PECVD)

A state-of-the-art single wafer cold-wall UHV-PECVD reactor was designed and built in the engineering research center at the University of Arkansas at Fayetteville (UAF) to conduct research on the synthesis of group IV semiconductors based alloys. The system was successfully

used to grow Ge and SiGe, GeSn, and SiGeSn. A schematic of the system layout and a lab photo of the system are shown in Fig. 2.3(a) and (b), respectively.

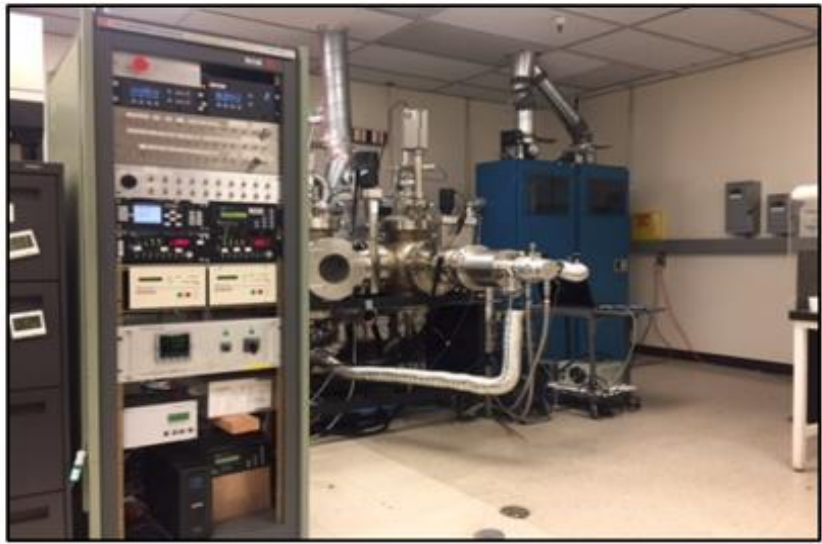
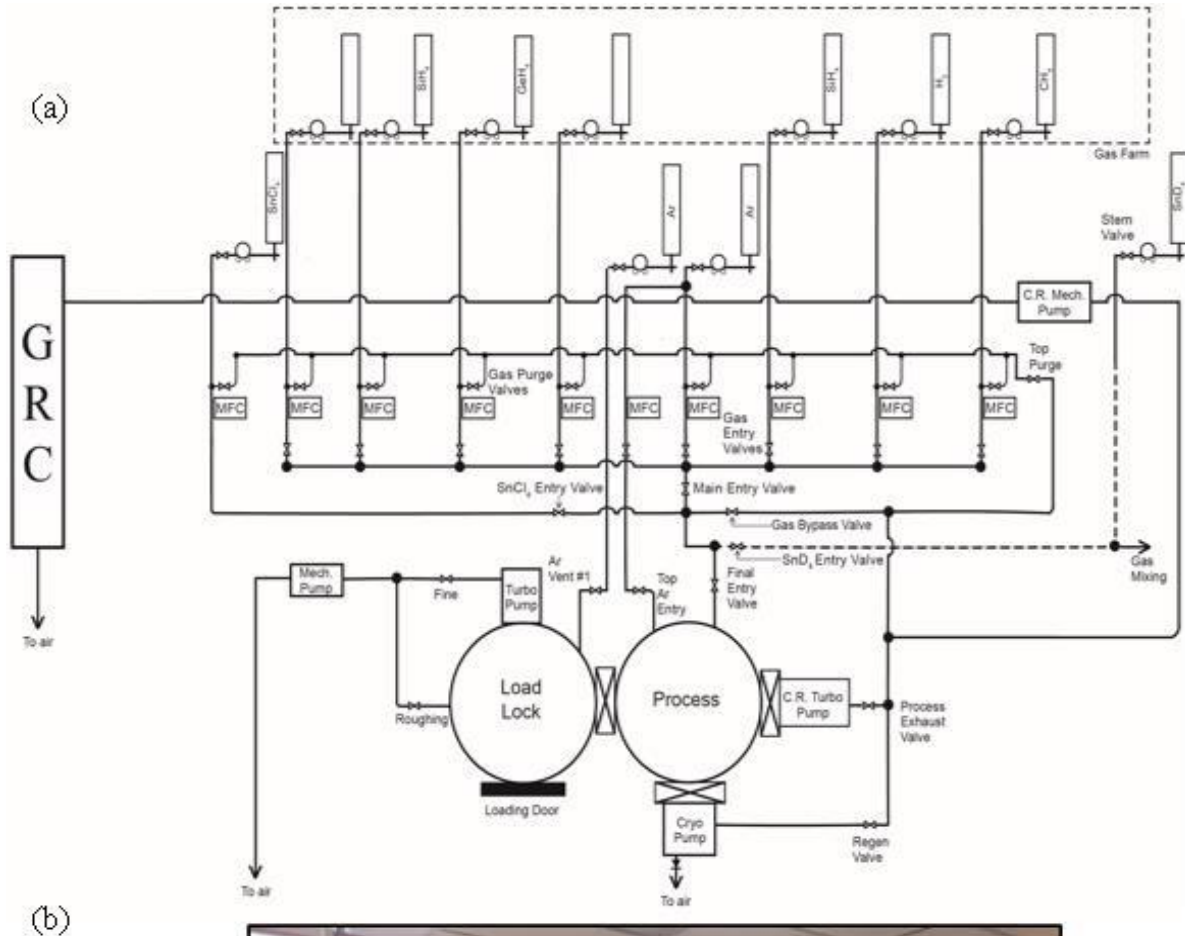


Figure 2.3: (a) Schematic layout of UAF's UHV-CVD system. (b) Photo of the system.

The UHV-CVD is a cold-wall system, and therefore no deposition is expected on the chamber walls. As shown in Fig. 2.3(a) the system consists of a load-lock chamber with a loading door that is used to load and unload the wafers. A process chamber is connected by a center gate valve to the load-lock chamber. The process chamber contains all features that are required to run the growth process, such as the heating assembly, gas manifold...etc. After opening the center gate valve, wafers are transferred from the load-lock to the process chamber using a magnetic arm with a wafer fork. For safety reasons, all gas bottles are placed outside the laboratory in a gas farm. The flow rate of precursors are controlled by mass flow controller (MFC) inside a gas manifold. The system has specialized capabilities, such as plasma enhancement, hot-filament, and gas mixing, that make it unique compared to other UHV-CVDs.

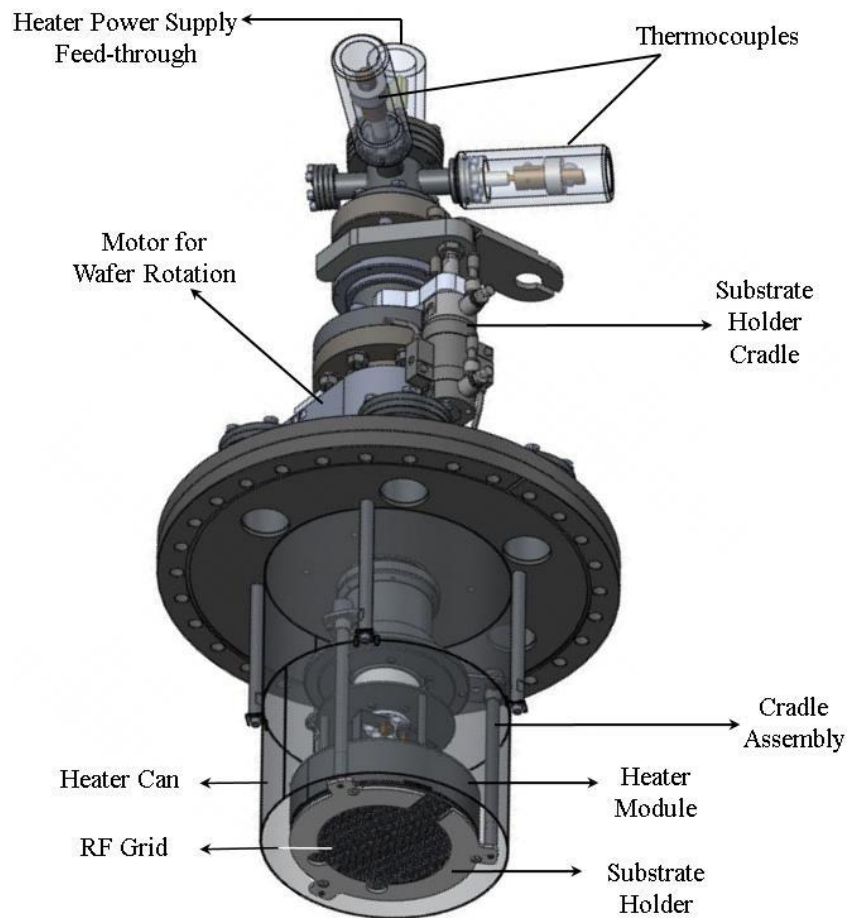


Figure 2.4: Deposition stage of the process chamber with heating and substrate components [91].

2.2.1 Heater and Substrate Assembly

Figure 2.4 presents heating and substrate assembly that is installed in the process chamber. The deposition stage is connected from the top to an UHV Design heater power supply. The heater can radiate the wafer with up to 1000°C, and placed in a position facing the backside of the wafer. The temperature was continuously monitored using a thermocouple thermometer. Both the power supply and the thermocouple connections are feed-through a flange by a tube to the heater module. To increase heat efficiency, heat shields made of tantalum alloys are placed above the heater, and both heater components are covered by a heater-can made of molybdenum alloy. A radio frequency (RF) (mesh) grid was located between the substrate holder and the heater. The RF grid, made of molybdenum, works as an electromagnetic shield to protect the heater module components from electromagnetic interference when the plasma enhancement growth is running.

The deposition stage also houses the substrate assembly, which contains the substrate holder, the cradle lifting device, and the substrate rotator that is supported by MagiGear vacuum motor. The motor helps the substrate holder to rotate with a speed of up to 80 rotation per minute. A large hollow torque tube is used to transmit the cradle rotation to the double stack MagiGear vacuum motor.

2.2.2 Vacuum

The UHV-CVD system is pumped using different vacuum pumps to reach the UHV level. Table 2.1 depicts the pumping ranges, gauges, and pumps. The load-lock chamber is pumped down by Edwards turbo-molecular pump backed by a scroll pump. The XDS-10 scroll pump starts from atmospheric level, and pumps the load-lock chamber down to reach vacuum level of 10^{-3} Torr. The turbo-molecular starts at 10^{-3} Torr, and continues pumping the system to 10^{-8} Torr. The process chamber is pumped down to 10^{-8} Torr by an STP Edwards corrosive resistant turbomolecular pump

that is backed by a QDP-40 corrosive resistant mechanical pump. In addition, a Marathon PC-8 cryogenic pump cooled by liquid helium is used to reach the base pressure of 10^{-10} Torr. The cryogenic pump helps in removing the oxygen and water vapor effectively. To measure the base pressure of each chamber, a Pirani gauge is mounted in the load-lock chamber while a cold cathode gauge (CCG) is used in the process chamber. The CCG is supported by an isolating valve to secure the CCG from high pressures during the growth. A gas reactor column (GRC) was used as a gas abatement system to process volatile process gases using high temperatures before exhausting them to atmosphere.

Table 2.1: Vacuum levels and pumps.

Vacuum Level	Pressure (Torr)	Flow Regime	Vacuum Gauge	Vacuum Pump
Atmospheric	760	Viscous	Pirani	-
Rough	10^{-3}	Transition	Capacitance Monometer	Scroll
High	10^{-6}	Molecular	Cold Cathode	Turbo-molecular
Very-high	10^{-9}	Molecular	Cold Cathode	Turbo-molecular
Ultra-high	10^{-12}	Molecular	Cold Cathode	Cryogenic

2.2.3 Wafer Cleaning

A standard clean 1 and 2 (SC-1/SC-2) RCA wet etching method is used in the cleaning process. Prior to growth, Si wafers were cleaned by using piranha etching for 10 min. The wafers were then dipped in dilute HF solution [$\text{H}_2\text{O}:\text{HF}$ (10:1) with 48% pure HF] for 2 min to remove native oxide and passivate the wafer surface with hydrogen. Finally, nitrogen gas was used to blow-dry the wafers before they were placed in the load-lock chamber. The cleaning process was performed in a class 10,000 clean room (ISO class 4) in the high density electronics center (HiDEC) at the University of Arkansas at Fayetteville.

2.2.4 Plasma Enhancement

Plasma, which is defined as a collection of free ionized charges, is commonly used in surface modification. It was found that plasma can significantly modify surface reaction dynamics even at low temperatures while the surface reaction kinetic in thermal CVD growth method drops at low temperatures [92]. The low surface reaction mechanism would lower the material quality. Similarly, the desorption process in the plasma enhancement growth is higher compared to the regular CVD growth; hence by products removal at low temperature is much faster with plasma. In addition, low power plasma enhances the dissociation ‘just in place’ is limited to the wafer surface. This feature allows the growth rate to be less sensitive to high growth temperature compared to the traditional CVD [92]. In this work, plasma enhancement in UHV-CVD was adopted to grow Sn based alloys that have never been grown using this method before. The overall procedure of the plasma growth process is presented in Fig. 2.5(a). Figure 2.5(b) is a view of the plasma discharge glow between the wafer and the metallic plate inside the process chamber.

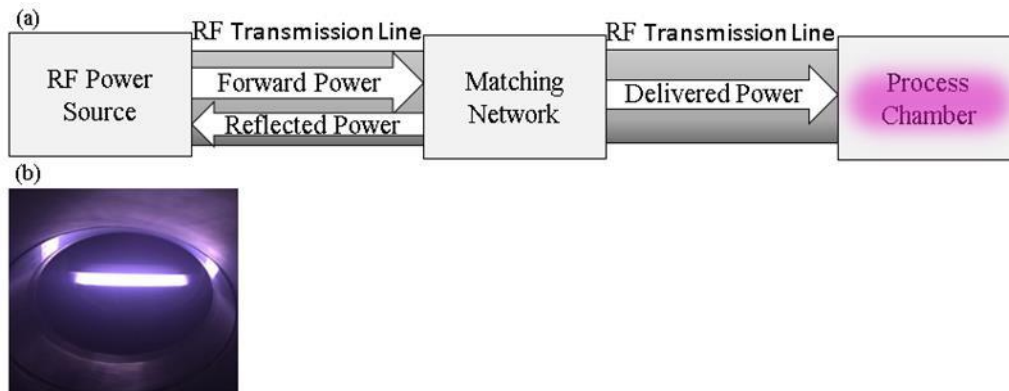


Figure 2.5: (a) Structure of the RF delivery components. (b) Side view of custom designed plasma electrode with active plasma in center, for UHV-CVD growth process of GeH_4 .

In general a power generator is used to generate the RF power that is transmitted to the chamber where the deposition process takes place. However, this process requires two major tools. First, a coaxial cable is required for RF power transmission. As shown in Fig. 2.6(a), the coaxial

cable consists of a center core made of copper surrounded for the RF power transmission while an aluminum hardware ground the reflected power of the RF powered electrode. The center core and the aluminum hardware are isolated from each other by alumina ceramic insulator. Outside the UHV-CVD chamber, the cable is surrounded by a plastic jacket. In UHV-CVD system, the cable is designed for UHV harsh environment such as excessive heat and high vacuum level as shown in Fig. 2.6(b). An L-shaped impedance matching network is used to filter and match the power source to the load.

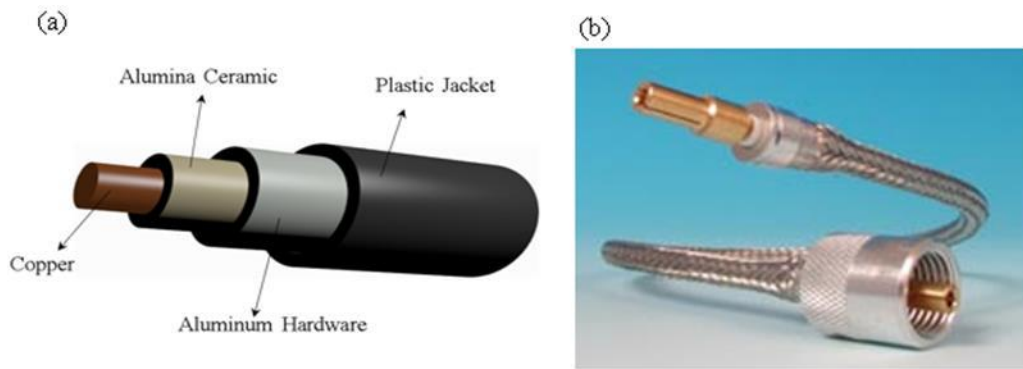


Figure 2.6: (a) RF coaxial cable that is used for RF power transmission outside the chamber. (b) Braided Stainless Steel coaxial cable for UHV environment.

The plasma enhancement feature was designed and implemented in the process chamber by using a capacitively coupled plasma (CCP) with 13.56 MHz RF power supply to generate Ar plasma. The CCP is an industrial standard plasma source that allows the use of 13.56 MHz without electromagnetic interference with other RF devices. The plasma assembly contains three major components: the upper electrode that also works as the sample holder, the lower electrode with a properly grounded plasma shield, and the heater/rotation components. Figure 2.7(a) illustrates the plasma setup design inside the process chamber with the upper electrode being powered by the RF source and the lower electrode is grounded. The electrode spacing is fixed at a distance of 20 mm to achieve consistent growth rates for all runs. The growth precursors and the Ar carrier gas were delivered horizontally to the chamber between the wafer and the plate.

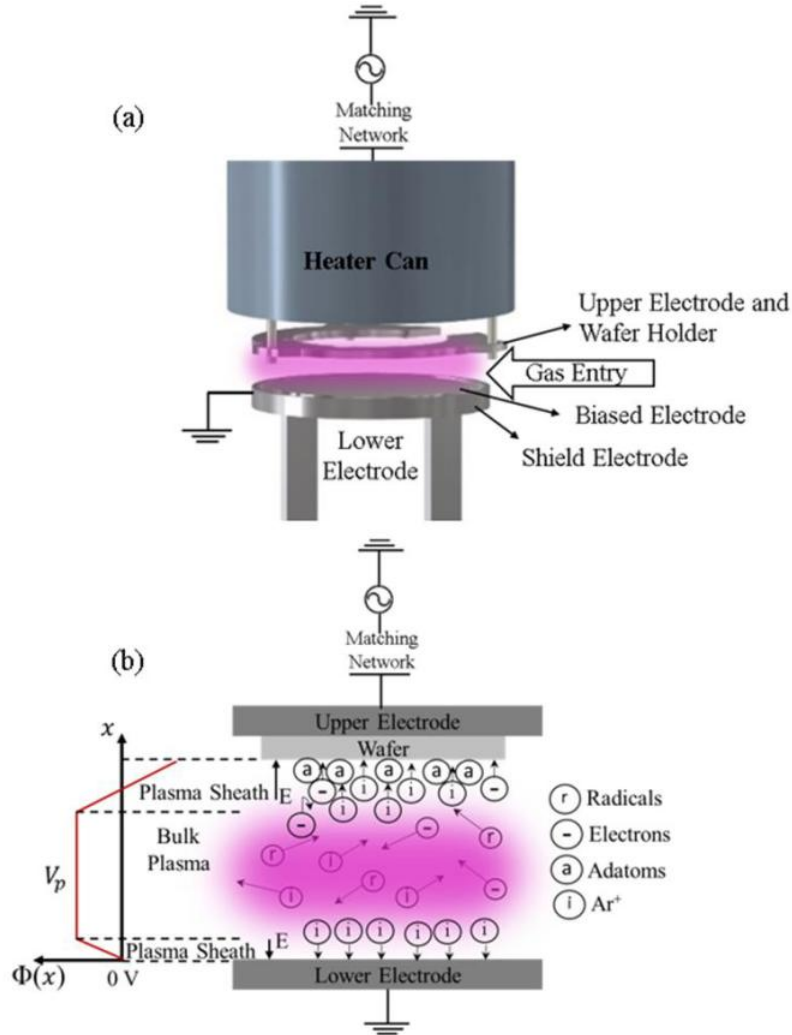
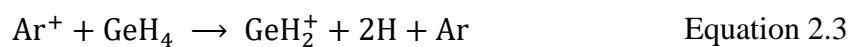
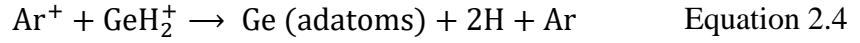


Figure 2.7: Schematic of PE setup inside UHV-CVD process chamber as: (a) The RF design inside the process chamber. (b) Shows the buildup of electric potential in both bulk plasma and sheath and the reaction mechanism when the upper electrode is powered.

The general growth mechanism of plasma enhancement CVD is illustrated in Fig. 2.7(b) when the upper electrode is powered and the lower electrode is grounded. The gases are dissociated into free radicals and ions to form the plasma glow. The decomposition process of GeH_4 can be summarized as follow:





Plasma can assist in the decomposition process of GeH_4 and thus increases the growth rate at low temperature. In addition, a high-voltage capacitive plasma sheath is shaped between the bulk plasma and the substrate. In the steady-state plasma discharge, the time-averaged potential profile $\Phi(x)$ of the bulk plasma region has a positive value (V_p). Near the sheath region, V_p drops sharply across the sheath to reach a negative value [5]. When the upper electrode is powered, plasma sheath tends to expel positive ions toward bulk plasma and confine most of them inside it. This mechanism is behind the creation of a built-in electric field (E), which accelerates the ions of precursors in the thick sheath region toward the substrate. As a result, ions arrive at the film surface with an energy that increases the collision probability among reactive ions. Therefore, the material quality of the film increases at low growth temperature because of the enhanced surface mobility of adatoms.



Figure 2.8: ASM's Epsilon[®] 2000 Plus RPCVD system.

2.3 Reduced Pressure Chemical Vapor Deposition (RP-CVD)

Our group established an external research cooperation with ASM America Inc. in Phoenix, AZ. The company owns an Epsilon[®] 2000 Plus single wafer RP-CVD. The process chamber has a cold wall quartz tube with a horizontal gas flow and a load-lock. In this work RP-CVD has been utilized to grow bulk SiGeSn/Ge/Si samples. The system was used also in the growth of SiGeSn/GeSn quantum wells.

Chapter 3: Characterization Methods

Characterization was the second step after growth. It helps in the investigation of the material and optical properties. In this chapter the basic principle, specification, and measurement condition of the most frequent techniques are presented. The first section discusses the material characterization methods while optical measurement techniques are discussed in the second section.

3.1 Material Characterization

3.1.1 Raman Spectroscopy

Raman is a vibrational spectroscopic technique that studies the interaction of absorbed light with the optical phonons. It is commonly known that Raman spectroscopy helps in the exploration of the crystallinity, strain, and composition of solids. When an incident laser beam interacts with the surface of the sample, three scattering mechanisms can occur. Figure 3-1(a) and (b) illustrate the interaction and surface scattering mechanisms. The scattering mechanisms are classified based on the transition from the vibrational energy states to the virtual energy states. If the incident photon energy with an energy $h\nu_i$, where h is Planck's constant and ν is the photon frequency, is equal to the scattered light, i.e. $h\nu_i = h\nu_f$, then this scattering mechanism is known as Rayleigh scattering. Raman scattering occurs if the scattered light loss or absorbed a phonon known as Stokes or anti-Stokes scattering, respectively, which causes an energy difference ΔE as depicted in Fig. 3.1(b). By measuring the scattered light wavelength, Raman shift can be calculated using the following equation:

$$\omega = \left(\frac{1}{\lambda_i} - \frac{1}{\lambda_s} \right) \times 10^7 \quad \text{Equation 3.1}$$

where ω is the Raman shift in unit of cm^{-1} , λ_i is the incident laser beam wavelength, and λ_s is the scattered wavelength from the sample.

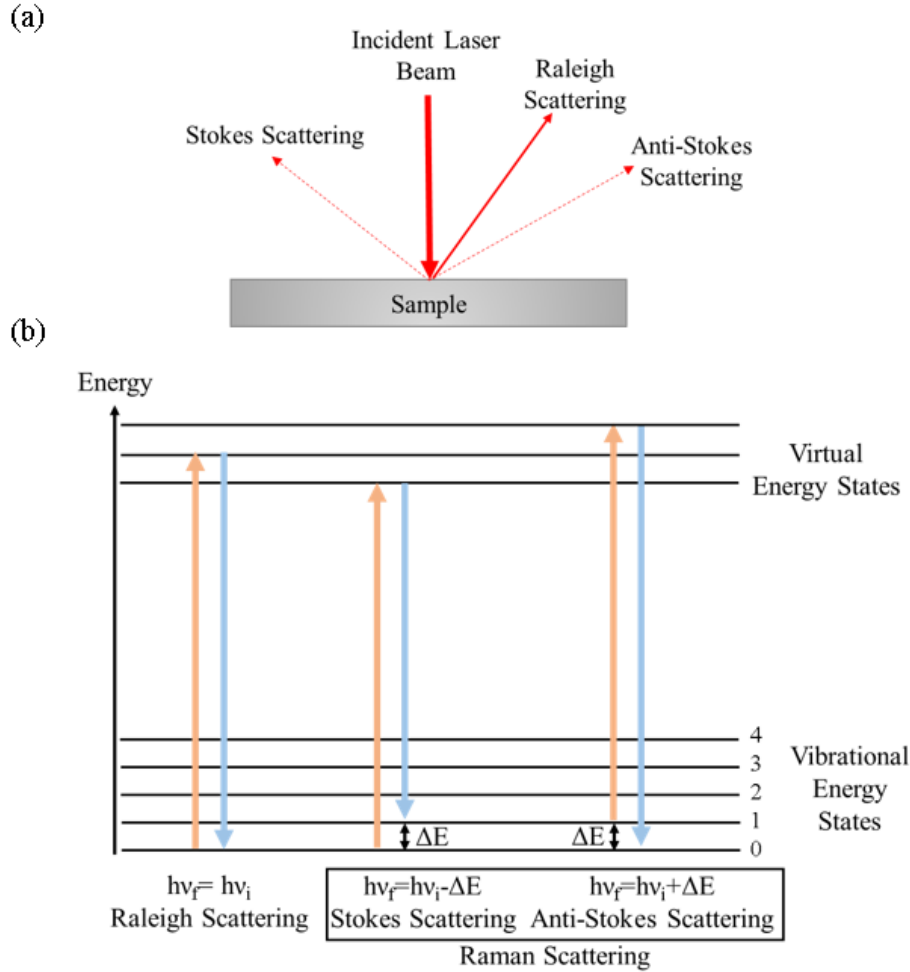


Figure 3.1: (a) Schematic of laser-matter surface interaction. (b) The interaction process of Raleigh and Raman.

In this work, the surface of the sample was shined by continuous wave (CW) 532 nm green laser or 632.8 nm red laser. The Raman measurements schematic is shown in Fig. 3.2. The unwanted back ground was filtered using bandpass filters. Specific mirrors were used to align the laser beam from the laser source to the sample. A neutral density filter had been used in the bath of the green laser, placed between mirror three and five, to attenuate the laser power. Double beam splitters were used to split the beam in two directions while lenses were used for beam focusing. The reflected Raman scattering light was collected using iHR550 spectrometer that has a nitrogen-cooled CCD (Charge Coupled Device) arrays.

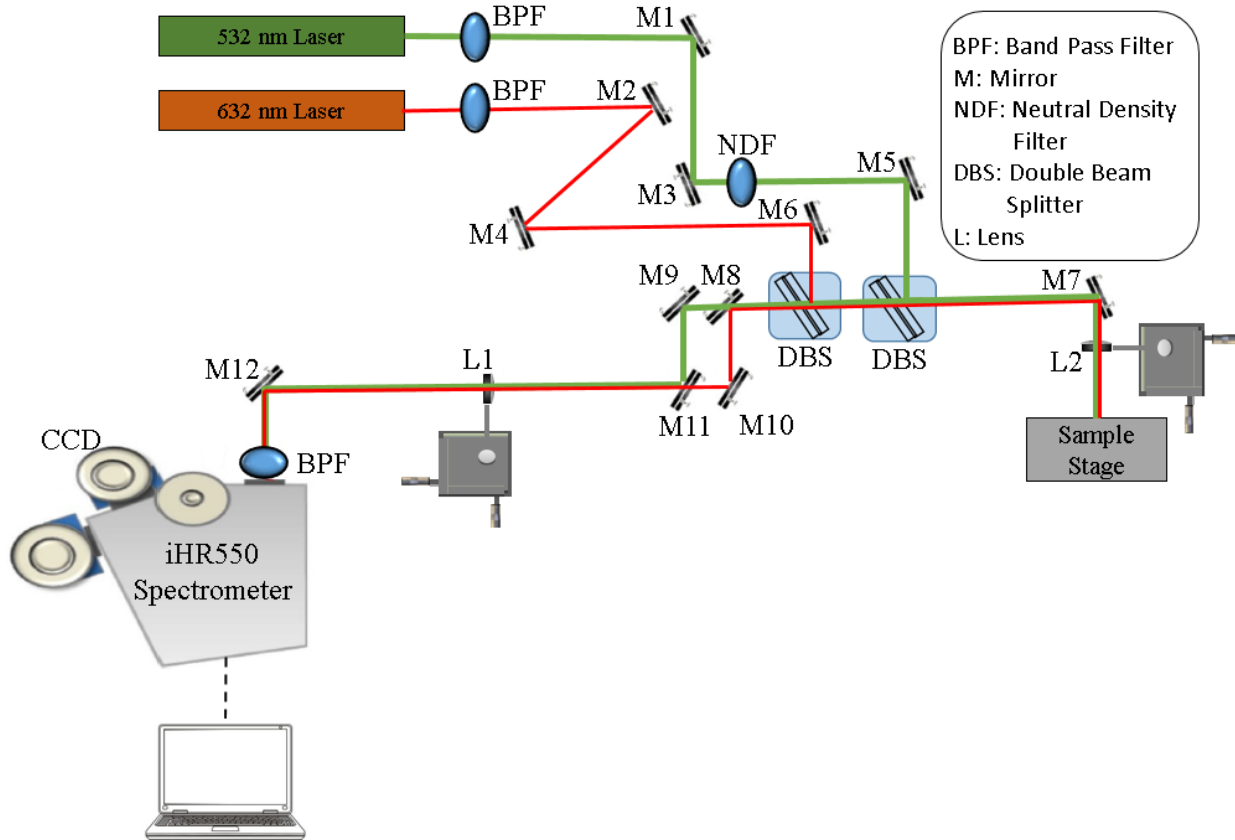


Figure 3.2: Schematic of the Raman setup with 532 nm and 632 nm lasers.

3.1.2 X-Ray Diffraction

X-Ray Diffraction (XRD) is a non-destructive technique that is used to determine lattice constants, material quality, strain, and composition of alloys. When two electrodes with high applied voltage accelerates electrons from an x-ray source toward the target (sample), two interaction mechanisms may occur. Either deceleration of electrons by the atoms of the sample or excitation of the sample atoms that result from elastic collision between electrons beam and atoms. The first mechanism is known by Bremsstrahlung radiation while the second is collision radiation. Both are responsible for x-ray generation.

For an incident x-ray beam in a crystal structure with atomic planes (lattice planes) distance d , d can be calculated from the reflected beam by using Bragg's law given by:

$$n\lambda = 2d\sin\theta \quad \text{Equation 3.2}$$

where n is the interference order ($n= 1, 2, 3, \dots$), λ is the incident x-ray wavelength, and θ is the diffraction angle. A schematic representation of two interaction geometries are shown in Fig. 3.3(a) and (b) for symmetrical and asymmetrical measurements, respectively. For the case of symmetrical measurement, the incident x-ray angle (ω_i) is fixed, i.e. is the same as the diffracted angle (ω_d) while 2θ changes at different planes as shown in Fig. 3.3(a). This scan method known as rocking curve (XRD-RC). For asymmetrical measurement, in addition to 2θ , ω_i varies and therefore ω_d as shown in Fig. 3.3(b). The XRD scan of the second case yields to a two dimensional scan of the structure in the reciprocal space known as reciprocal space mapping (RSM). As shown in Fig. 3.4, it is noted that RSM scans give more information about the crystal structure compared to XRD-RC. This is because lateral correlation and the mosaic spread broadening directions in the XRD-RC scan, which is normally in the q_z or (004) direction, are coupled. In contrast, XRD-RSM scan, normally in the (224) direction or the q_x and q_z , allows the lateral correlation and the mosaic spread directions to be decoupled [93].

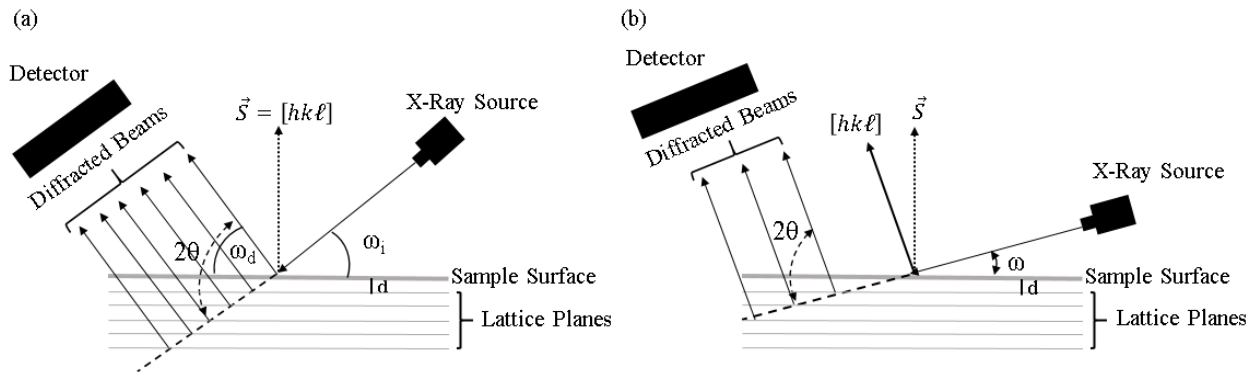


Figure 3.3: Geometry of the two diffraction methods from lattice planes: (a) For symmetrical scan with 2θ varies ($\omega_i = \omega_d$) and (b) for asymmetrical scan with both 2θ and ω vary.

In this work, XRD measurements were carried out using Philips X'pert PRO diffractometer equipped with a Ge (220) monochromator, the system is shown in Fig. 3.5. The XRD-RC scans

were taken along the (004) direction while XRD-RSM scans were taken from diffraction along the (-2-24) direction. The measured XRD-RSMs have reciprocal lattice units (rlu) with the q_x and q_z that were converted to real space units with the in-plane (a_{\parallel}) and out-of-plane (a_{\perp}) lattice constants using equations as follow:

$$a_{\parallel} = 10\sqrt{2(q_x)^2} + 0.019 \quad \text{Equation 3.3}$$

$$a_{\perp} = 40/q_z - 0.012 \quad \text{Equation 3.4}$$

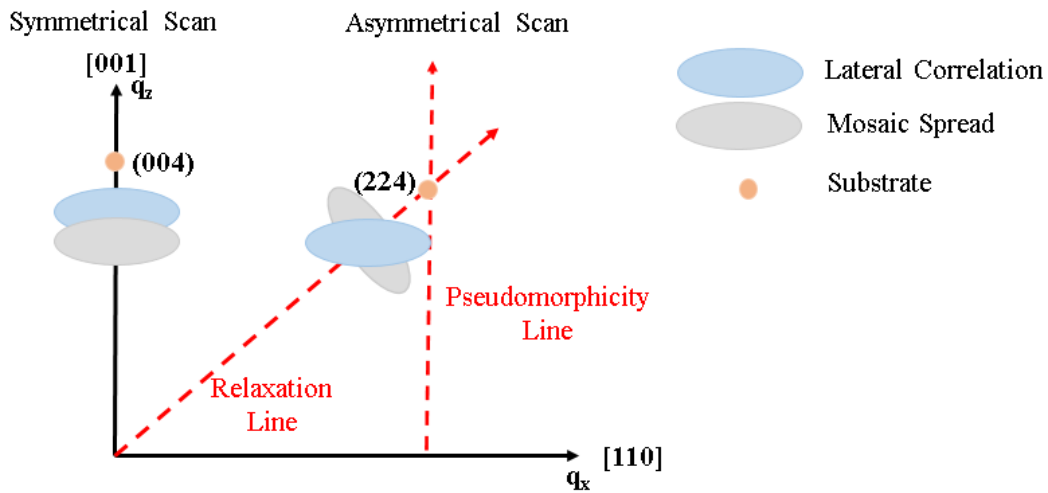


Figure 3.4: Illustration of effect of lateral correlation and peak spread on peak-boarding in (004) and (224) directions.

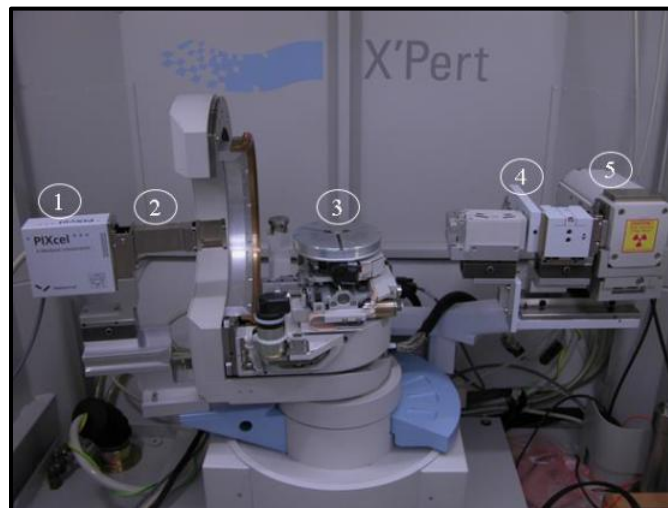


Figure 3.5: Photo of Philips X'pert PRO XRD system in the Institute for Nanoscience Engineering at the University of Arkansas. From left to right: (1) detector; (2) diffraction optics; (3) sample stage; (4) detector slits; and (5) x-ray source.

3.1.3 Transmission Electron Microscopy

Transmission electron microscopy (TEM) is a nondestructive microscopic technique that utilizes the interaction of high energy beam of electrons with very thin samples. TEM provides informative feedback about the structure of the sample using images, diffraction, and energy-dispersive X-ray spectroscopy (EDXS). The general concept of TEM is similar to optical microscope, however, beam source and lenses are quite different. Figure 3.6 presents a comparison between optical microscope and TEM. In addition to the beam source that is electrons instead of light in optical microscope, electron microscope uses electromagnetic lenses to control and focus the electron beam. Condenser lens is used to focus electrons of the first crossover on the specimen (sample). An objective lens is set in electrons direction after the sample that collects the scattered electrons and creates the first image. The beam is then expanded by a projector lens, and the final image is presented on a phosphor screen.

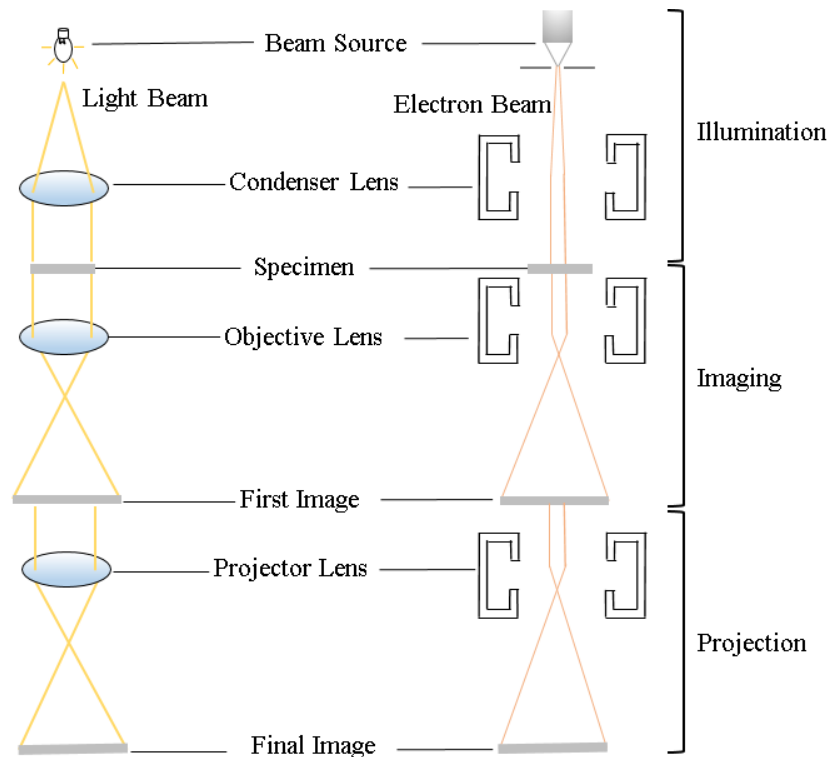


Figure 3.6: A comparison between optical and electronic microscopes.

In order to get a high quality TEM images, sample preparation must be well done. The sample preparation process is shown in Fig. 3.7. In the sample preparation laboratory, a small piece of the sample was glued with another piece face to face. The sample was placed on the heater under 180°C for two hours after it was compressed into a clamping vise. An Allied High Tech Products Inc. polisher was used for mechanical thinning until reaching a thickness of $< 20 \mu\text{m}$. A copper grid with 2 mm-diameter concentric hole was used to hold the sample for the next steps. Fischione 1010 low-angle ion milling machine was used to make a hole in the middle of the sample. The final thickness of the optically transparent area around the hole is roughly 50-300 nm, which is sufficient for TEM imaging. A high-resolution cross-sectional TEM images, viewed from $[\bar{1}10]$ direction, were taken using a Cs corrected Titan 80-300 with a Schottky field emission gun (FEG) that is operated at 300 kV. In addition, TF20 with electron sources operated at 200 keV was also used.

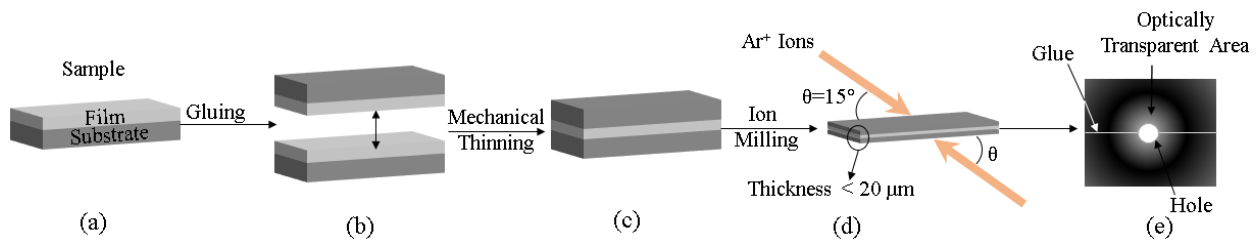


Figure 3.7: TEM sample preparation sequence. (a) Piece of the sample; (b) gluing; (c) mechanical thinning (polishing); (d) ion milling; (e) top illustration of the final TEM sample shows the hole surrounded by an optically transparent area.

3.2 Optical Characterization

3.2.1 Ellipsometry

Ellipsometry is a sensitive optical characterization technique that uses the interaction of an incident polarized light with the surface of a thin film sample to determine the phase change of a reflected light. The reflected light is measured as a function of psi (ψ) and delta (Δ). Figure 3.8 shows a schematic representation of the experimental concept of ellipsometric measurement. The reflected

light beam carries information about the film, such as optical constants (n , k , ϵ_1 , and ϵ_2), from which the optical absorption of the thin film can be calculated as:

$$\alpha = \frac{1}{d} \ln \left(\frac{\sqrt{(1-R)^4 + 4T^2R^2} - (1-R)^2}{4TR^2} \right) \quad \text{Equation 3.5}$$

where α is the optical absorption, and d , R , and T are the film thickness, reflectance, and transmittance, which can be calculated by:

$$d = \frac{\lambda}{2\sqrt{n_1^2 - \sin^2 \varphi}} = \frac{1}{2n_1\Delta(1/\lambda)} \quad \text{Equation 3.6}$$

$$R = \frac{(n_0 - n_1)^2 + k_1^2}{(n_0 + n_1)^2 + k_1^2} \quad \text{Equation 3.7}$$

$$T = \frac{1-R}{1+R} \quad \text{Equation 3.8}$$

where λ is the light wavelength, n_1 is the refractive index of the film, and φ is the incident light with the incident normal [94].

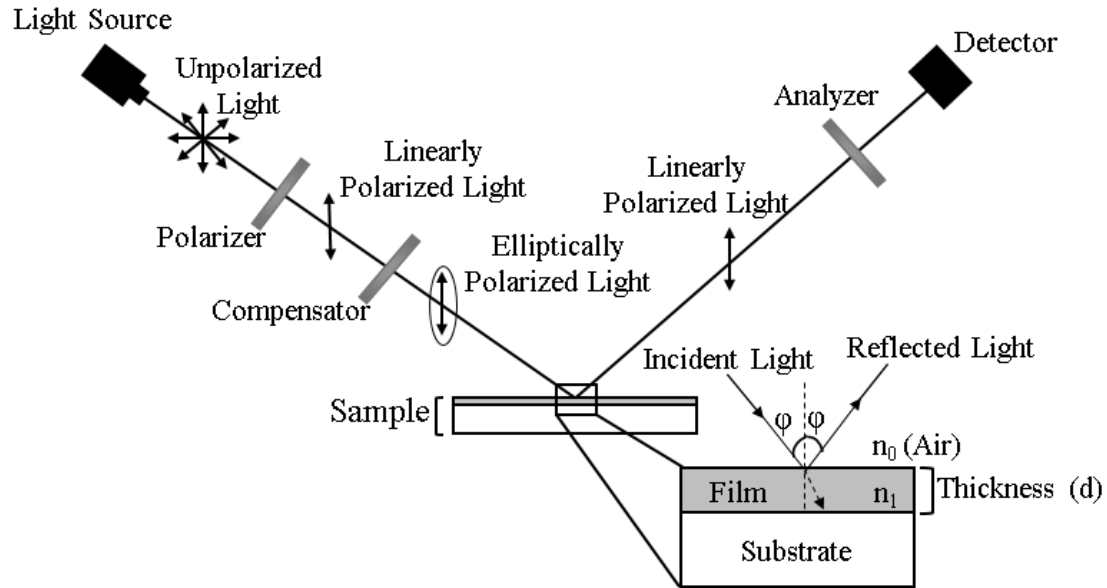


Figure 3.8: Schematic of basic concept of ellipsometry. The interaction and reflection polarized light from surface of a thin film sample.

A Variable-Angle Spectroscopic Ellipsometry (WVASE32) was used to collect spectroscopic data in the range of 0.496 - 4.768 eV (260 - 2500 nm) with a resolution of 10 nm at different angles of incidence (65° , 70° and/or 75°). The data fitting process was performed using a built-in WVASE32® software. In fact, each sample was analyzed using multiple-layer model consisting of a Si substrate and the film. The film could be one or several layers. The surface layer of the model consist of 50% air and 50% of the very top layer of the film. Moreover, the dielectric function of each layer was described using Johs-Herzinger model. After performing normal fit for ellipsometry data, the absorption coefficient data were obtained, and then were fitted by applied physical model near the band edge. As an example, the generated experimental Ψ , Δ , and the data from the model fit of a $\text{Si}_{0.19}\text{Ge}_{0.783}\text{Sn}_{0.027}$ sample are shown in Fig. 3.9.

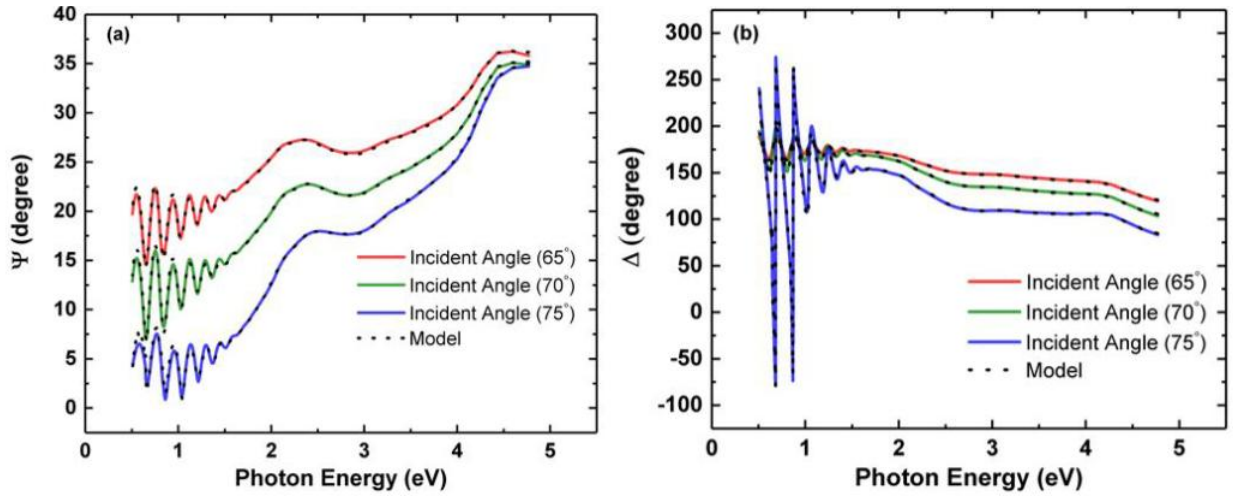


Figure 3.9: Experimental ellipsometry data and model fitting of a $\text{Si}_{0.19}\text{Ge}_{0.783}\text{Sn}_{0.027}$ sample. (a) Ψ spectra and (b) Δ spectra.

3.2.2 Photoluminescence

Photoluminescence (PL) is the resulting radiation from the recombination process of an excited electron in the conduction band with a hole in the valance electron to create an electron-hole pair (EHP). Thus, PL helps in studying the bandgap nature of semiconductor materials. A schematic of the photoluminescence process is shown in Fig. 3.10. When an incident photon, with an energy

equal or greater than the bandgap difference, it excites an electron in the valance band to an energy level (E) at the same wave vector (k) in the conduction band. The electron is then recombine with the hole in a reverse phenomenon to create EHP and emits light or heat equal to the bandgap difference. However, the recombination process must satisfy the law of momentum conservation. Here, we have two possible recombination processes. (1) A radiative recombination as shown in Fig. 3.10(a) in which the momentum is conserved, and the EHP recombination occur in the same k value. (2) A Shockley-Read-Hall (SRH) non-radiative recombination, which involves recombination through defect centers in the k space. These centers allows electrons to recombine with holes by taking any momentum difference between the hole and the electron via lattice vibration and phonons absorption, which generates heat instated of light. For low quality materials, the SRH recombination is usually dominated, and it generates a weak PL comper to the radiative recombination.

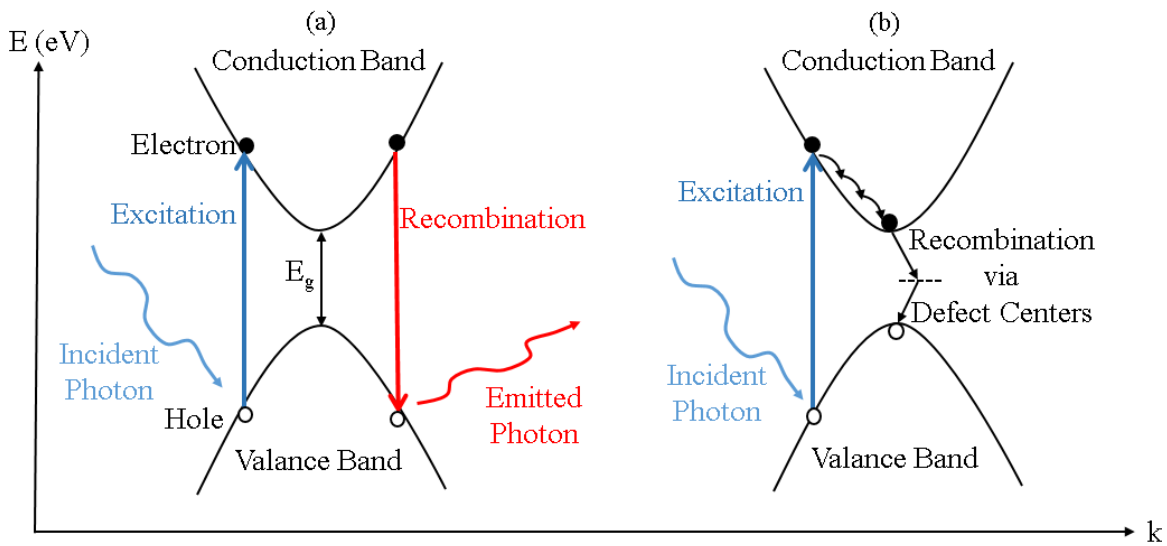


Figure 3.10: Illustration of the conduction and valance band in the E-K diagram in semiconductors that shows the photoluminescence process. (a) Radiative recombination and (b) Shockley-Read-Hall recombination.

Si-Ge-Sn alloys in this study were pumped using 532 nm continuous wave laser and a 1064 nm pulsed laser. The pumping parameters of each laser are listed in Table 3.1. A schematic of the

PL setup is shown in Fig. 3.11. A set of iris (pin holes) and mirrors were used to align the laser beam to the sample holder. The laser beam was focused on the sample using a CaF₂ plano-convex lens with focal length of 10 cm. The CaF₂ collecting lens is made of a material that transmits 90% of the light in the range 500-5000 nm. The CaF₂ sent the excited light using gold-coated mirrors designed for infrared range to the spectrometer. A thermoelectric (TE) cooled lead sulphide (PbS) with a cut-off at 3 μm, liquid nitrogen cooled extended-InGaAs with a cut-off at 2.3 μm, and a LN₂ cooled indium antimonide (InSb) with a cut-off at 5 μm photodetectors are connected to a iHR320 HORIBA spectrometer with a grating that has the blazing wavelength of 2000 nm and groove (gr) density of 600 gr/mm. Lock-in amplifier and optical choppers were used to amplify the electrical signal and to reduce the noise interference.

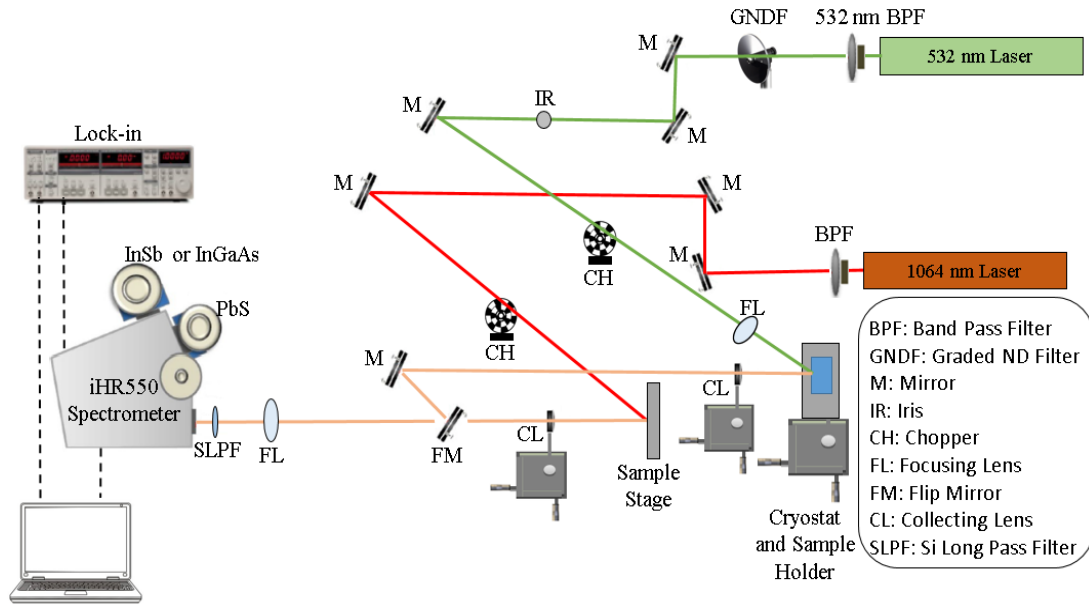


Figure 3.11: Figure 3-11: Optical alignment of the PL measurements setup of the 532 nm and 1064 nm lasers. The major instrumentation tools are also shown.

Table 3.1: Pumping lasers parameters [95].

Laser Wavelength (nm)	Spot Diameter (μm)	Average Power (mW)	Average Power Density (kW/cm ²)	Excitation Carrier Density (Photon/s/cm ²)	Penetration Depth (nm)		
					Ge	GeSn	SiGeSn
532	65	500	15	4.1×10 ¹⁹	~ 36	~ 21	~ 19
1064	52	140	6	3.5×10 ²²	~ 1006	~ 418	~ 503

Chapter 4: One-step Germanium-on-Silicon Using RF in UHV-PECVD

4.1 Introduction

The difficulty of growing Ge-on-Si arises as a result of the large lattice mismatch (4.2%) between the Ge ($a_{\text{Ge}} = 5.657 \text{ \AA}$) epilayer and the Si ($a_{\text{Si}} = 5.431 \text{ \AA}$) substrate. This may introduce a network of misfit dislocations at the Ge/Si interface, resulting in high threading dislocation density (TDD) in the Ge layer. Another hurdle to Ge-on-Si growth is surface roughness, measured by the root mean-square (RMS) value of the surface peaks and valleys. At low growth temperature, Ge-on-Si starts in a two-dimensional layer-by-layer mode. After a certain critical thickness and as the growth temperature becomes higher than $\sim 375^\circ\text{C}$, the film starts to relieve the strain that is caused by lattice mismatch. Growth in this stage is mainly affected by the surface energy, which causes a three-dimensional island-like mode, which causes surface roughness. These two issues, namely high TDD and surface roughness, can reduce device performance in practical applications. Therefore, different growth methods have been developed to address these issues.

This chapter presents the growth method of Ge-on-Si using plasma enhancement in UHV-CVD using low-cost GeH_4 . Ge films were grown in a single step at low temperatures ($250\text{-}450^\circ\text{C}$) without a post-deposition annealing. The crystallinity was determined by Raman. The growth rates in the temperature range of $350\text{-}450^\circ\text{C}$, which produced crystalline films, were studied at different pressures (0.1, 0.3, and 0.5 Torr). X-ray diffraction measurements reveal that these crystalline Ge films were slightly compressively strained. The optical quality was investigated using room temperature photoluminescence and ellipsometry spectroscopic techniques. The material quality was examined by the transmission electron microscopy and by counting etch-pit density in the scanning electron microscopy. The growth rate, material and optical qualities were also compared between plasma enhancement and non-plasma enhanced growths at 400°C .

4.2 Experimental Procedure

In this study, the RF power was fixed at a high-power level (50 W) for all growth runs. In addition, the substrate was rotated at 20 revolutions per minute (rpm) to insure growth uniformity across the wafer. Four-inch (100) p-type Si wafers with a resistivity range of 5-20 $\Omega\cdot\text{cm}$ were used as substrates. To ensure film uniformity across the wafer, the wafer was baked at the designated temperature for 20 min before starting the growth. The growth temperatures were in the range of 250 to 450°C. The chamber pressure was fixed at 0.1, 0.3, and 0.5 Torr, and the growth time was varied between 5 and 25 min. The GeH_4 and Ar flow rates were fixed at 5 and 200 sccm, respectively.

The structural properties study was conducted using an X'pert PRO diffractometer equipped with a Ge (220) monochromator high resolution x-ray diffractometer (XRD) has been used to determine the samples lattice sizes, crystallographic quality, and strain. Transmission electron microscope (TEM) images have been taken to study crystal orientation and defects. A high resolution TITAN 80-300 with field emission electron beam source operated at 300 KV was used for this purpose. A Variable-Angle Spectroscopic Ellipsometry (Woolam Model VASE32) was used to determine the thickness and absorption coefficient study. The data fitting was processed using the built-in WVASE32[®] software. A 532 nm green laser Raman setup with 30 mW power and 10-second integration time was used as a significant tool to probe the material quality. The system is connected to a Horriba (iHR 550) spectrometer with a camera cooled by liquid nitrogen. Photoluminescence (PL) was performed for each growth at room temperature to examine the optical quality of the Ge epilayer. The system was equipped with a 1064 nm pulsed laser with 5 ns pulse duration and 45 kHz repetition rate to excite charge carriers. The emission

was collected by a spectrometer equipped with a thermoelectrically cooled PbS detector with cut-off wavelength at 3.0 μm .

4.3 Results and Discussion

4.3.1 Growth Findings

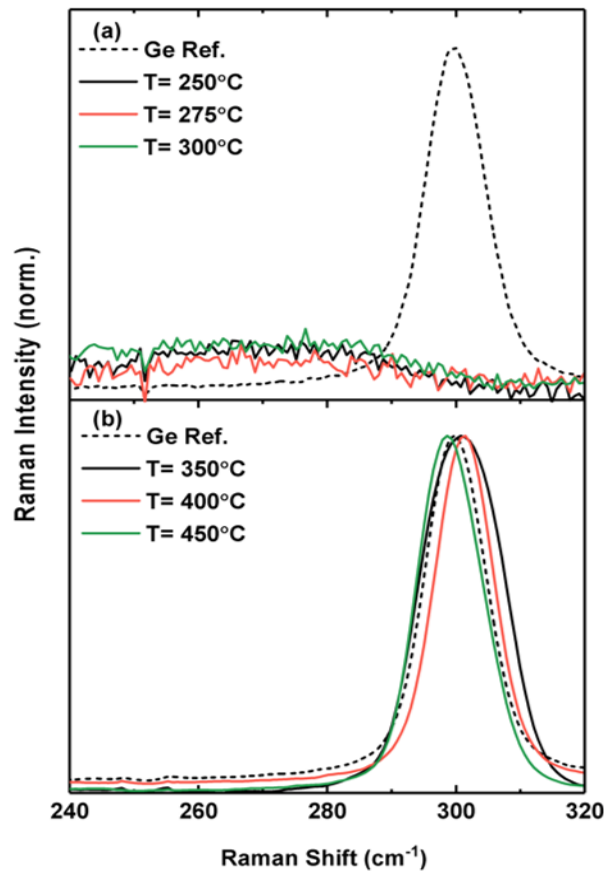


Figure 4.1: Normalized and stacked Raman results. (a) At the temperature range 250-300°C. (b) At the temperature range 350-450°C.

Raman spectroscopy was first used to explore the material crystallinity in the growth temperature range from 250 to 450°C. In this temperature range all other growth parameters were fixed. The results are shown in Fig. 4.1(a) and (b). The figures were normalized and stacked for clarity. The growth at the low temperature range (250-300°C) is shown in Fig. 4.1(a). The absence of a clear shape peaks and the appearance of much broadened peaks near 260 cm^{-1} indicates amorphous Ge films for this temperature range. However, as the temperature increases to 350°C

and above, a transition from amorphous to crystalline Ge films was observed as shown in Fig. 4.1(b). This is noticed by the formation of clear and defined peaks near 300 cm^{-1} that corresponds to the relaxed LO Ge-Ge mode. The LO Ge-Ge peaks are localized close to the crystalline Ge reference curve (the dashed line). Figure 4.2 shows that the peaks of the LO Ge-Ge modes shift toward higher wave numbers compared to bulk Ge reference for 350 and 400°C growths. The shift toward longer wavenumbers compared to a relaxed Ge layer indicates compressively strained Ge layer. However, as the growth temperature increases to 450°C, the peak position shifts to 298.5 cm^{-1} , which indicates tensile strained Ge layer. As Fig. 4.2 shows, the FWHM became smaller when the temperature was increased beyond 350°C, which indicates improved material quality. Based on these findings, our subsequent growths were focused at this temperature range (350-450°C).

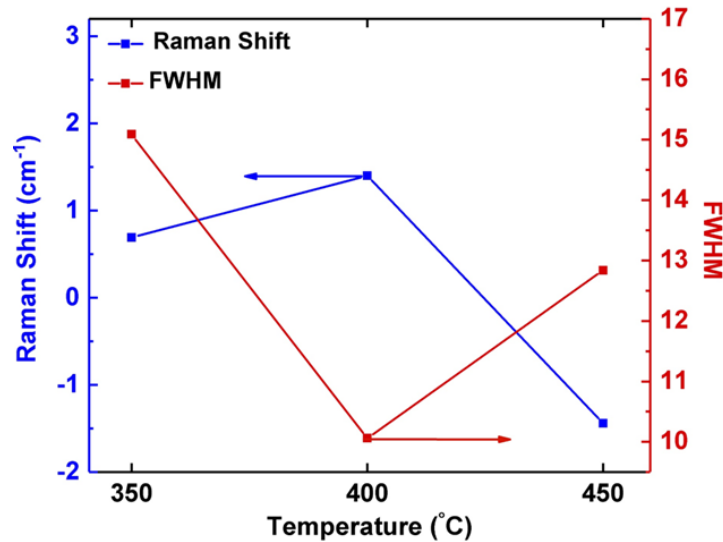


Figure 4.2: Raman shift and peak FWHM variation at temperatures that exhibit Ge-Ge LO modes at the temperature range 350-450°C.

The variation of the thickness and GR have been determined in order to explore plasma effect in enhancing dissociation rate at low temperatures (350-450°C) and at different growth times and pressures. Figures 4.3(a), (b), and (c) show linear fitting of the thickness as a function

of growth time for the three chosen growth temperatures. The Ge film thickness increases monotonically with time for all pressures. However, the results show consistent linear increase with pressure and time at 400°C. In addition, it is observed that the maximum achieved thickness is at 0.3 Torr pressure at all temperatures. This is associated with the change in the mean free path as the pressure changes. The mean free path (λ), which is defined as the average zigzag (not straight) distance for a molecules to travel between two subsequent collisions, plays a significant role in the GR and depends on the pressure.

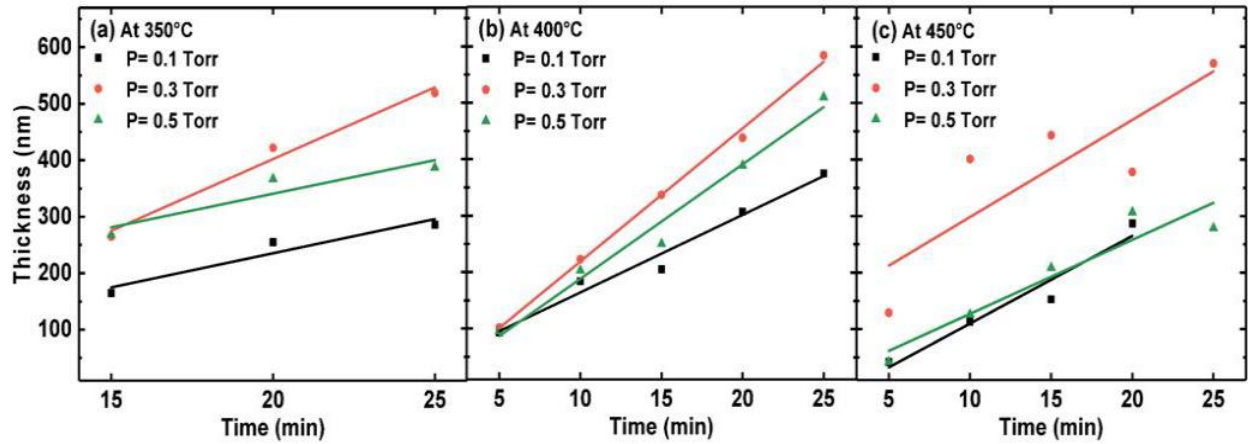


Figure 4.3: Film thickness versus growth time at three different temperatures: (a) 350°C, (b) 400°C, and (c) 450°C. Solid lines show linear fittings.

The relation between the chamber pressure and the mean free path of the reactants molecules is given by [96]:

$$\lambda = \frac{k_B T}{\sqrt{2} \pi d^2 p} \quad \text{Equation 4.1}$$

where k_B is Boltzmann constant, and its value is $1.38 \times 10^{-23} \text{ J.K}^{-1}$, T is the growth temperature in kelvin, d is the molecular diameter ($d \approx 3.8 \text{ \AA}$), and p is the chamber pressure. At 0.1 Torr, λ calculations reveal 13 cm. It means the distance between GeH_4 radicals is high enough to allow them to arrive and deposit on the wafer's surface. As the pressure increases, the mean free path of radicals decreases from 13 cm at 0.1 Torr to 4.4 and 2.6 cm at 0.3 and 0.5 Torr, respectively. The

decreased λ results in more collisions; thus the reaction species recombine before reaching the sample surface. Also, the material available for growth was more at higher pressure which might cause a balance between the mean free path effect and reactants availability.

The growth rate (GR) was then evaluated for each temperature with the results shown in Fig. 4.4. For $P=0.1$ Torr, the GR increases linearly with temperature. At the pressure, the growth is within the surface reaction limited regime, which is affected by the pressure. As the pressure increases to 0.3 Torr, the GR drops monotonically with temperature. In this growth domain, the growth process is within the GeH_4 depletion region. The reactants in this region start to dissipate away from the substrate surface to deposit in the surrounding parts, such as chamber walls and heater assembly. For 0.5 Torr chamber pressure, the growth rate started from a minimum at 350°C , which is dominated by surface reactions, to a maximum at 400°C . At this particular point, the growth is controlled by mass transport phenomenon as discussed in chapter 2. In this domain, the growth does not depend on substrate temperature but on the precursor delivery to the substrate. The drop at 450°C is again a result of gas depletion. It is noted also that at 0.5 Torr the GR is lower compared to 0.3 Torr, which could be explained by less effect of plasma at this pressure.

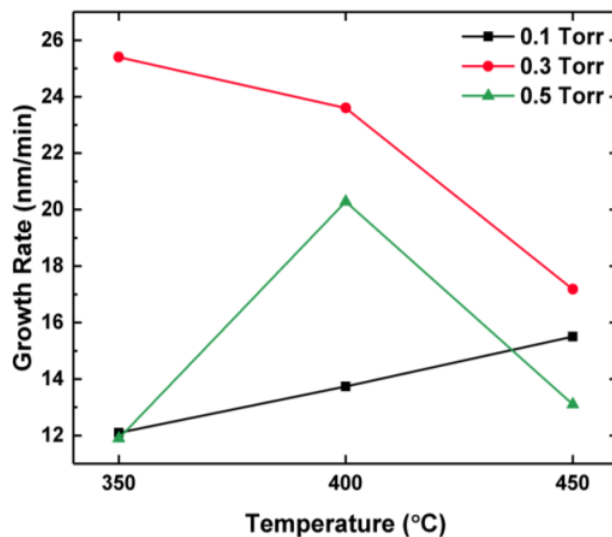


Figure 4.4: Growth rate as a function of pressure at the three selected temperatures 350, 400, and 450°C . Solid lines indicate linear fittings.

4.3.2 Material and Optical Characterization

In this section, the material and optical properties are discussed for selected growths at 400 and 450°C and pressure values of 0.1, 0.3, 0.5 Torr in two sets: i) three samples (A₁, A₂, and A₃) at 400°C; ii) three samples (B₁, B₂, and B₃) at 450°C. The detailed sample information is listed in Table 4.1.

Table 4.1: Summary of sample information and XRD results.

Sample	Growth		Thickness (nm)	Lattice Constants		Strain (%)	Relaxation (%)
	Temperature (°C)	Pressure (Torr)		a_{\perp} (nm)	a_{\parallel} (nm)		
A ₁	400	0.1	375	5.6667	5.6454	-0.22	94.46
A ₂		0.3	584	5.6707	5.6400	-0.32	92.10
A ₃		0.5	510	5.6676	5.6442	-0.24	93.92
B ₁	450	0.1	496	5.6674	5.6445	-0.24	94.05
B ₂		0.3	570	5.6599	5.6545	-0.06	98.48
B ₃		0.5	307	5.6613	5.6527	-0.09	97.67

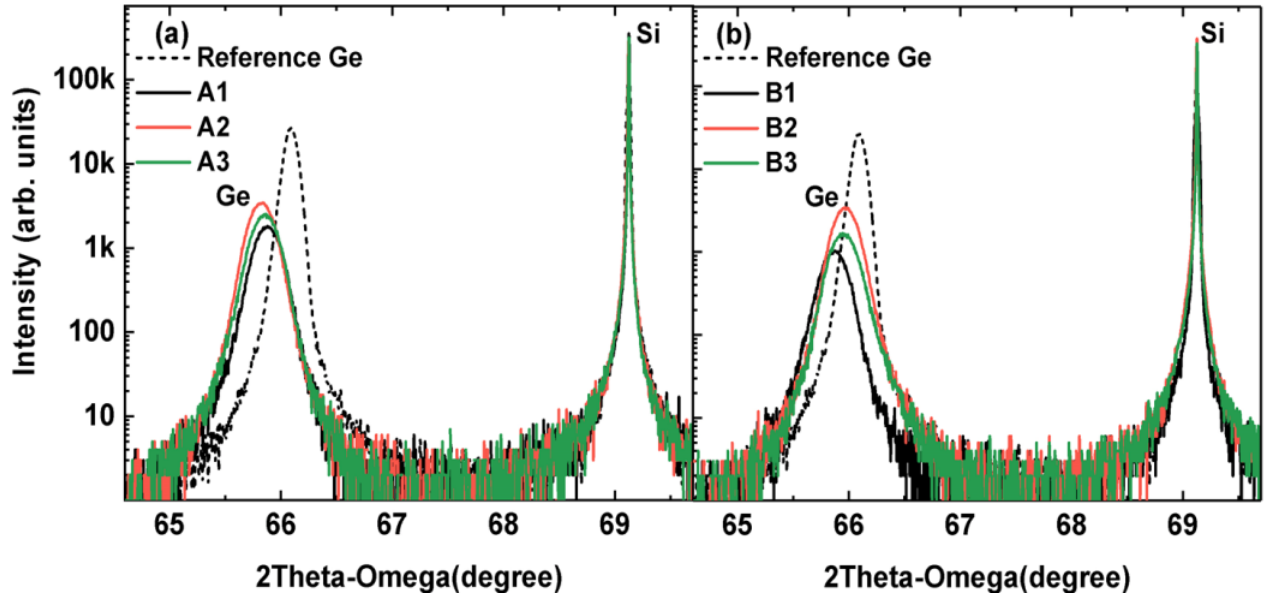


Figure 4.5: Illustration of the 2Theta-Omega XRD scans measured from the (004) plane of the samples. (a) At 400°C and (b) at 450°C. The reference Ge sample is used for comparison.

Figure 4.5 shows symmetric (004) 2θ - ω rocking curves of the selected samples at 400 and 450°C and as the pressure is changing. Both figures show dominant peaks located at $\sim 69^\circ$ that belong to the Si substrate and a second peak at $\sim 66^\circ$ for the Ge epilayer. The Ge peak position is subject to the effect of the growth pressure and strain. At 0.1 Torr, the plots show a 2θ value at 65.87° close to the relaxed Ge peak for both temperatures. However, when the pressure is increased, the Ge peak positions move from 65.84 and 65.87° at 400°C to 65.97 and 65.97° at 450°C for 0.3 and 0.5 Torr, respectively. The shift in the Ge peak position to higher angles near 66° indicates an enhanced relaxation in Ge films at 450°C. However, this is associated with more broadening of Ge peaks at 450°C. This might be a result of more defects that were generated as the Ge films start to relax at 450°C. In addition, it indicates a reduction in the compressive strain as the out-of-plane lattice constant (a_\perp) shifted closer to that of fully relaxed Ge reference.

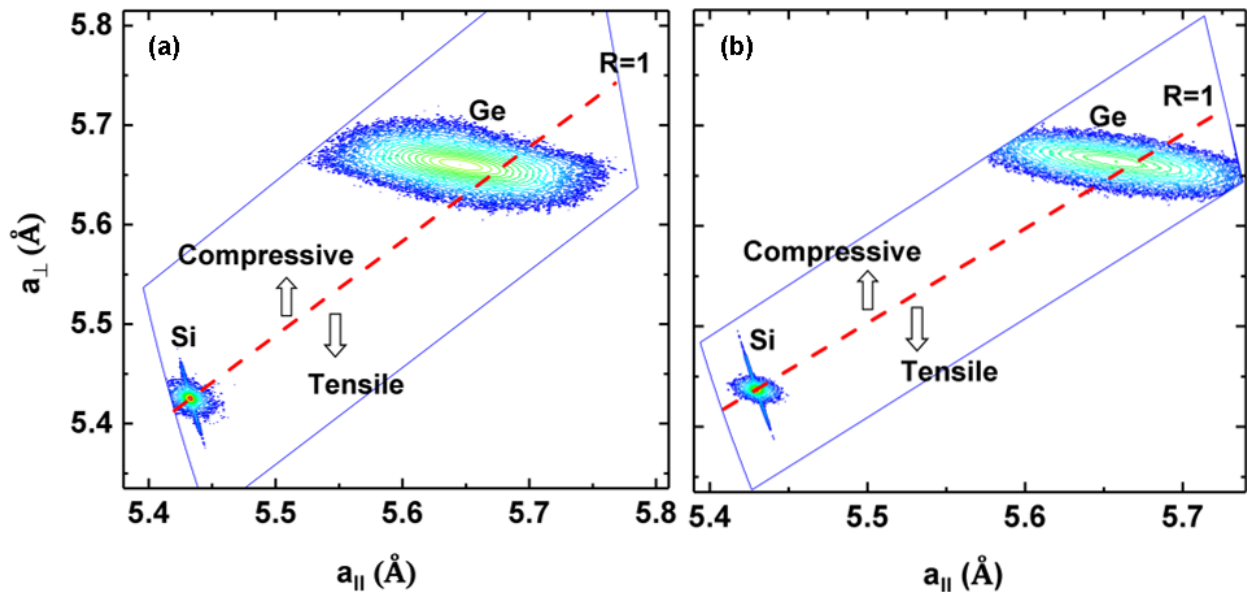


Figure 4.6: XRD-RSM contour plots from the $(\bar{2}\bar{2}4)$ direction. (a) Sample A3 and (b) sample B3.

To determine the strain and relaxation XRD reciprocal space maps (RSMs) of a typical two samples were measured along the asymmetrical $(\bar{2}\bar{2}4)$ direction. The results are presented in Fig. 4.6(a) and (b) for samples A3 and B3, respectively. The RSMs contour plots indicate that the films

were partially strained and close to the relaxation line (R=1). However, the contour plots centers intensity indicate low quality material. In addition, the in-plane lattice constants (a_{\parallel}) and the out-of-plan lattice constants (a_{\perp}) are located in similar positions above the relaxation line. That is a sign of both samples exhibit compressive strain.

In addition, 2Theta-Omega XRD results were used in the determination of strain and relaxation measurements. The out-of-plan lattice constants (a_{\perp}) of the Ge films were extracted from Bragg's law [97]:

$$a_{\perp} = \frac{2\lambda}{\sin\theta} \quad \text{Equation 4.2}$$

where $\lambda = 1.54 \text{ \AA}$ using $\text{CuK}\alpha_2$ line x-ray source and θ is the Ge peak position from XRD scans in Fig. 5. The in-plane lattice constants (a_{\parallel}) were then computed using the following equation [97]:

$$a_{\parallel} = \left(\frac{1+\nu}{2\nu} \right) \left[a_{\text{Ge}} - a_{\perp} \left(\frac{1-\nu}{1+\nu} \right) \right] \quad \text{Equation 4.3}$$

where $\nu = 0.271$ is the Poisson's ratio of Ge and a_{Ge} is the relaxed lattice constant of Ge. The strain and relaxation were then calculated using the functions:

$$\text{Strain} = \frac{a_{\parallel} - a_{\text{Ge}}}{a_{\text{Ge}}} \times 100 (\%) \quad \text{Equation 4.4}$$

$$\text{Relaxation} = \frac{a_{\parallel} - a_{\text{Si}}}{a_{\text{Ge}} - a_{\text{Si}}} \times 100 (\%) \quad \text{Equation 4.5}$$

where $a_{\text{Si}} = 5.431 \text{ \AA}$ is the relaxed lattice constant of the Si substrate. The results are shown in Table 4.1. The strain calculations reveal compressively grown Ge films that decreases as the temperature increases to 450°C . This corresponds to a larger a_{\perp} lattice constant at high temperature that approaches the lattice constant of a relaxed Ge reference. Moreover, the relaxation results show similar trend with a maximum value at 450°C and 0.3 Torr. However, all relaxation results are above 92%, which is an indication that Ge film thicknesses are close to the critical thickness.

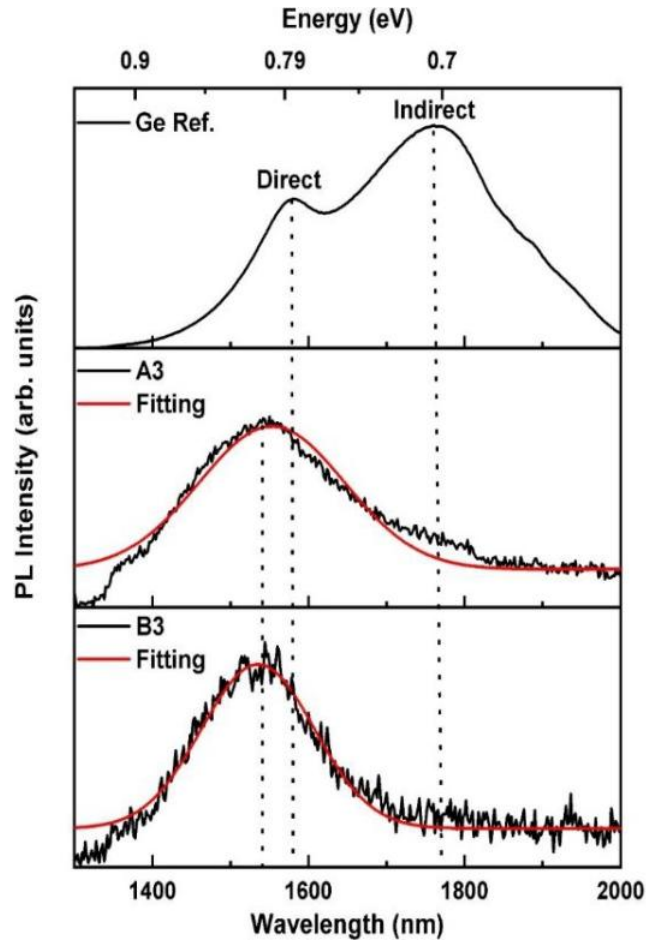


Figure 4.7: Stacked PL spectra of samples A3 and B3 compared to bulk Ge reference. Solid red lines show PL fittings.

The optical quality was examined by using room temperature PL. The PL signal was only observed for samples that were grown at 400 and 450°C. Some typical results from PL study at 400 and 450°C in a 0.5 Torr chamber pressure are compared to bulk Ge reference as shown in Fig. 4.7. For the Ge reference sample, two major peaks were observed. One peak at 1576 nm that was attributed as the direct bandgap peak, and the second is the strong peak near 1780 nm that was assigned as an indirect bandgap peak. The appearance of the indirect bandgap peak in the reference Ge sample is a feature of high quality material. Both A3 and B3 samples exhibit major peaks at a wavelength located near 1550 nm that were attributed to the carrier recombination of the direct bandgap energy. In addition, both samples show weak signs of indirect bandgap peaks near 1775

nm. The weak indirect bandgap peak appearance indicates improved material quality through radiative recombination rather than the non-radiative recombination induced by defects.

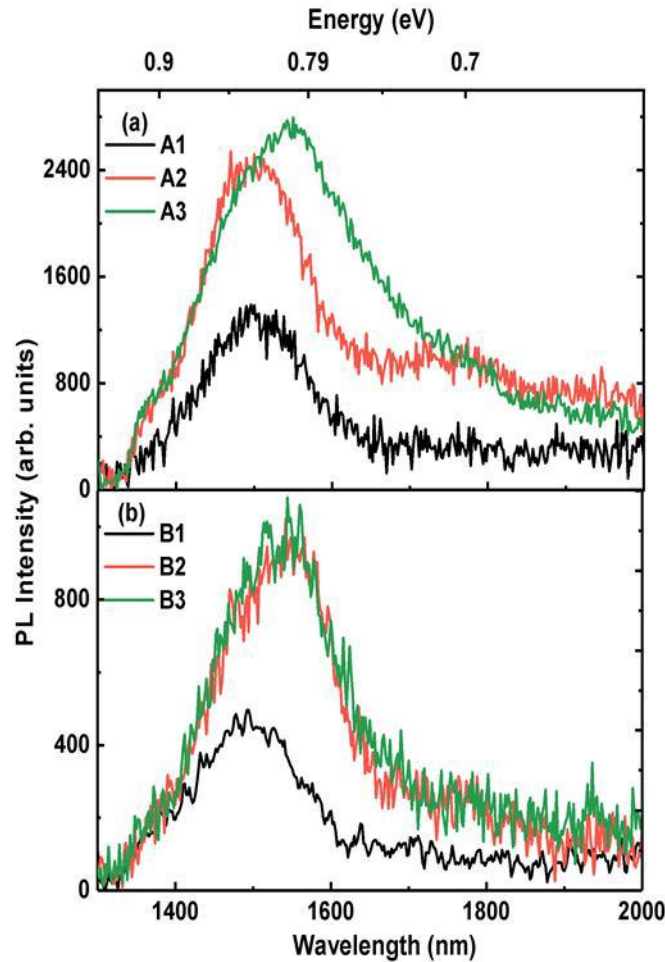


Figure 4.8: Room temperature PL spectra of the two sets of samples. (a) At 400°C (A1, A2, and A3) and (b) at 450°C (B1, B2, and B3).

The effect of chamber pressure variation on the PL behavior is shown in Fig. 4.8(a) and (b). Photoluminescence intensity and peak position improve toward crystalline Ge behavior as the pressure increases to 0.3 and 0.5 Torr. Sample A2 in Fig. 4.8(a) in particular exhibits an improved indirect bandgap peak. In addition, the PL spectrum of sample A3 becomes more intense compared to other samples. The enhanced PL intensity in sample A3 is an indication of improved optical quality that results from the radiative recombination in the direct bandgap position as samples are

close to relax. Growth at 450°C depicts similar trends with clear indirect bandgap feature in sample B2.

Room temperature spectroscopic ellipsometry was used to study the optical absorption behavior. The results are shown in Fig. 4.9. The absorption coefficient of Ge reference sample is shown for comparison. The spectral cut-off wavelength of all curves are similar to that of bulk Ge reference. However, as shown in Fig. 4.9(a), the absorption curves diverge from the behavior of a bulk Ge reference due to the dominant compressive strain. On the other hand, as the temperature is increased to 450°C, the absorption coefficient follows a similar trend to that of bulk Ge reference as shown in Fig. 4.9(b). This could be a result of the reduced strain and increased relaxation of growths at 450°C.

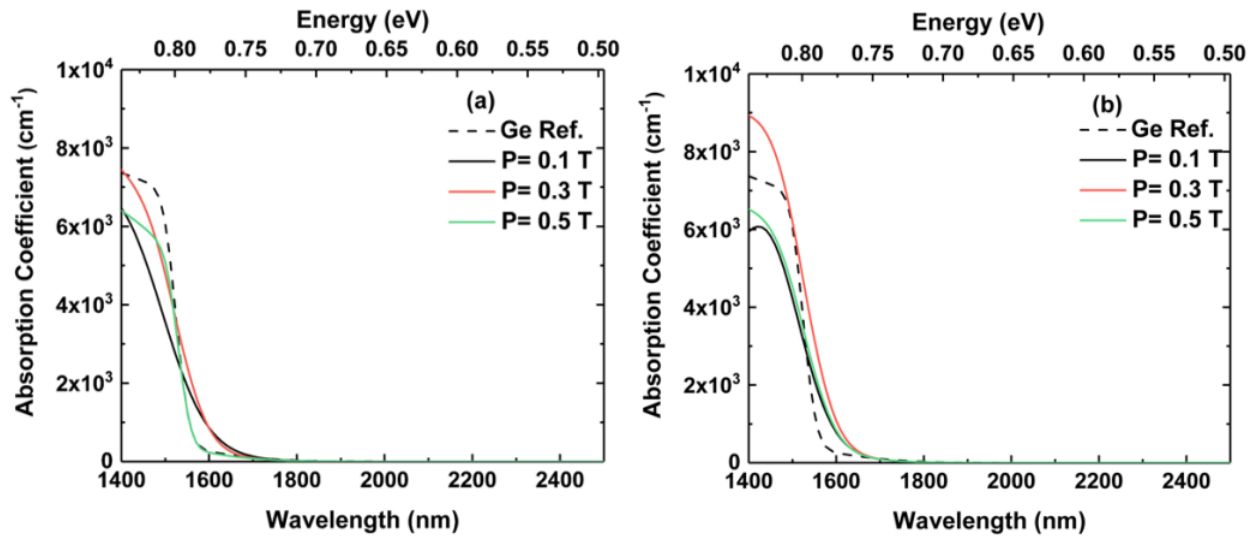


Figure 4.9: Absorption coefficient curves as the temperature and pressure change. (a) At 400°C and (b) at 450°C. Dashed lines represent the absorption coefficient curves of a bulk Ge reference.

Due to improved optical quality of sample A3, it was further investigated using TEM. Figures 4.10 (a) and (b) show the cross sectional TEM images of sample A3 that magnify the Ge/Si interface at different scales. It is noticed from the dark field TEM image in Fig. 4.10(a) that the defects are generated at the Ge/Si interface and propagate through the Ge film all the way to the surface. Figure 4.10(b) shows a bright field TEM image of the Ge/Si interface from another spot

of the Ge/Si interface. It shows TDD that propagate the film, but to some extent do not reach the surface.

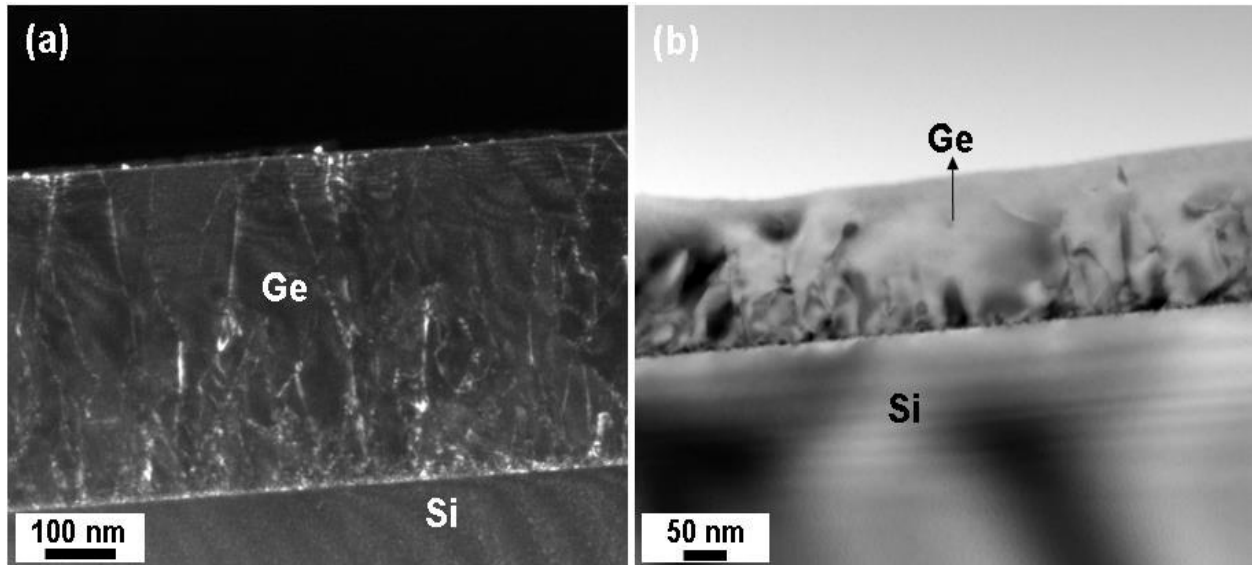


Figure 4.10: TEM imaging of the sample A3. (a) Dark field cross-sectional TEM image. (b) Bright field cross-sectional TEM image. Both images shows threading dislocations that were generated at the Ge/Si interface, and propagated through the entire film.

To estimate the TDD of the Ge layer an EPD measurement was carried out using an SEM. The results are shown in Figs. 4.11(a), (b), and (c) after exposing the sample to EPD solution. The SEM energy dispersive x-ray (EDX) map that displays Ge on the surface after the EPD process is shown in Fig. 4.11(a). The EDX map of the Ge surface depicts uniformity of the Ge film after the etching process as Fig. 4.11(a) shows. The SEM image in Fig. 4.11(b) shows a flattened surface of the etched Ge film with a single etch pit dot. The image of the EPD is shown in Fig. 4.11(c). The black dots represent pits that appear on the surface area of an $43.8 \mu\text{m} \times 50.6 \mu\text{m}$ SEM image of the sample A3. A set of four images was used to accurately determine TDD. The results of the EPD counts give an average TDD of $4.5 \times 10^8 \text{ cm}^{-2}$. The large EPD number comes from the large lattice mismatch between Ge and Si by recalling that this is only one step growth and no subsequent annealing was done to reduce TDD. However, the TDD in this study is two order of magnitude

less than a similar study [46]. Another reason for TDD generation in this study might be the radiation damage due to the presence of highly energetic ions that bombard the surface [43].

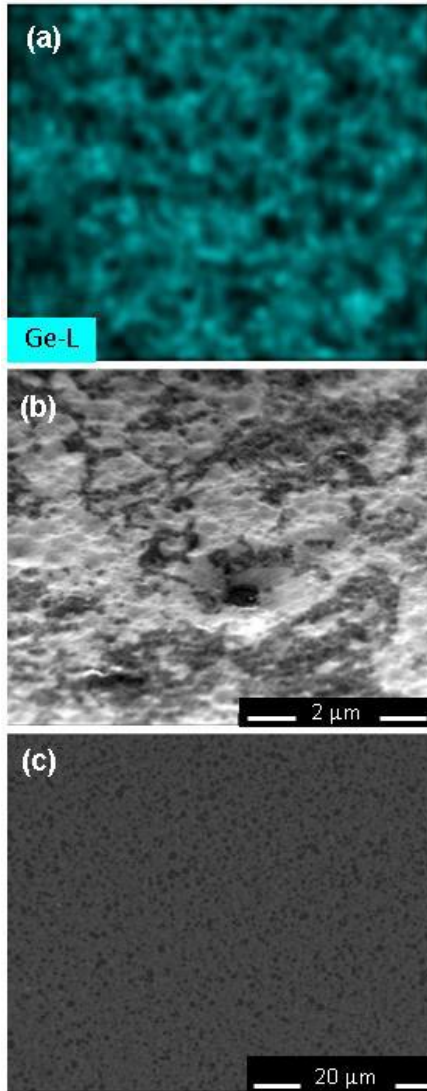


Figure 4.11: SEM imaging of the sample A3. (a) EDX surface map of the etched Ge layer. (b) Surface view shows the Ge film after etching. (c) An SEM image of the Ge film surface after it was exposed to etch pit solution; the black dots represent pit density near the

4.3.3 Comparison of material and optical properties of Plasma Enhancement and Non-Plasma

Enhancement:

The variation of the Ge film thickness using plasma enhancement and non-plasma enhancement deposition techniques was studied at 400°C under the same growth conditions (e.g. flow rates and

pressure). The results are presented in Fig. 4.12. It shows substantial improvement in the Ge film thickness as the plasma enhancement method produces more dissociated GeH_4 radicals near the surface. The GR at these condition has increased from 11 nm/min in the case of non-plasma enhancement to 19 nm/min for plasma enhancement growths.

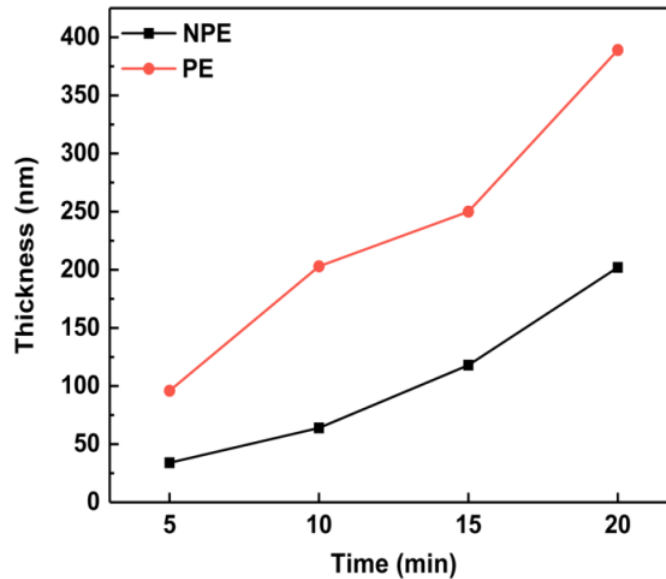


Figure 4.12: A comparison between the thickness of plasma enhanced (PE) and the non-plasma enhanced (NPE) growths at 400°C .

The effect of plasma enhancement on the material and optical qualities of Ge epitaxy is also compared using sample A3 to that was grown in the same growth conditions with non-plasma enhancement at 400°C in UHV-CVD system. The results of the material and optical comparison are illustrated in Fig. 4.13. As shown in Fig. 4.13(a), the material quality of crystallinity is improved as the FWHM of the Ge peak in XRD becomes slightly smaller than with the non-plasma enhancement growth. In addition, plasma enhancement growth introduces more compressive strain as can be seen from the shift in its Ge peak position. However, the variation in peak intensities between the two methods is due to the higher thickness in the case of plasma enhancement growth. The optical quality, on the other hand, has been significantly improved. While plasma enhancement growth demonstrated PL spectra as discussed before, the non-plasma enhancement

growth has no room temperature PL spectra as shown in Fig. 4.13(b). The weak PL performance might appear as a result of material quality issues, such as Ge/Si interface defects that block the recombination and suppress the optical quality. This indicates plasma enhancement can play a key role in improving the material and optical quality when growing Ge-on-Si at low temperatures in UHV-CVD systems.

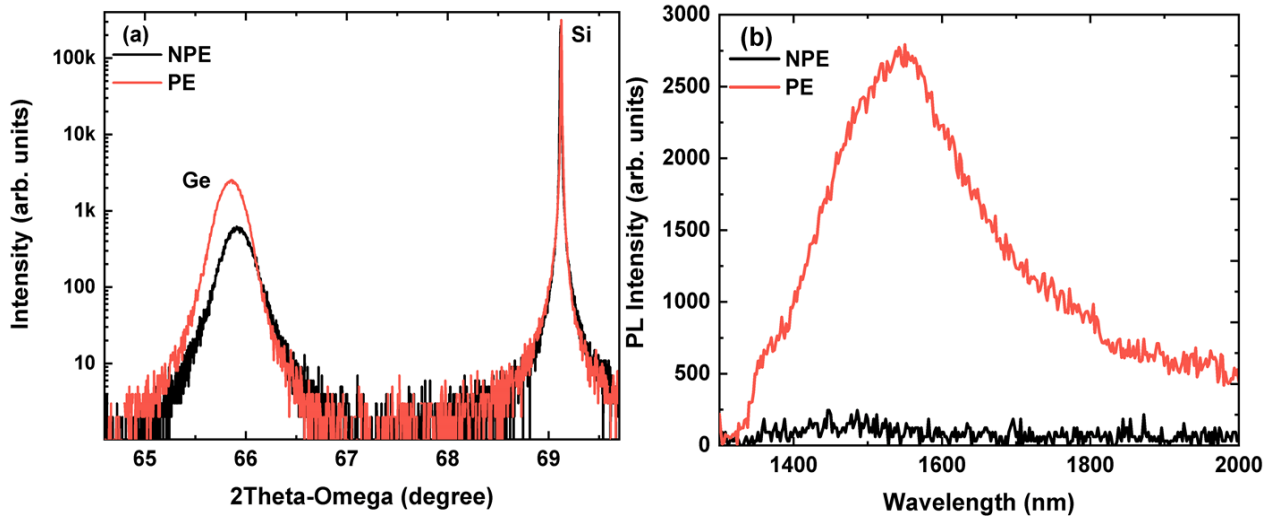


Figure 4.13: (a) XRD (004) rocking curve for material comparison between plasma enhancement (PE) and non-plasma enhancement (NPE) growths at 400°C. (b) Shows PL spectra comparison for optical quality improvement for the same samples.

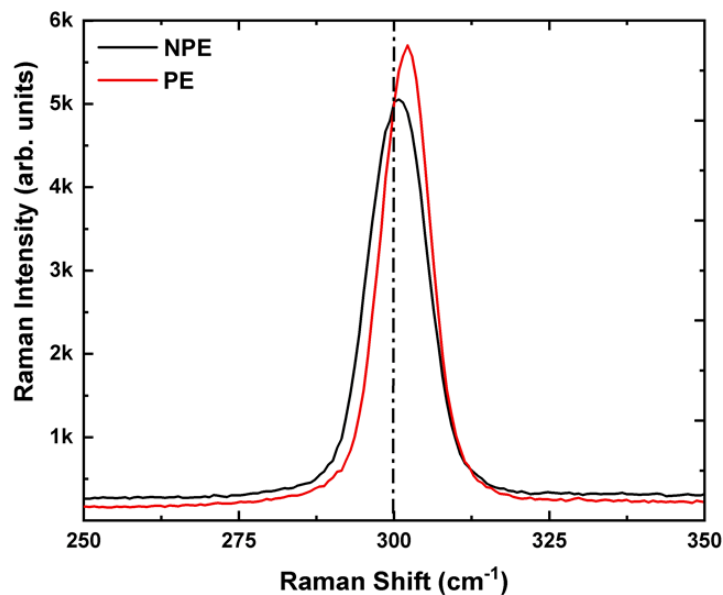


Figure 4.14: Raman comparison between the plasma enhancement (PE) sample and the non-plasma enhancement (NPE) sample.

Raman spectroscopy was taken for both samples to look for more comparison of the plasma enhancement method. The results are shown in Fig. 4.14. Both the non-plasma enhancement and the plasma enhancement possess an LO Ge-Ge mode above 300 cm^{-1} , which indicates compressively strain samples. However, for the case of plasma enhancement that shift is slightly higher. These results are consistent with XRD results in Fig. 4.13(a). Furthermore, the increased intensity of the plasma enhanced sample indicates improved material quality.

4.4 Tin Incorporation in One-step Ge Layer Using Plasma Enhancement

In this section, the role of Sn incorporation on the material and optical properties of a one-step Ge layer was studied using plasma enhancement growth. A set of two GeSn samples were grown directly on Si using plasma enhancement method. The growth temperature was set at 350°C for sample C and 400°C for sample D. The pressure, flow rate, and growth time were fixed at 0.3 Torr, 1:5:200 sccm (SnCl₄:GeH₄:Ar), and 20 min. The RF power supply was fixed at 50 W. Table 4.2 shows the growth condition of each sample. Samples A and B are Ge (Sn= 0%) samples that were grown using plasma enhancement for comparison.

Table 4.2: Summary of growth conditions of GeSn samples A and B.

Sample	Growth Temperature ($^\circ\text{C}$)	Pressure (Torr)	Flow Rate (SnCl ₄ :GeH ₄ :Ar) (sccm)	Growth Time (min)
A	350	0.3	0:5:200	25
B	400	0.3	0:5:200	20
C	350	0.3	1:5:100	20
D	400	0.3	1:5:200	20

Figure 4.15(a) shows a photograph of the plasma discharge operation inside the chamber between the wafer and the lower electrode. The plasma glow could be divided into three spots. Spot I and II are between the substrate and lower electrode a white glow that corresponds to GeH₄ and Ar discharge. Spot III is close to the gas inlet, and its glow was a navy blue plasma that results

from GeH_4 and SnCl_4 discharge. To examine the GeSn film uniformity across the wafer, the substrate rotation was disabled during the growth. After the growth was completed, the initial view of the substrate showed GeSn film that was grown non-uniformly in three spots. These are a cloudy spot at the edge of the wafer and a shiny area at the center of the Si wafer. These spots were marked as spots I (center), II, and III (edge). A photograph of the substrate is shown in Fig. 4.15(b). The origin of these spots comes from the plasma discharge discrepancy near the wafer surface, which causes varied Sn incorporation across the Si wafer. It was found that spot III possesses more Sn as a result of faster SnCl_4 decomposition near the gas inlet.

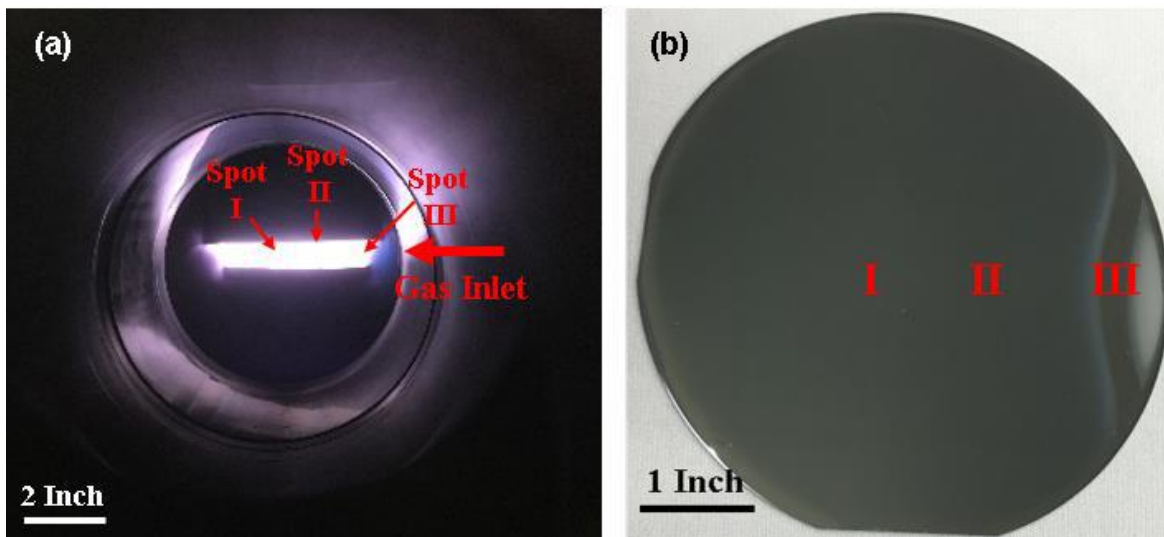


Figure 4.15: (a) A photograph from inside the chamber during the plasma generation of a GeSn growth. (b) A photograph of a GeSn sample that was grown with plasma enhancement. The wafer features three distinct spots (I, II, and III).

A growth rate comparison of the two GeSn samples compared to the Ge samples that were grown at the same growth conditions with plasma enhancement is shown in Fig. 4.16. For spot III (I), the calculated growth rates were measured to be 57.7 (35.2) nm/min and 51.4 (25.4) nm/min for sample C and sample D, respectively. For Ge samples, the measured growth rates were 21.1 and 21.9 nm/min for A and B, respectively. Therefore, Sn incorporation in GeSn samples enhances

the growth rate almost twice compared to Ge samples. This because of the exothermic chemical reaction effect that was introduced by adding SnCl₄ to the growth chamber.

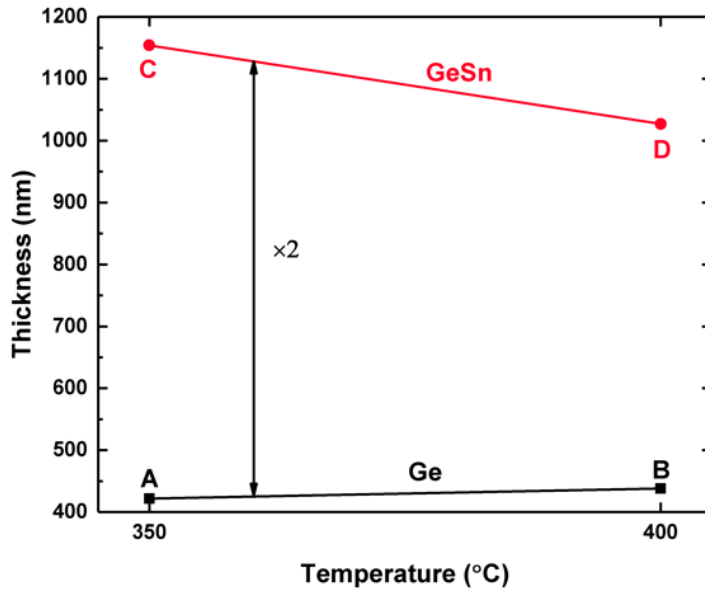


Figure 4.16: Thickness of two Ge samples compared to two GeSn samples that were grown using plasma enhancement (PE).

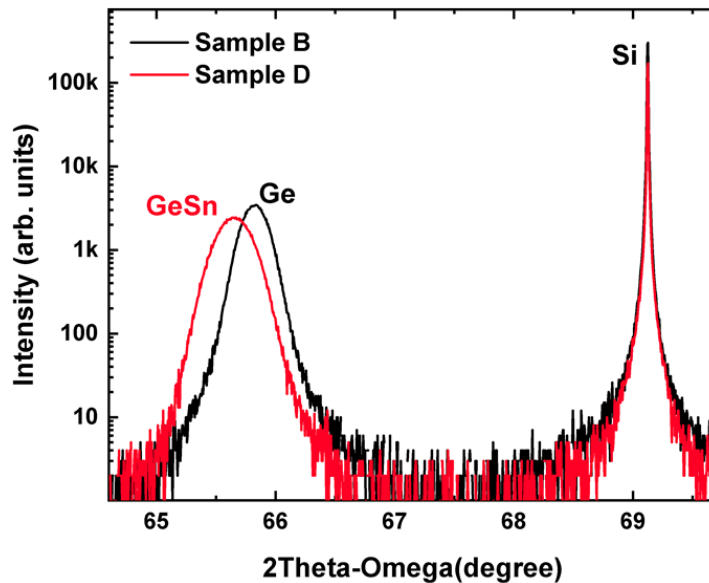


Figure 4.17: The 2θ - ω XRD curves of samples B and D from the (004) direction.

XRD measurement was done at the spot marked as III in order to investigate the material quality and to determine strain and Sn incorporation. The rocking curve scan of sample B

compared to sample D along the (004) direction is shown in Fig. 4.17. For each sample, the figure shows two peaks that can be resolved. A strong Si substrate peak near 69° while the Ge peak from sample B slightly lower than 66° , and the GeSn peak from sample D was observed at 65.6° . Incorporating Sn in sample D shifts the Ge peak in sample B to lower angle. In fact, incorporating Sn into Ge crystal will increase the out-of-plane (a_{\perp}) lattice constant, which lowers the peak angle. Sample B exhibits a narrow Ge peak compared to sample D that has a broadened GeSn peak, which suggests the wide range of Sn incorporation.

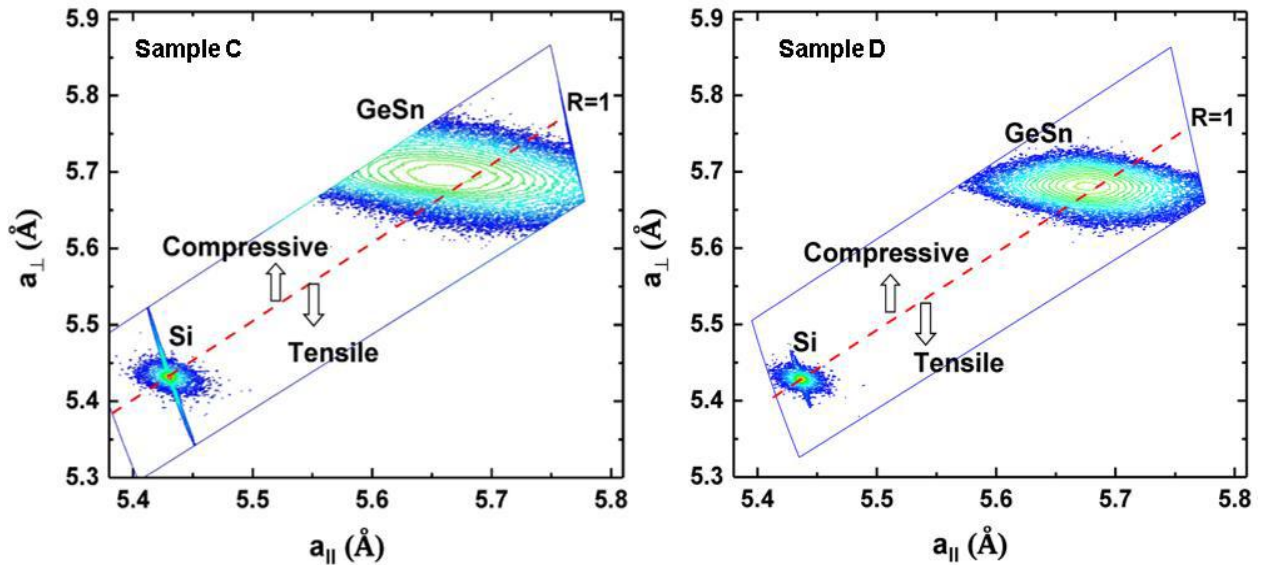


Figure 4.18: XRD-RSM contour plots of samples C and D from the $(\bar{2}\bar{2}4)$ direction.

For strain and Sn composition determination of each GeSn layer, the XRD-RSMs of samples C and D were measured along the asymmetrical $(\bar{2}\bar{2}4)$ plane. The results are presented in Fig. 4.18. The approach of GeSn contour plots to the relaxation line is an indication of becoming close to fully relaxed. The relaxation was calculated to be 92% and 97% for sample C and D, respectively. Sn incorporation was estimated from the data fitting of RSMs using -0.066 \AA bowing parameter of GeSn lattice constant. The results of Sn incorporation calculation in sample C and D were found to be 3-6% and 3%, respectively. The Sn incorporation in sample C has increased from

0.75% using non-plasma enhancement GeSn growth (not shown) to 3% in sample D. This indicates that plasma enhancement significantly enhances Sn incorporation in GeSn material system.

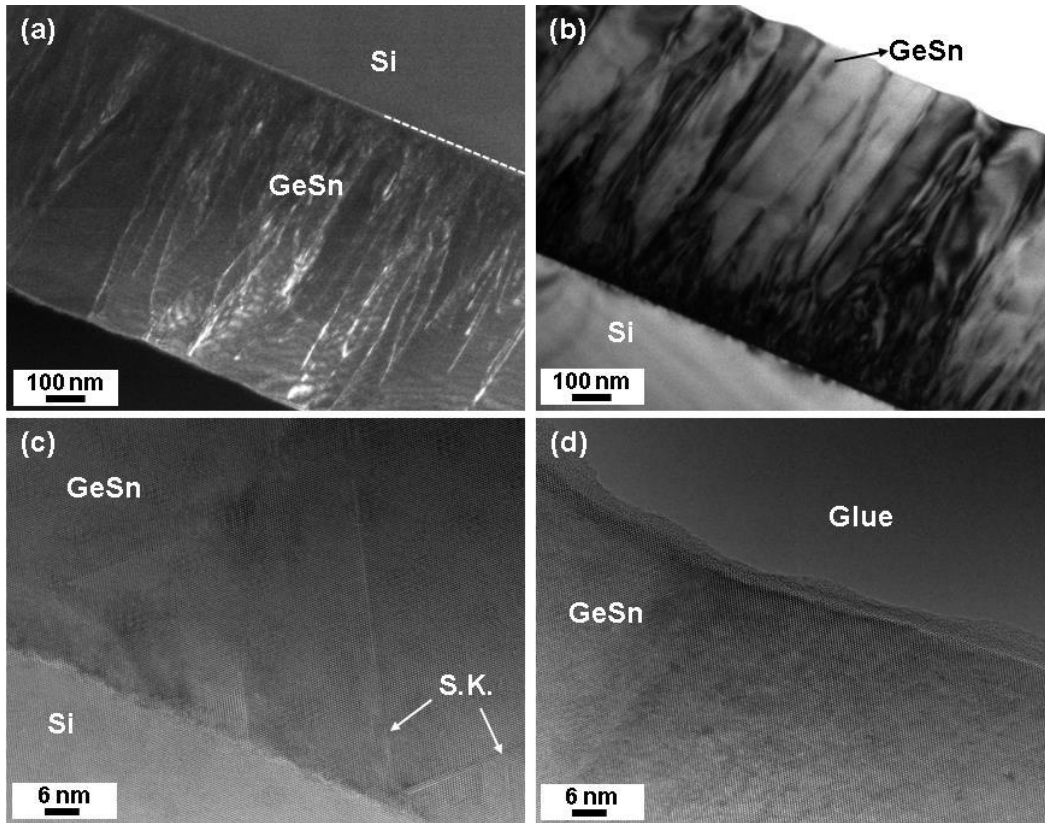


Figure 4.19: TEM images of sample D. (a) and (b) Dark and bright field TEM image of sample B (spot III), respectively. (c) A zoom-in image of the interface between GeSn and Si. Stacking faults (S.F.) are clearly seen at the interface. (d) A zoom-in TEM image of the GeSn surface.

Furthermore, material investigation was extended to TEM imaging for sample D to investigate the material quality. A 1027 nm GeSn film thickness was measured using TEM images. A dark and bright field TEM images of sample D at spot III are shown in Fig. 4.19(a) and (B), respectively. The threading dislocations were observed near the GeSn/Si interface to accommodate the large lattice mismatch between GeSn and Si. These threading dislocations propagate through the entire GeSn film. Based on TEM analysis results, the density of these threading dislocations was estimated to be $TDD \sim 10^9 \text{ cm}^{-2}$. The high-resolution TEM images of sample D are shown in Fig. 4.19(c) and (d) of GeSn/Si and the GeSn surface, respectively. The diamond cubic structure

is an indication of a single crystal GeSn epitaxy on Si with the ultra-high growth rate by plasma enhancement. As Fig. 4.19(c) depicted, the GeSn-on-Si interface was accommodated by crystal defects of the type stacking faults (S.F.) along (111) and $(\bar{1}\bar{1}1)$ directions.

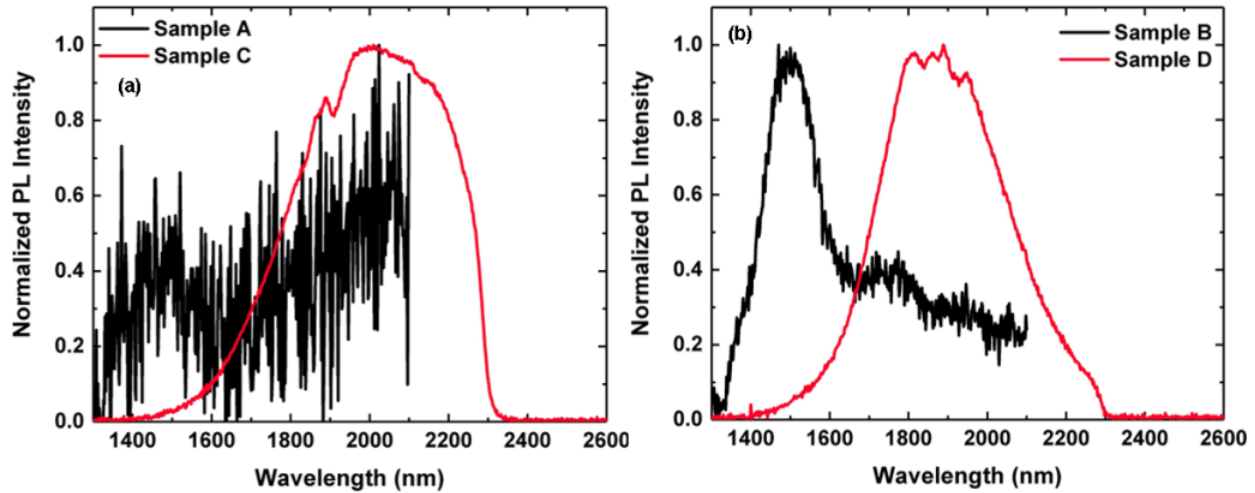


Figure 4.20: Comparison of PL shift as Sn incorporated. (a) Sample A and C at 350°C. (b) Sample B and D at 400°C.

Room temperature PL of the two GeSn samples C and D compared to Ge samples A and B are displayed in Fig. 4.20. The PL was measured using a 1064 nm laser with 500 mW pumping power. In addition, InGaAs detector was used for GeSn samples while PbS detector was used for Ge samples. For the case of sample C and D, PL emission comes mainly from the direct bandgap. The indirect bandgap was not noticed due to nonradioactive recombination by crystal defects. From Fig. 4.20(a), the PL of sample A is noisy and its direct and indirect bandgap peaks were not clearly identified. However, for sample C, the direct bandgap PL peak was clear noticed at ~ 2000 nm. The shift of the direct bandgap peak from 1576 nm in bulk Ge to 2000 nm in the GeSn sample is caused by Sn incorporation. Figure 4.20(b), on the other hand, shows PL results of Ge sample B and GeSn sample D that were grown at 400°C. The PL of sample B depicts two PL peaks near 1575 nm and 1680 nm that were assigned to the direct and indirect bandgaps, respectively.

Moreover, only one peak was noticed for GeSn sample that was assigned as a direct peak. This peak was shifted to ~ 1860 nm due to Sn incorporation in sample D.

4.5 Conclusion

Plasma with high power RF was utilized in UHV-CVD to enhance the growth of Ge-on-Si at low temperatures. The growth was investigated in a wide range of temperatures (250-450°C), chamber pressures, and growth time. Raman and X-ray diffraction results indicate that crystalline and compressively strained Ge-on-Si films were achieved at temperatures in the range 350-450°C. Photoluminescence results depict improved optical quality at 400 and 450°C with an optimal result for of the growth (A3) at 400°C and 0.5 Torr. TEM results for the sample A3 show defective Ge layer. This might appear from the lattice mismatch in the Ge/Si interface, relaxation, and the ionic bombardment that is associated with the use of high-power plasma in this study. TDD was estimated by using EPD counting in SEM to be 4.5×10^8 cm⁻², which is reasonable since no graded buffer, second growth step at high temperature, and post annealing were used for material improvement. Table 4.3 provides some recent achievements in Ge-on-Si growth using different CVD and other growth methods. It is clear from the table that the discussed growth method can compete with other high temperature methods. The plasma enhancement and non-plasma enhancement comparison in UHV-CVD system implies plasma enhancement can improve the material and optical qualities of a one-step Ge epitaxy at 400°C. Further investigation of the effect of low plasma power growth and two-step growth on improving the material and optical quality is discussed in chapter 5.

For GeSn plasma enhancement growth, the plasma technique shows higher growth rate at 51.4nm/min compared to the same growth technique for Ge. In addition, Sn incorporation has been increased significantly using this growth method. The plasma enhancement attempt to grow GeSn

indicates that it offers surface reaction dynamics to increases not only the growth rate and quality, but also Sn incorporation.

Table 4.3: Summary of typical Ge growth methods by other research groups compared with this work.

Growth System	Growth Procedure			Pos. Anne. (°C)	TDD (cm ⁻²) or RMS (nm)	Reference
	Precursor	Step	Temp. LT/HT (°C)			
LP-CVD	Ge ₄ H ₁₀	Two	380/425	680	RMS= 0.5	[98]
RP-CVD	GeH ₄	Two	350/600	800	TDD= 8×10 ⁶	[99]
UHV-CVD	GeH ₄	Three	350/630/Graded SiGe/630	No	TDD< 1.5×10 ⁶	[100]
PECVD	GeH ₄	Two	250/400	600	TDD= 3.3×10 ⁸	[101]
PECVD	GeH ₄	Two	350/500	<600	RMS= 0.55	[45]
HDP-CVD	GeH ₄	One	460	No	TDD~ 1×10 ¹⁰	[46]
UHV- PECVD	GeH ₄	One	400	No	TDD= 4.5×10 ⁸	This work

Chapter 5: High Quality Ge Buffer Layer Grown by Plasma Enhancement in UHV-CVD System for Photonic Devices

5.1 Introduction

The need for high speed electronics has driven research efforts to develop photonic devices that are compatible with complementary metal–oxide–semiconductor (CMOS) technology. To satisfy the industrial goal for high volume production with low cost, these photonic devices have to be grown monolithically using group IV semiconductors with CMOS devices. In addition, the growth process of the photonic device has to be at low temperatures to prevent the CMOS device from any thermal damage.

In this chapter, Ge-on-Si using the two-step method following the same growth procedure to improve the material quality further. Two-step Ge buffer layers were grown close in the low temperature range. The post growth thermal processing was eliminated in order to reduce the thermal budget further. With the help of plasma enhancement, the second step temperature was gradually dropped from 600 to 450°C. Material and optical characterization of selected Ge buffer layers indicate that the plasma enhancement method could maintain high quality Ge film with low root mean square (RMS) surface roughness. A further comparison step was done to examine material and optical properties of GeSn films that were grown on Ge buffer layers grown with plasma enhancement compared to non-plasma enhancement.

5.2 Experimental

This research milestone was conducted after the UHV-CVD machine was maintained. The heating assembly in the deposition stage had been reconstructed. That included new heater and new heater elements (fastener threads, posts...etc.). The maintenance also included cleaning the inside of the growth chamber from any Ge and α -Sn residuals. During the heater assembly reconstruction,

loosen hardware on the plasma power circuit was fixed. The plasma coaxial cable, which installed inside the chamber to connect the lower electrode to the RF power source, was also replaced with a new one. The shortening problem during the plasma enhancement deposition that resulted from deposited Ge on the RF grid and other heater components was also fixed. The machine was tested by growing several Ge growths to check the drift of thickness and to calibrate the system after maintenance. All growth runs were done under the same chamber pressure (1.0 Torr) for 10 min for each, but different flow rates (F.R.) and temperatures. Figure 5.1 illustrates the drift in growth thickness after the maintenance. As shown in Fig. 5.1, the deposition thickness after maintenance became almost 4.5 times higher. The large change in the deposition rate indicates that replacing heater elements enhanced the efficiency of the heater.

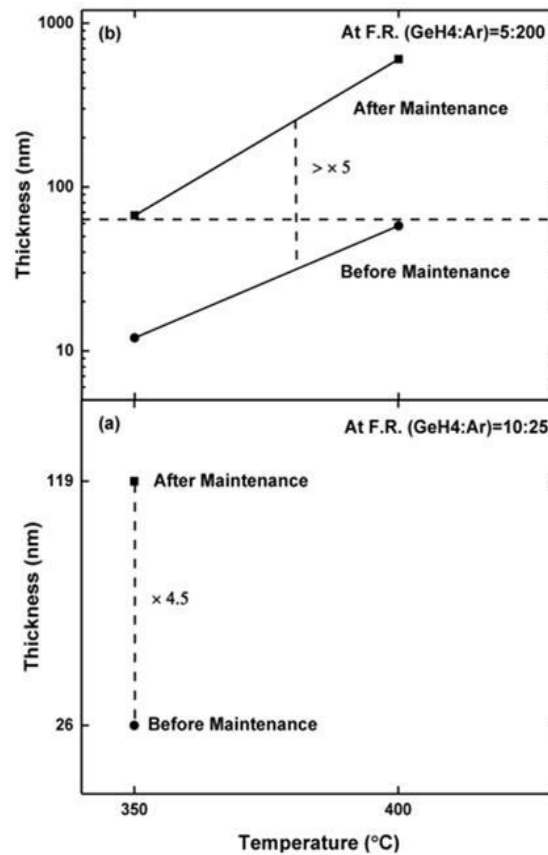


Figure 5.1: Calibration results for selected growth before and after maintenance. (a) Shows the drift in growth thickness at 350°C under F.R. of 10:25 (GeH4:Ar). (b) A log scale illustration of the variation of thickness before and after maintenance at 350°C and 400°C under F.R. of 5:200.

In this study, a capacitively coupled plasma (CCP) setup in the UHV-CVD growth chamber with a base pressure of 3×10^{-9} Torr was utilized. The CCP was fed by a 13.56 MHz radio frequency (RF) power supply that is matched by an L-shaped automatic impedance matching network. Figure 1 shows the plasma enhancement configuration. The substrate holder within the upper electrode setting was powered by the RF power source while the lower electrode assembly was grounded. The electrode spacing was fixed at 20 mm. In addition, the substrate holder was designed to be rotated to ensure growth uniformity. Four-inch Si (001) substrates were used after they were cleaned by the standard RCA wet-cleaning method followed by a final hydrofluoric acid dip to hydrogen terminate the surface dangling bonds. Prior to starting the growth process, the wafer was baked for 20 min at the desired growth temperature to remove the passivation layer and ensure film uniformity. Germane (GeH_4) was used as the Ge precursor while argon (Ar) was used as a carrier gas and an ion source. The flow rate and the chamber pressure were fixed at the optimal values of GeH_4/Ar (1:40) and 1 Torr, respectively. The growth of the LT seed layer was done at 375°C to promote the layer-by-layer growth mechanism. The flow of gases was then shut off, and the temperature was ramped up at a rate of $\sim 12^\circ\text{C}/\text{min}$ to the second step growth temperature.

The growth of the GeSn layer was done with non-plasma enhancement in the same system. The dilution ratio of GeH_4 , tin tetrachloride (SnCl_4) as Sn precursor, and Ar as a carrier gas was fixed at 1:0.0025:10, respectively. The temperature and pressure were set at 270°C and 2.0 Torr, respectively, while the growth time was fixed at 60 min. The same growth conditions were used for all GeSn growth in order to study the effect of the plasma enhancement Ge buffer compared to the non-plasma enhancement Ge buffer.

Thickness and absorption coefficient of each sample were measured using a variable-angle spectroscopic ellipsometry system (Model WVASE32[®]) in the wavelength range from 1400 to

2500 nm. The crystallinity was checked after each growth using Raman spectroscopy with 632.8 nm laser beam. Room temperature PL spectra were measured using a pulsed 1064 nm laser with 340 mW pumping power and a continuous wave 532 nm laser with 500 mW pumping power for Ge buffer layers and GeSn films, respectively. The PL setup is connected to a thermoelectric-cooled lead sulfide (PbS) detector with the wavelength detection cut-off at 3 μm , which is sufficient to collect emissions from both the direct and indirect transitions for both Ge and GeSn. Phillips X'pert PRO high-resolution X-ray diffractometer (HRXRD) was used to study the crystallographic structure, strain, and material composition. Morphology of Ge buffers was measured using a Bruker D3100 with Nanoscope V atomic force microscope (AFM). The images were flattened, and the RMS surface roughness was measured. Scanning electron microscopy (SEM) was utilized for surface micrographs that were used later to estimate the TDD. Transmission electron microscopy (TEM) was performed to determine the material quality further using FEI Titan and TF20 with electron sources of 300 and 200 keV, respectively.

5.3 Results and Discussions

5.3.1 One-step Ge Layer

In the previous chapter, growth with grounded substrate holder configuration was discussed. The chamber maintenance made it possible to generate plasma at low RF powers as low as 2 W. Hence, it was vital to explore the plasma enhancement capability in the UHV-CVD system at different powers. A single step Ge layer was first grown in the range of temperatures from 400 to 525°C and the RF power range from 0 to 30 W to optimize the growth conditions. Figure 5.2(a) shows the variation of thickness with RF power at a fixed wafer temperature of 400°C. As compared to the non-plasma enhancement at P= 0 W, the thickness increases monotonically until 5 W, and starts to decrease beyond 5 W. It must be noted that the substrate holder was powered; hence it is

subjected to ion bombardment during deposition. The high growth rate at $P < 5$ W results from high dissociation rate while at 5 W the decomposition rate is compensated by the etching rate. Above 5 W, the etching rate effect dominates, which causes a reduction in the film thickness. This could be due to excessive energetic ions that bombarded the film surface and displaced Ge adatoms on the surface [102], [103].

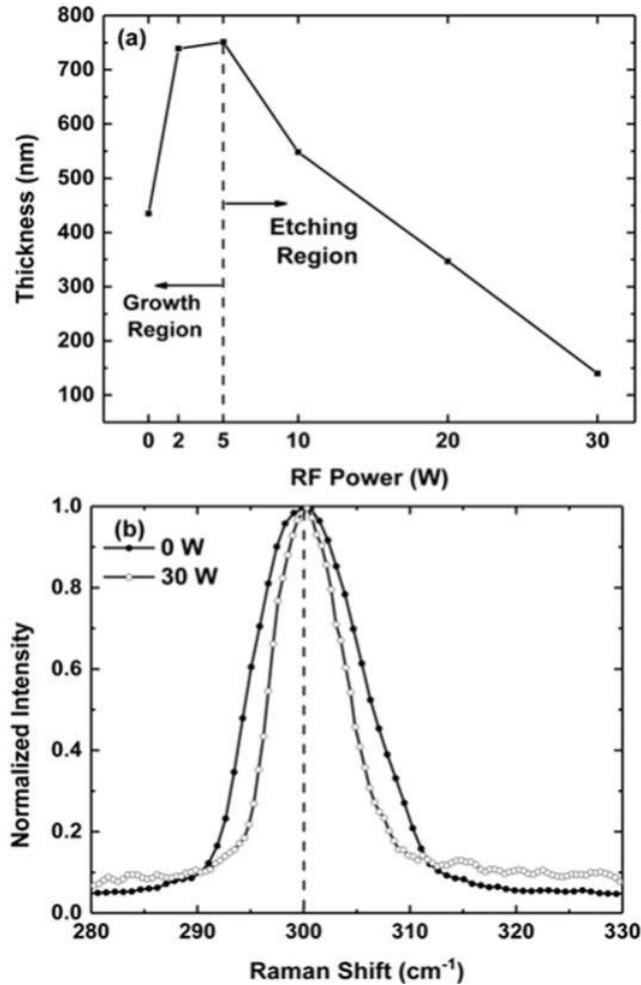


Figure 5.2: (a) Variation of thickness with the applied RF power for one-step Ge growth at 400°C. (b) Raman shift comparison between non-plasma (0 W) and plasma (30 W) enhancement for samples were grown at 400°C. The dashed line corresponds to the Ge-Ge mode of a relaxed Ge layer.

Figure 5.2(b) shows Raman spectra of a sample that was grown using non-plasma enhancement ($P = 0$ W) compared to those of a sample grown using plasma enhancement growth at $P = 30$ W. The dashed line shows the position of a relaxed Ge peak. The figure shows a well

detected Raman peak at 300 cm^{-1} that corresponds to longitudinal optical (LO) Ge-Ge mode, which suggests a fully-relaxed Ge films. However, Raman peak of the growth at 0 W exhibits wider full-width at half-maximum (FWHM) compared to that of the growth at 30 W. The reduction in FWHM of the Ge-Ge peak at 30W is an indication of improved material quality.

The role of the chamber pressure on the variation of thickness of Ge films using plasma enhancement in UHV-CVD system was also investigated. Figure 5.3 shows the thickness and mean free path calculation using equation 4.1 at selected values of pressures in the range from 0.3 to 1 Torr. As the pressure increases the thickness starts to increase, which results from the existence of large amount of radicals at high pressures. The mean free path, on the other hand, is longer at low pressures and drops at high pressures. In general, longer mean free path allows the reactants to reach the wafer surface before collision with other, which yields a higher growth rate. But, as Fig. 5.3 illustrates, the thickness at high growth pressures of 0.7 and 1 Torr are the highest while the mean free path are low. This could be explained by higher dissociation rate at high growth pressures using plasma enhancement that overcomes the high collision probability between GeH_4 radicals.

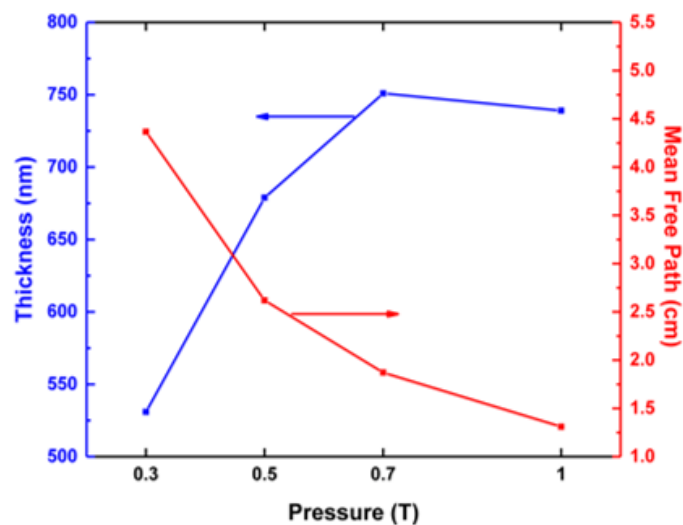


Figure 5.3: Variation of thickness and mean free path as a function of chamber pressure of growths at an applied RF power of 4 W and at a growth temperature of 400°C .

5.3.2 Two-step Ge Buffer Layer using Non-plasma Enhancement

In this section, Ge buffer layer was grown by using UHV-CVD with non-plasma enhancement. As mentioned earlier, the Ge buffer layer will be used as a separation layer for subsequent GeSn growths. The first step of the Ge layer in this section was grown at 375°C, and the second step was grown at 600°C with nearly half flow rate of the GeH₄ in the first step. A second sample with the same growth recipe was grown, but with in situ thermal annealing step followed the second step. The annealing was at 800°C for 30 min under very low F.R. of GeH₄ (0.001 sccm). The Ge buffer layer thickness on both samples was measured using ellipsometry. The as grown sample, marked as A, has a 972 nm film thickness while the annealed sample, marked as A*, has an 824 nm thickness.

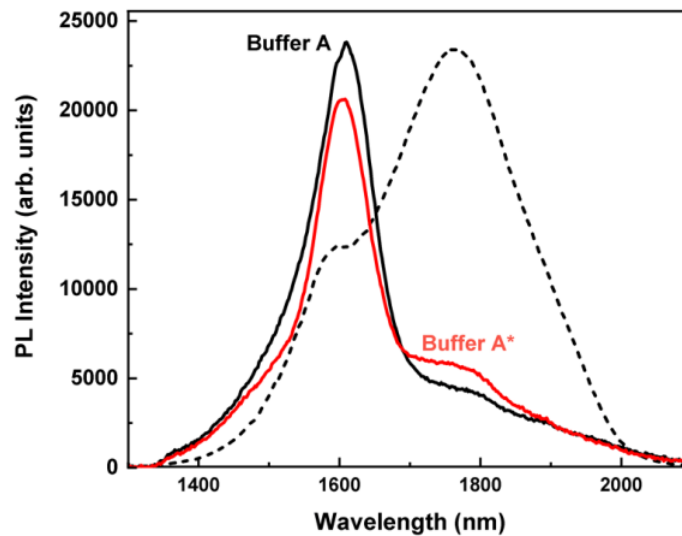


Figure 5.4: Room temperature PL spectra of sample A as-grown and after thermal annealing A*. The dashed line depicts RT PL of bulk Ge.

To determine the modification of optical properties, room temperature PL spectrum was measured using 1064 nm with 340 mW power for both samples. The results are shown in Fig. 5.4. The figure also shows bulk Ge reference as a dashed line for comparison. The reference Ge sample shows a strong peak near 1780 nm that reflects the indirect bandgap emission, which is expected since Ge is indirect bandgap material. Such a peak is an indication of ultrahigh quality material.

As compared with the reference Ge, sample A and A* are exhibiting a strong peak near 1590 nm, which are attributed as the direct bandgap peak. The enhanced direct bandgap peak of sample A and A* is an indication of a built up tensile strain that lowers the Γ valley. The tensile strain came from the thermal coefficient mismatch between Ge and Si when the samples were cooled to room temperature. Near 1800 nm, a feature of small peak is clearly noticed for the annealed sample as a sign of improved material quality. In addition, the discrepancy in shows intense PL peak for sample A since it is thicker than A* while the narrower FWHM of sample A* indicates also enhanced material quality.

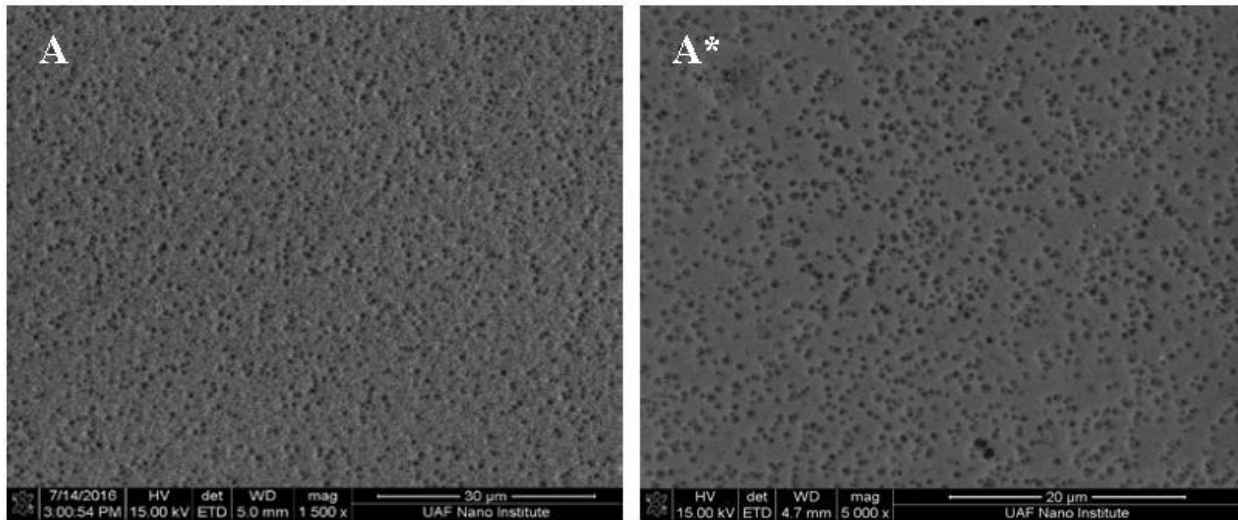


Figure 5.5: SEM micrographs of the as-grown buffer A and the annealed buffer A* that show etch pit on the surface.

Further investigations were conducted to explore the material and surface quality. Figure 5.5 presents SEM micrographs with etch pits. The etchant solution was prepared using the same method that was discussed in the previous chapter. The etch pit counting gives TDDs with an average of $1.84 \times 10^7 \text{ cm}^{-2}$ and $5 \times 10^7 \text{ cm}^{-2}$ for sample A and A*, respectively. The high TDD of sample A* could be give rise to the loner etching time, which etched almost all the second layer. Surface roughness of each sample was measured using AFM. The results are presented in Fig. 5.6. Surface roughness indicates increased RMS value from 1.04 nm to 1.42 nm after annealing. The

higher RMS value of the annealed sample was because of increased surface mobility during the annealing step.

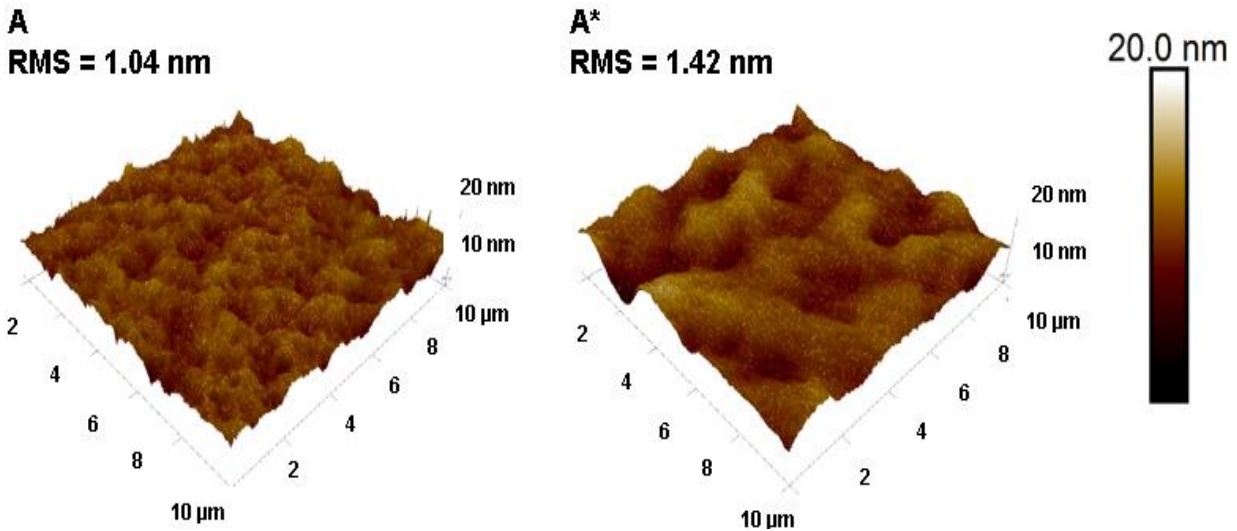


Figure 5.6: AFM images and RMS values of sample A and A*. Images were taken on a surface area of 10 × 10 μm² scans for each sample.

To conclude, from the optical and material characterization it is clearly noticed that the improvement is not significant. Hence, sample A was used to compare the plasma enhancement sample to the conventional growth technique.

5.3.3 Two-step Ge Buffer Layer using Plasma Enhancement

2 nd Step	Plasma Enhanced Temperature } Variable Power } GeH ₄ F.R.: 5 sccm } Ar F.R.: 200 sccm } Fixed Ch. Press: 1 Torr } Time: 10 min }
1 st Step	Non-plasma Enhancement T= 375 °C GeH ₄ F.R.: 5 sccm Ar F.R.: 200 sccm Ch. Press.= 1 Torr Growth Time= 10 min
Si(100) Substrate	

Figure 5.7: Two-step Ge buffer cross section that shows growth parameters of each step.

In this section, the role of plasma enhancement in lowering the growth temperature of the second step is investigated. During the growth, the first step is adjusted while the second step all parameters were fixed except substrate temperature and RF power. Figure 5.7 shows the growth cross section and parameters.

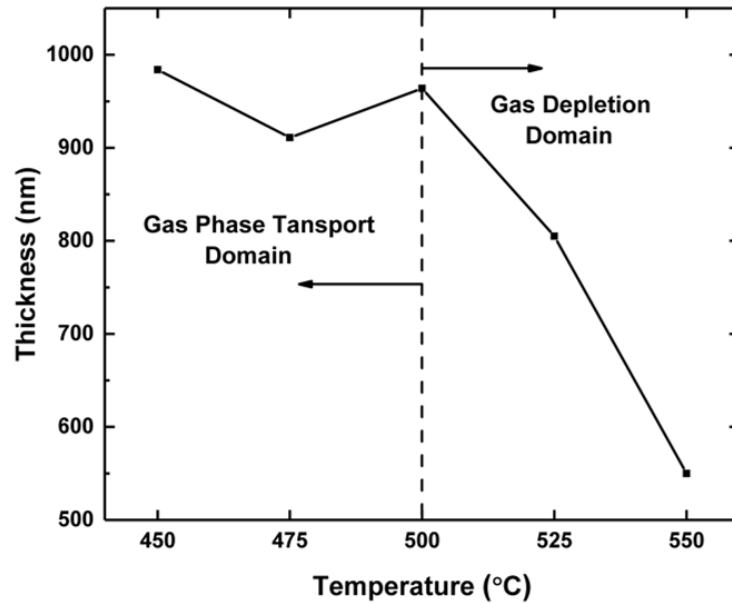


Figure 5.8: The variation of the growth thickness with temperature at an RF power of 5 W.

To further improve the material quality a two-step approach was used for the Ge buffer layer. A set of five Ge samples were grown using this method with the second step grown by plasma enhancement. For each sample, the seed layer growth was done using non-plasma enhancement at 375°C and 1 Torr. The thickness of the initially Ge seed layer was measured to be 230±15 nm. The second step was grown at an RF power of 5 W, and at different temperatures in the range from 450 to 550°C. The results of the deposited thickness as a function of growth temperature are shown in Fig. 5.8. It is observed that the Ge buffer thickness decreases with increasing the substrate temperature. The drop in the total thickness comes mainly from the second growth step. This could be a result of low number of reactants at growth temperatures beyond 500°C. At this growth temperature range, the growth region moves from gas-phase transport

regime in which the growth is less sensitive to temperature variation to the gas depletion regime in which some reactants decompose faster and deposit on the heater components before reaching the growth zone [104]. In addition, at high growth temperatures the mobility of Ge adatoms on the surface increase dramatically, which means that Ge adatoms becomes more active. Under Ar bombardment, the chemical-absorbed Ge adatoms are more easily to be displaced out of the surface, which results in the reduction of the thickness.

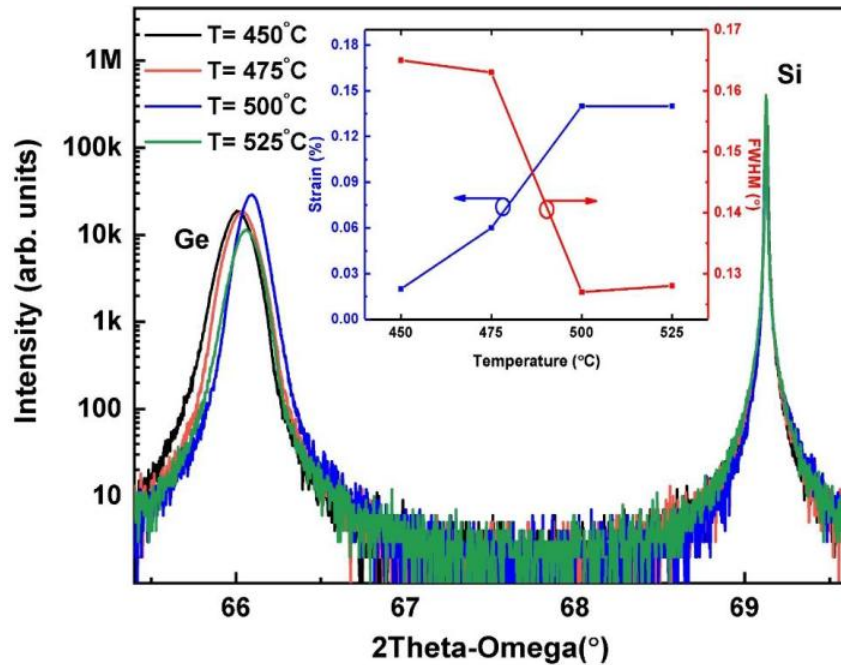


Figure 5.9: Temperature-dependent XRD around the Bragg angle of (004) of growths at 5 W. Inset shows the calculated strain and FWHM of each Ge curve.

Further characterization was focused on the temperature range from 450 to 525°C. The XRD rocking curves from the (004) direction of this temperature range are plotted in Fig. 5.9. The plot shows two major peaks. The main sharp peak near 69° is attributed to the Si substrate while the peaks that appear near 66° are assigned to Ge films. Strain was calculated for each sample using Ge peak position from 2θ-ω scans; the computing hypothesis is described elsewhere [105]. The inset of Fig. 5.9 shows a plot of the strain and the FWHM of each Ge peak. In general, all samples possess tensile strain. However, as the temperature increases to 500 and 525°C, the amount

of strain becomes one order of magnitude higher than 450 and 475 °C. In addition, FWHM decreases with increasing the temperature. It shows a maximum at 450 °C and a minimum at 500 °C. The Ge peaks broadening are ranging from 0.127° to 0.165° at 500 °C and 450 °C; respectively, which indicates improved crystallographic quality with temperature.

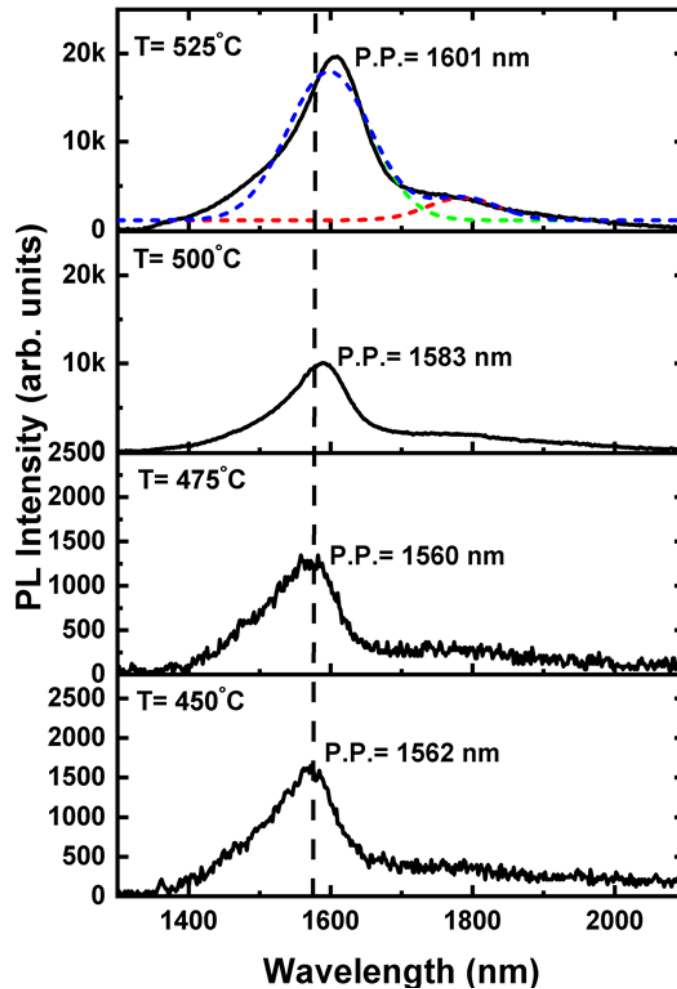


Figure 5.10: Room temperature PL spectra as the temperature changes from 450 to 525 °C at 5 W. The direct bandgap position of a bulk Ge is marked by dashed lines.

The optical quality of the films were monitored through room temperature PL using a 1064 nm pulsed laser as the substrate temperature and plasma power were varied. The results are presented in Fig. 5.10. Dashed lines are references of the direct bandgap position of a relaxed Ge (1576 nm). In the case of temperature variation as in Fig. 5.10, the PL measurements for samples

grown at 450 and 475°C reveal low direct bandgap intensity compared to those of samples grown at other temperatures while the indirect bandgap peaks are not easily discerned. This is associated with the non-radiative recombination by defects. In such a case, numerous electron-hole pairs recombine at defect-mediated energy states through the nonradioactive Shockley-Read-Hall recombination mechanism. In addition, the samples grown at 450 and 475°C growth temperatures have PL peak positions slightly longer than a relaxed Ge (dashed line), which indicates a small amount of remnant tensile strain was created. As the substrate temperature is increased to 500 and 525°C, a direct bandgap peak near 1600 nm is noticed, which is then compared with that of a relaxed Ge bulk reference (dashed line). The presence of these intense and sharp PL peaks near the direct bandgap at these growth temperatures is an indication of increased tensile strain, which can be noticed by peak positions shift to longer wavelength. Such an increase in the tensile strain helps in pumping more electrons to the direct valley enhancing the direct bandgap transition. These conclusions are additional signs of improved crystallinity at this temperature range [106, 107], which are consistent with XRD findings. It is also noticed that the PL spectrum of the growth at 525°C possesses a small peak above 1700 nm that is attributed to the indirect bandgap. In order to determine its peak position, the PL spectrum was fitted by Gaussian fitting. The result depicts that the indirect bandgap peak is located near 1800 nm. The existence of the indirect bandgap peak is an indication of enhanced material quality.

To determine the effect of RF power on the second step of the Ge buffer layer, a set of seven wafers were grown in the RF power range from 5 to 40 W at 525°C. The XRD rocking curves from the (004) direction were measured and plotted in Fig. 5.11. The Ge peaks indicate all samples exhibit high crystallinity since they feature narrow peaks. In addition, it is clearly observed that all are exhibiting tensile strain since they show peak position higher than 66°. The

inset of Fig. 5.11 shows a plot of the strain and the FWHM of each Ge peak. The amount strain has a highest value at 30 W and a minimum at 20 W. On the other hand, FWHMs indicate that the growth at 30 W possesses the best crystallinity since it has the lowest FWHM value. Therefore, an RF power of 30 W produced the best material quality.

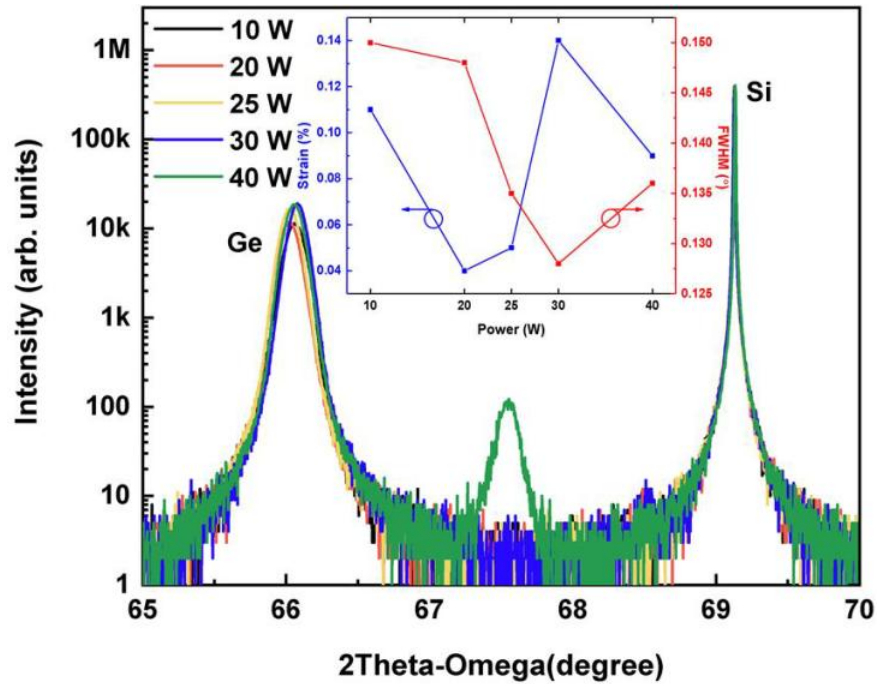


Figure 5.11: Power-dependent XRD around the Bragg angle of (004) of growths at 525°C. Inset shows the calculated strain and FWHM of each Ge curve.

The PL measurements of the RF power dependent study using a 1064 nm laser is shown in Fig. 5.12. The results show a major peak near 1600 nm that was attributed to direct bandgap peaks. The intensity of the direct bandgap peak varies depending on the power. Growth at 15 and 40 W show the lowest PL intensity while the growth at 30 W exhibits the highest PL intensity and the longest PL shift. This could be explained based on the tensile calculations from XRD-RC measurements. In this case, the high strain lowers the direct bandgap valley further and enhances the radiative recombination. In addition, the high tensile strain pushes the PL peak position to 1603 nm away from the direct bandgap position of the relaxed Ge reference line.

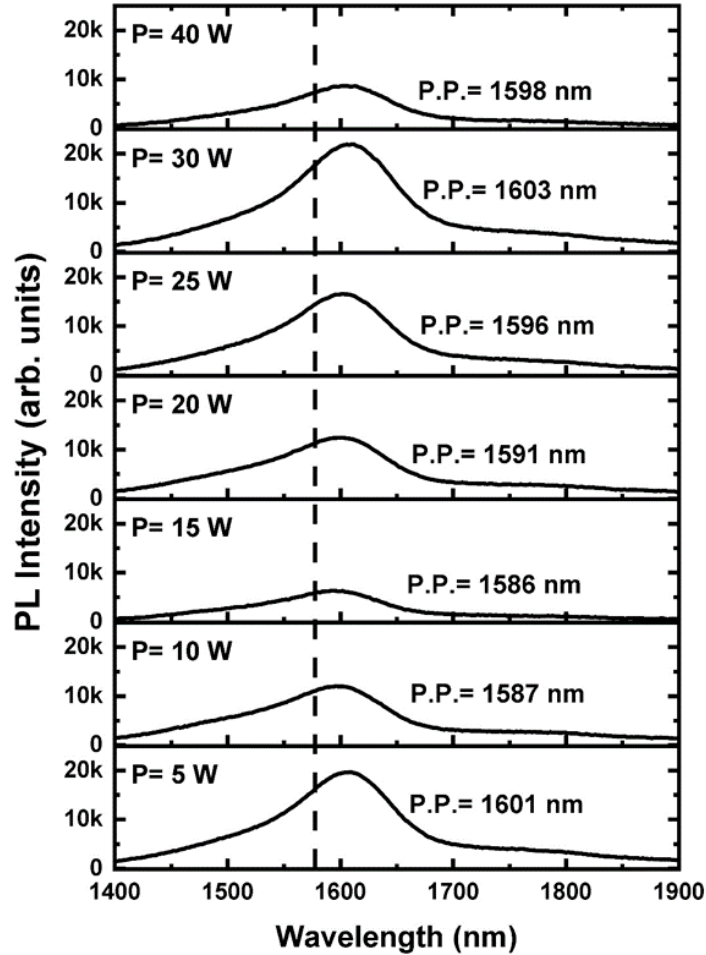


Figure 5.12: Room temperature PL spectra as the RF power changes at 525°C. The direct bandgap position of a bulk Ge is marked by dashed lines.

5.3.4 Material, Surface, and Optical Properties Comparison between Non-plasma Enhancement and Plasma Enhancement Ge Buffers

In order to make more exploration about the effect of plasma enhancement on the material and optical quality, a comparison between plasma enhancement and non-plasma enhancement is presented. Table 5.1 lists the growth conditions of one Ge buffer grown by non-plasma enhancement (buffer A) and two Ge buffer layers grown by plasma enhancement method (buffer B and C). The growth temperature of the first step was fixed at 375°C for all buffers. The second step growth temperature was 600°C for buffer A, and it was dropped to 525°C for buffer B to compare how far the temperature reduction can affect the material and optical properties. For

buffer C, the growth procedure was slightly different. The growth temperature of the second step was lowered further to 500°C while plasma enhancement was used to grow the first step.

Table 5.1: Ge buffer IDs and growth conditions, RMS, and EPD of buffers A, B, and C.

Buffer	Growth				Thickness (nm)	RMS (nm)	TDD (cm ⁻²)
	1 st Step		2 nd Step				
	P (W)	T (°C)	P (W)	T (°C)			
A	0	375	0	600	972	1.04	1.84×10 ⁷
B	0	375	30	525	627	2.80	2.7×10 ⁷
C	30	375	30	500	614	2.07	7.4×10 ⁷

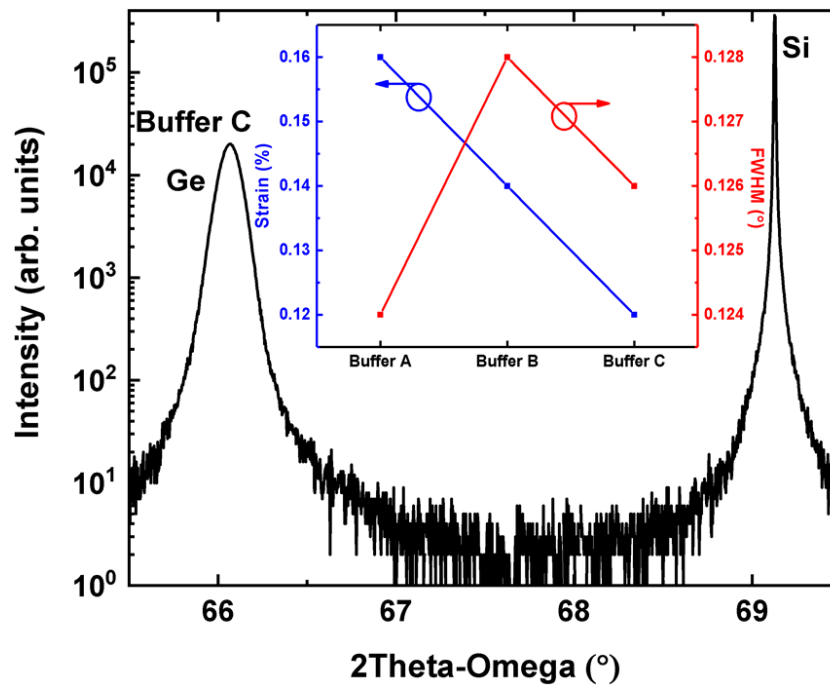


Figure 5.13: XRD (004) rocking curve of buffer C. The inset shows the calculated strain and the FWHM of each buffer.

Figure 5.13 shows XRD rocking curve scan along the (004) direction of buffer C. The peak near 66.05° is associated with Ge buffer can be clearly resolved from Si substrate peak at 69°. The inset of Fig. 5.13 shows the strain and FWHM of buffer A, B, and C. Buffer A exhibits a higher tensile strain of 0.16% while the strain amount linearly decreases to 0.14 and 0.12% for buffer B and C, respectively. The increase in the strain value with temperature was due to thermal coefficient mismatch between Ge and Si when cooling the system from high growth temperature

to room temperature. The relatively narrow FWHM of Ge peaks indicates a high degree of crystallographic alignment of a single mosaic structure with the Si substrate. In addition, buffer A possesses slightly lower FWHM compared to B and C. However, the FWHMs of all buffers still maintain a perfect shape of a material with high crystallinity.

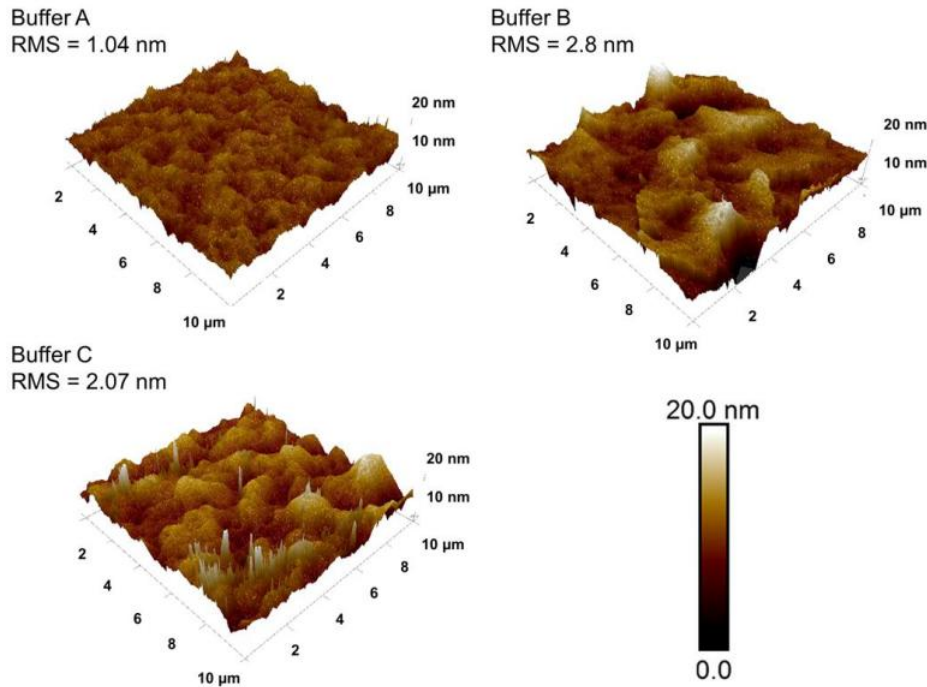


Figure 5.14: Topographical three-dimensional AFM surface images and RMS values for buffer A, B, and C.

The visual inspection of the surface after each growth was specular. However, further surface characterization was required. The surface roughness caused by the relaxation mechanism for the selected buffers was measured using AFM. Figure 5.14 shows the results of a 10×10 μm² scans with the RMS values of the surface peak-to-valley height. The RMS value for sample A indicates atomically flat surfaces morphology with RMS value of 1.04 nm. However, as the plasma enhancement was introduced in samples B and C, the RMS value were increased to 2.80 and 2.07 nm, respectively. The increased surface roughness is a sign of an increased adatoms surface mobility, which gained the energy through ion bombardment process. By decreasing the growth

temperature and using plasma enhancement in the first step, the RMS surface roughness was reduced in sample C to 2.07 nm. Such an atomically flat surfaces is an ideal platforms for subsequent epitaxy.

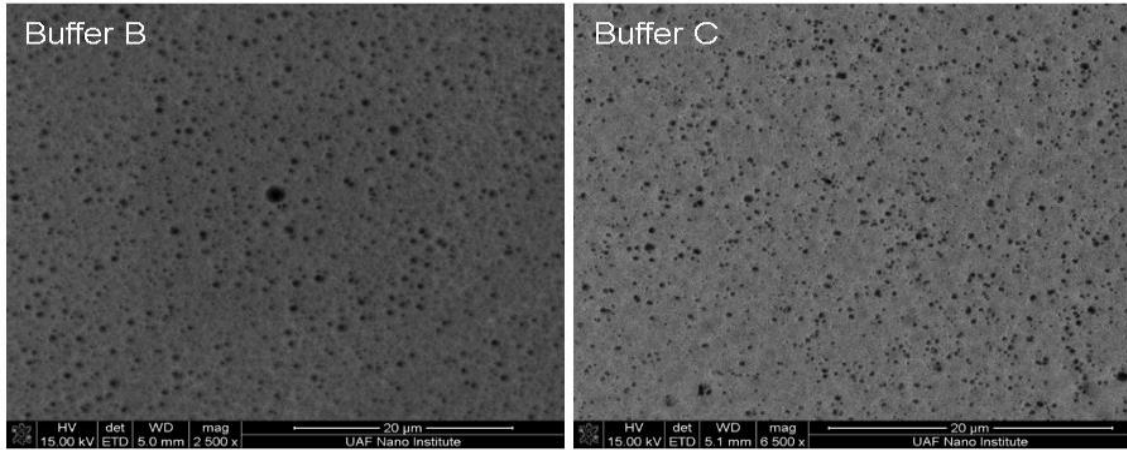


Figure 5.15: SEM micrographs of selected surface areas of buffer B and C after exposure to EPD solution. The measured EPD of buffer B and C are $2.7 \times 10^7 \text{ cm}^{-2}$ and $7.4 \times 10^7 \text{ cm}^{-2}$, respectively.

An etch pit density (EPD) was performed in order to delineate TDD in Ge buffers using wet chemical etching. An iodine-based defect etchant was prepared by mixing 67 mL of acetic acid (CH_3COOH), 20 mL of nitric acid (HNO_3), 10 mL of hydrogen fluoride (HF), and 30 mg of iodine (I_2) [40]. Each sample was immersed in the etchant at room temperature for 10 s. Surfaces of the etched samples were imaged using SEM. Figure 5.15 shows typical results of an SEM micrograph with $51 \times 44 \mu\text{m}^2$ and $39 \times 31 \mu\text{m}^2$ of buffer B and C, respectively. The black dots on the surface represents threading dislocations, where each pit belongs to a single threading dislocation. The EPD is calculated by counting the number of etch pits of the image divided by the image size. The average EPD for three different spots of SEM images with different magnifications was measured for each sample. The results are presented in Table 5.1. Buffer A shows a TDD of $1.84 \times 10^7 \text{ cm}^{-2}$, which is in good agreement with similar growth procedure with a two-step technique ($400^\circ\text{C}/600^\circ\text{C}$) in UHV-CVD system [39]. The slightly high TDD in buffer A results

from omitting the HT cycle annealing, which reduces TDD significantly [99]. For buffer B and C, the TDD increases to $2.7 \times 10^7 \text{ cm}^{-2}$ and $7.4 \times 10^7 \text{ cm}^{-2}$, respectively.

Figure 5.16 presents room temperature PL that was measured for each sample using a 1064 nm laser with 340 mW laser power. All samples exhibit similar peak shape with varied intensities. However, the PL spectra of Ge buffers A and B are almost identical. These results are consistent with strain and TDD calculations that were previously discussed. The low TDDs of sample A and B can contribute in higher PL intensity. On the other hand, higher TDD in buffer C deteriorates the radiative recombination and reduces the PL intensity. It is also clear that PL results were affected by strain. The higher the tensile strain the smaller the energy difference between the direct and indirect valleys and thus the number of electrons occupying the direct valley becomes higher. This is noticed also as PL peak positions (P.P.) are shifted to longer wavelengths as the strain values increase, which make the bandgap narrower.

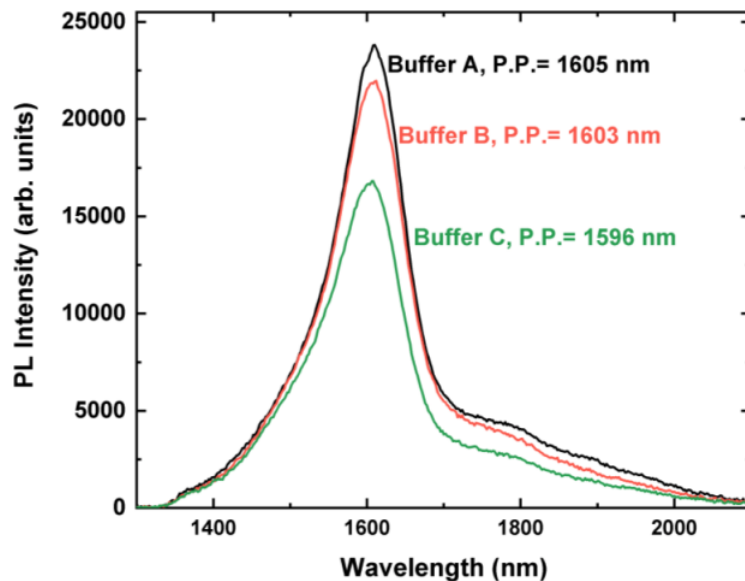


Figure 5.16: Room temperature PL spectra of buffer A, B, and C measured using 1064 nm laser with 340 mW power.

The absorption measurement of each buffer was taken using Ellipsometry in the wavelength range from 1400 to 2500 nm. The results are presented in Fig. 5.17. The dashed line

represents bulk Ge reference for comparison. The absorption values of buffer A and B are slightly lower than the bulk Ge reference sample while buffer C exhibit the lowest absorption coefficient. All buffers possess an absorption edge close to the bulk Ge reference with a cutoff wavelength of nearly 1580 nm. Near the direct bandgap edge, the absorption coefficient can be fitted by using the following equation:

$$(\alpha h\nu)^2 = A(h\nu - E_g^\Gamma) \quad (1)$$

where α is the absorption coefficient of direct bandgap transition, $h\nu$ is the photon energy, A is the constant and E_g^Γ is the direct bandgap energy. The data fitting and the E_g^Γ extraction results are presented in the inset of Fig. 5.17, where E_g^Γ is evaluated from the intercept at $\alpha=0$. Buffer A provides a E_g^Γ value similar to bulk Ge reference (0.8 eV) while the E_g^Γ value of buffer B is 0.79 eV. The lower E_g^Γ value is due to the tensile strain, which is consistent with the previous discussions. The E_g^Γ value of buffer C was not evaluated because the absence of the linearity near its direct bandgap edge.

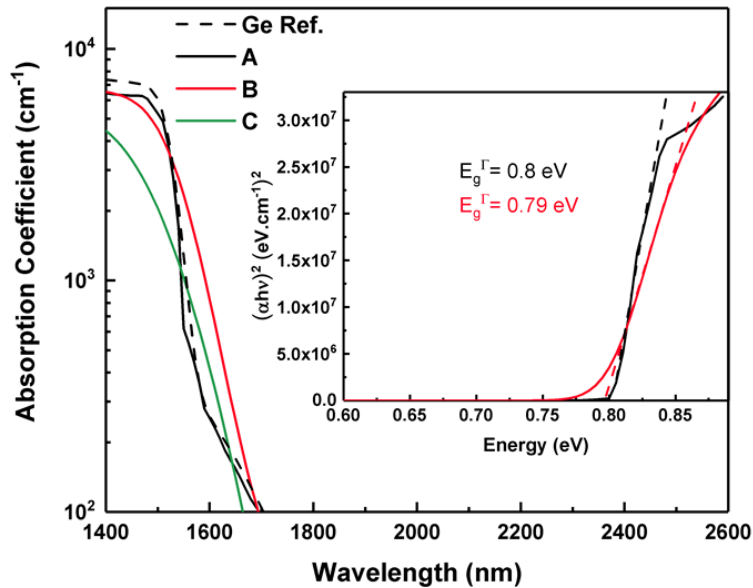


Figure 5.17: Absorption coefficients of buffer A, B, and C. The dashed line is a Ge reference for comparison. Inset: absorption fitting and direct bandgap determination.

5.3.5 Active GeSn Layer Comparison on Non-plasma Enhancement and Plasma Enhancement Ge Buffers

A GeSn layer (sample D) was grown on non-plasma enhancement buffer (buffer A). To obtain side-by-side comparison, another GeSn active layer (sample E) was grown with exactly the same growth conditions on buffer B that utilizes plasma enhancement. This step was conducted to demonstrate the capability of the plasma enhancement growth procedure for future optoelectronic applications.

To validate the crystal quality, strain, and composition of each sample, XRD reciprocal space mapping (RSM) was employed. Figure 5.18 shows XRD-RSMs of samples D and E that were performed from asymmetrical ($\bar{2}\bar{2}4$) plane. In both samples Ge and GeSn diffraction peaks appear almost at the same lattice positions. A summary of the extracted information is shown in table 5.2. Both buffer layers of samples D and E have the same in-plane ($a_{||}$) and out-of-plane (a_{\perp}) lattice constants are having the same values at 5.67 nm and 5.65 nm, respectively. For the active GeSn layers, sample E shows less pseudomorphicity compared to sample D. The strain was calculated as -0.51% and -0.33% for sample D and E, respectively. In addition, the FWHM of the diffraction patterns along the lateral correlation of the $a_{||}$ Ge buffer and the GeSn layer were extracted to highlight the material quality as well [93]. The results are presented in Table 5.2. The FWHM of Ge buffers and the GeSn films in both samples are close to each other, which indicate close density of TDs [108]. Moreover, the calculations of Sn incorporation in both samples reveal similar Sn composition (see Table 5.2).

Table 5.2: RSM results of two GeSn films.

Sample	Buffer	Ge Buffer		GeSn		$a_{ }$ FWHM (\AA)		Strain (%)	Sn (%)
		$a_{ }$ (\AA)	a_{\perp} (\AA)	$a_{ }$ (\AA)	a_{\perp} (\AA)	Ge	GeSn		
D	A	5.67	5.65	5.67	5.72	0.0043	0.01	-0.51	5.6
E	B	5.67	5.65	5.68	5.71	0.0046	0.03	-0.33	5.3

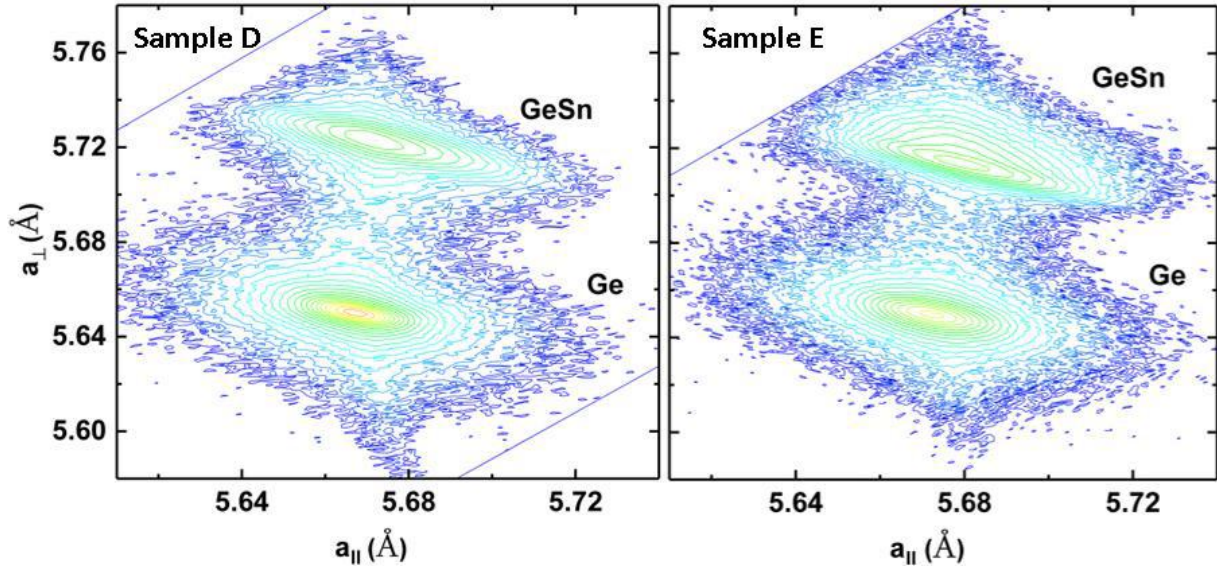


Figure 5.18: Asymmetrical RSM scans from the $(\bar{2}\bar{2}4)$ plane of sample D and E.

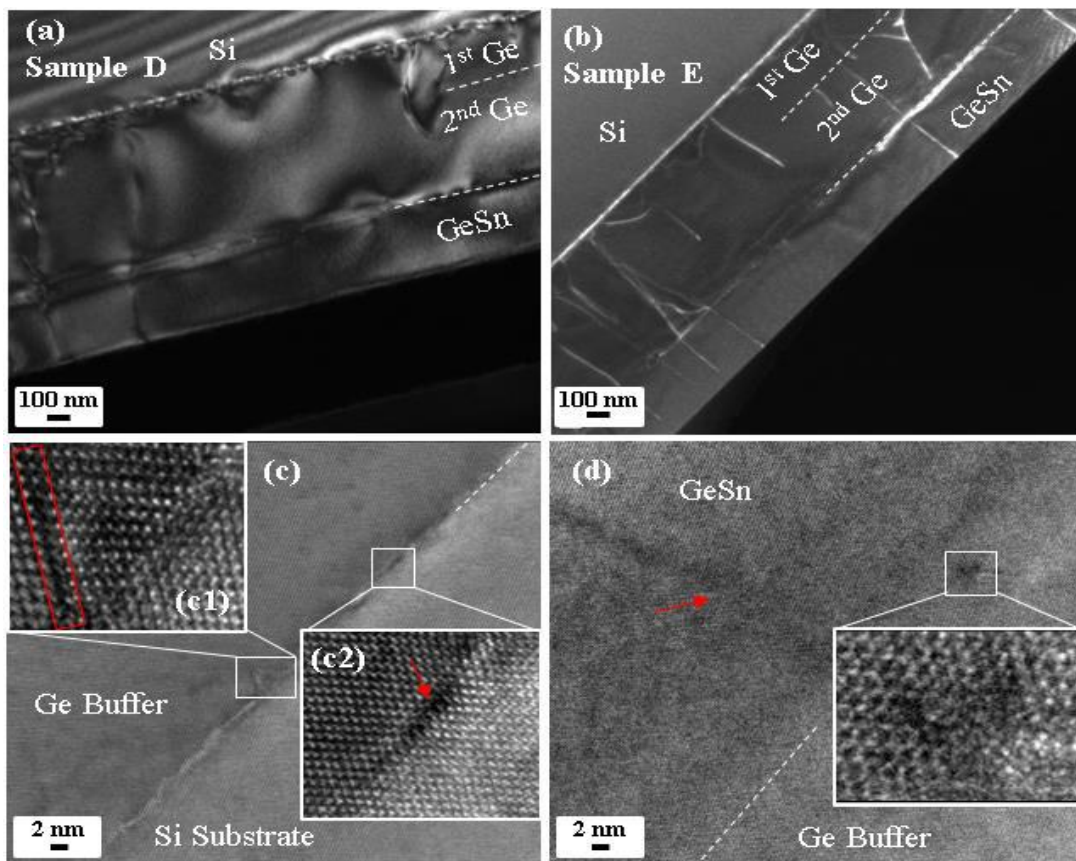


Figure 5.19: Cross sectional TEM. Dark field TEM images of (a) sample D and (b) sample E. (c) High resolution TEM images of the first step Ge/Si interface of sample E. Insets: HR-TEM images of two selected defects near the interface in c1 highlighted by red frame and c2 pointed by an arrow. (d) HR-TEM of the second step GeSn/Ge interface of sample E. A TD propagating the GeSn is pointed with an arrow. Inset: HR-TEM image of an interfacial defect.

Figure 5.19 presents cross sectional TEM images of sample D and E viewed from the $[\bar{1}10]$ direction. A dark field TEM image of each sample are shown side by side in Fig. 5.19 (a) and (b) for comparison using 200 keV and 300 keV beam sources, respectively. The thicknesses of the Ge buffer and the GeSn layer of sample D (E) was measured to be 729 (740) and 319 (335) nm, respectively. The variation in the Ge buffer layer thickness was due to machine growth drift after regular maintenance. Both buffers are accommodated with TDDs that appear as dislocation cores propagating to GeSn films. High resolution TEM images were taken for the Ge/Si and GeSn/Ge interfaces of sample E that are presented in Fig. 5.19(c) and (d), respectively. Figure 5.19(c) shows the Ge/Si interface, which illustrates a single crystal epitaxy. However, at the interface some defects were observed and analyzed using high resolution scanning TEM (HR-TEM). The insets of Fig. 5.19(c) show a HR-TEM of two selected defects, which reveal stacking faults along the (111) planes and misfit dislocations as in c1 and c2, respectively. In addition, at the GeSn/Ge interface as presented in the inset of Fig. 5.19(d), HR-TEM shows the formation of mixed defects, such as misfit dislocations and point defect that could be attributed as Frenkel vacancy defect. The point defect could results from ionic bombardment due to the plasma enhancement in the second step, which causes atomic displacement.

Room temperature PL was characterized for samples D and E using 532 nm laser with 500 mW excitation power. The results are plotted in Fig. 5.20. The figure indicates, not only the PL FWHMs are similar but also peaks positions of both samples D (1930 nm) and E (1946 nm), which indicate similar Sn incorporation, and are in good contracts with Sn evaluation using RSM.

5.4 Conclusion

In conclusion, two-step high quality Ge buffer layers were successfully grown using plasma enhancement in UHV-CVD at different RF powers and temperatures. Systematic material and

optical characterizations indicate that this method can definitely produce a Ge buffer at low temperatures with similar quality to non-plasma enhancement that was grown using the conventional LT/HT method at high temperatures. A 75°C reduction in the second step growth temperature was achieved with the help of plasma enhancement. Our growth approach produces a device quality material with slightly low TDD ($2.7 \times 10^7 \text{ cm}^{-2}$) and flat surface with low surface roughness (RMS = 2.8 nm). Growth of GeSn as an active layer on the virtual plasma and non-plasma enhancement buffers gave almost the same optical and material quality with similar Sn incorporation.

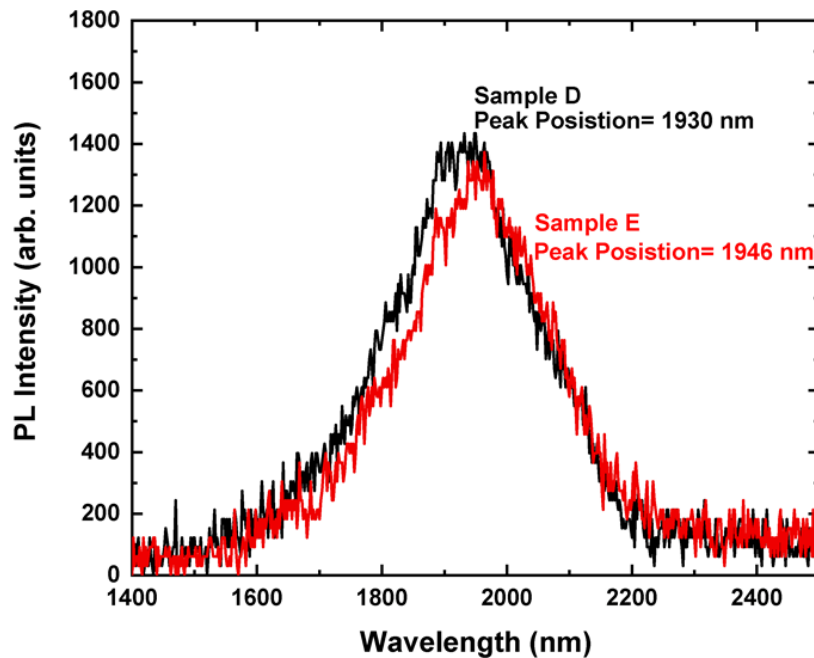


Figure 5.20: Room temperature PL for sample D and E measure using 532 nm green laser with 500 mW excitation power.

Chapter 6: Structural and Optical Properties of SiGeSn Alloys for Si Photonics Devices

6.1 Introduction

The unique optical properties of SiGeSn make it of great potential in Si photonics applications. For example, the compositions of Si and Sn can be chosen in a way that the SiGeSn/GeSn/SiGeSn double heterostructures or quantum wells not only form type-I alignment but also are lattice matched, which is promising for light extraction, such as laser applications. The SiGeSn alloy with 1.0 eV direct bandgap energy can also be used as an intermediate layer in the multi-junction (MJ) space solar cell systems comprising of III-V junctions, thereby leading to a much cheaper option of using Si substrate [81], [109]. Each portion of the solar spectrum is absorbed by a certain layer in the MJ solar cell. Therefore, the solar spectrum is divided between blue cell (>1.8 eV), green cell (1.8-1.4 eV) and red cell (<1.4 eV). The current state of the art solar cell is constructed by InGaP/InGaAs on Ge substrates with a maximum efficiency of $\sim 29\%$. However, the red cell does not reach its maximum efficiency because of the broad spectrum it covers. To further increase its absorption efficiency, a SiGeSn 1.0 eV bandgap cell is added. From design perspective, all the three cells are grown lattice-matched, and by adding the fourth 1.0 eV cell that is lattice matched with Ge and GaAs is challenging. Therefore, growing low-defect SiGeSn alloys are crucial for the development of group IV photonics.

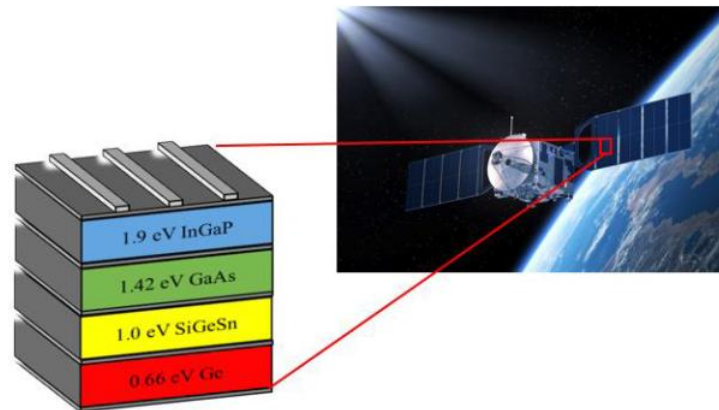


Figure 6.1: Schematic of the proposed space solar photovoltaic with $\text{Si}_x\text{Ge}_{1-x-y}\text{Sn}_y$ junction.

In this chapter, a series of SiGeSn alloy samples with various Si and Sn compositions and thicknesses were grown on Ge-buffered Si substrates. The growth was conducted by using low-cost commercially available silane (SiH_4), germane (GeH_4), and tin-tetrachloride (SnCl_4) precursors in a standard industrial reduced pressure chemical vapor deposition (RPCVD) reactor. Si and Sn compositional- and film thickness-dependent material and optical properties have been characterized using X-ray diffraction (XRD), Raman, photoluminescence (PL), and ellipsometry spectroscopies. Moreover, thermal stability in harsh growth environment, such as in subsequent III-V growth, was studied for future multi-junction solar cell applications. In situ rapid thermal annealing at 650°C was conducted to investigate the enhanced material quality and direct bandgap emission, which were confirmed by XRD, transmission electron microscopy, Raman, and PL measurements.

6.2 Experimental

The eight-inch single wafer RPCVD reactor of the type Epsilon® 2000 Plus was used to grow $\text{Si}_x\text{Ge}_{1-x-y}\text{Sn}_y$ alloys. The epitaxial deposition system, which is designed for high-volume semiconductor manufacturing, is a cold-wall quartz tube and load-lock chamber that is supplied with a horizontal gas flow.

A two-step growth of strain-relaxed Ge buffer with a thickness of ~ 700 nm was grown first. The role of the Ge buffer is to minimize the lattice mismatch between $\text{Si}_x\text{Ge}_{1-x-y}\text{Sn}_y$ films and the Si(100) substrate while a two-step growth is used to improve the Ge buffer quality by avoiding island formation that appears in a high temperature single step growth. Both Ge layers were grown using GeH_4 diluted with H_2 at 0.2 Torr chamber pressure. The Ge seed layer, 150 nm thick, was first grown in low temperature (LT) at $T < 400^\circ\text{C}$. Then, the temperature was increased to the high temperature step (HT) at 600°C . After the temperature was stabilized at 600°C , the remaining ~ 500

nm was grown. A cross sectional transmission electron microscopy (TEM) image of the Ge/Si interface is shown in Fig. 6.2, which shows a 90° Lomer misfit dislocation as an indication of film relaxation [110]. From x-ray diffraction results (not shown) all the Ge buffers in this study exhibit tensile strain. Finally, a post-growth in situ annealing was done at >800°C to improve the material quality further. After Ge buffer growth, hydrogen gas was used to cool the chamber. Then, GeH₄, SiH₄, and SnCl₄ were flown in the chamber. A bubbler vessel at room temperature contains the SnCl₄ gas, and a piezoelectric acoustic sensor is used to measure the up-stream flow from bubbler. The growth of Si_xGe_{1-x-y}Sn_y films was completed in the same chamber at temperatures < 350°C. A cross sectional view of the samples structure is shown in Fig. 6.3.

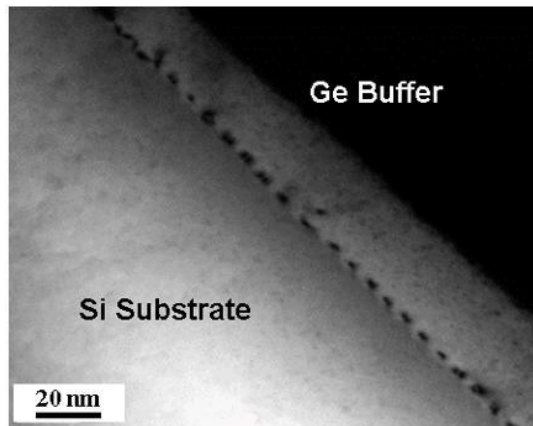


Figure 6.2: Dark field cross sectional TEM image of the Ge/Si interface. The black points with periodic spacing ranging from 4 to 9 nm located near the interface are 90° Lomer misfit dislocations to accommodate the large lattice mismatch between Si and Ge.

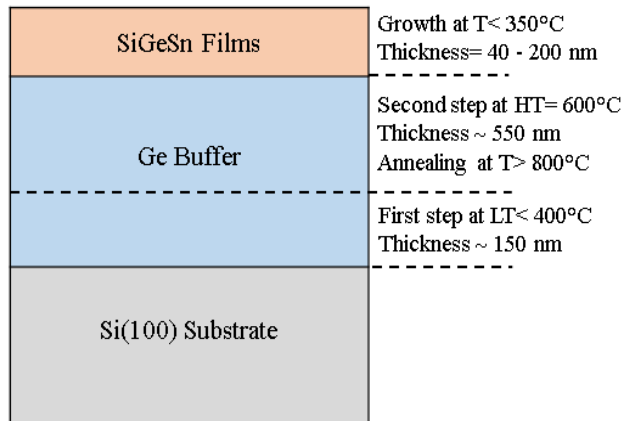


Figure 6.3: A cross sectional view of the samples structure and growth procedure.

To determine the compositions of Si and Sn in each SiGeSn alloy, the high-resolution x-ray diffraction (HRXRD) and Rutherford backscattering spectroscopy (RBS) techniques were employed. The Sn composition was first obtained from RBS and then the Si composition was extracted via XRD based on the Sn composition. Figure 6.4(a) shows a typical Si (100) channeling and random RBS spectra of a SiGeSn sample with a 50-nm film thickness and 7.3 at.% and 5.5 at.% incorporation of Si and Sn, respectively. RUMP software was used to fit the peaks. In addition, secondary ion mass spectrometry (SIMS) had been used as a second tool for composition and thickness determination. Figure 6.4(b) shows SIMS profile of a typical $\text{Si}_{0.117}\text{Ge}_{0.859}\text{Sn}_{0.025}$ sample.

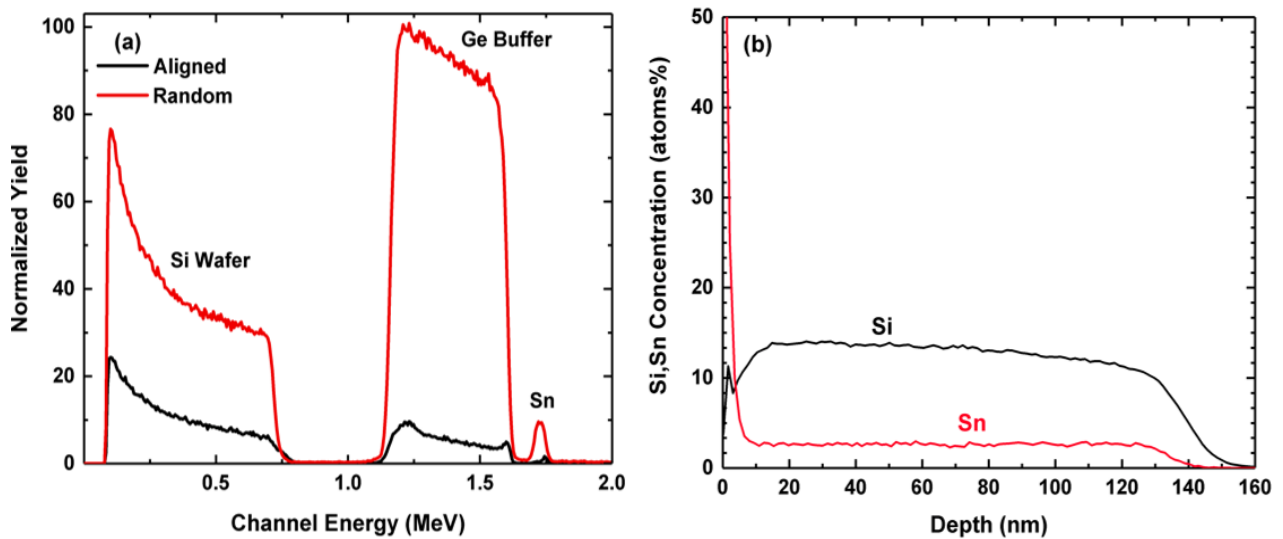


Figure 6.4: (a) normalized channeling and random RBS spectra of a $\text{Si}_{0.073}\text{Ge}_{0.872}\text{Sn}_{0.055}$ sample; (b) SIMS profile of a $\text{Si}_{0.117}\text{Ge}_{0.859}\text{Sn}_{0.025}$ sample.

Study of the structural properties was conducted using a Phillips X'pert PRO diffractometer equipped with a Ge (220) monochromator HRXRD. A TITAN transmission electron microscope (TEM) has been used to study crystal orientation and defects. The crystallinity and Sn incorporation were studied with Raman spectroscopy equipped with a 5 mW 632-nm laser. Temperature-dependent photoluminescence (PL) measurement was performed by using a 532-nm

continuous wave laser with the power of 500 mW as pumping source. The PL emissions were sent to an iHR spectrometer and then were collected by a liquid-nitrogen-cooled InGaAs detector. A Variable-Angle Spectroscopic Ellipsometry (Woolam Model VASE32) was used to measure the thickness and to investigate the spectral absorption coefficient in the range of 0.496-4.768 eV (260-2500 nm) with a resolution of 10 nm at three angles of incidence (65°, 70°, and 75°). The data fitting process was performed using the built-in WVASE32 software. The detailed data fitting procedure can be found elsewhere [111].

Table 6.1: Summary of SiGeSn samples composition and thickness.

Sample	Composition		Thickness (nm)
	Si (%)	Sn (%)	
A	7.3	5.5	50
B	7.3	5.5	150
C	7.3	5.5	200
D	9.5	5.5	50
E	10.0	5.5	50
F	11.6	2.5	150
G	12.0	9.0	40
H	13.0	6.6	55
J	19.0	2.7	40

Three sets of SiGeSn samples were investigated in this study. Section 6.3 is discussing three samples (A, B, and C) with the same Si and Sn compositions of 7.3 and 5.5 at.% but different film thicknesses ranging from 50 to 200 nm. Section 6.4 discusses three samples (A, D, and E) with the same Sn composition of 5.5% and film thickness of 50 nm but different Si compositions ranging from 7.3 to 10.0%. Section 6.5 is discussing four samples (F, G, H, and J) with relatively high Si incorporations of 11.6, 12.0, 13.0 and 19.0%. The Si and Sn composition with the SiGeSn

film thickness of each sample are listed in Table 6.1. The material and optical characterization of all were done and compared.

6.3 SiGeSn Alloys with Similar Compositions but with Different Thicknesses

6.3.1 Material Properties

Figure 6.5 shows the 2θ - ω scans from symmetric (004) planes of samples A, B, and C that have the same Si and Sn composition (7.3 at.% and 5.5 at.%) but with different films thicknesses. The curves were aligned with Si substrate peaks at 69° . The peak from the Ge buffer is noticed at 66° while the peaks at angles below 66° are assigned to the SiGeSn films. The SiGeSn peak of sample A is located far from the Ge peak while the peaks of samples B and C are located closer to the Ge buffer peak. In fact, SiGeSn peaks are slightly shifted towards higher angles as the thickness increases in samples B and C. In addition, the out-of-plane (a_\perp) lattice constant shrinks as the thickness increases, which causes strain relaxation of the material in thicker films. It is also clear that the peak intensity of the SiGeSn films are vary. The SiGeSn peak intensity increases by one order of magnitude as the film thickness increases from 50 in sample A to 200 nm in sample C.

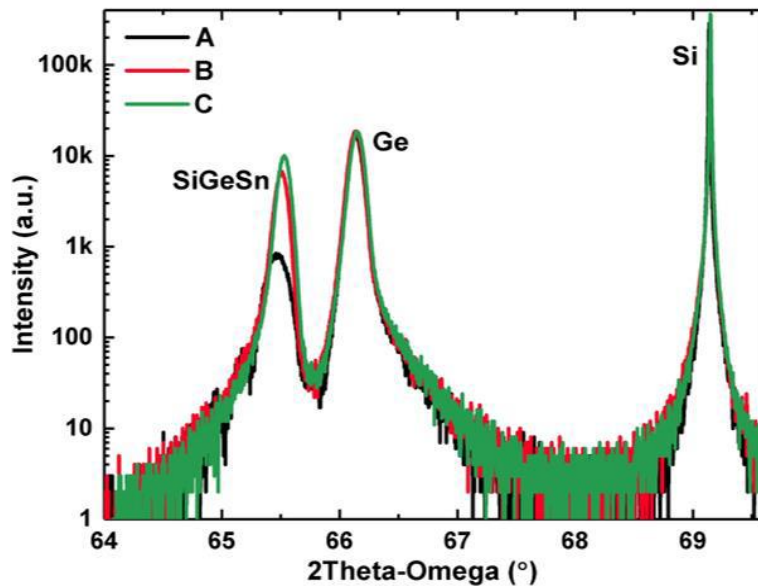


Figure 6.5: 2θ - ω scan from (004) plane for three samples A, B, and C that feature the same Si and Sn compositions but different film thicknesses.

Table 6.2: Summary of material information of SiGeSn films in samples A, B, and C.

Sample	Composition		Thickness (nm)	RSM Results		Relaxed SiGeSn (Å)	*Strain (%)
	Si (%)	Sn (%)		$a_{ }$ (Å)	a_{\perp} (Å)		
A	7.3	5.5	50	5.6733	5.7022	5.6893	-0.28
B	7.3	5.5	150	5.6671	5.6937	5.6788	-0.26
C	7.3	5.5	200	5.6678	5.6906	5.6820	-0.22

* The negative value of strain indicates the compressive strain.

Reciprocal space map (RSM) contours of samples A, B, and C are plotted in Fig. 6.6. The plots show two major diffraction peaks that belong to the Ge buffer and the SiGeSn film (Si substrate is not shown). The small contours above the SiGeSn diffraction peak in sample A are thickness fringes, which indicate high quality interface. The plots of each indicate that the SiGeSn layer was grown almost fully pseudomorphic to Ge buffer as they feature slightly the same in-plane lattice constant ($a_{||}$). Being below the critical thickness for the $\text{Si}_{0.073}\text{Ge}_{0.872}\text{Sn}_{0.055}$ layers, these films predominantly show pseudomorphicity even for the 200-nm thick film in agreement with our theoretical calculations although a slight relaxation in the compressive strain was observed as the film thickness increased. In addition, the shift of the SiGeSn contour toward Ge buffer in sample C indicates a tendency for relaxation. The $a_{||}$ and a_{\perp} lattice constants for each sample were extracted from RSM contour plots. The results are shown in Table 6.2. Since $a_{\perp} > a_{||}$, it clarifies the previous observation of pseudomorphicity. The relaxed lattice constant was calculated theoretically using Vegard's law for ternary alloy, given by [112]:

$$a_{\text{SiGeSn}} = a_{\text{Ge}}(1 - x - y) + a_{\text{Si}}x + a_{\text{Sn}}y + b_{\text{SiGe}}x(1 - x) + b_{\text{GeSn}}y(1 - y) \quad \text{Equation 6.1}$$

where $a_{\text{Ge}} = 5.657 \text{ \AA}$, $a_{\text{Si}} = 5.431 \text{ \AA}$, and $a_{\text{Sn}} = 6.491 \text{ \AA}$, x and y are the composition of Si and Sn, respectively, b_{SiGe} and b_{GeSn} are the bowing parameters with the values -0.26 and 1.66 \AA , respectively. However, in this work the relaxed lattice constant was calculated experimentally using different method.

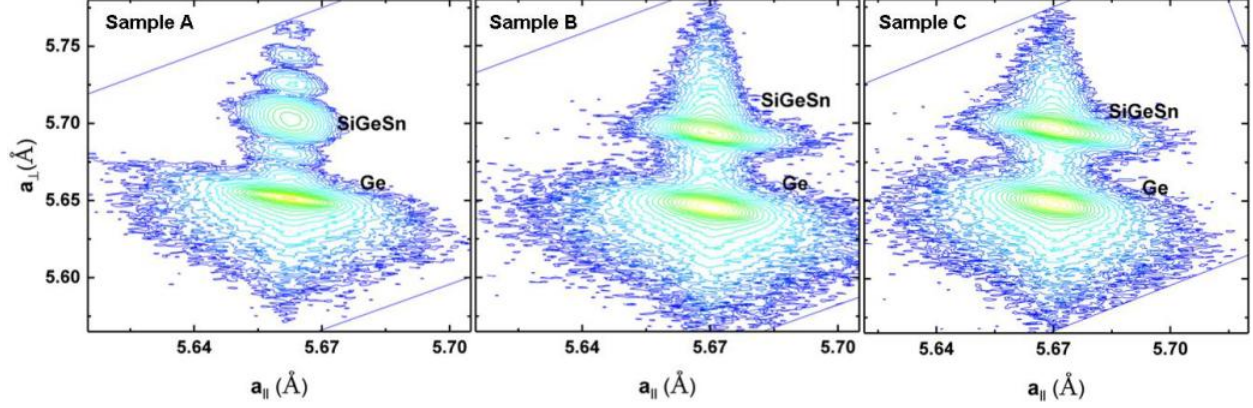


Figure 6.6: RSMs from $(\bar{2}\bar{2}4)$ plane for samples A, B, and C with similar compositions but different thicknesses.

The RSMs results are presented in Table 6.2, which indicate that $a_{||}$ are close to the theoretical relaxed lattice constant while a_{\perp} are not. The experimental relaxed lattice constant and the strain information of each sample were calculated using the information from RSMs by using the following equation:

$$a_{\text{SiGeSn}} = \frac{a_{\perp}^{\text{SiGeSn}} + 2\nu a_{||}^{\text{SiGeSn}}}{1 + 2\nu} \quad \text{Equation 6.2}$$

where ν is the Poisson's ratio, and can be calculated as:

$$\nu = \frac{C_{12}^{\text{SiGeSn}}}{C_{11}^{\text{SiGeSn}}} = \frac{(1-x-y)C_{12}^{\text{Ge}} + xC_{12}^{\text{Si}} + yC_{12}^{\text{Sn}}}{(1-x-y)C_{11}^{\text{Ge}} + xC_{11}^{\text{Si}} + yC_{11}^{\text{Sn}}} \quad \text{Equation 6.3}$$

where C is the elastic modules, and its value for each element is given in Table 6.3.

Table 6.3: C_{11} and C_{12} of Si, Ge, and Sn [113].

Element	Si	Ge	Sn
C_{11}	166	129	69
C_{12}	64	48	29

Finally, the strain (ϵ) can be calculated as:

$$\epsilon = \frac{a_{||}^{\text{SiGeSn}} - a_{\text{SiGeSn}}}{a_{\text{SiGeSn}}} \times 100\% \quad \text{Equation 6.4}$$

The results are presented in Table 6.3. It is noticed that strain values are negative for all the samples, which supported the previous claims that all samples are pseudomorphic. In addition, the strain value decreases as the film thickness increases.

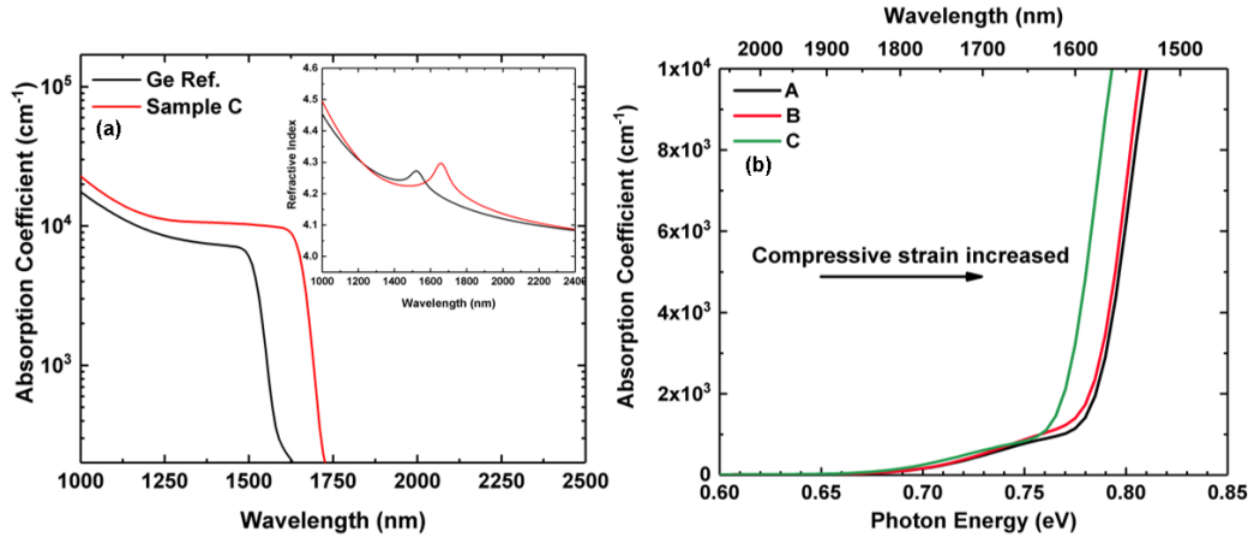


Figure 6.7: (a) Absorption coefficient of sample C. Inset: the refractive index of the same sample. (b) Absorption curves as a function of energy of each sample.

6.3.2 Optical Properties

The samples were characterized by photoluminescence (PL) and ellipsometry to study their optical properties. Spectroscopic ellipsometry was used to determine the refractive index (n), absorption coefficient (α), and to verify the thickness. The n and α are compositional dependent; therefore, Si and Sn incorporation in the Ge lattice will affect the optical properties mostly near the band edge. The optical properties of a bulk Ge sample is also shown as a reference in order to compare the changes in the optical properties of the SiGeSn films. The results are plotted as a function of wavelength in Fig. 6.7(a) for sample C. Because of the influence of Sn incorporation, it is clear that the cut-off wavelength extended to 1740 nm compared to Ge reference sample that has a cut-off wavelength \sim 1576 nm. Moreover, the vertical drop of the absorption near the direct bandgap is similar to bulk Ge. The inset of Fig. 6.7(a) shows the measured refractive index as a function of

the wavelength. The longer wavelength shift in the curve position indicates that the bandgap of the SiGeSn film was shrunk. Incorporation of 7.3% Si and 5.5% Sn causes a shift to longer wavelengths, which implies that influence of Sn is grater as it decreases the SiGeSn bandgap.

Figure 6.7(b) shows the spectral absorption coefficient curves of samples A, B and C. Near the band edges, the band can be approximated as a parabolic band, and the absorption coefficient rises with photon energy as:

$$(\alpha_D hv)^2 = A^2(hv - E_g^\Gamma) \quad \text{Equation 6.5}$$

where α_D is the absorption coefficient for the direct transition, A is a constant, E_g^Γ is the Γ valley bandgap energy where A and E_g^Γ are material dependent parameters. Equation 6.5 depicts the linear relationship between $(\alpha_D hv)^2$ and the photon energy hv . The linear fitting gives the intercept as the direct bandgap E_g^Γ , and the slope as the value of parameter A^2 . The value of A was calculated as $(6.23 \pm 1.04) \times 10^4 \text{ cm}^{-1}(\text{eV})^{-1/2}$. With respect to the direct transition near band edge that has the value of A , the absorption coefficient can be modelled once E_g^Γ was determined. The results are listed in Table 6.4. Since the increase in film thickness relaxes the material, and consequently reduces the bandgap energy, the absorption cut-off edge shifts from 0.78 for sample A to 0.75 eV for sample C as the film thickness increases, which was assigned to direct bandgap absorption. The indirect bandgap absorption features small value, and hence cannot be extracted accurately due to the equipment limitations.

Table 6.4: Summary of optical characterization results of samples A, B, and C.

Sample	Direct Bandgap (eV)	
	Ellipsometry	PL
A	0.78	0.76
B	0.77	-
C	0.75	-

Figure 6.8 shows the room temperature PL spectra of samples A, B, and C. Two peaks and one shoulder can be clearly observed, and interpreted based on bandgap energy calculation [114] as following: i) the peak at ~ 0.79 eV was assigned to the overlap of direct bandgap emissions from Ge and SiGeSn; ii) the peak at ~ 0.67 eV was attributed to the indirect bandgap emission from Ge buffer; iii) the shoulder at ~ 0.63 eV was associated with the indirect bandgap emission from SiGeSn. For sample A, since the SiGeSn layer features wider bandgap compared to the Ge buffer, the SiGeSn could act as barrier and therefore most photo-generated carriers remain confined in the Ge buffer resulting in the Ge emission dominating the PL. For samples B and C, due to the penetration depth of 532-nm pump laser (< 100 nm) being less than the film thickness, the photon absorption and recombination occur mainly in the SiGeSn layer, leading to the emission from SiGeSn contributing equally to the PL (considering that the carrier confinement still affects the carrier re-distribution).

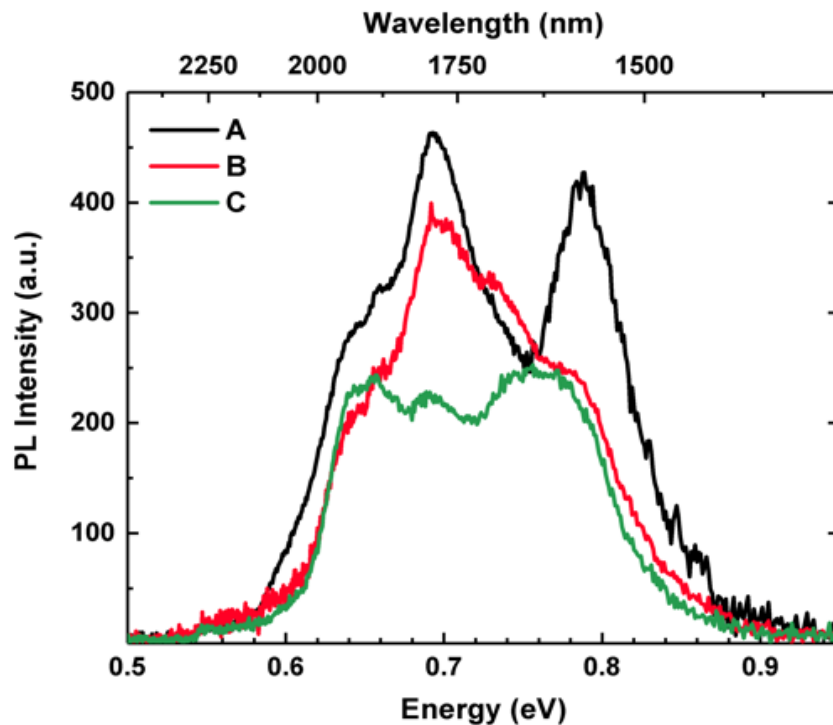


Figure 6.8: Room temperature PL spectra as a function of energy and wavelength for samples A, B, and C.

6.3.3 SiGeSn Based Photoconductors

Sample A and C were fabricated into photoconductors. A 500 and 1000 μm square mesas lengths of samples A and C, respectively, were patterned by using wet chemical etching. To create Ohmic contacts, the process was followed by the deposition of a 10 nm-thick Cr and 200 nm-thick Au. An interdigitated electrodes with 12 μm finger width and 24 μm spacing were used. This could lower the carrier transit time, and thus enhances the photoconductive gain [115]. Fourier transform infrared (FTIR) spectrometer to perform the spectral response measurements. A white light, coming from the internal tungsten source, was externally focused and normally incident onto the entire sample active SiGeSn layer upon exit of the interferometer.

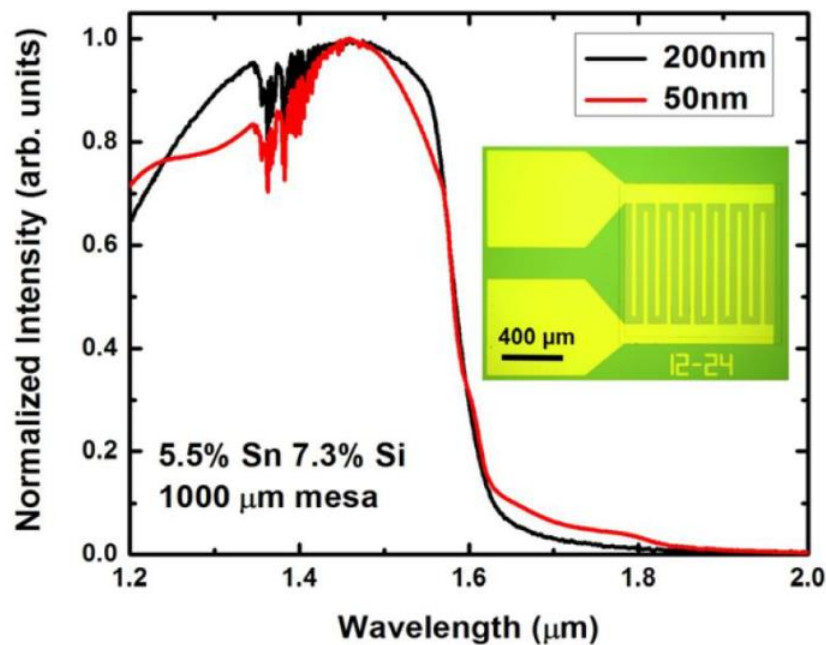


Figure 6.9: Room temperature spectral response of a SiGeSn based photoconductors that were fabricated using sample A and C with a cut-off wavelength near 1.8 μm . Inset: optical image from the top of the device [116].

The room temperature spectral response of photoconductors of each sample are displayed in Fig. 6.9. The inset shows optical image from the top of the device that has a side length of 1000 μm . The “12-24” sign on the device is an indication of the finger width (12 μm) and the spacing (24 μm) (interdigitated electrode design). It is clear from the spectral response figure that both

devices feature similar spectral cut-off wavelength near 1.8 μm , which is attributed to the indirect bandgap absorption. This result is close to the indirect bandgap absorption of bulk Ge. Near 1.6 μm a falling edge was noticed. It might be associated with the direct bandgap absorption, which is also close to the bulk Ge direct bandgap edge. The absorption curve measured from FTIR is consistent with the data extracted from the ellipsometry spectroscopy.

6.4 SiGeSn Alloys with Similar Sn Compositions and Thickness but with Different Si Compositions

6.4.1 Material Properties

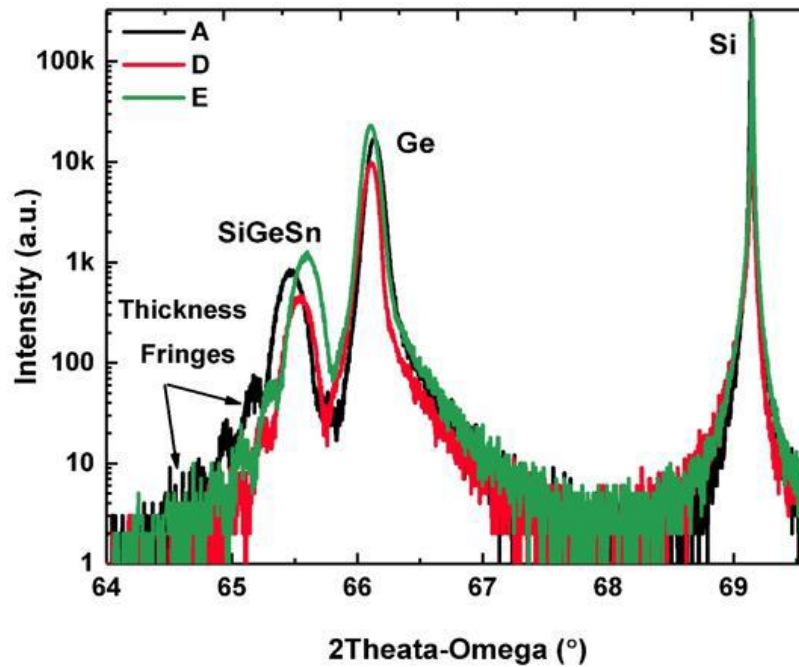


Figure 6.10: 2θ - ω scan from (004) plane for three samples A, D, and E that feature the same Sn compositions and film thicknesses but with different Si compositions.

In this section XRD and Raman were used to characterize the material quality of samples A, D, and E. The 2θ - ω scans of $\text{Si}_x\text{Ge}_{0.945-x}\text{Sn}_{0.055}$ films with the same Sn composition and film thickness but different Si compositions (samples A, D, and E) are presented in Fig. 6.10. The plot shows a well-shaped SiGeSn peaks at diffraction angles below the Ge buffer peak. Increasing Si incorporation from 7.3 to 10% in $\text{Si}_x\text{Ge}_{0.945-x}\text{Sn}_{0.055}$ shifts the SiGeSn peaks toward the Ge peaks

as expected. However, the shift of sample D and E is almost the same because the close Si amount in both samples. As a_{\perp} of SiGeSn decreases with more Si incorporation, the cubic lattice constant of the SiGeSn alloy becomes smaller, which causes a decline in the compressive strain. In addition, thickness fringes are clearly discernible below the SiGeSn peaks. Thickness fringes are signs for highly strained films. It form due to constructive interference between the reflected X-ray beams from the film interfaces, which demonstrate pseudomorphicity with smooth morphology in these high-quality material films [117].

Table 6.5: Summary of material information of SiGeSn films in samples A, D, and E.

Sample	Composition		Thickness (nm)	RSM Results		Relaxed SiGeSn (\AA)	*Strain (%)
	Si (%)	Sn (%)		a_{\parallel} (\AA)	a_{\perp} (\AA)		
A	7.3	5.5	50	5.6733	5.7022	5.6893	-0.28
D	9.5	5.5	50	5.6610	5.6815	5.6723	-0.19
E	10.0	5.5	50	5.6665	5.6841	5.6765	-0.18

* The negative value of strain indicates the compressive strain.

The RSM plots of samples A, D, and E are depicted in Fig. 6.11 and the lattice determination are shown in Table 6.5. It is obvious that all samples exhibit pseudomorphic growth as the SiGeSn diffraction peaks are aligned with the Ge buffer. This can be conformed also from Table 6.5 as $a_{\perp} > a_{\parallel}$. Moreover, increasing Si composition decreases a_{\perp} of SiGeSn, which draws the SiGeSn diffraction peak toward the Ge buffer as can be noticed in the RSMs of samples D and E. The a_{\parallel} is shifted to lower values as Si introduced. Strain of samples D and E was computed following the same procedure in the previous section. The results are presented in Table 6.5. It is clear that the strain amount decreases from -0.28 to -0.19% when the Si composition increases from 7.3 to 9.5% in samples A and D, respectively. However, as Si composition increases from 9.5% sample D to 10% in sample E, strain amount is almost the same. This is due to the relatively similar Si fractions in sample D and E.

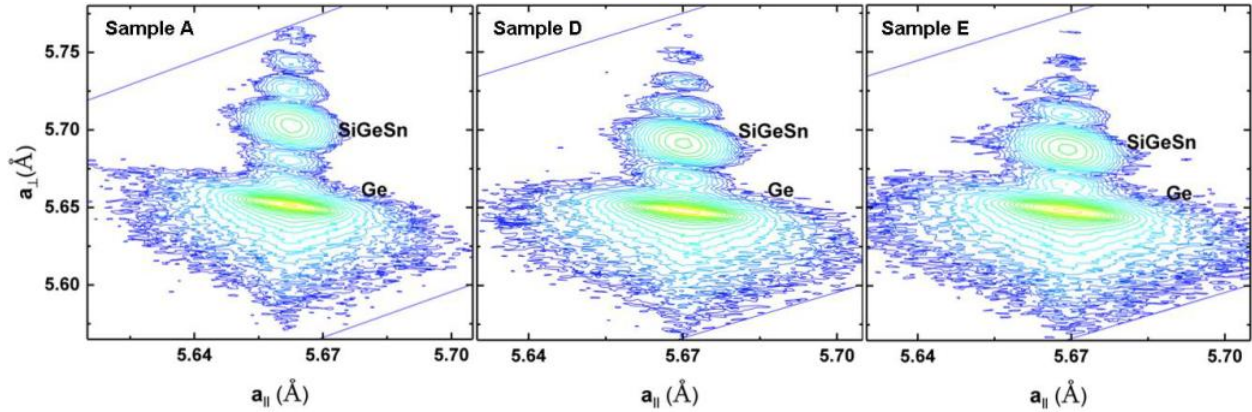


Figure 6.11: RSMs from $(\bar{2}\bar{2}4)$ plane for samples A, D, and E with similar Sn compositions and thicknesses but different Si compositions.

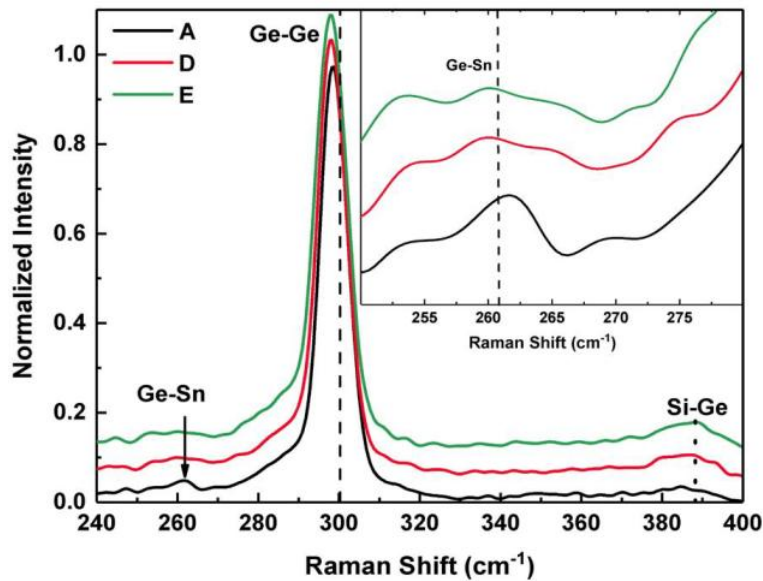


Figure 6.12: Raman spectra of samples A, D, and E. The inset shows a zoomed-in plot of the Ge-Sn modes region.

Raman spectroscopy was used to investigate the SiGeSn film crystallinity. Figure 6.12 shows normalized Raman spectra of the samples A, D, and E that were measured at room temperature. The spectra were stacked for clarity. For each curve, the Ge-Ge longitudinal optical (LO) peak was observed at slightly less than 300 cm^{-1} close to the standard Raman shift of the reference Ge. The shift of Ge-Ge LO peak in SiGeSn samples is mainly due to the Sn and Si incorporation in Ge lattice which changes the average bond size and strength of Ge-Ge lattice. Another peak with relatively lower intensity was observed at $\sim 385\text{ cm}^{-1}$, which corresponds to the

Si-Ge bond. As Si incorporation increases, the peak shifts towards larger Raman shift, i.e., towards Si-Si bond at 520 cm^{-1} (not shown here). The inset of Fig. 6.12 shows a magnified illustration of the expected Ge-Sn mode positions. For sample A, the hump at $\sim 262\text{ cm}^{-1}$ is associated with the Ge-Sn bond [118].

6.4.2 Optical Properties

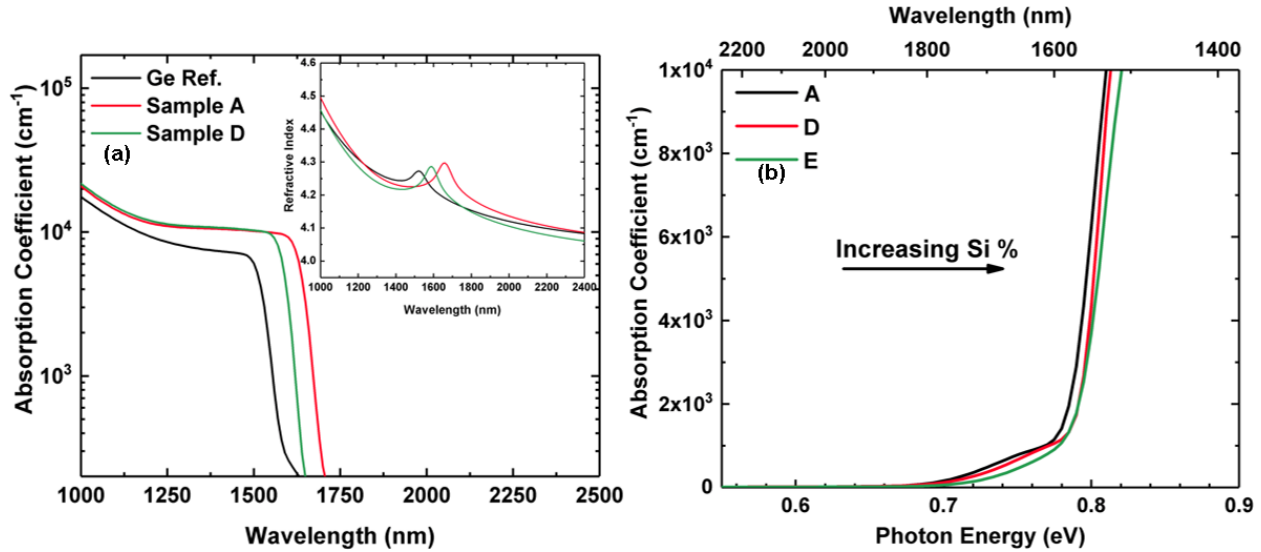


Figure 6.13: (a) Absorption coefficient of sample D. Inset: the refractive index of the same sample. (b) Absorption curves as a function of energy of samples A, D, and E.

Optical characterization was conducted to investigate the optical quality of each sample. Figure 6.13(a) shows the spectroscopic ellipsometry results as a function of wavelength for samples A and D. The absorption of a Ge reference is also shown for comparison. Incorporating more Si in sample D makes the bandgap wider and shifts the cut-off wavelength from 1740 nm for sample A to ~ 1580 nm for sample D, which is very close to the cut-off wavelength of the Ge reference. The measured refractive index as a function of the wavelength of both samples are shown in the inset of Fig. 6.13(a). The peak of the curve of sample D shifts to smaller wavelength as its bandgap becomes larger compared to sample A. Incorporation of more Si causes a shift to shorter wavelength, which implies the increased SiGeSn film bandgap. The spectral absorption

coefficient curves of samples A, D and E as a function of photon energy are displayed in Fig. 6.13(b). The linear fitting was done as explained in the previous section. The results are listed in Table 6.6, which conforms the observation from Fig. 6.13(a). The bandgap of each sample was shifted to higher values as the Si incorporation increases. However, sample D and E exhibit similar bandgaps since they have similar Si compositions.

Table 6.6: Summary of optical characterization results of samples A, D, and E.

Sample	Direct Bandgap (eV)	
	Ellipsometry	PL
A	0.75	0.76
D	0.8	0.81
E	0.8	0.82

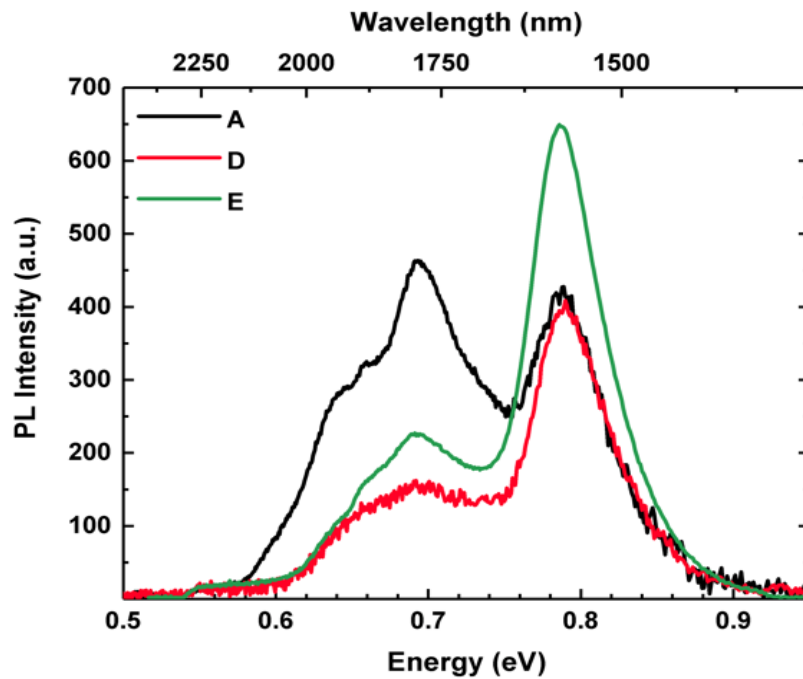


Figure 6.14: Photoluminescence spectra as a function of energy and wavelength of samples A, D, and E measured at room temperature.

The PL spectra of samples A, D, and E are plotted in Fig. 6.14. For each spectrum, the Ge emission dominates the PL since SiGeSn film thicknesses are below the penetration depth of the 532 nm laser. As Si content increases, the ratio of emissions from SiGeSn over Ge decreases,

which is due to the fact that indirect bandgap dominates more in alloys with higher Si incorporation. Moreover, shoulders at ~ 0.62 eV, which are associated with the indirect bandgap emission from SiGeSn films, shift towards higher energy as Si composition increases. This is expected because of the increased indirect bandgap energy with more Si incorporated in the alloy.

6.5 Lattice Matched SiGeSn/Ge Structures

From the previous section we noticed that Si incorporations could compensate the lattice mismatch, which would help in the growth of lattice matched SiGeSn/Ge. In this section SiGeSn alloys with different Sn incorporation and relatively high Si content is investigated.

6.5.1 Material Properties

In this section samples F, G, H, and J were characterized using XRD, RSM, and TEM. Figure 6.15 shows the 2θ - ω scans of SiGeSn samples with relatively high Si incorporation of 11.6% (sample F), 12.0% (sample G), 13% (sample H), and 19% (sample J), the corresponding Sn compositions are 2.5, 9.0, 6.6 and 2.7%, respectively. Due to the higher incorporated Si, the SiGeSn peak shifts considerably towards larger angle, resulting in partial overlap of the SiGeSn and Ge peaks as seen in samples F and J. The broadened peaks at 66° in sample F and J indicate the existence of two overlapped peaks. For sample G, the lower angle shoulder (circled in red) was attributed to the SiGeSn peak. While for samples F and J, since more Si and less Sn are incorporated compared to sample G and H, the SiGeSn peaks of samples F and J feature more overlap with the Ge peak, which indicates it perfectly lattice-matched SiGeSn films to the Ge buffer. For a further increase of Sn composition in the SiGeSn films like in samples G and H. The out-of-plane lattice constant (a_{\perp}) of the SiGeSn becomes bigger thus SiGeSn peaks of G and H shift away from Ge buffer peak, and consequently pseudomorphicity introduced in the SiGeSn layers.

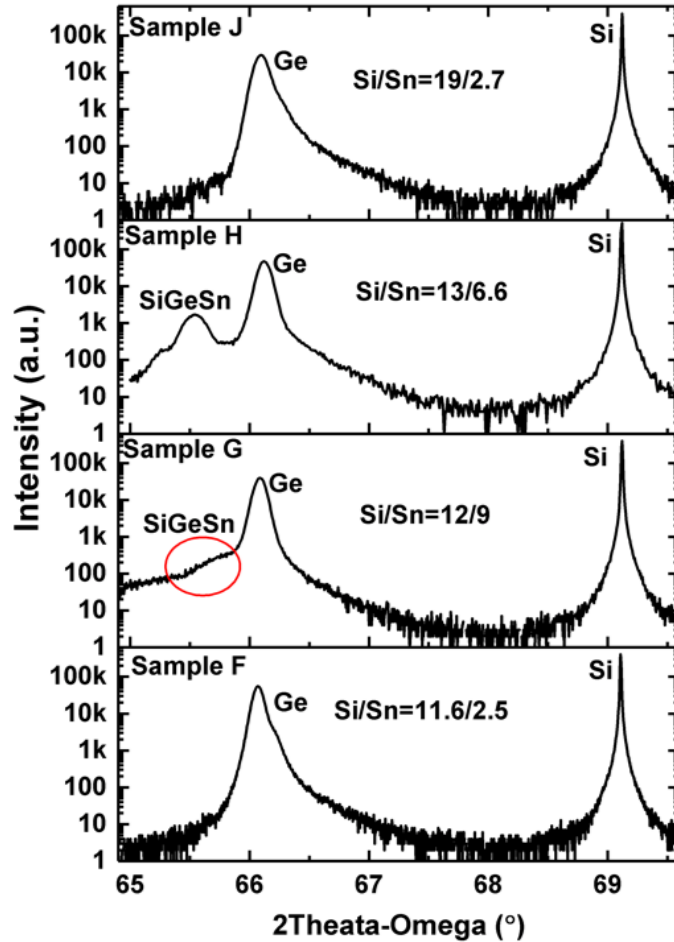


Figure 6.15: 2θ - ω scans from (004) plane for the four SiGeSn samples F, G, H, and J that feature relatively high Si incorporation.

The RSM contour plots of samples F, G, H, and J are shown in Fig. 6.16. The information of each plot was extracted and the strain was calculated. The plots further confirm the existence of SiGeSn diffraction peak only for sample H. However, for samples F, G, and J the contours of SiGeSn layers and the Ge buffer are mostly overlapped leading to the broadened contour plots. In addition, the broadened areas below the Ge buffer in samples F and J (circled in red) are indications of tensile strain while broadened area approaching the Ge buffer from the top in sample G (circled in red) is an indication of increased tensile strain. Moreover, the a_{\perp} lattice constants of samples F, G, and J are smaller than the in-plane lattice constants (a_{\parallel}), which conforms the existence of the tensile strain. The case in sample H is the opposite, where a_{\perp} lattice constant is bigger than a_{\parallel} ,

which confirms that SiGeSn is pseudomorphically grown on Ge buffer. The strain calculations in Table 6.7 reveal similar findings with strain values ranging between +0.31% (tensile) to -0.25% (compressive).

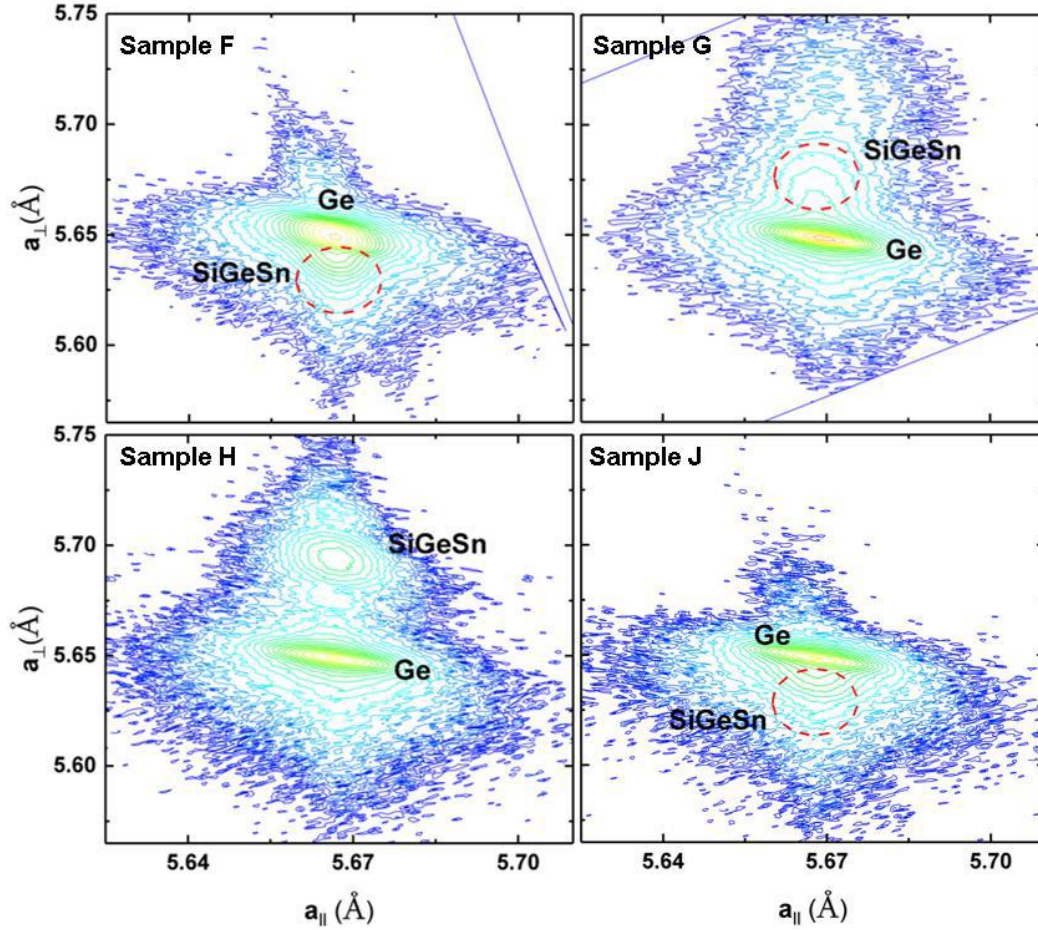


Figure 6.16: RSM contour plots for the four SiGeSn samples F, G, H, and J that feature relatively high Si incorporation

Table 6.7: Summary of material information of SiGeSn films in samples F, G, H, and J.

Sample	Composition		Thickness (nm)	RSM Results		Relaxed SiGeSn (Å)	*Strain (%)
	Si (%)	Sn (%)		$a_{ }$ (Å)	a_{\perp} (Å)		
F	11.6	2.5	150	5.6684	5.6361	5.6508	+0.31
G	12.0	9.0	40	5.6657	5.6566	5.6608	+0.09
H	13.0	6.6	55	5.6644	5.6908	5.6787	-0.25
J	19.0	2.7	40	5.6683	5.6409	5.6538	+0.26

* The negative value of strain indicates the compressive strain while the positive value indicates tensile strain.

Figure 6.17(a) and (b) shows dark field and high resolution TEM images of sample H. From the dark field image in Fig. 6.17(a), it is clear that most defects are generated and trapped near the Si and Ge interface. However, at some positions, the threading dislocations could propagate through the Ge buffer layer as well as the Ge/SiGeSn interface to the SiGeSn layer. This might be caused by the pseudomorphic growth of SiGeSn alloy on the Ge buffer layer. Figure 6.17(b) illustrates the high resolution TEM image of SiGeSn/Ge interface. There interface is clear from any defects or misfit dislocation, which confirms close to lattice matched SiGeSn/Ge buffer. It also verifies the high quality pseudomorphic growth since most areas feature the low defect density.

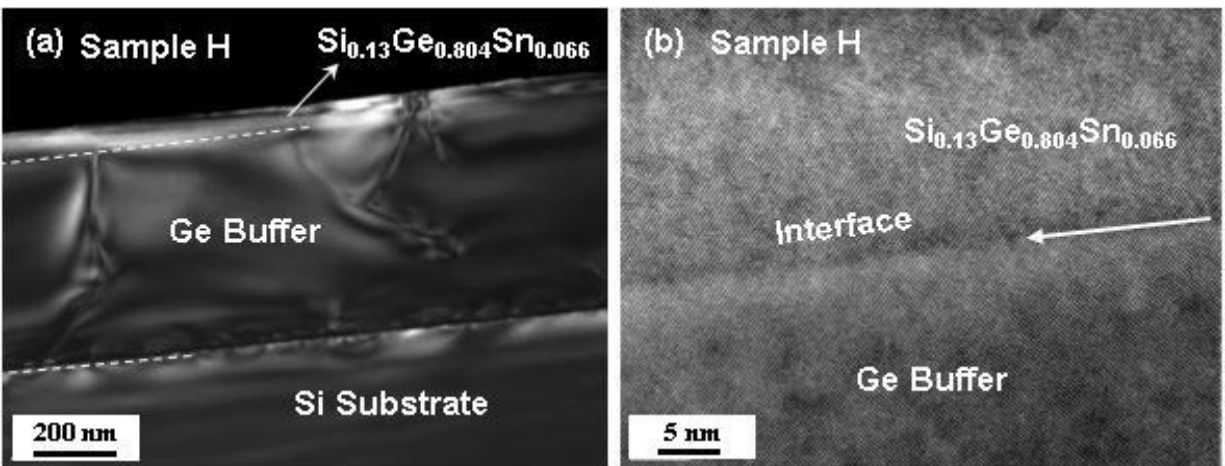


Figure 6.17: Dark field (DF) and high resolution (HR) TEM images of sample H. (a) Shows the DF TEM of a cross sectional view of all layers. Dislocations that are initiated from misfit dislocations in the Ge/Si interface propagate through the Ge buffer to the SiGeSn film. (b) The HRTEM image of Si_{0.13}Ge_{0.804}Sn_{0.066}/Ge interface verifies high quality growth.

For lattice matched samples, a typical dark field and high resolution TEM images of samples F and J are presented in Fig. 6.18. For sample F, as Fig. 6.18(a) illustrates, threading dislocations exist in the Ge buffer. In addition, the SiGeSn film of sample F shows a low density of threading dislocations that propagate the SiGeSn/Ge interface to the film. A high resolution TEM image of the SiGeSn film is shown in Fig. 6.18(b). The image depicts the SiGeSn film with

high crystallinity. For sample J, it is clear from the cross sectional TEM image of sample F that the Ge buffer possesses very low defects density. The threading dislocations that were generated from the lattice mismatch between Si substrate and Ge buffer are trapped close to the Si/Ge interface. In addition, no threading dislocation propagate from the Ge buffer towards the SiGeSn layer. Such a very low defect density resulting in high material quality of SiGeSn alloy. The high resolution TEM images of the SiGeSn films of samples F and J indicate high quality crystalline films.

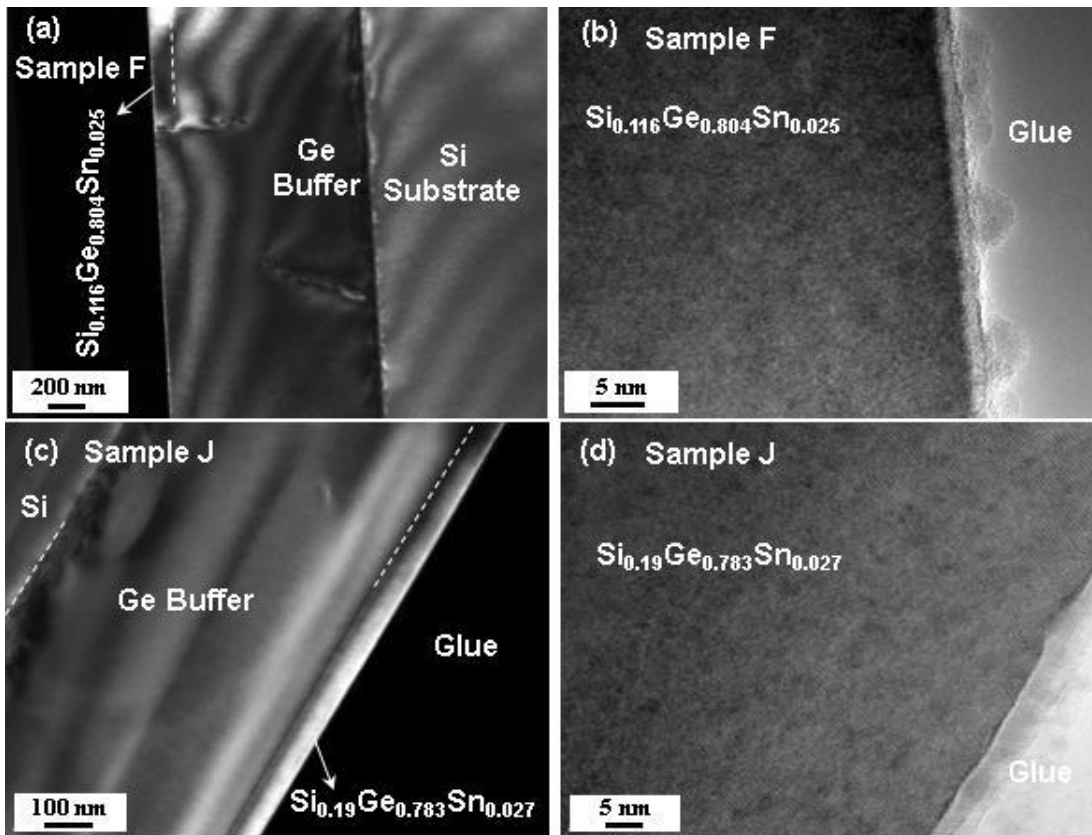


Figure 6.18: Dark field (DF) and high resolution (HR) TEM images of lattice matched samples F and J. (a) DF TEM cross sectional image of sample F. (b) HRTEM image of sample showing only the top SiGeSn film. (c) Shows the cross section of the Si_{0.19}Ge_{0.783}Sn_{0.027} film grown on a Ge buffer and (d) shows HR TEM of the SiGeSn film.

6.5.2 Optical Properties

Samples were further characterized optically to explore their optical quality. Figure 6.19(a) shows the results of samples F, G, H, and J compared to the absorption of a Ge reference. By taking into

account that Sn fraction in both samples is very close, only Si incorporating plays the significant role in the absorption behavior. The cut-off wavelength of sample G \sim 1870 nm while for sample for sample J is \sim 1300 nm. This results from more Si incorporation in sample J that shifts the cut-off wavelength to lower value far below the bulk Ge. This can be taken as an indication of increased bandgap energy in sample J. The refractive index of samples F and J are presented in the inset of Fig. 6.19(a). The peak of the curve in sample J shifts to smaller wavelength as its bandgap becomes larger compared to sample H. Incorporation of more Si causes a shift to shorter wavelength, which implies the increased SiGeSn film bandgap.

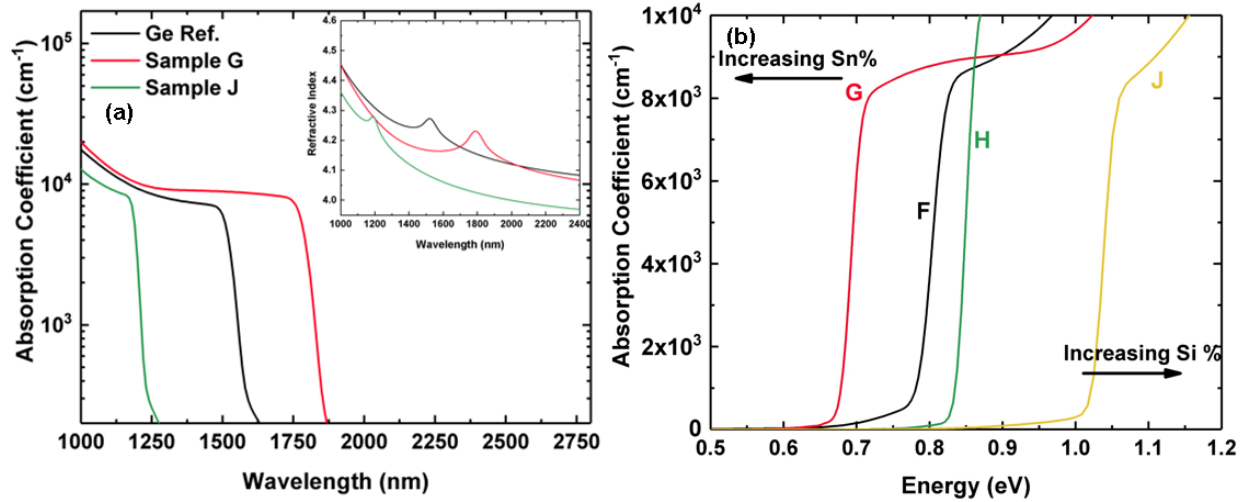


Figure 6.19: (a) Absorption coefficient of sample D. Inset: the refractive index of the same sample. (b) Absorption curves as a function of energy of samples F, G, H, and J.

Table 6.8: Summary of optical characterization results of samples F, G, H, and J.

Sample	Direct Bandgap (eV) from Ellipsometry
F	0.80
G	0.68
H	0.84
J	1.0

The spectral absorption coefficient curves of samples F, G, H, and J as a function of photon energy are shown in Fig. 6.19(b). In this figure the role of Si compared to Sn is clearly seen. Increasing Si shifts with relatively low Sn in SiGeSn film shifts the energy to higher value as in sample J whereas increasing Sn with respect to Si gives an opposite effect as in sample G. However, the amount of Si in samples F and H is compensated by Sn incorporation. The linear fitting was done as explained in the previous section. The results are listed in Table 6.8, which conforms the observation from the figure. The bandgap of sample Ge was shifted to lower values while J that has the heights Si fraction compared to Sn is shifted to higher bandgap.

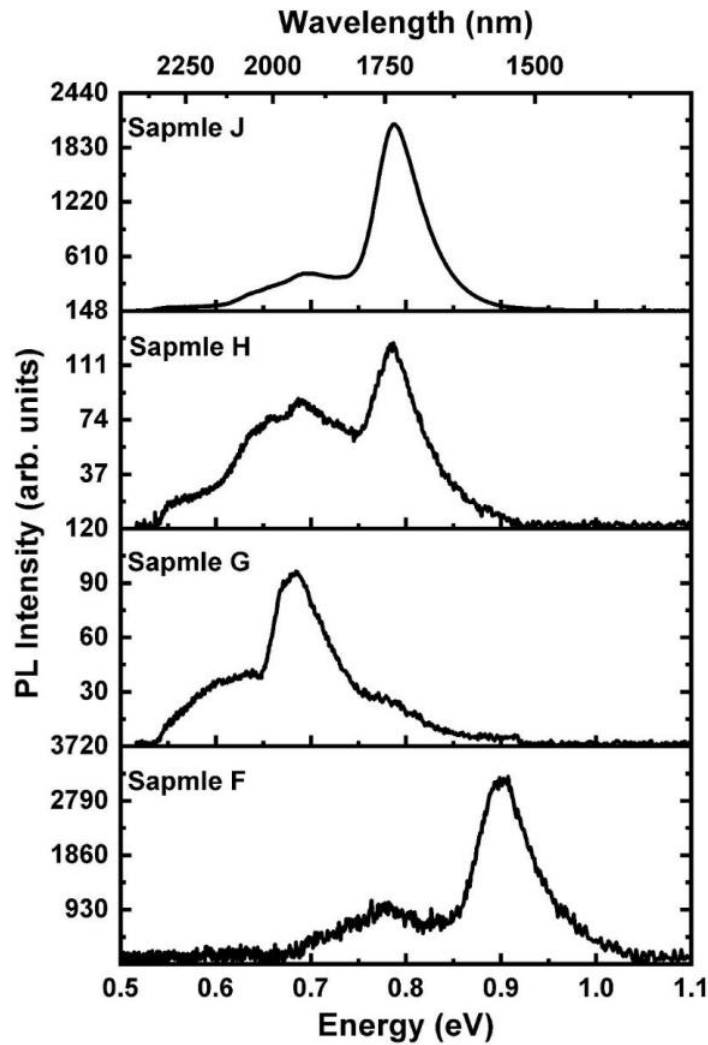


Figure 6.20: Photoluminescence spectra as a function of energy and wavelength of samples F, G, H, and J measured at room temperature.

Figure 6.20 shows room temperature PL spectra of samples F, G, H, and J. Since the SiGeSn films thickness of samples G, H, and J can be penetrated easily by the 532 nm laser, most of the PL contribution comes from the Ge buffer. Therefore, decoupling SiGeSn peaks from Ge buffer layer could not be achieved for further PL investigation. For sample F, since the SiGeSn thickness (150 nm) is deeper than the penetration depth of the 532 nm laser. Hence, the PL profile is mainly from the SiGeSn film. As noticed, Si composition affects the PL spectrum by shifting its peaks to higher energy. However, as Sn increases with similar Si as in sample G, the incorporation of 9% Sn overcompensates the 12% Si incorporation-induced bandgap indirectness, a narrower direct bandgap of SiGeSn compared to that of Ge was obtained, leading to the direct peak red-shift of SiGeSn. For samples H and J, two main peaks with a strong higher energy peak at ~ 0.8 eV and a lower energy peak at ~ 0.69 eV were observed. These two peaks were assigned to the overlapped direct bandgap emissions from Ge and SiGeSn, and overlapped indirect bandgap emissions, respectively. The direct bandgap energy separation between Ge and SiGeSn is too small hence their direct transitions cannot be identified from PL spectra. While for the indirect bandgap transition, the broadened peak in sample H indicates that both SiGeSn and Ge emissions contribute to PL.

For further investigation about the recombination process, temperature-dependent PL was utilized, which shows the variation of peak position and intensity as a function of temperature. The temperature-dependent PL spectra of samples F and J are shown in Fig. 6.21. For sample F in Fig. 6.21(a), a SiGeSn PL peak at 300 K was observed near 0.79 eV. The second peak at 300K near 0.7 eV is attributed as the direct bandgap emission of the Ge buffer. The emission contribution comes from the Ge buffer since its bandgap is smaller than SiGeSn film in sample F. As the temperature decreases, a two strong peaks near 0.56 and 0.48 eV are observed. These peaks might

come from the direct and indirect emissions, respectively. For sample J in Fig. 6.21(b), as the temperature decreases, PL peaks shift toward higher energies due to bandgap increase as expected. Moreover, the overall PL intensity decreases as the temperature decreases with the direct peaks dropping more rapidly than the indirect peaks, resulting in the direct peaks dominating the PL at 300 K whereas the indirect peaks dominate the PL at the temperatures below 100K. This PL spectra behavior indicates that sample J is a typical indirect bandgap material. In fact, adding Sn into Ge would engineer the bandgap towards direct bandgap while incorporation of Si shifts the bandgap to the opposite direction. Therefore, the bandgap property can be tuned by independently controlling the Si and Sn compositions. The broad peaks that appear at ~ 0.6 eV are attributed to radiative recombination from states introduced by the impurities and other defects in the $\text{Si}_{0.19}\text{Ge}_{0.783}\text{Sn}_{0.027}$ film [114].

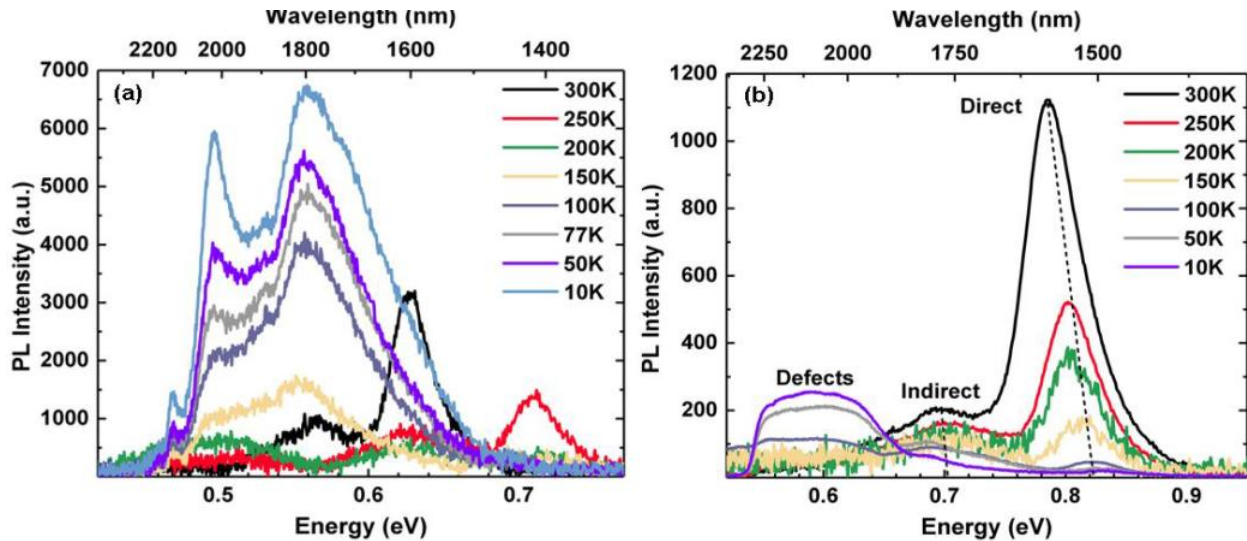


Figure 6.21: Temperature-dependent photoluminescence spectra as a function of energy and wavelength of (a) sample F and (b) sample J.

The line-widths of the direct and indirect transitions in the temperature-dependent PL spectra of sample J were extracted after Gaussian fitting was performed. The results are plotted in Fig. 6.22(a). As expected, for the indirect peaks the line-widths decrease dramatically as the temperature decreases. However, the line-widths of the direct peaks become slightly wider with

decreasing temperatures. This behavior confirms that sample J is indirect bandgap material. The peak positions of both the direct and indirect peaks were extracted and fitted using the Varshni equation:

$$E_{\text{SiGeSn}}(T) = E_{\text{SiGeSn}}(0) - \alpha T^2 / (T + \beta) \quad \text{Equation 6.6}$$

where $E_{\text{SiGeSn}}(0)$ is the bandgap energy at 0K, α and β are fitting parameters. The results are presented in Fig. 6.22(b) and the parameters are given in Table 6.9.

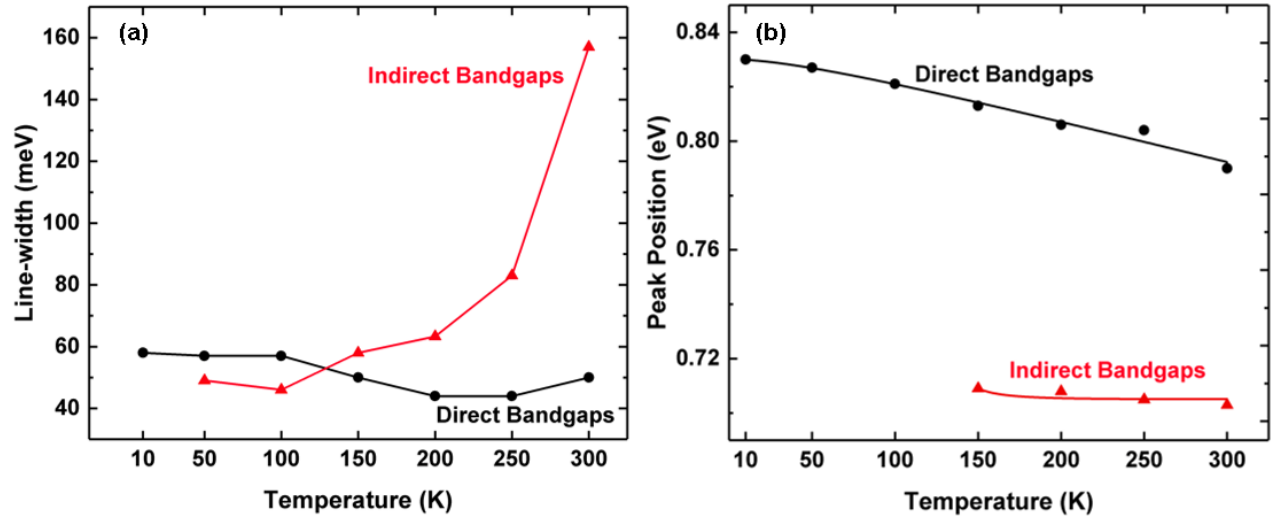


Figure 6.22: Temperature-dependent analysis of the PL spectra of sample J as a function of (a) Line-widths and (b) PL peak positions. The solid lines in (b) denote Varshni fittings.

Table 6.9: Varshni's equation fitting parameters of sample J.

Peak	$E_{\text{SiGeSn}}(0)$ (eV)	α (eV/K)	β (K)
Direct	0.83	1.55×10^{-4}	69
Indirect	0.70	N/A	N/A

The power dependent PL with a power up to 400mW at the three temperatures 300K, 77K, and 10K were performed . At 300K, the direct bandgap dominates from 400 to 200 mW. As the power decreases to 100 and 50 mW, the PL spectra becomes noisy as the signal noise ratio becomes high. As the temperature decreases to 77 and 10K, only the indirect bandgap dominates at all

powers. This is an indication of the high material quality as most of carriers are recombine by the radiative process.

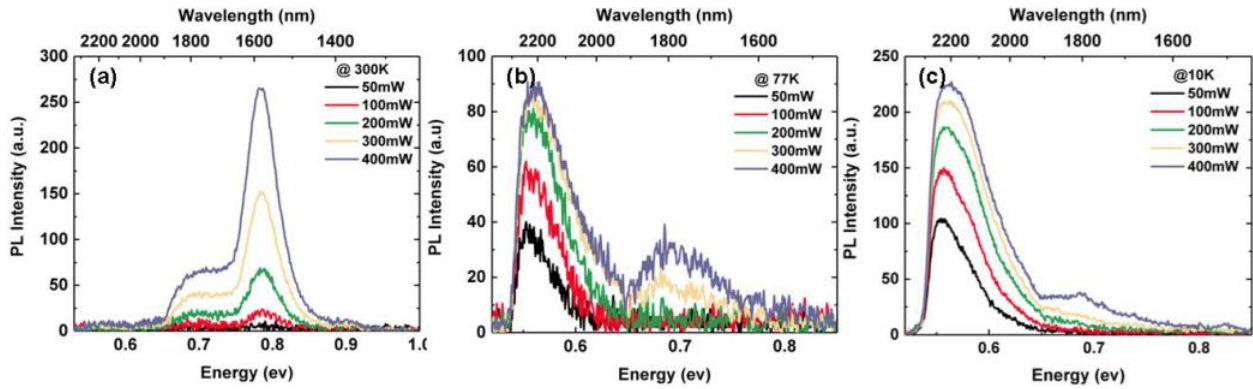


Figure 6.23: Power-dependent measurements of sample J at three temperatures (a) 300K, (b) 77K, and (c) 10K.

6.5.3 Annealing Study

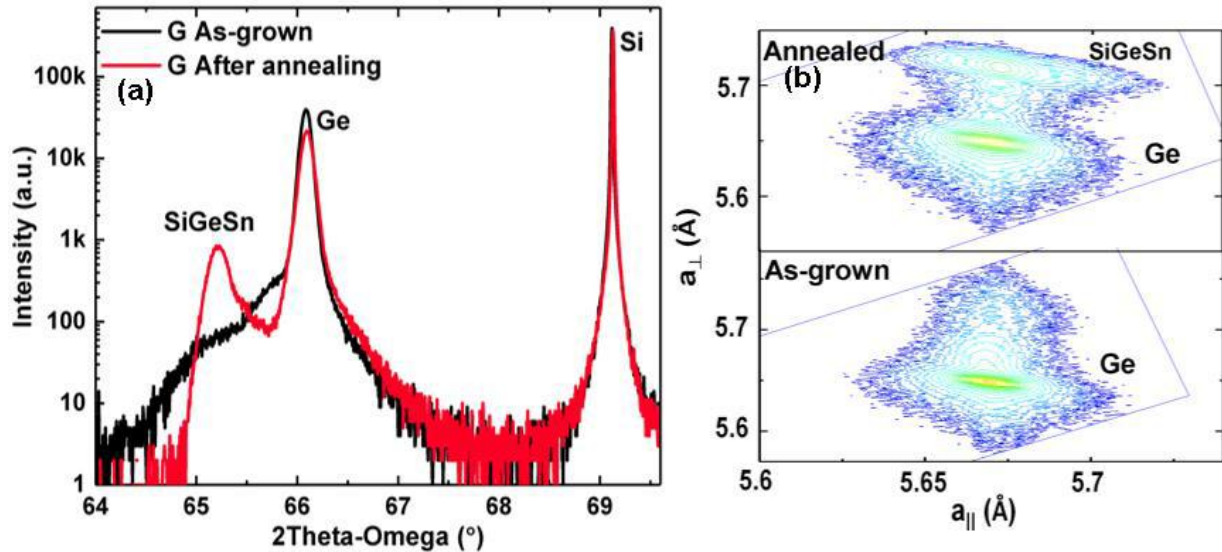


Figure 6.24: (a) 2θ - ω scans and (b) RSM contour plots of sample G as-grown and after annealing.

To investigate the thermal stability of the SiGeSn alloy for potential MJ solar cells applications, in situ annealing was performed with sample G at 650°C in H₂ ambient for 2 minutes at atmospheric pressure. The material and optical properties were characterized for as-grown and after annealing samples, and the results were compared to illustrate the effects of thermal treatment.

Since the SiGeSn alloy is a viable candidate for a solar cell junction within an III-V based high efficiency MJ junction solar PV system, annealing study was conducted to investigate the material property under thermal treatment. Sample G was selected as it features relatively high Si and Sn compositions, and the annealing temperature of 650°C was set to investigate the thermal stability under a typical MOCVD deposition temperature for III-V materials. Figure 6.24(a) shows 2θ - ω scans of sample G (as-grown) and after annealing. It can be seen that the SiGeSn peak features reduced peak line-width and increased peak intensity after annealing, indicating the improved material quality. The RSM contour plots of sample G (as-grown) and after annealing are shown in Fig. 6.24(b). Unlike RSM for the as-grown sample, the SiGeSn contour after annealing can be clearly resolved from broadened Ge plot, confirming the improved material quality. Moreover, the out-of-plane lattice constant of the annealed sample increases while the in-plane lattice constant remains almost the same, suggesting the almost unchanged pseudomorphicity of the material.

The material quality was further investigated by the cross-sectional TEM images of sample G as-grown and after annealing. Figure 6.25(a) shows TEM image of sample G as-grown, which clearly illustrates black and white thickness fringes. The arrows at the Ge buffer/Si interface indicate the stacking fault defects due to dissociation of dislocations at the [111] plane. Threading dislocations that propagate through the Ge buffer are resulting from the large lattice mismatch in the Ge/Si interface. The high-resolution image of SiGeSn/Ge interface as-grown is shown in Fig. 6.25(b), which illustrates a few misfit dislocations and provides evidence of lattice matched growth. The TEM image of sample G after annealing is shown in Fig. 6.25(c). The smooth cross-section with no observed threading dislocations in SiGeSn/Ge/Si interfaces implies improved material quality as a result of the annealing process. The high-resolution TEM image of SiGeSn/Ge

interface shown in Fig. 6.25(d) illustrates periodic defects with ~ 250 nm spacing on average that are interpreted as Lomer dislocations. Such dislocations appear in the SiGeSn/Ge interface to accommodate the increased vertical lattice constant as the annealed SiGeSn film tends to approach relaxation.

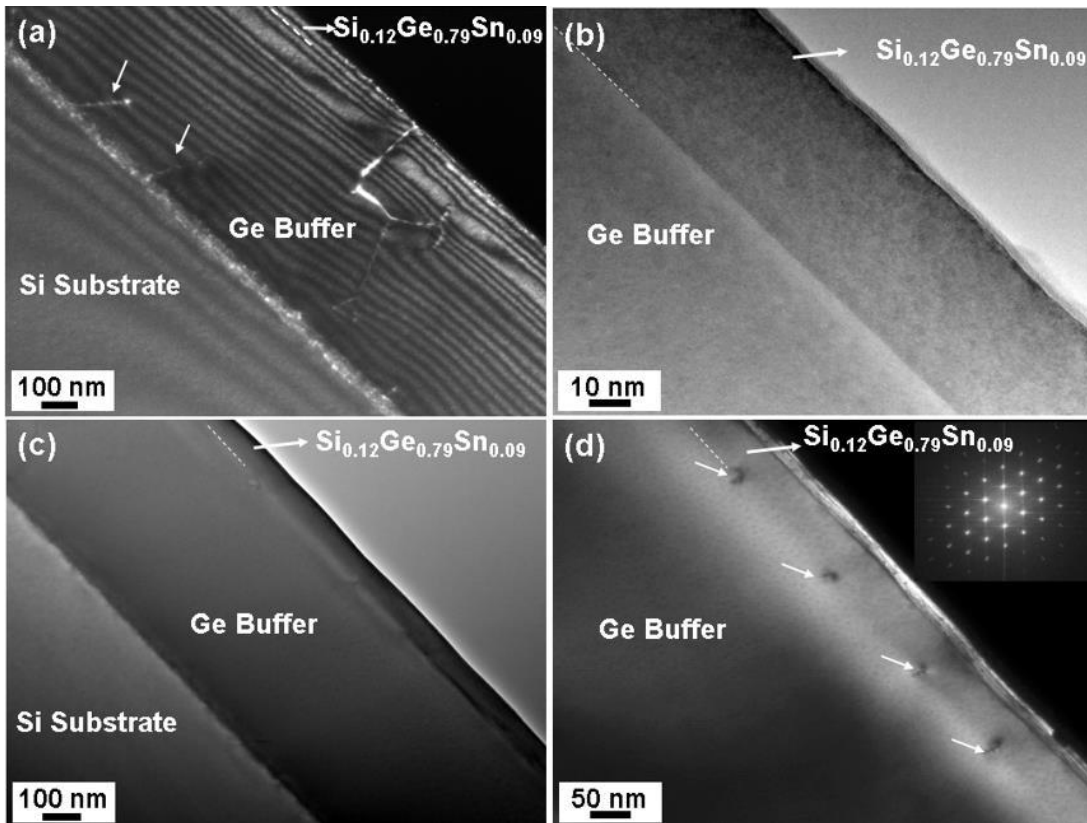


Figure 6.25: Cross sectional TEM of sample G. As-grown in (a) and (b). After rapid thermal annealing in (c) and (d).

Optical characterization including Raman and PL spectroscopy were also performed to study the optical properties of the material under thermal treatment. Raman spectroscopy shown in Fig. 6.26(a) indicates that after annealing the Ge-Ge LO mode is slightly lower than that of the as-grown sample, while the peak intensity and line-width almost remain the same. However, the Ge-Sn and Si-Ge modes show improved crystallinity as a result of the rapid thermal annealing. Figure 6.26(b) shows the PL spectra of as-grown and annealed samples. Compared to the PL spectrum of the as-grown sample, the PL peaks of the annealed sample shows a blue-shift, which

is mainly due to the slightly relaxed material in high temperature environment. The improved material quality under thermal treatment suggests that the growth of SiGeSn alloy can be subjected to higher temperatures during the MJ junction solar cell growth without much detrimental effects, since the material quality could remain the same or even be improved slightly.

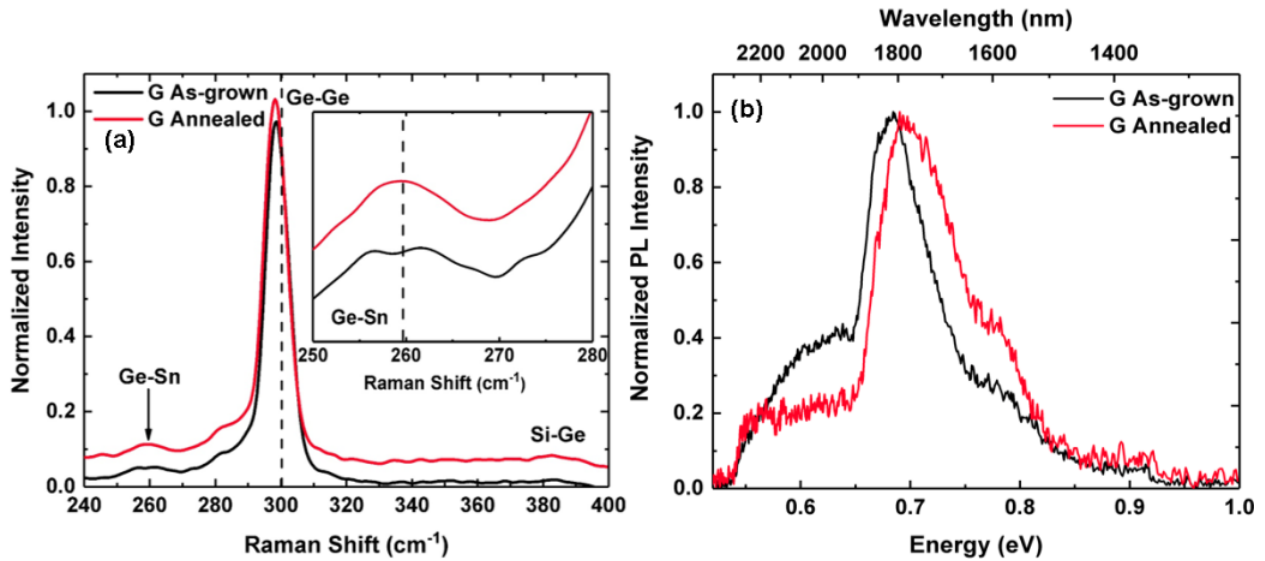


Figure 6.26: Sample G as-grown and after annealing. (a) Stacked Raman spectra. The inset shows the Ge-Sn modes. (b) PL spectra.

6.6 Conclusion

In summary, SiGeSn alloys with various film thicknesses and varied Si and Sn compositions were grown on strain relaxed Ge buffered Si substrates via a standard industrial RP-CVD reactor using commercial precursors, GeH_4 , SiH_4 , and SnCl_4 . The material quality was checked with XRD-RSM and TEM. The XRD 2θ - ω scans showed the Si and Sn compositional- and film thickness-dependent material properties. The SiGeSn peaks indicated the pseudomorphicity of thin samples with relatively low Si incorporation in $\text{Si}_x\text{Ge}_{0.945-x}\text{Sn}_{0.055}$. Some samples with high Si and low Sn incorporation did not exhibit a SiGeSn peak in the XRD 2θ - ω scans, which was a first indication of a latticed matched SiGeSn/Ge growth. RSM contour plots conformed pseudomorphicity of $\text{Si}_x\text{Ge}_{0.945-x}\text{Sn}_{0.055}$ films and lattice matching from the XRD 2θ - ω observations. From RSMs the

strain calculations revealed compressive strain for pseudomorphic samples and tensile strain for lattice matched samples. The spectral absorption coefficient of the alloys was studied by spectroscopic ellipsometry, which showed sharp absorption with shorter cut-off wavelength for high Si samples and longer cut-off wavelength for high Sn samples. Since SiGeSn films thicknesses were below the laser penetration depth, the room temperature PL spectra exhibited direct and indirect emissions from SiGeSn films, which were overlapped with emission peaks from Ge buffer. In addition, temperature-dependent PL study for a lattice matched SiGeSn sample indicated indirect bandgap emission. Moreover, the annealing study was performed for a SiGeSn to investigate the material property and direct bandgap emission under thermal treatment, which was aimed to study the thermal stability in harsh growth environment for space MJ solar cell applications. The results showed an improved material quality as indicated by XRD-RSM and TEM that suggests SiGeSn is a versatile candidate for being part of a well-designed MJ of solar cell stack.

Chapter 7: SiGeSn Double Barrier in GeSn Quantum Well for Laser Diode Applications

7.1 Introduction

Direct bandgap quantum well (QW) structures with type-I band alignment is highly desired because they can be used as efficient light emitters, such as GeSn LED and laser devices. Using SiGeSn as a barrier is preferred for two reasons: (1) it provides a better optical confinement compared to Ge; (2) the bandgap energy and lattice constant of SiGeSn alloys can be tuned independently by varying the compositions [119], [95].

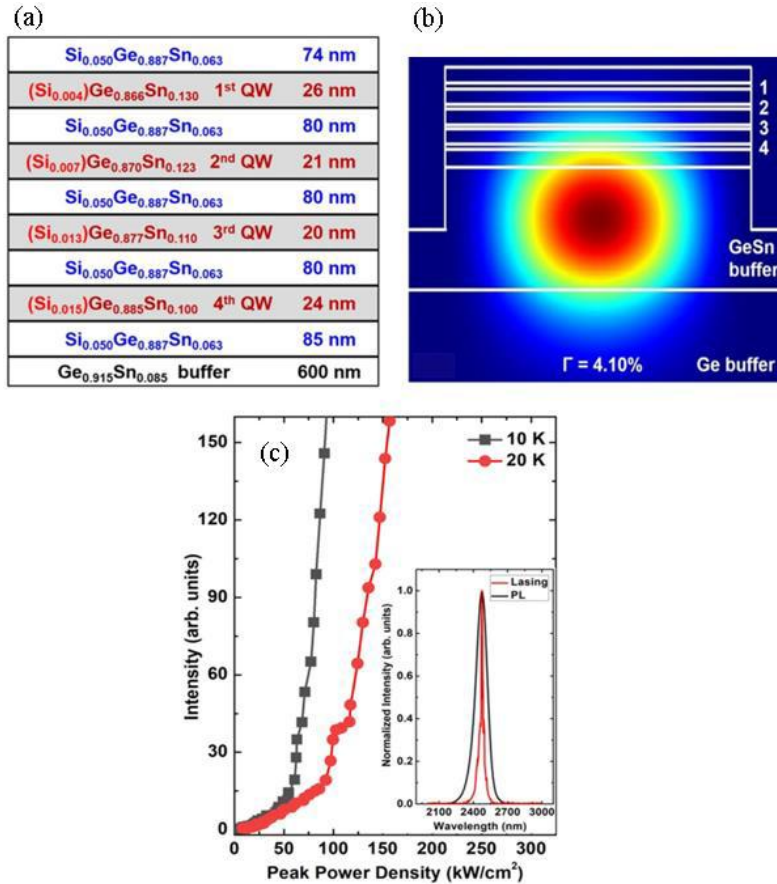


Figure 7.1: (a) Cross section of a 4QWs GeSn with SiGeSn barriers and thick GeSn buffer. (b) Calculated TE mode with an average optical confinement $\Gamma = 4.1\%$. (c) Laser-output versus pumping-laser-input of the same 4QWs sample. The inset shows the lasing and PL spectra at 10 K [120].

It has been demonstrated that double SiGeSn barrier with GeSn (SiGeSn/GeSn/SiGeSn) QW on Ge buffer provides a type-I indirect bandgap alignment with sufficiently low optical

confinement. The same study suggests that the growth of relaxed and lattice matched GeSn buffer above the Ge buffer would enhance the GeSn QW directness with sufficient optical confinement [119]. Recently, Joe et al. [120] showed that a 4QWs SiGeSn/GeSn/SiGeSn with relaxed GeSn buffer, as shown in Fig. 7.1(a), provides a total optical confinement factor of 4.1 % in the transverse electric (TE) mode of the GeSn QW regions as shown in Fig. 7.1(b). This material system exhibits lasing characteristic at low temperatures (≤ 90 K) with low lasing thresholds of 25 and 62 kW/cm² at 10 and 77K, respectively.

7.2 Experimental

In this work, a single GeSn QW with double SiGeSn barrier were grown using an industry standard ASM Epsilon[®] 2000-Plus reduced pressure chemical vapor deposition (RPCVD) system. Low-cost and commercially available SiH₄, GeH₄, and SnCl₄ precursors were used as Si, Ge, and Sn sources, respectively. Prior to QW growth, a 900-nm-thick Ge buffer layer was grown by a two-step growth method following the same procedure that was discussed in the previous chapter. In addition, a relaxed GeSn buffer was grown on the Ge buffer to allow more Sn incorporation in the GeSn well. The GeSn quantum well and the double SiGeSn barrier were grown pseudomorphically with respect to the GeSn buffer layer. After the growth, material characterizations were performed. Secondary ion mass spectroscopy (SIMS), high resolution X-ray diffraction (HRXRD) rocking curve, and reciprocal space mapping (RSM) were employed to measure Si and Sn compositions and the degree of strain of each layer. Each layer thickness was measured from cross-sectional transmission electron microscopy (TEM) images.

For optical characterization, the sample was loaded in a helium-cooled cryostat with a temperature in the range from 10 to 300 K. A 532 nm excitation laser source with an average power of 500 mW and 65 μ m spot size was focused on the SiGeSn/GeSn/SiGeSn QW sample. A

standard off-axis configuration with a lock-in technique with a 377 Hz optical chopper were used to perform low noise temperature-dependent photoluminescence (PL) measurements. PL emission was spectrally collected and analyzed by an iHR320 spectrometer that was supported by an indium antimonide (InSb) detector (high signal-to-noise ratio). The InSb detector is cooled using liquid nitrogen and has a cut-off wavelength 5 μm .

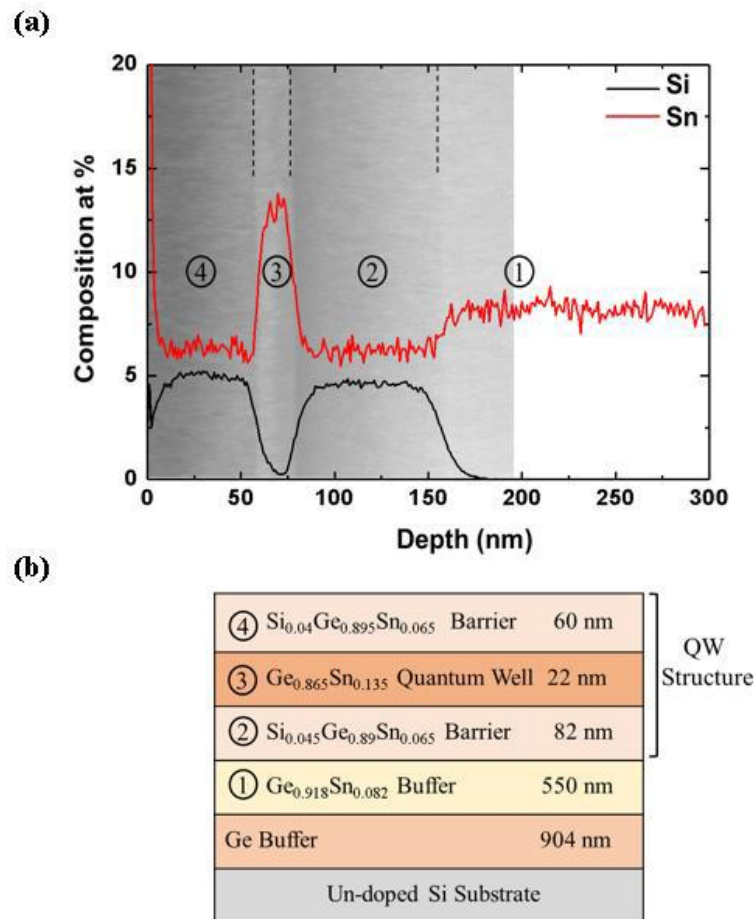


Figure 7.2: (a) SIMS profile of the sample in this study. The TEM image is overlapped with SIMS profile to illustrate the material quality of each layer. (b) Cross sections of the sample (not to scale) that summarizes the layers thicknesses and compositions. Numbers help in the identification of each layer in SIMS and TEM.

7.3 Results and Discussions

Figure 7.2(a) shows the SIMS profile and the TEM image of the SiGeSn/GeSn/SiGeSn QW sample. From SIMS, the GeSn QW incorporated a Sn amount of 13.5 % while the Sn fraction for

the GeSn buffer is 8.2 %. The compositions of Si and Sn in each SiGeSn barrier were estimated as 4 % and 6.5 %, respectively. The TEM image shows that each layer can be easily resolved. The smooth interfaces between the layers indicates a high quality material with low threading dislocations. A schematic of the sample cross section view, layers thicknesses and compositions are shown in Fig. 7.2(b).

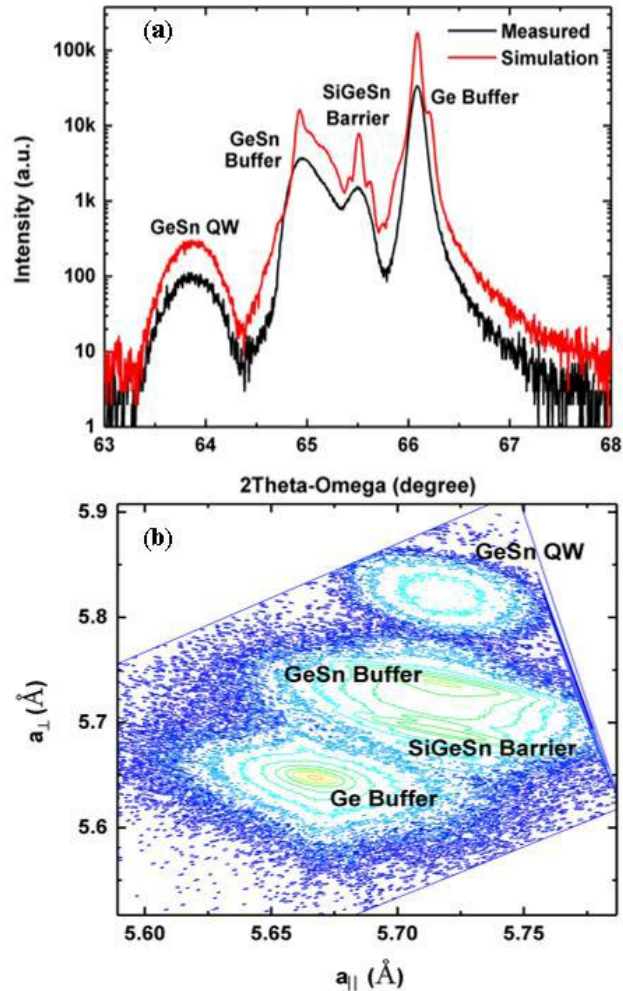


Figure 7.3: (a) Rocking curve scan of the SiGeSn/GeSn/SiGeSn QW along the (004) direction. The black and red curves show the measured and simulated data, respectively. (b) RSM plot of the sample along the asymmetrical $(\bar{2}\bar{2}4)$ plane.

The HRXRD rocking curve ($2\theta-\omega$) scan of the SiGeSn/GeSn/SiGeSn QW sample, which is measured symmetrically along the (004) plane, is shown in Fig. 7.3 (a). The measured data is plotted as black curve. The peaks of Ge, SiGeSn, and GeSn are evidently appeared. The strong

and narrow peak, which is located at $\sim 66^\circ$, is assigned to a high quality Ge buffer layer. The peak that is observed at $\sim 65.5^\circ$ corresponds to the SiGeSn barriers ($\sim 4\%$ Si and 6.5% Sn) while the lower peak at $\sim 65^\circ$ is associated to the GeSn buffer layer (8.2% Sn). The wide peak below $\sim 64^\circ$ is interrupted as a rich Sn layer, which is apparently reflected from the GeSn well (13.5% Sn). In order to conduct in-depth analysis of the SiGeSn/GeSn/SiGeSn QW sample, the XRD simulation was done. The simulation data is presented as red curve in Fig. 7.3 (a). From the simulated $2\theta-\omega$ scan curve, the lattice constant and layer thickness can be determined. The measured thickness of each layer from the simulated $2\theta-\omega$ scan is slightly consistent with TEM, indicating the precisely controlled material growth process. The RSM scan, which is measured asymmetrically along the $(\bar{2}\bar{2}4)$ plane, is shown in Fig. 7.3 (b). The figure shows a clear superposition of four layers, which correspond to the Ge buffer, the strain relaxed $\text{Ge}_{0.918}\text{Sn}_{0.082}$ buffer, the $\text{Si}_{0.04}\text{Ge}_{0.895}\text{Sn}_{0.065}$ barriers and the $\text{Ge}_{0.866}\text{Sn}_{0.135}$ well. The diffraction patterns of the GeSn QW and SiGeSn barriers indicate that they were pseudomorphically grown with the relaxed GeSn buffer.

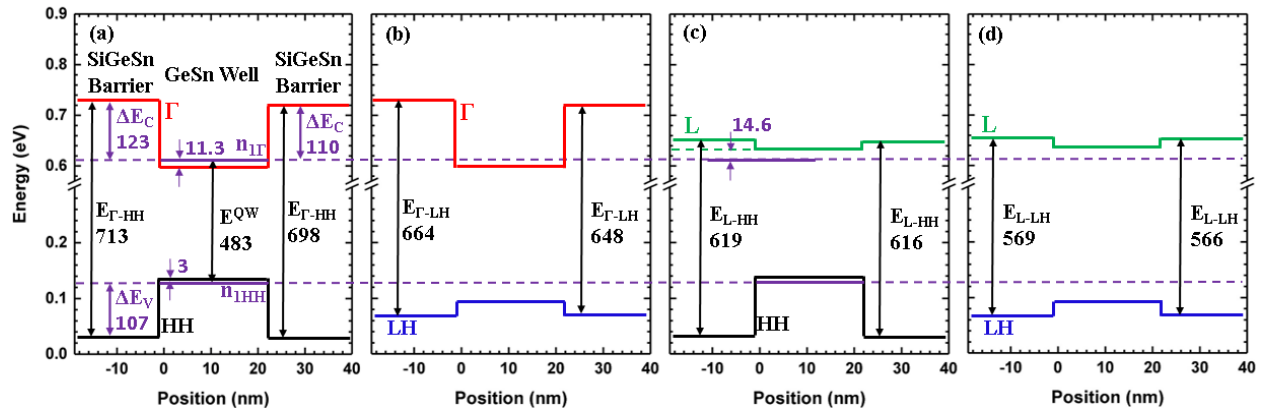


Figure 7.4: The calculated band diagram results showing the carrier confinement and the possible band-to-band optical transitions between (a) Γ -HH; (b) Γ -LH; (c) L-HH; and (d) L-LH. Units are in meV.

The band diagram of the QW sample was calculated at 300K using data from the measured QW structure. In the calculation process for both the electronic band structure and the quantized energy levels, an approximated effective mass and propagation matrix approach were used [121].

Table 7.1 lists the parameters that were used in calculating the band diagram. Bowing parameters of $b_{\Gamma} = 1.95$ and $b_L = 0.68$ with validity for Sn rich alloys were used. Strain calculations reveal $\sim 0.46\%$ tensely strained SiGeSn barriers and -0.88% compressively strained GeSn well. The first quantized energy levels ($n_{1\Gamma}$) were calculated as 11.3 meV above the Γ valley minimum and 3 meV below the heavy hole (HH) band maximum (n_{1HH}) in the conduction band (CB) and valence band (VB), respectively. The calculation methods of the band offsets for CB and VB are discussed elsewhere [19], [122]. A type-I band alignment was proven upon the calculation results in the SiGeSn/GeSn/ SiGeSn quantum structure. The results are presented in Fig. 7.4. The barrier height of each interface is shown in Fig. 7.4 (a) and (b). Due to the existence of slightly higher Si fraction in the bottom SiGeSn barrier, the barrier height between the SiGeSn bottom barrier and the GeSn well region in the conduction band (ΔE_C) was calculated as 123 meV while for the top SiGeSn it was 110 meV. The split of between the HH and the LH in the VB occurred because of the strain in the QW structure. In the VB, the calculated barrier height was 107 meV. For the L valley, the first quantized energy level (n_{1L}) was calculated to be 14.6 meV, which allows electrons in the n_{1L} to be thermally excited at room temperature to populate the L valley in the GeSn well and then populate the L valley in the bottom SiGeSn barrier. This would lead to carrier population in the L valley, which ultimately enhances the indirect radiative recombination process at room temperature. However, the 110 and 123 meV in the Γ valley provides a sufficient carrier confinement, which lowers the electron escape probability from the well sides. This will limit the chances for optical transition that could be initiated from multiple recombination mechanisms in different layers. Figure 7.4 (a) and (b) illustrates the possible transitions from the Γ valley in the CB to the HHs and LHs in the VB. In addition, phonon assisted mechanism in the indirect bandgap

transitions could occur from the L valley to the VB. Such a transitions are illustrated in Figs. 7.4 (c) and (d). The detailed transition mechanisms are discussed in the following PL section.

Table 7.1: List of parameters that were used in the band structure calculations.

Lattice constants			
	Si	Ge	Sn
a (Å)	5.4307	5.6573	6.4892
Effective mass			
	Si	Ge	Sn
$m_{e^*}\Gamma$	0.528	0.038	0.058
$m_{e,l^*}L$	1.659	1.57	1.478
$m_{e,t^*}L$	0.133	0.807	0.075
Luttinger's parameters			
	Si	Ge	Sn
Υ_1	4.22	13.38	-14.97
Υ_2	0.39	4.24	-10.61
Averaged valance band energies			
	Si	Ge	Sn
$\Delta E_{V_{av}}$	-0.48	0	0.69
Band gaps			
	Si	Ge	Sn
$E_{g\Gamma}$	4.185	0.8041	-0.413
E_{gL}	1.65	0.6637	0.092
Δ	0.044	0.29	0.8
Deformation potentials			
	Si	Ge	Sn
ac Γ	-10.06	-8.24	-6
acL	-0.66	-1.54	-2.14
av	2.46	1.24	1.58
bv	-2.1	-2.9	-2.7
Elastic Constants			
	Si	Ge	Sn
C11	165.77	0.8041	-0.413
C12	63.93	0.6637	0.092
Bowling Parameters			
	GeSn	SiGe	SiSn
$b(E_{CL})$	0.68	0.335	2.124
$b(E_{CT})$	1.95	0.21	3.915

Figure 7.5 shows the normalized temperature-dependent PL spectra of the SiGeSn/GeSn/SiGeSn QW sample. The PL results were stacked for clarity. The multipeak feature was observed

in the temperature range 300-150K. At 300K, a major peak at 2884 nm (0.43 eV, annotated as QW peak) was observed. The small and lower wavelength peak at ~ 2650 nm (0.468 eV) was attributed to the atmospheric absorption of water vapor. In addition, a peak located at wavelength position of ~ 2400 nm (0.52 eV) was observed at temperatures from 300 to 200 K. As the temperature decreases, the QW peaks are shifted toward shorter wavelengths. Compared to other reference samples, the PL spectra (not shown here) display a clear single peak and peak shift at temperatures from 300 to 10 K. The PL peak features broadened linewidth between 200 and 100K, which indicates the existence of more than a peak that were partially overlapped.

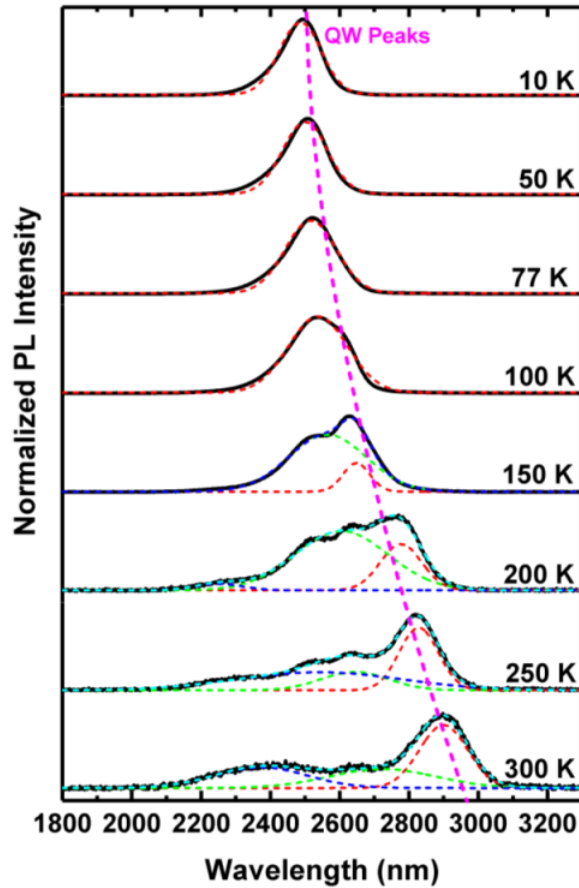


Figure 7.5: Temperature-dependent PL spectra of the SiGeSn/GeSn/SiGeSn QW sample. The dashed line is for eye guidance of the QW peak shift.

The QW peaks of the SiGeSn/GeSn/SiGeSn sample were fitted by Gaussian fitting to determine the characteristics of each peak in terms of the peak position, full width at half maximum

(FWHM), and integrated PL intensity. The results are compared with a type-I direct bandgap QW that has the same composition in the well region, but with GeSn (8.5 % Sn) double barrier [123].

The sample cross section is shown in Fig. 7.6.

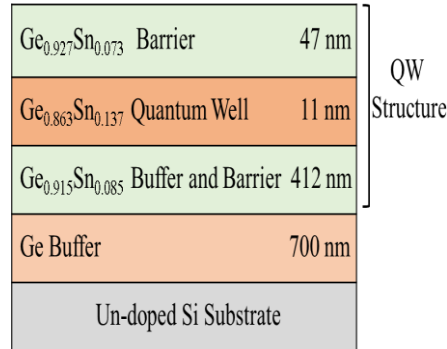


Figure 7.6: The cross section of a typical GeSn/GeSn/GeSn QW that has shown a type-I direct bandgap behavior.

Figure 7.7(a) shows a plot of peak positions from the temperature-dependent PL of the reference sample with GeSn barriers and the QW with SiGeSn barriers (this work) as a function of temperature. It is obvious that the QW peak positions with SiGeSn barriers follow a similar trend with the reference GeSn QW sample with GeSn barriers, which indicates the validity of the Gaussian fitting method. The discrepancy of energies between both samples is mainly due to the quantum confinement effect that results in the transition energy between $n_{1\Gamma}$ and n_{1HH} in the QW, which is larger in the SiGeSn barrier compared to the QW with GeSn barrier. Figure 7.7 (b) shows the FWHM of the SiGeSn/GeSn/SiGeSn QW sample compared the reference sample with GeSn barriers. Since the QW emission exhibits the narrower line-width, the FWHMs of QW peaks with SiGeSn barriers are smaller than that of the sample with GeSn barrier at 250 and 300K. However, as the temperature exceeds 250K, the FWHM of the sample with SiGeSn barriers becomes wider compared to the GeSn well with GeSn barriers. Figure 7.7 (c) shows the integrated PL intensity of the SiGeSn/GeSn/SiGeSn QW. The integrated PL intensity increases with decreasing the temperature. This is a typical behavior of a direct bandgap material. At low temperatures, defects

are frozen, which enhances the radiative recombination. When the temperature moves to higher values, the defects start to suppress the integrated PL intensity. At room temperature, the thermal energy of electrons becomes high thus the carrier population of the direct bandgap increases, which increases the radiative recombination. Compared to the sample with GeSn barriers, the integrated PL intensity is ~ 6 times higher, which indicates enhanced optical confinement when using SiGeSn as barriers.

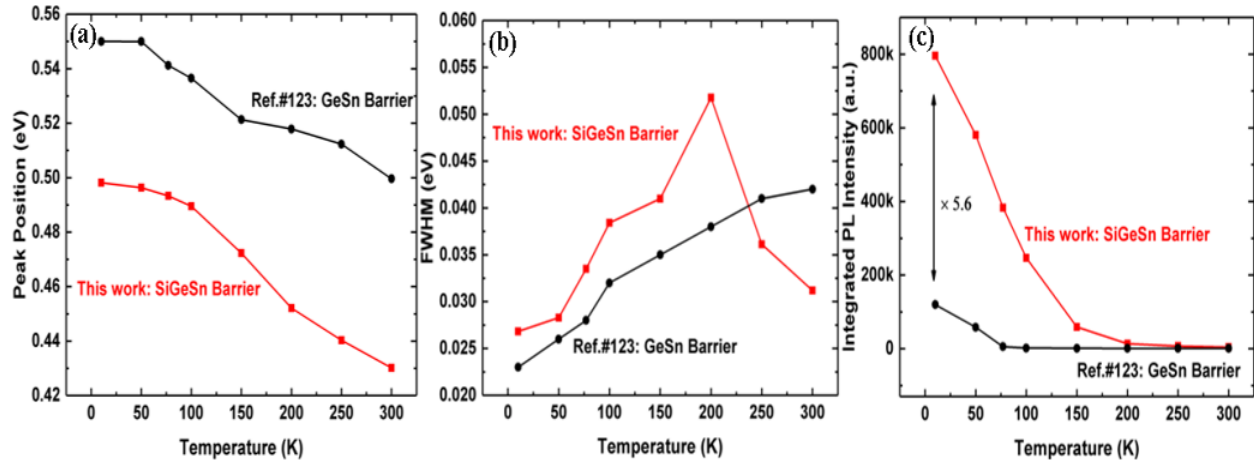


Figure 7.7: PL results of the SiGeSn/GeSn/SiGeSn sample (a) PL peak positions, (b) FWHM, and (c) integrated PL. A type-I direct bandgap GeSn/GeSn/GeSn QW is shown for comparison.

7.4 Conclusion

In conclusion, the material and optical properties of a single QW with the structure $\text{Si}_{0.045}\text{Ge}_{0.89}\text{Sn}_{0.065}/\text{Ge}_{0.865}\text{Sn}_{0.135}/\text{Si}_{0.045}\text{Ge}_{0.89}\text{Sn}_{0.065}$ was investigated. The band structure calculation and systematic PL study indicated that by using SiGeSn double barriers on a relaxed $\text{Ge}_{0.918}\text{Sn}_{0.082}$ buffer, this QW structure possesses a direct bandgap transition in the well layer and type-I band alignment. The QW emission peak at 2884 nm was observed at 300K. As the temperature decreased to 10K, the PL peak intensity of the QW increased dramatically. An optical comparison of the PL results between the $\text{Ge}_{0.865}\text{Sn}_{0.135}$ well in this study compared to a GeSn well with $\text{Ge}_{0.915}\text{Sn}_{0.085}$ barriers was also investigated. The results indicate improved optical confinement in the case of SiGeSn barrier.

Chapter 8: Summary and Future Work

8.1 Summary

This dissertation is discussing the growth and characterization of Si-Ge-Sn material system for industrial low cost and CMOS compatible Si-photonics devices. The first chapter addresses the growth of a one-step Ge films at low temperatures using plasma enhancement at 50 W in UHV-CVD system. The growth temperature was varied in the low range of 250-450°C to make this growth process compatible with the CMOS technology. The material and optical properties of the grown Ge films were investigated. They reveal growth of crystalline films in the temperature range of 350-450°C. In particular, the growth temperature at 400°C shows reasonable material and optical qualities with defect level in the intermediate range of $4.5 \times 10^8 \text{ cm}^{-2}$. This result was achieved without any material improvement steps such as graded SiGe buffer or thermal annealing. A comparison between plasma enhancement and non-plasma-enhanced growths, in the same machine at otherwise the same growth conditions was done for further conformation about the quality. The results indicate increased growth rate and improved material and optical qualities for plasma enhancement growth. The same method was used with the incorporation of Sn for GeSn/Si using plasma. The results show the growth of a single crystalline GeSn on Si substrate at low growth temperature at 350°C with the growth rate of 51.4 nm/min and Sn content up to 6%. Using this method, a relaxed GeSn films with 1 μm thickness were achieved despite of the huge lattice mismatch between GeSn and Si.

To improve the material quality of Ge for actual device applications, a two-step approach at low temperature was adopted. High quality Ge buffer layers were grown by a two-step method using plasma enhancement in UHV-CVD system. Growth of Ge buffer layers with low threading dislocation density on the order of 10^7 cm^{-2} with root mean square roughness values on the order

of several nm were achieved under low thermal budget. Photoluminescence and ellipsometry characterization reveal optical characteristics close to a Ge buffer layer grown by non-plasma enhancement method at high temperatures. Growth comparison of an active group IV layer, such as GeSn, on plasma enhancement and non-plasma enhancement Ge buffer layers was carried out to examine the material and optical stability for further device applications. Material and optical investigations indicate that the low temperature plasma enhancement method was successful due to the comparable quality of the resulting films for practical applications, could replace the high temperature non-plasma enhancement method. This work provides a promising growth process for industry to deposited Ge under conditions compatible with CMOS technology.

The structural and optical properties of bulk SiGeSn alloys had been studied. A series of SiGeSn alloys with various Si and Sn compositions and thicknesses were grown on Ge-buffered Si substrates by using low-cost commercially available SiH₄ and GeH₄ precursors in a standard industrial RP-CVD system. The material and optical investigations indicated that Si and Sn are compositional and film thickness dependent. A Si_{0.073}Ge_{0.872}Sn_{0.055} based photoconductors with two different thicknesses were demonstrated. A 1.8 μm spectral cut-off wavelength was obtained with good agreement with ellipsometry measurement results. In addition, lattice matched growths with different Si and Sn compositions were achieved for three different samples. The material and optical qualities revealed low defect with enhanced PL emission. However, further investigation indicated an indirect bandgap material. Moreover, thermal stability of a selected SiGeSn sample in harsh growth environment, such as in subsequent III-V growth, was studied for future multi-junction photovoltaic applications. In situ rapid thermal annealing at 650°C was conducted to achieve enhanced material quality and improved PL emission, which were confirmed by XRD, transmission electron microscopy, Raman, and PL measurements.

Finally, SiGeSn alloys were used as barrier in GeSn single QW to enhance the optical confinement. A $\text{Si}_{0.045}\text{Ge}_{0.89}\text{Sn}_{0.065}/\text{Ge}_{0.865}\text{Sn}_{0.135}/\text{Si}_{0.045}\text{Ge}_{0.89}\text{Sn}_{0.065}$ quantum structure was grown on relaxed GeSn buffer using industrial standard RP-CVD and low-cost commercially available SiH_4 and GeH_4 . A direct bandgap $\text{Ge}_{0.865}\text{Sn}_{0.135}$ QW was achieved that was impossible to achieve if only a Ge buffer was used. In addition, the quantum well features a type-I band alignment as revealed from band structure calculations and optical transition analysis. The intensity of the PL spectra of the QW peaks were dramatically increased at low PL temperatures. This optical feature confirmed that the $\text{Ge}_{0.865}\text{Sn}_{0.135}$ QW is a direct bandgap material. In addition, a PL comparison with a similar QW sample that has a GeSn barriers revealed enhanced optical confinement.

8.2 Future Work

8.2.1 Plasma Enhancement UHV-CVD

The plasma enhancement in UHV-CVD system shows significant potential that could be utilized to grow future Si-photonics monolithically with CMOS devices. However, this growth technique was only used in this study to grow Ge buffer layer with preliminary GeSn growth investigation.

Future growth and characterization study could be dedicated to the following:

1. Plasma enhanced GeSn study can be further extended using the results from non-plasma enhancement growth window as a baseline to grow high quality GeSn in the UHV-CVD system. The ultimate goal of this point is to grow the structure GeSn/Ge buffered Si substrate with high quality GeSn and high Sn incorporation all by plasma enhancement at $T < 400^\circ\text{C}$. The high growth rate can be utilized to grow thick and relaxed GeSn layer, which enhances Sn incorporation.
2. Plasma enhancement could be also used to grow low temperature SiGe alloys. However, this task is little bit complicated compared to the previous point. In addition to the flow

rate optimization control, SiH_4 decomposes at high temperatures, which will increase the low temperature bar.

3. The results from above can be used an approach to grow SiGeSn on Ge buffered Si substrate. In addition, SiGeSn barriers in GeSn QW structures could also be grown in UHV-CVD using the growth capability of plasma enhancement at low temperatures.

8.2.2 Hot-Filament

Hot-filament is another method that helps in the decomposition of CVD reactants at low substrate temperatures. A schematic of the hot-filament feature in the UHV-CVD system is shown in Fig. 8.1. The gas entry tube is equipped with a hot tungsten filament that is connected to a power source. The power source supplies the tungsten filament with electrical current that can produce high temperatures in the gas entry tube from 1400 to 2100°C. This amount of temperature is fairly enough to dissociate precursors before reaching the substrate.



Figure 8.1: Schematic diagram of the hot-filament design in the UHV-CVD system.

References

- [1] Y. Vlasov, W. M. J. Green, F. Xia, “High-throughput silicon nanophotonic wavelength-insensitive switch for on-chip optical networks,” *Nat. Photonics*, vol. 2, pp. 242-246, April 2008.
- [2] Editorial, “Simply silicon,” *Nat. Photonics*, vol. 4, pp. 491, Aug. 2010.
- [3] J. Leuthold, C. Koos, W. Freude, “Nonlinear silicon photonics,” *Nat. Photonics*, vol. 4, pp. 535-544, Aug. 2010.
- [4] G. T. Reed and C. E. Jason Png “Silicon optical modulators,” *Materials Today*, vol. 8, no.1, pp. 40-50, January 2005.
- [5] R. Soref, D. Buca, and S.-Q. Yu, “Group IV Photonics: Driving Integrated Optoelectronics,” *Opt. Photonics News*, vol. 27, no. 1, pp. 32-39, Jan. 2016.
- [6] D. Thomson, A. Zilkie, J. E Bowers, T. Komljenovic, G. T Reed, L. Vivien, D. Marris-Morini, E. Cassan, L. Viot, J.-M. Fédéli, J.-M. Hartmann, J. H. Schmid, D.-X. Xu, F. Boeuf, P. O’Brien, G. Z. Mashanovich, M. Nedeljkovic, “Roadmap on silicon photonics,” *Journal of Optics*, vol. 18, pp. 073003, 2016.
- [7] X. Wang, J. Liu, “Emerging technologies in Si active photonics,” *Journal of Semiconductors*, vol. 39, no. 6, pp. 061001, June 2018.
- [8] M. Asghari, A. V. Krishnamoorthy, “Silicon photonics Energy-efficient communication,” *Nat. Photonics*, vol. 5, pp. 268-270, May 2011.
- [9] W. Bogaerts, M. Fiers, P. Dumon, “Design Challenges in Silicon Photonics,” *IEEE Journal of Selected Topics in Quantum Electronics*, vol. 20, no. 4, pp. 8202008, July/August 2014.
- [10] R. A. Soref and C. H. Perry, “Predicted band gap of the new semiconductor SiGeSn,” *J. Appl. Phys.*, vol. 69, no. 1, pp. 539–541, 1991.
- [11] R. A. Soref and L. Friedman, “Direct-gap Ge/GeSn/Si and GeSn/Ge/Si heterostructures,” *Superlattices Microstruct.*, vol. 14, no. 2–3, p. 189, Sep. 1993.
- [12] Silicon waveguided components for the long-wave infrared region,” *Journal of Optics A: Pure and Applied Optics*, vol. 8, pp. 840-848, 2006.
- [13] L. Tsybeskov, D. J. Lockwood, M. Ichikawa, “Silicon Photonics: CMOS Going Optical,” *Proceedings of the IEEE*, vol. 97, no. 7, pp. 1161-1165, July 2009.
- [14] T. Pham, W. Du, H. Tran, J. Margetis, J. Tolle, G. Sun, R. A. Soref, H. A. Naseem, B. Li, and S.-Q. Yu, “Systematic study of Si-based GeSn photodiodes with 2.6 μm detector cutoff for short-wave infrared detection,” *Opt. Express*, vol. 24, no. 5, pp. 4519–4531, 2016.

- [15] S. Wirths, R. Geiger, N. Von Den Driesch, G. Mussler, T. Stoica, S. Mantl, Z. Ikonic, M. Luysberg, S. Chiussi, J. M. Hartmann, H. Sigg, J. Faist, D. Buca, D. Grutzmacher, "Lasing in direct-bandgap GeSn alloy grown on Si," *Nat. Photonics*, vol. 9, no. 2, pp. 88–92, 2015.
- [16] S. Al-Kabi, S. A. Ghetmiri, J. Margetis, T. Pham, Y. Zhou, W. Dou, B. Collier, R. Quinde, W. Du, A. Mosleh, J. Liu, G. Sun, R. A. Soref, J. Tolle, B. Li, M. Mortazavi, H. A. Naseem, and S.-Q. Yu, "An optically pumped 2.5 μm GeSn laser on Si operating at 110 K," *Appl. Phys. Lett.*, vol. 109, no. 17, p. 171105, Oct. 2016.
- [17] N. von den Driesch, D. Stange, S. Wirths, D. Rainko, I. Povstugar, A. Savenko, U. Breuer, R. Geiger, H. Sigg, Z. Ikonic, J.-M. Hartmann, D. Grützmacher, S. Mantl, and D. Buca, "SiGeSn Ternaries for Efficient Group IV Heterostructure Light Emitters," *Small* 13(16), 1603321 (2017).
- [18] J. Tolle, R. Roucka, A. Chizmeshya, J. Kouvetakis, V. R. D'Costa, and J. Menéndez, "Compliant tin-based buffers for the growth of defect-free strained heterostructures on silicon," *Appl. Phys. Lett.* 88(25), 252112(2006).
- [19] G. Sun, R. Soref, and H. Cheng, "Design of an electrically pumped SiGeSn/GeSn/SiGeSn double-heterostructure midinfrared laser," *J. Appl. Phys.* 108(3), 033107 (2010).
- [20] M. Fleischer, "The Abundance and Distribution of the Chemical Elements in the Earth's Crust," *Journal of Chemistry Education*, vol. 31, p. 446, 1954.
- [21] W. Maly, "Cost of Silicon Viewed from VLSI Design Perspective," Carnegie Mellon University, Pittsburgh, Pennsylvania.
- [22] M. Cooke, "Pseudo-direct gaps for efficient light emission and absorption," *Semiconductor Today*, 2014.
- [23] M. J. Suess, R. Geiger, R. A. Minamisawa, G. Schiefler, J. Frigerio, D. Chrastina, G. Isella, R. Spolenak, J. Faist, H. Sigg, "Analysis of enhanced light emission from highly strained germanium microbridges," *Nat. Photonics*, vol. 7, pp. 466-472, June 2013.
- [24] M. L. Lee, C. W. Leitz, Z. Cheng, A. J. Pitera, T. Langdo, M. T. Currie, G. Taraschi, E. A. Fitzgerald, D. A. Antoniadis "Strained Ge channel p-type metal–oxide–semiconductor field-effect transistors grown on Si_{1-x}Gex/Si virtual substrates," *Appl. Phys. Lett.*, vol. 79, no. 20, pp. 3344-3346, November 2001.
- [25] G. E. Stillman, V. M. Robbins, N. Tabatabaie, "III-V Compound Semiconductor Devices: Optical Detectors," *IEEE Transactions on Electron Devices*, vol. ED-31, no. 11, November 1984.
- [26] S. Fama, L. Colace, G. Masini, G. Assanto, H.-C. Luan, "High performance germanium-on-silicon detectors for optical communications," *Appl. Phys. Lett.*, vol. 81, no. 4, pp. 586-588, July 2002.
- [27] Bean, J. C., "Strained-Layer Epitaxy of Germanium-Silicon Alloys," *Science* 1985, 230, 127–131.

- [28] M. T. Currie, S. B. Samavedam, T. A. Langdo, C. W. Leitz, and E. A. Fitzgerald, "Controlling threading dislocation densities in Ge on Si using graded SiGe layers and chemical-mechanical polishing," *Appl. Phys. Lett.*, vol. 72, no. 14, pp. 1718-1720, April 1998.
- [29] J. M. Hartmann, A. Abbadie, A. M. Papon, P. Holliger, G. Rolland, T. Billon, J. M. Fedeli, M. Rouviere, L. Vivien, and S. Laval, "Reduced pressure-chemical vapor deposition of Ge thick layers on Si(001) for 1.3-1.55 μm photodetection," *J. Appl. Phys.*, vol. 95, no. 10, pp. 5905-5913, 2004.
- [30] D. J. Eaglesham and M. Cerullo, "Dislocation-Free Stranski-Krastanow Growth of Ge on Si(100)," *Phys. Rev. Lett.*, vol. 64, no. 16, pp. 1943 - 1950, 1990.
- [31] J. Michel, J. Liu, and L. C. Kimerling, "High-performance Ge-on-Si photodetectors," *Nat. Photonics* 4, 527 (2010).
- [32] M. T. Currie, S. B. Samavedam, T. A. Langdo, C. W. Leitz, and E. A. Fitzgerald, *Appl. Phys. Lett.* 72, 1718 (1998).
- [33] B. Cunningham, J. O. Chu, and S. Akbar, "Heteroepitaxial growth of Ge on (100) Si by ultrahigh vacuum, chemical vapor deposition," *Appl. Phys. Lett.*, vol. 59, no. 27, pp. 3574-3576, December 1991.
- [34] A. Baskaran and P. Smereka, "Mechanisms of Stranski-Krastanov growth," *Journal of Applied Physics*, vol. 111, no. 4, pp. 044321, February 2012.
- [35] G. Dehlinger, S. J. Koester, J. D. Schaub J. O. Chu, Q. C. Ouyang, A. Grill, "High-Speed Germanium-on-SOI lateral PIN photodiodes," *IEEE Photonics Technology Letters*, vol. 16, no. 11, pp. 2547-2549, November 2004.
- [36] Y. Bogumilowicz, J.M. Hartmann, C. Di Nardo, P. Holliger, A.-M. Papon, G. Rolland, T. Billon, "High-temperature growth of very high germanium content SiGe virtual substrates," *Journal Crystal Growth*, vol. 29, pp. 523-531, 2006.
- [37] A. Nayfeh, C. O.Chui, K. C. Saraswat, and T. Yonehara, "Effects of hydrogen annealing on heteroepitaxial-Ge layers on Si: Surface roughness and electrical quality," *Appl. Phys. Lett.*, vol. 85, no. 14, October 2004.
- [38] L. Colace, G. Masini, F. Galluzzi, G. Assanto, G. Capellini, L. Di Gaspare, E. Palange, F. Evangelisti, "Metal–semiconductor–metal near-infrared light detector based on epitaxial Ge/Si," *Appl. Phys. Lett.*, vol. 72, no. 24, pp. 3175-3177, June 1998.
- [39] J.M. Hartmann, J.-F. Damlencourt, Y. Bogumilowicz, P. Holliger, G. Rolland, T. Billon, "Reduced pressure-chemical vapor deposition of intrinsic and doped Ge layers on Si(0 0 1) for microelectronics and optoelectronics purposes," *Journal Crystal Growth*, vol. 274, pp. 90-99, 2005.

- [40] H.-C. Luan, D. R. Lim, K. K. Lee, K. M. Chen, J. G. Sandland, K. Wada, L. C. Kimerling, "High-quality Ge epilayers on Si with low threading-dislocation densities," *Appl. Phys. Lett.*, vol. 75, no. 19, pp. 2909-2911, November 1999.
- [41] K. H. Lee, S. Bao, G. Y. Chong, Y. H. Tan, E. A. Fitzgerald, C. S. Tan, "Defects reduction of Ge epitaxial film in a germanium-on-insulator wafer by annealing in oxygen ambient" *Appl. Phys. Lett. Materials*, vol. 3, p. 016102, 2015.
- [42] J. Wang, S. Lee, "Ge-Photodetectors for Si-Based Optoelectronic Integration," *Sensors*, vol. 11, pp. 696-718, 2011.
- [43] W. J. Varhue, J. M. Carulli, G. G. Peterson, and J. A. Miller, "Low temperature epitaxial growth of Ge using electron-cyclotron-resonance plasma-assisted chemical vapor deposition," *J. Appl. Phys.* 71, 1949 (1992).
- [44] C. G. Littlejohns, A. Z. Khokhar, D. J. Thomson, Y. Hu, L. Basset, S. A. Reynolds, G. Z. Mashanovich, G. T. Reed, and F. Y. Gardes, *IEEE Photonics Journal* 7, 1 (2015).
- [45] G. Dushaq, M. Rasras, and A. Nayfeh, "Low temperature deposition of germanium on silicon using radio frequency plasma enhanced chemical vapor deposition," *Thin Solid Films*, vol. 636, no. 31, pp. 585-592, August 2017.
- [46] E. A. Douglas, J. J. Sheng, J. C. Verley, and M. S. Carroll, "Argon-germane in situ plasma clean for reduced temperature Ge on Si epitaxy by high density plasma chemical vapor deposition," *J. Vac. Sci. Technol. B*, vol. 33, no. 4, pp. 041202, August 2015.
- [47] S. Groves and W. Paul, "Band Structure of Gray Tin," *Physical Review Letters*, vol. 11, no. 5, pp. 194-196, 1963.
- [48] R. Farrow, "The stabilization of metastable phases by epitaxy," *Journal of Vacuum Science and Technology B*, vol. 1, pp. 222 - 228, 1983.
- [49] R. Farrow, D. Robertson, G. Williams, A. Cullis, I. Y. G.R. Jones and P. Dennis, "The growth of metastable, heteroepitaxial films of α -Sn by metal beam epitaxy," *Journal of Crystal Growth*, vol. 54, pp. 507-518, 1981.
- [50] J. Menendez, K. Sinha, H. Hochst and M. A. Engelhardt, "Phonons in epitaxially grown α -Sn_{1-x}Ge_x alloys," *Appl. Phys. Lett.* 57, no. 380, 1998.
- [51] C. H. L. Goodman, "Direct-gap group IV semiconductors based on tin," *IEEE Proc.* 129, 1982.
- [52] J. Kouvetakis, J. Menendez and A. Chizmeshya, "Tin-based group IV semiconductors: New platform for opto- and microelectronics on silicon," *Annual Reviews*, vol. 36, pp. 497-554, 2006.
- [53] G.-E. Chang, S.-W. Chang, and S. L. Chuang, "Strain-Balanced Ge_zSn_{1-z}/SixGe_ySn_{1-x-y} Multiple-Quantum-Well Lasers," *IEEE J. Quantum Electron.*, vol. 46, no. 12, pp. 1813-1820, 2010.

- [54] R. Beeler, R. Roucka, A. V. G. Chizmeshya, J. Kouvetakis, and J. Menéndez, “Nonlinear structure-composition relationships in the $\text{Ge}_{1-y}\text{Sn}_y/\text{Si}(100)$ ($y < 0.15$) system,” *Phys. Rev. B*, vol. 84, no. 3, p. 035204, July 2011.
- [55] P.R. Pukite, A. Harwit, S.S. Iyer, “Molecular beam epitaxy of metastable, diamond structure $\text{Sn}_x\text{Ge}_{1-x}$ alloys,” *Appl. Phys. Lett.*, vol. 54, no. 21, pp. 2142-2144, 1989.
- [56] H. Li, C. Chang, T. P. Chen, H. H. Cheng, Z. W. Shi, and H. Chen, “Characteristics of Sn segregation in Ge/GeSn heterostructures,” *Appl. Phys. Lett.*, vol. 105, no. 15, pp. 1–4, 2014.
- [57] H. Li, C. Chang, T. P. Chen, H. H. Cheng, Z. W. Shi, and H. Chen, “Characteristics of Sn segregation in Ge/GeSn heterostructures,” *Appl. Phys. Lett.*, vol. 105, no. 15, pp. 1–4, 2014.
- [58] S. Gupta, R. Chen, B. Magyari-Kope, H. Lin, Bin Yang, A. Nainani, Y. Nishi, J. S. Harris, and K. C. Saraswat, “GeSn technology: Extending the Ge electronics roadmap,” in 2011 International Electron Devices Meeting, 2011, p. 16.6.1-16.6.4.
- [59] R. Hickey, N. Fernando, S. Zollner, J. Hart, R. Hazbun, and J. Kolodzey, “Properties of pseudomorphic and relaxed germanium $_{1-x}$ tin x alloys ($x < 0.185$) grown by MBE,” *J. Vac. Sci. Technol. B, Nanotechnol. Microelectron. Mater. Process. Meas. Phenom.*, vol. 35, no. 2, p. 021205, Mar. 2017.
- [60] L. Kormoš, M. Kratzer, K. Kostecki, M. Oehme, T. Šikola, E. Kasper, J. Schulze, and C. Teichert, “Surface analysis of epitaxially grown GeSn alloys with Sn contents between 15% and 18%,” *Surf. Interface Anal.*, vol. 49, no. 4, pp. 297–302, Apr. 2017.
- [61] W. Wang, Q. Zhou, Y. Dong, E. S. Tok, and Y.-C. Yeo, “Critical thickness for strain relaxation of $\text{Ge}_{1-x}\text{Sn}_x$ ($x \leq 0.17$) grown by molecular beam epitaxy on Ge(001),” *Appl. Phys. Lett.*, vol. 106, no. 23, p. 232106, Jun. 2015.
- [62] H. Lin, R. Chen, W. Lu, Y. Huo, T. Kamins, and J. Harris, “Structural and optical characterization of $\text{Si}_x\text{Ge}_{1-x-y}\text{Sn}_y$ alloys grown by molecular beam epitaxy,” *Appl. Phys. Lett.* 100(14), 141908 (2012).
- [63] J. Zheng, S. Wang, T. Zhou, Y. Zuo, B. Cheng, and Q. Wang, “Single-crystalline $\text{Ge}_{1-x-y}\text{Si}_x\text{Sn}_y$ alloys on Si (100) grown by magnetron sputtering,” *Opt. Mater. Express* 5(2), 287–294 (2015).
- [64] P. M. Wallace, C. L. Senaratne, C. Xu, P. E. Sims, J. Kouvetakis, and J. Menéndez, “Molecular epitaxy of pseudomorphic $\text{Ge}_{1-y}\text{Sn}_y$ ($y = 0.06-0.17$) structures and devices on Si/Ge at ultra-low temperatures via reactions of Ge_4H_{10} and SnD_4 ,” *Semicond. Sci. Technol.*, vol. 32, no. 2, p. 025003, Feb. 2017.
- [65] R. Chen, S. Gupta, Y.-C. Huang, Y. Huo, C. W. Rudy, E. Sanchez, Y. Kim, T. I. Kamins, K. C. Saraswat, and J. S. Harris, “Demonstration of a Ge/GeSn/Ge Quantum-Well Microdisk Resonator on Silicon: Enabling High-Quality Ge(Sn) Materials for Micro- and Nanophotonics,” *Nano Lett.*, vol. 14, no. 1, pp. 37–43, Jan. 2014.

- [66] W. Dou, M. Benamara, A. Mosleh, J. Margetis, P. Grant, Y. Zhou, S. Al-Kabi, W. Du, J. Tolle, B. Li, M. Mortazavi, and S.-Q. Yu, “Investigation of GeSn Strain Relaxation and Spontaneous Composition Gradient for Low-Defect and High-Sn Alloy Growth,” *Sci. Rep.*, vol. 8, no. 1, p. 5640, Dec. 2018.
- [67] N. von den Driesch, D. Stange, S. Wirths, D. Rainko, I. Povstugar, A. Savenko, U. Breuer, R. Geiger, H. Sigg, Z. Ikonc, J.-M. Hartmann, D. Grützmacher, S. Mantl, and D. Buca, “SiGeSn Ternaries for Efficient Group IV Heterostructure Light Emitters,” *Small* 13(16), 1603321 (2017).
- [68] H. H. Radamson, M. Noroozi, A. Jamshidi, P. E. Thompson, and M. Östling, “Strain engineering in GeSnSi materials,” *ECS Trans.* 50(9), 527–531 (2013).
- [69] L. Jiang, C. Xu, J. D. Gallagher, R. Favaro, T. Aoki, J. Menéndez, and J. Kouvetakis, “Development of Light Emitting Group IV Ternary Alloys on Si Platforms for Long Wavelength Optoelectronic Applications,” *Chem.Mater.* 26(8), 2522–2531 (2014).
- [70] Y. Bogumilowicz, J. M. Hartmann, R. Truche, Y. Campidelli, G. Rolland, and T. Billon, “Chemical vapour etching of Si, SiGe and Ge with HCl; applications to the formation of thin relaxed SiGe buffers and to the revelation of threading dislocations,” *Semicond. Sci. Technol.*, vol. 20, no. 2, pp. 127–134, Feb. 2005.
- [71] J. Mathews, R. T. Beeler, J. Tolle, C. Xu, R. Roucka, J. Kouvetakis, and J. Meñdez, “Direct-gap photoluminescence with tunable emission wavelength in Ge 1-y Sny alloys on silicon,” *Appl. Phys. Lett.*, vol. 97, no. 22, pp. 19–22, 2010.
- [72] E. Kasper, J. Werner, M. Oehme, S. Escoubas, N. Burle, and J. Schulze, “Growth of silicon based germanium tin alloys,” *Thin Solid Films*, vol. 520, no. 8, pp. 3195–3200, Feb. 2012.
- [73] M.-Y. Ryu, T. R. Harris, Y. K. Yeo, R. T. Beeler, and J. Kouvetakis, “Temperature-dependent photoluminescence of Ge/Si and Ge_{1-y}Sn_y/Si, indicating possible indirect-to-direct bandgap transition at lower Sn content,” *J. Appl. Phys.*, vol. 102, pp. 171908, 2013.
- [74] S. A. Ghetmiri, W. Du, J. Margetis, A. Mosleh, L. Cousar, B. R. Conley, L. Domulevicz, A. Nazzal, G. Sun, R. A. Soref, J. Tolle, B. Li, H. A. Naseem, S. -Q. Yu, “Direct-bandgap GeSn grown on silicon with 2230 nm photoluminescence,” *Appl. Phys. Lett.*, vol. 105, no. 15, p. 151109, 2014.
- [75] F. Gencarelli, B. Vincent, J. Demeulemeester, A. Vantomme, A. Moussa, A. Franquet, A. Kumar, H. Bender, J. Meersschaut, W. Vandervorst, R. Loo, M. Caymax, K. Temst, and M. Heyns, “Crystalline Properties and Strain Relaxation Mechanism of CVD Grown GeSn,” *ECS J. Solid State Sci. Technol.*, vol. 2, no. 4, pp. P134–P137, Jan. 2013.
- [76] C. L. Senaratne, J. D. Gallagher, T. Aoki, and J. Kouvetakis, “Advances in Light Emission from Group-IV Alloys via Lattice Engineering and n-Type Doping Based on Custom-Designed Chemistries,” *Chem. Mater.*, vol. 26, pp. 6033–6041, 2014.

- [77] T. R. Harris, Y. K. Yeo, M-Y Ryu, R. T. Beeler, and J. Kouvetakis “Observation of heavy- and light-hole split direct bandgap photoluminescence from tensile-strained GeSn (0.03% Sn),” *J. Appl. Phys.*, vol. 116, pp. 103502, 2014.
- [78] G. He and H. A. Atwater, “Interband Transitions in $\text{Sn}_x\text{Ge}_{1-x}$ Alloys,” *Phys. Rev. Lett.*, Vol. 79, no. 10, pp. 1937-1940, Sep. 1997.
- [79] K. Alberi, J. Blacksberg, L.D. Bell, S. Nikzad, K.M. Yu, O.D. Dubon, W. Walukiewicz, “Band anticrossing in highly mismatched $\text{Sn}_x\text{Ge}_{1-x}$ semiconducting alloys,” *Phys. Rev. B* 77, p.p. 073202, 2008.
- [80] L. Jiang, C. Xu, J. D. Gallagher, R. Favaro, T. Aoki, J. Menéndez, J. Kouvetakis, Development of Light Emitting Group IV Ternary Alloys on Si Platforms for Long Wavelength Optoelectronic Applications,” *Chem. Mater.*, vol. 26, pp. 2522–2531, Jul. 2014.
- [81] V. R. D’Costa, Y.-Y. Fang, J. Tolle, J. Kouvetakis, and J. Mene’ndez, “Tunable Optical Gap at a Fixed Lattice Constant in Group-IV Semiconductor Alloys,” *Phys. Rev. Lett.*, vol. 102, pp. 107403, Mar. 2009.
- [82] Z. Alferov, “Double heterostructure lasers: Early days and future perspectives,” *IEEE J. Sel. Top. Quantum Electron.*, vol. 6, no. 6, pp. 832–840, 2000.
- [83] B. Schwartz, M. Oehme, K. Kostecky, D. Widmann, M. Gollhofer, R. Koerner, S. Bechler, I. A. Fischer, T. Wendav, E. Kasper, J. Schulze, M. Kittler, “Electroluminescence of GeSn/Ge MQW LEDs on Si substrate,” *Opt. Lett.*, vol. 40, no. 13, pp. 3209–3212, 2015.
- [84] D. Stange, N. von den Driesch, D. Rainko, C. Schulte-Braucks, S. Wirths, G. Mussler, A. T. Tiedemann, T. Stoica, J. M. Hartmann, Z. Ikonik, S. Mantle, D. Grutzmacher, D. Buca, “Study of GeSn based heterostructures: towards optimized group IV MQW LEDs,” *Opt. Express*, vol. 24, no. 2, pp. 1358–1367, 2016.
- [85] G.-E. Chang, S.-W. Chang, and S. L. Chuang, “Strain-Balanced $\text{Ge}_z\text{Sn}_{1-z}/\text{Si}_x\text{Ge}_y\text{Sn}_{1-x-y}$ Multiple-Quantum-Well Lasers,” *IEEE J. Quantum Electron.*, vol. 46, no. 12, pp. 1813–1820, 2010.
- [86] G. Sun, R. A. Soref, and H. H. Cheng, “Design of a Si-based lattice-matched room-temperature GeSn/GeSiSn multi-quantum-well mid-infrared laser diode,” *Opt. Express*, vol. 18, no. 19, p. 19957, Sep. 2010.
- [87] G. Sun, R. A. Soref, and H. H. Cheng, “Design of an electrically pumped SiGeSn/GeSn/SiGeSn double-heterostructure midinfrared laser,” *J. Appl. Phys.*, vol. 108, no. 3, p. 033107, 2010.
- [88] S. Sivaram, “Chemical vapor deposition: thermal and plasma deposition of electronic materials,” Springer, 1995.
- [89] Y. Xu, X.-T. Yan, “Chemical vapour deposition: An integrated engineering design for advanced materials,” Springer, 2010.

- [90] H. O. Pierson, "Handbook of chemical vapor deposition: Principles, technology, and applications," Noyes Publications, 1999.
- [91] Instruction Manual, 4" Epicentre Stage, UHV Design Ltd.
- [92] M. A. Lieberman, A. J. Lichtenberg, "Principles of plasma discharges and materials processing," John Wiley & Sons, Inc., 2005.
- [93] M. Erdtmann, T. A. Langdo, "The Crystallographic Properties of Strained Silicon Measured by X-Ray Diffraction," *J Mater Sci: Mater Electron*, vol. 17, pp. 137-147, 2006.
- [94] D. K. Schroder, "Semiconductor material and device characterization," John Wiley & Sons, Inc., 2006.
- [95] W. Du, S. A. Ghetmiri, J. Margetis, S. Al-Kabi, Y. Zhou, J. Liu, G. Sun, R. A. Soref, J. Tolle, B. Li, M. Mortazavi, and S.-Q. Yu, "Investigation of optical transitions in a SiGeSn/GeSn/SiGeSn single quantum well structure," *J. Appl. Phys.*, vol. 122, p. 123102, 2017.
- [96] L. Bing-Chi, L. Kai, K. Xiao-Li, Z. Ji-Qiang, H. Yu-Dan, L. Jiang-Shan, W. Wei-Dong, T. Yong-Jian, "Sputtering pressure influence on growth morphology, surface roughness, and electrical resistivity for strong anisotropyberyllium film," *Chin. Phys. B*, vol. 23, no. 6, pp. 066804, April 2014.
- [97] D. Chen, Z. Xue, X. Wei, G. Wang, L. Ye, M. Zhang, D Wang, S. Liu, "Ultralow temperature ramping rate of LT to HT for the growth of high quality Ge epilayer on Si (100) by RPCVD," *Appl. Surf. Sci.*, vol. 299, pp.1-5, 2014.
- [98] C. Xu, R.T. Beeler, L. Jiang, G. Grzybowski, A.V.G. Chizmeshya, J. Menendez, J. Kouvetakis, "New strategies for Ge-on-Si materials and devices using non-conventional hydride chemistries: the tetragermane case," *Semicond. Sci. Technol.*, vol. 28, pp. 105001, July 2013.
- [99] D. Choi, Y. Ge, J.S. Harris, J. Cagnon, S. Stemmer, "Low surface roughness and threading dislocation density Ge growth on Si (001)," *J. Cryst. Growth*, vol. 310, pp. 4273-4279, July 2008.
- [100] C. Chen, C. Li, S. Huang, Y. Zheng, H. Lai, S. Chen, "Epitaxial growth of germanium on silicon for light emitters," *Int. J. Photoenergy*, vol. 2012, pp. 1-8, 2012.
- [101] C.G. Littlejohns, A.Z. Khokhar, D.J. Thomson, Y. Hu, L. Basset, S.A. Reynolds, G.Z. Mashanovich, G.T. Reed, and F.Y. Gardes, "Ge-on-Si plasma-enhanced chemical vapor deposition for low-cost photodetectors," *IEEE Photonics J.*, vol. 7, no. 1, pp. 6802408, August 2015.
- [102] X. Jiang, W. J. Zhang, M. Paul, C.-P. Klages, "Diamond film orientation by ion bombardment during deposition," *Appl. Phys. Lett.*, vol. 68, no. 14, pp. 1927-1929, 1996.
- [103] M. Schreck, S. Gsell, R. Brescia, and M. Fischer, "Ion bombardment induced buried lateral growth: the key mechanism for the synthesis of single crystal diamond wafers," *Scientific Reports*, vol. 7, pp. 1-8, March 2017.

- [104] J. Hart, R. Hazbun, D. Eldridge, R. Hickey, N. Fernando, T. Adamc, S. Zollner, and J. Kolodzey, "Tetrasilane and digermane for the ultra-high vacuum chemical vapor deposition of SiGe alloys," *Thin Solid Films*, vol. 604, pp. 23–27, March 2016.
- [105] Y.H. Tan and C.S. Tan, "Growth and characterization of germanium epitaxial film on silicon (001) using reduced pressure chemical vapor deposition," *Thin Solid Films*, vol. 520, pp. 2711–2716, November 2011.
- [106] T.-H. Cheng, K.-L. Peng, C.-Y. Ko, C.-Y. Chen, H.-S. Lan, Y.-R. Wu, C. W. Liu, and H.-H. Tseng, "Strain-enhanced photoluminescence from Ge direct transition," *Appl. Phys. Lett.*, vol. 96, pp. 211108, May 2010.
- [107] S. Saito, F. Yannick Gardes, A. Z. Al-Attili, K. Tani, K. Oda, Y. Suwa, T. Ido, Y. Ishikawa, S. Kako, S. Iwamoto, and Y. Arakawa, "Group IV light sources to enable the convergence of photonics and electronics," *Frontiers in Materials*, vol. 1, no. 15, pp. 1-15, September 2014.
- [108] H. Lin, Y. Huo, Y. Rong, R. Chen, T. I. Kamins, J. S. Harris, "X-ray diffraction analysis of step-graded $\text{In}_x\text{Ga}_{1-x}\text{As}$ buffer layers grown by molecular beam epitaxy," *Journal of Crystal Growth*, vol. 323, pp. 17–20, December 2013.
- [109] S. Essig, M. A. Steiner, C. Allebe, J. F. Geisz, B. Paviet-Salomon, S. Ward, A. Descoedres, V. LaSalvia, L. Barraud, N. Badel, A. Faes, J. Levrat, M. Despeisse, C. Ballif, P. Stradins, and D. L. Young, "Realization of GaInP/Si Dual-Junction Solar Cells With 29.8% 1-Sun Efficiency," *IEEE J. of Photovoltaics*, vol. 6, no. 4, pp. 1012–1019, July 2016.
- [110] J. N. Stirman, P. A. Crozier, David J. Smith, F. Phillipp, G. Brill and S. Sivananthan, "Atomic-scale imaging of asymmetric Lomer dislocation cores at the Ge/Si(001) heterointerface," *Appl. Phys. Lett.*, vol. 84, no. 14, pp. 2530-2532, April 2004.
- [111] H. Tran, W. Du, S. A. Ghetmiri, A. Mosleh, G. Sun, R. A. Soref, J. Margetis, J. Tolle, B. Li, H. A. Naseem, and S.-Q. Yu, "Systematic study of $\text{Ge}_{1-x}\text{Sn}_x$ absorption coefficient and refractive index for the device applications of Si-based optoelectronics," *J. Appl. Phys.*, vol. 119, no. 10, p. 103106, 2016.
- [112] P. Moontragoon, R. A. Soref, and Z. Ikonik, "The direct and indirect bandgaps of unstrained $\text{Si}_x\text{Ge}_{1-x-y}\text{Sn}_y$ and their photonic device applications," *J. Appl. Phys.*, vol. 112, no. 7, p. 073106, Oct. 2012.
- [113] S. Wirths, D. Buca, and S. Mantl, "Si–Ge–Sn alloys: From growth to applications," *Prog. Cryst. Growth Charact. Mater.*, vol. 62, no. 1, pp. 1–39, January 2016.
- [114] A. A. Tonkikh, C. Eisenschmidt, V. G. Talalaev, N. D. Zakharov, J. Schilling, G. Schmidt, and P. Werner, "Pseudomorphic GeSn/Ge(001) quantum wells: Examining indirect band gap bowing," *Appl. Phys. Lett.*, vol. 103, no. 3, p. 032106, Jul. 2013.
- [115] T. N. Pham, W. Du, B. R. Conley, J. Margetis, G. Sun, R. A. Soref, J. Tolle, B. Li, and S. -Q. Yu, "Si-based $\text{Ge}_{0.9}\text{Sn}_{0.1}$ photodetector with peak responsivity of 2.85 A/W and longwave cutoff at 2.4 μm ," vol. 51, no. 11, pp. 854–856, May 2015.

- [116] Wei Du, S Al-Kabi, S. A. Ghetmiri, H. Tran, T. Pham, B. Alharthi, A. Mosleh, J. Margetis, J. Tolle, H. A Naseem, M. Mortazavi, G. Sun, R. Soref, B Li, S.-Q. Yu, “Development of SiGeSn Technique Towards Mid-Infrared Devices in Silicon Photonics” ECS Transactions, vol. 75, no. 8, pp. 231-239, May 2016.
- [117] S. Wirths, D. Buca, Z. Ikonic, P. Harrison, A. Tiedemann, B. Holländer, T. Stoica, G. Mussler, U. Breuer, J. Hartmann, D. Grützmacher, and S. Mantl, “SiGeSn growth studies using reduced pressure chemical vapor deposition towards optoelectronic applications,” Thin Solid Films, vol. 557, pp. 183–187, April 2014.
- [118] J.-H. Fournier-Lupien, S. Mukherjee, S. Wirths, E. Pippel, N. Hayazawa, G. Mussler, J. M. Hartmann, P. Desjardins, D. Buca, and O. Moutanabbir, “Strain and composition effects on Raman vibrational modes of silicon-germanium-tin ternary alloys,” Appl. Phys. Lett., vol. 103, no. 26, pp. 263103, December 2013.
- [119] S. A. Ghetmiri, Y. Zhou, J. Margetis, S. Al-Kabi, W. Dou, A. Mosleh, W. Du, A. Kuchuk, J. Liu, G. Sun, R. A. Soref, J. Tolle, H. A. Naseem, B. Li, M. Mortazavi, and S.-Q. Yu, “Study of a SiGeSn/GeSn/SiGeSn structure toward direct bandgap type-I quantum well for all group-IV optoelectronics,” Opt. Lett., vol. 42, no. 3, pp. 387-390, February 2017.
- [120] J. Margetis, Y. Zhou, W. Dou, P. C. Grant, B. Alharthi, W. Du, A. Wadsworth, Q. Guo, H. Tran, S. Ojo, G. Abernathy, A. Mosleh, S. A. Ghetmiri, G. B. Thompson, J. Liu, G. Sun, R. Soref, J. Tolle, B. Li, M. Mortazavi, and S.-Q. Yu, “All group-IV SiGeSn/GeSn/SiGeSn QW laser on Si operating up to 90 K,” Appl. Phys. Lett., vol. 113, no. 22, p.p. 221104, November 2018.
- [121] W. Dou, S. A. Ghetmiri, S. Al-Kabi, A. Mosleh, Y. Zhou, B. Alharthi, W. Du, J. Margetis, J. Tolle, A. Kuchuk, M. Benamara, B. Li, H. A. Naseem, M. Mortazavi, and S. Q. Yu, “Structural and Optical Characteristics of GeSn Quantum Wells for Silicon-Based Mid-Infrared Optoelectronic Applications,” J. Electron. Mater., vol. 45, no. 12, pp. 6265–6272, 2016.
- [122] M. Jaros, “Simple analytic model for heterojunction band offsets,” Phys. Rev. B, vol. 37, no. 12, pp. 7112–7114, Apr. 1988.
- [123] P. C. Grant, J. Margetis, Y. Zhou, W. Dou, G. Abernathy, A. Kuchuk, W. Du, B. Li, J. Tolle, J. Liu, G. Sun, R. A. Soref, M. Mortazavi, and S.-Q. Yu, “Direct bandgap type-I GeSn/GeSn quantum well on a GeSn- and Ge- buffered Si substrate,” AIP Adv., vol. 8, no. 2, p. 025104, Feb. 2018.

Appendix A: Published, Submitted, and Planned Publications

In this work, chapter 4 was published in the Journal of Electronic Materials. Chapter 5 is submitted to the Journal of Applied Surface Science. The results of chapter 6 was published in Optical Materials Express. Chapter 7 results are planned to be published in the Journal of Applied Physics.

1. **Bader Alharthi**, Joe Margetis, Huong Tran, Sattar Al-kabi, Wei Dou, Seyed Amir Ghetmiri, Aboozar Mosleh et al. "Study of material and optical properties of $\text{Si}_x\text{Ge}_{1-x-y}\text{Sn}_y$ alloys for Si-based optoelectronic device applications," Optical Materials Express, vol. 7, no. 10, pp. 3517-3528, 2017.
2. **Bader Alharthi**, Joshua M. Grant, Wei Dou, Perry C. Grant, Aboozar Mosleh, Wei Du, Mansour Mortazavi, Baohua Li, Hameed Naseem, and Shui-Qing Yu, "Heteroepitaxial Growth of Germanium-on-Silicon Using Ultrahigh-Vacuum Chemical Vapor Deposition with RF Plasma Enhancement," Journal of Electronic Materials, vol. 47, no. 8, pp. 4561-4570, 2018.
3. **Bader Alharthi**, Wei Dou, Perry C. Grant, Joshua M. Grant, Wei Du, Timothy Morgan, Baohua Li, Mansour Mortazavi, Hameed Naseem, and Shui-Qing Yu, "Growth of High Quality Ge Buffer using Plasma Enhancement via UHV-CVD System for Photonic Devices Applications," submitted to Applied Surface Science.
4. **Bader Alharthi**, Wei Dou, Perry C. Grant, Huong Tran, Wei Du, Baohua Li, Hameed Naseem, and Shui-Qing Yu, "SiGeSn Double Barrier in GeSn Quantum Well for Laser Diode Applications," Planned to be submitted to Journal of Applied Physics.

A.1: List of Peer Reviewed Published Papers

1. **Bader Alharthi**, Joshua M. Grant, Wei Dou, Perry C. Grant, Aboozar Mosleh, Wei Du, Mansour Mortazavi, Baohua Li, Hameed Naseem, and Shui-Qing Yu, "Heteroepitaxial Growth of Germanium-on-Silicon Using Ultrahigh-Vacuum Chemical Vapor Deposition with RF Plasma Enhancement," Journal of Electronic Materials, vol. 47, no. 8, pp. 4561-4570, 2018.
2. **Bader Alharthi**, Joe Margetis, Huong Tran, Sattar Al-kabi, Wei Dou, Seyed Amir Ghetmiri, Aboozar Mosleh et al. "Study of material and optical properties of $\text{Si}_x\text{Ge}_{1-x-y}\text{Sn}_y$ alloys for Si-based optoelectronic device applications." Optical Materials Express, vol. 7, no. 10, pp. 3517-3528, 2017.
3. **Bader Alharthi**, Wei Dou, Perry C. Grant, Joshua M. Grant, Wei Du, Timothy Morgan, Baohua Li, Mansour Mortazavi, Hameed Naseem, and Shui-Qing Yu, "Growth of High Quality Ge Buffer using Plasma Enhancement via UHV-CVD System for Photonic Devices Applications," submitted to Applied Surface Science.
4. **Bader Alharthi**, Wei Dou, Perry C. Grant, Huong Tran, Wei Du, Baohua Li, Hameed Naseem, and Shui-Qing Yu, "SiGeSn Double Barrier in GeSn Quantum Well for Laser Diode Applications," Planned to be submitted to Journal of Applied Physics.
5. Perry C. Grant, Wei Dou, **Bader Alharthi**, Joshua M. Grant, Huong Tran, Gray Abernathy, Aboozar Mosleh, Wei Du, Baohua Li, Hameed Naseem, and Shui-Qing Yu, "UHV-CVD

Growth of High Quality GeSn Using SnCl₄: From Growth Optimization to Prototype Devices,” Submitted to Journal of Applied Physics.

6. Joe Margetis, Yiyin Zhou, Wei Dou, Perry C. Grant, **Bader Alharthi** et al. “All group-IV SiGeSn/GeSn/SiGeSn QW laser on Si operating up to 90 K,” Appl. Phys. Lett., vol. 113, no. 22, p.p. 221104, November 2018.
7. Wei Dou, **Bader Alharthi**, Perry C. Grant, Joshua M. Grant, et al. "Crystalline GeSn growth by plasma enhanced chemical vapor deposition." Optical Materials Express, vol. 8, no. 10, pp. 3220-3229, 2018.
8. Perry C. Grant, Wei Dou, **Bader Alharthi**, Joshua M. Grant, Aboozar Mosleh, Wei Du, Baohua Li, Mansour Mortazavi, Hameed A. Naseem, and Shui-Qing Yu. "Comparison study of the low temperature growth of dilute GeSn and Ge." Journal of Vacuum Science & Technology B, Nanotechnology and Microelectronics: Materials, Processing, Measurement, and Phenomena, vol. 35, no. 6, pp. 061204, 2017.
9. Wei Du, Sattar Al-Kabi, Seyed Ghetmiri, Huong Tran, T. Pham, **Bader Alharthi**, et al, “Development of SiGeSn Technique Towards Mid-Infrared Devices in Silicon Photonics.” ECS Transactions, vol. 75, no. 8, pp. 231-239, 2015.
10. Wei Dou, Seyed Ghetmiri, Sattar Al-Kabi, Aboozar Mosleh, Yiyin Zhou, **Bader Alharthi**, et al. “Structural and Optical Characteristics of GeSn Quantum Wells for Silicon-Based Mid-Infrared Optoelectronic Applications.” Journal of Electronic Materials, vol. 45, no.12, pp. 6265-6272, 2016.
11. Aboozar Mosleh, Murtada Alher, Larry Cousar, Hussam Abu-safe, Wei Dou, Perry C. Grant, Sattar Al-Kabi, S. A. Ghetmiri, **Bader Alharthi**, H. Tran, W. Du, M. Benamara, B. Li, M. Mortazavi, S.-Q. Yu, and H. Naseem, “Enhancement of Material Quality of (Si)GeSn Films Grown By SnCl₄ Precursor,” ECS Transactions, vol. 69, no. 5, pp. 279-286, 2015.

A2: List of Conference Proceedings

1. **Bader Alharthi**, A. Mosleh, J. Margetis, Sattar Al-Kabi, Seyed Ghetmiri, Huong Tran, et al., “CVD growth and characterization of Si_xGe_{1-x-y}Sn_y alloys for high efficiency multi-junction solar cells.” IEEE Photovoltaic Specialists Conference (PVSC), pp.2817–2821, 2016.